Ecole doctorale Sciences de l'Ingénieur (SPI)

Laboratoire Mécanique de Lille (UML)

Thèse pour l'obtention du grade de Docteur délivré par

l'Université de Lille

Discipline : Mécanique des solides, des matériaux, des structures et des surfaces

préparée et soutenue publiquement par

Lamyae Lakhal

le 14 octobre 2019

Influence of microstructure on the properties of composite materials reinforced with unidirectional fibers

---

Sous la direction de :

M. Yves BRUNET **M. Toufik KANIT**

Jury :

M. Thierry DESOYER, Professeur, Ecole centrale de Marseille	Président
Mme. Naima BELAYACHI, Maître de Conférence, Polytech'Orléans	Rapporteure
M. Issam DOGHRI, Professeur, Université catholique de Louvain	Rapporteur
M. Fouad ERCHIQUI, Professeur, Université du Québec (UQAT)	Examinateur
M. Yves BRUNET, Maître de Conférence , Université de Lille	Directeur de thèse
M. Toufik KANIT, Maître de Conférence , Université de Lille	Directeur de thèse

Ecole doctorale Sciences de l'Ingénieur (SPI)

Laboratoire Mécanique de Lille (UML)

Thèse pour l'obtention du grade de Docteur délivré par

l'Université de Lille

Discipline : Mécanique des solides, des matériaux, des structures et des surfaces

préparée et soutenue publiquement par

Lamyae Lakhal

le 14 octobre 2019

Influence de la microstructure sur les propriétés des matériaux composites renforcés de fibres unidirectionnelles

---

Sous la direction de :

M. Yves BRUNET **M. Toufik KANIT**

Jury :

M. Thierry DESOYER, Professeur, Ecole centrale de Marseille	Président
Mme. Naima BELAYACHI, Maître de Conférence, Polytech'Orléans	Rapporteure
M. Issam DOGHRI, Professeur, Université catholique de Louvain	Rapporteur
M. Fouad ERCHIQUI, Professeur, Université du Québec (UQAT)	Examinateur
M. Yves BRUNET, Maître de Conférence , Université de Lille	Directeur de thèse
M. Toufik KANIT, Maître de Conférence , Université de Lille	Directeur de thèse

Acknowledgements

Acknowledgements / Remerciements

When I first started my PhD, the day I will be facing my computer, filling an acknowledgments page, seemed so remote, almost unreal. And then during the last three years, whenever things perhaps got a little too intense, I often times found myself thinking about that very day, picturing how everything is going to work out eventually and how easy it will be to fill that last blank page.

Yet today, I can honestly say that this one of the most daunting pages that I have ever had to write. I am almost certain it is not the case for every PhD student and so I take the full responsibility for everything I claim here.

Condensing a three-year-worth of one's life in a couple of pages is no easy task, even less so for those who are blessed or cursed, which ever might be your take on the matter, with a sense of details. So I will be making a conscious effort to be brief and honest, to keep my emotions at bay and mostly, to give credit where it's due to the best of my abilities.

In advance, I would like to apologize for the very little I will be sharing, as not doing so will lead to a deeply personal writing that would be irrelevant in this context. I do believe that the people concerned will read through the lines anyway and that hopefully, my apology to them would be accepted.

So first, I would like to thank both my PhD supervisors: M. Kanit Toufik, for believing in me and for giving the atypical academic background I had to offer at the time the chance to prove once again that many roads, if not all, can and will lead to Rome. I will forever be grateful to you for this opportunity that has turned to be far greater and richer than what I had originally anticipated. Then, my deepest regards go to M. Yves Brunet, for everything I have learnt beside him in those three years, the amount of which can simply not be put into words. Thank you for the unconditional help and support, for timelessly sharing all your scientific insight with me day in and day out, for pushing me when necessary and slowing down when it could not have gone otherwise. I also am thankful for all the coffee breaks, the talks and discussions, the books and for Paul Auster who is now one of my favorite authors of all time, whom I might have never come across if it weren't for you. I am fully aware that this meagre testimony does not even begin to do these three years justice, but like the literary side of me often says: sometimes all the vocabulary in the world is just not enough.

I would then like to thank the jury members who have kindly accepted to take time to look into my work and suggest valuable modifications and adjustments: Mrs. Naima Belayachi, Mr. Fouad Erchiqui and Mr. Issam Doghri. A special mention to Mr. Thierry Desoyer who had presided this jury. I would also like to express my sincere gratitude for the aforementioned jury members for all their interesting questions and insights during my PhD defense which animated and enriched the discussion in the most positive way.

Last but not least, I would like to thank what I call my backstage crew, the one in the dark keeping things rolling. First, I would like to thank Youcef and Rachid for introducing me to the software part my work, for sharing their knowledge and even their workspace at times with me and for being my first colleagues and friends when I arrived. Special acknowledgments also go to my best friend Nawal, simply for being who she is, for always being there for me whenever I needed her, for our countless four pm coffee breaks that undeniably helped the both of us let off some of the steam that inevitably builds up. Thank you for all the night-ins, the delicious foods, the memes, the laughter and every other little bits and pieces. I wish you the very best luck for the remainder of your PhD and here is to many more years of friendship to come.

The list could go on endlessly, so i will try to be short once again. I would like to thank all the ladies working at the coffee corner of the library for being so benevolent, for sharing some of our special moments and for the bond we had by the end of the three years. I am also deeply and forever grateful for the old and the new friends I have luckily encountered on this journey in different contexts ranging from work to gym to mundane day-to-day life: Amine, Alaa, Ayoub, Mokhtar, Rami, Lisa, Sara, Charaf-eddine, Tarek, Abdel… and all the others that I might have forgotten. To all of you: thank you.

A big thank you obviously goes to my parents for solidly and consistently supporting me since 1993, to Ilyass, Safae and Hanae without whom nothing would be the same, and to the rest of my family for their love.

To conclude, my most profound gratitude goes to the mysterious machinery of things that despite every wrong choice I might have made, had still managed to set me on the right path towards what had changed my life utterly. No matter where this same machinery may lead, I was, I am and I will forever be greatly thankful for that which shall not be named.

Lamyae Lakhal

November 16th, 2019

Abstract/Résumé

Abstract

Throughout this work, the influence of microstructures of non-overlapping aligned fiber reinforced composites on macroscopic elastic properties has been quantified with numerical homogenization on FEM simulations. The radial distribution function (Rdf) has proven to be the best second order correlation to describe fiber spatial distributions. Numerical samples with controlled Rdfs were built with simulated annealing and their effective values were evaluated. Due to the non-overlapping condition, Rdf exhibits a peak for distances from 1 to 1.5 diameter.

When Rdf peak increases, elastic moduli increase as well. From this result, new bounds that frame any equilibrium system of aligned fiber composites were established. The corresponding microstructures for lower and upper bounds were respectively a Percus-Yevick distribution of fibers and packed fibers.

Résumé

L'influence de la microstructure sur l'élasticité à l'échelle macroscopique de matériaux composites renforcés par des fibres alignées sans chevauchement est quantifiée par homogénéisation numérique (FEM). La fonction de paires (Rdf) s'est montrée comme étant la corrélation du second ordre la plus efficace pour décrire la répartition spatiale des fibres. Des échantillons numériques dont la Rdf est contrôlée ont été construits par « «simulated annealing » et leurs propriétés effectives calculées. La condition de non-chevauchement entraine un pic de la Rdf pour des distances comprises entre 1 et 1,5 diamètre.

Les coefficients d'élasticité augmentent avec le pic de la Rdf. Ces résultats ont conduit à établir de nouvelles bornes pour les systèmes de fibres parallèles en équilibre. Les microstructures correspondant aux bornes inférieures et supérieures sont respectivement une répartition des fibres de Percus-Yevick et une agglomération des fibres.

Table of Contents

List of notations

Notations

a	Scalar
$\boldsymbol{a}$	Vector
$\underline{a}$	Second order tensor
$\underline{\underline{a}}$	Fourth order tensor
$\langle \ \rangle$	Volume averaging

Abbreviations

KUBC	Kinematic Uniform Boundary Conditions
PBC	Periodic Boundary Conditions
PBCT	Periodic Boundary Conditions for Thermal conductivity
PY	Percus-Yevick
Rdf	Radial distribution Function
RSA	Random Sequential Adsorption
RVE	Representative Volume Element
SA	Simulated Annealing
SD	Sticky Disks
UGT	Uniform Gradient Temperature

Symbols

β	Boltzmann factor
λ	Thermal conductivity
λ_i	Thermal conductivity of inclusions
λ_m	Thermal conductivity of matrix

μ	Effective shear modulus
μ_i	Shear modulus of inclusions
μ_m	Shear modulus of matrix
υ	Poisson coefficient
ρ	Particle density
$\rho_N^{(n)}$	n −particle density
A	Integral range
C	Contrast
$C(0)$	Local variance
$C(h)$	Covariance
C_{S_1}	Coarseness
d	Fiber diameter
E	Young modulus
E_i	Young modulus of inclusions
E_m	Young modulus of matrix
$g(r)$	Radial distribution function
g_N^n	n −particle distribution functions
I	Characteristic function
k	In-plane effective bulk modulus
K_i	Bulk modulus of inclusions
K_m	Bulk modulus of matrix
N	Number of inclusions
r	Spatial coordinates
S_n	n −point correlation functions
U	Potential energy
V_f	Volume fraction of inclusions

Introduction

The first materials used by Men were wood and leather due to availability and interesting mechanical properties. These organic composites are naturally produced with no control over their composition and physical behavior. With fire domestication, metals and ceramics were created to obtain stiffer but inevitably heavier materials. It is until the nineteenth century that the first elastomers were used, namely natural rubber and later, with the progress of petrochemical industries, its synthetic version. While being very light, the mechanical behavior of elastomers restrained their use to very specific applications. The ever growing industrial demand in the twentieth century has led to the production of new stiff and still light materials: the composites. They mimic internal structures of natural materials such as wood and are made by adding stiff reinforcements (fibers, grains,…) to a light matrix. The obtained materials have enhanced mechanical properties with both the density of elastomers and stiffness of metals and ceramics. As composites are built with at least two phases of different properties, it is difficult to predict their exact response to external strains or stresses but generally possible to approximately determine the properties of a fictive homogeneous equivalent material (HEM).

The homogenization process was first initiated by Einstein **(Einstein 1906)** in his calculations of the viscosity of suspensions based on the analogy between momentum flux density tensors and stress tensors. In case of elasticity of heterogeneous media, the crucial work was that carried out by Eshelby **(Eshelby 1957)** about the stress and strain fields in an infinite elastic matrix containing an elastic inclusion. He suggested an analytical solution for effective values based on the uniformity of both strain and stress fields inside the inclusion. This pioneer work by Eshelby has spawned a large amount of studies about homogenization techniques.

Homogenization has since been the focus of many works given that the effective properties of the composite also equivalent to those of the HEM are very sensitive to the distribution of each phase. Due to fabrication processes, this distribution or microstructure is often not well known and effective properties can only be determined in the frame of bounds, the most known being those of Hashin and Shtrikman (**Hashin-Shtrikman (1962) (1963)**).

The aim of this study is to quantify the influence of microstructure on mechanical behavior of two-phased composites by numerical simulations on adequate samples. This necessitates in addition of the laws of the behavior of each individual component, a mathematical modelization of the spatial distribution of each phase.

For simplicity, mechanical behavior will be limited to linear elasticity and sample geometries to similar parallel fiber reinforced composites for which the physical problem can be reduced

to a two dimensional one. All the results and the tools developed in this study can easily be generalized to 3D situations in which fibers are replaced by spheres. More complex laws of behavior can also be tackled. Though the restriction to 2D situations does not include all fiber reinforced composites, it is of high interest when strong anisotropy is required in mechanical behavior.

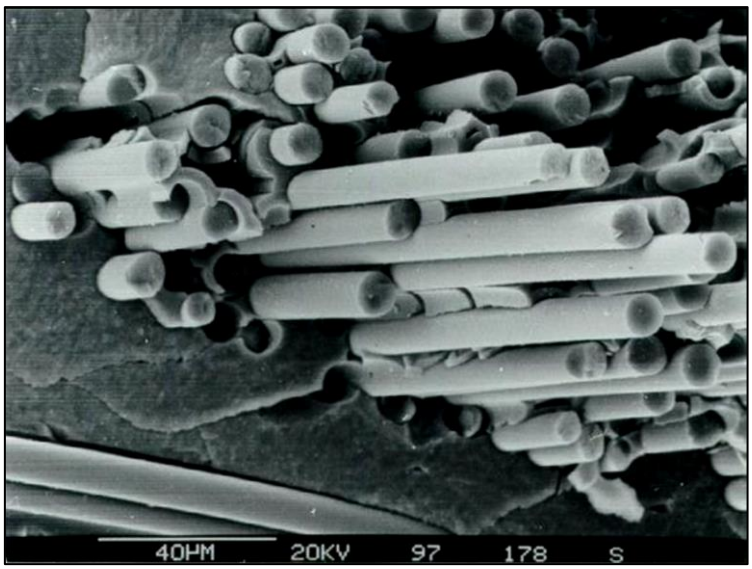

Fiber-reinforced ceramic composed of SIC fibers and SIC matrix
(Wikipedia)

The present study is on non-overlapping fiber composites which correspond to real industrial composites, nevertheless, overlapping configurations will be used for comparison as their microstructures are described by very simple statistics according to a Poisson law.

This manuscript will be structured in two parts: part I will tackle the statistical tools for morphology description, homogenization techniques and finite element methods and part II will provide a detailed presentation of this work. As the knowledge used in this work comes from different fields of science: mechanical engineering, statistical physics of liquid state, optimization processes,… The sources from literature will not be provided in a dedicated chapter but rather introduced when necessary.

In part I, tighter bounds than those of Hashin and Shtrikman will be introduced. They usually take the microstructures into account through the two and three-point probability functions. It will be shown that for identical aligned fiber reinforced composites, the radial distribution function (Rdf) contains more information about microstructure and could be a more suitable morphological descriptor. The heuristic simulated annealing method initially developed for optimization processes will be adapted to generate samples controlled by their Rdf. The tools based on numerical homogenization that will allow the determination of effective elastic moduli will be validated.

Part II is structured in four chapters in which the reasoning is progressively built leading up to the determination of new bounds on effective elastic moduli suitable for non-overlapping equilibrium systems. The following questions will be addressed in the different chapters.

- What are the relevant tools to describe microstructures from a physical point of view?

- Is contrast an important parameter in elaborating models of elastic behavior for composites?

- How does the Rdf of fibers capture microstructure features that affect the elasticity of composites?

- What microstructures correspond to the highest and lowest stiffness of composites?

Part 1

Chapter 1

Morphology

The macroscopic properties of heterogeneous materials are determined not only by the characteristics of each of their components but also highly by the details of the microstructure itself. Hence, the quantitative morphological characterization of random media, especially two-phased media in our case, becomes important. The different morphological parameters that affect the effective properties are the shape and the local distribution of each phase. Over the years, the significant effect that the microstructure has on the properties of composites had made predicting their reliability and their behavior questionable and led to the use of high safety factors in real applications. An accurate modelling of composite materials in different industrial sectors has then become a priority.

In the two-phase case of disconnected inclusions within a matrix, a way to describe the morphologies of heterogeneous media is the statistical mechanics, a fundamental field of modern physics. It was developed in the second half of the 19th century and was mainly the work of Ludwig Boltzmann along with other scientists such as J.C Maxwell and J.W Gibbs. It is an approach based on statistical methods that allow a microscopic description of the physical behavior. Statistical mechanics is defined as a set of pure mathematical techniques that can be applied to almost any physical system even with large degrees of freedom, no matter what laws that system obeys. This aspect of statistical mechanics is what makes it one of the pillars of modern physics: it almost certainly remains valid throughout the changes between old theories, laws and approximations and newly discovered ones, making it a highly reliable tool regardless of the constant occurring updates in the scientific domain.

The focus in this work is on two-phase heterogeneous microstructures for which the morphological descriptors are different types of correlation functions, see **Torquato (1998)**.

This chapter is divided into two sections. The first one introduces the morphological descriptors provided by statistical-physics literature and the second describes the methods we used in this study to generate samples according to specific morphological descriptors.

I- Morphological descriptors

In this section, we start with describing general two-phase media and progressively focus on the special case of equilibrium two-dimensional disk systems which is a good representation of cross-sections of parallel fiber reinforced composites. As these tools are initially used in statistical physics, an intermediate sub-section for identical particles will be introduced.

I-1 Two-phase media

I-1-1 Characteristic function

Each sample of a total volume $V = V_1 \cup V_2$ representative of a heterogeneous random medium is composed of two regions: a phase 1 region V_1 and a phase 2 region V_2.

In practical situations, composite materials are rarely made of two phases as shown on figure I-1 of a cemented granular media in which variation in the granular phase properties can be observed.

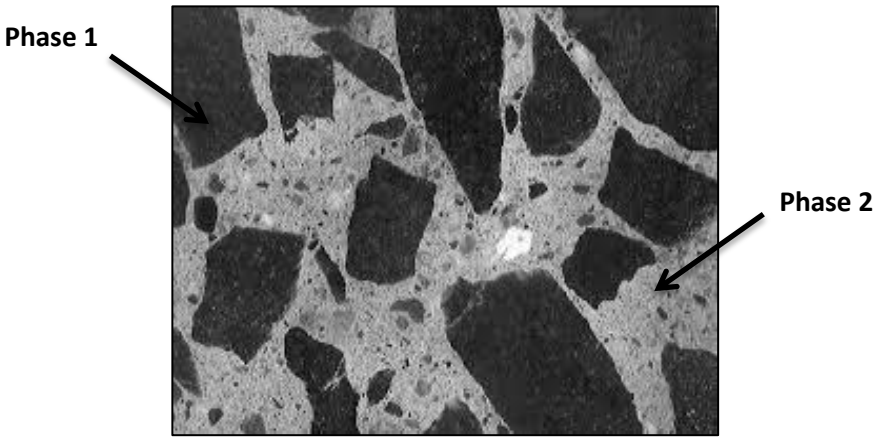

Figure I-1. A cross-section of a cemented granular media

A means for modelling such composites is to consider two uniform phases by introducing the characteristic function $I(\boldsymbol{x})$ of phase 1 defined by :

$$I(\boldsymbol{x}) = \begin{cases} 1, & \boldsymbol{x} \in \mathrm{V}_1 \\ 0, & \boldsymbol{x} \in \mathrm{V}_2 \end{cases} \quad (1)$$

$I(\boldsymbol{x})$ is a separate random variable that takes the values 0 or 1 according to whether the position vector is in V_1 or V_2 (figure I-2).

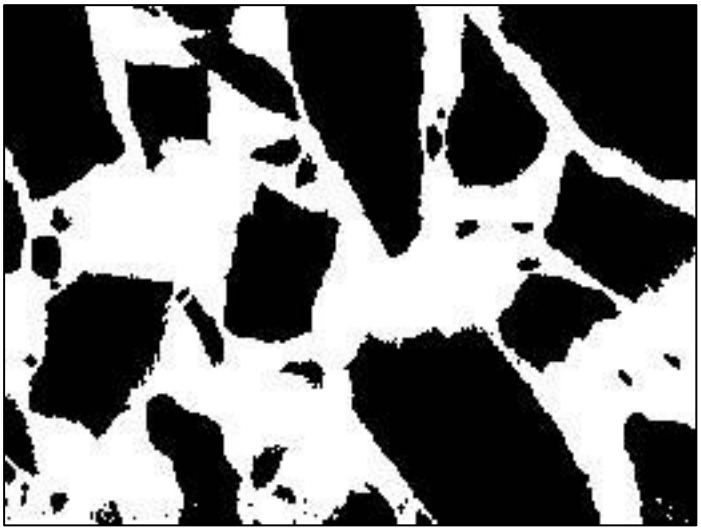

Figure I-2. The characteristic function $I(x)$ of a cross-section of the cemented granular media in figure I-1

A complete knowledge of $I(\boldsymbol{x})$ gives a full description of the sample's morphology.

The first information given by the characteristic function is the volume fraction of phase 1:

$$V_f = \frac{1}{V}\int_V I(\boldsymbol{x})\, d\boldsymbol{x} \tag{2}$$

I-1-2 The n −point probability functions

Further than the integral form of V_f in equation (2), the characteristic function $I(x)$ can provide finer information about the microstructure through the n −point probability functions S_n that are statistical specifications of two-phased microstructures **Torquato and Stell (1982).** The n −point probability functions are defined according to the relation:

$$S_n(\boldsymbol{x_1}, \dots, \boldsymbol{x_n}) = \langle \prod_{i=1}^{n} (I(\boldsymbol{x_i}) - V_f) \rangle \quad (3)$$

Where the brackets ⟨ ⟩ denote volume averaging.

The physical interpretation of $S_n(\boldsymbol{x_1}, \dots, \boldsymbol{x_n})$ is the probability of simultaneously finding n points with positions $x_1, \dots, x_n$ all in one phase, namely the particle phase 1.

For statistically homogeneous and isotropic media, the n −point probability function depends solely on the relative positions with regard to an arbitrary point $\boldsymbol{x_1}$:

$$S_n = S_n(\boldsymbol{x_{12}}, \dots, \boldsymbol{x_{1n}}) \quad (4)$$

Where $\boldsymbol{x_{1i}} = \boldsymbol{x_i} - \boldsymbol{x_1}$

When $n \to \infty$ and all the S_n are known, the n −point probability functions provide a full description of the heterogeneous medium.

The n −point probability functions S_n is a statistical method used to describe any given two-phased random heterogeneous media based only on the relative position of each phase. However, calculating the different $S_{1,\dots,}S_n$ remains a difficult task that requires a highly significant computational time.

I-2 Systems of identical particles

For a macroscopic system consisting of N identical particles enclosed in a volume V, the particle density $\rho = \frac{N}{V}$ holds the same information as volume fraction V_f.

For such systems, the required information is limited to the particle-center distribution and the n −point probability functions S_n can be replaced by a mathematically more simplified tool, namely the n −particle distribution functions also called the n −body distribution functions in cases of more general distributions of inclusions that are not necessarily particles.

I-2-1 The n -particle densities

Let $\mathbf{r}^n = \mathbf{r}_1, \dots, \mathbf{r}_n$ be the coordinates of the N particles. The n −particle densities $\rho_N^{(n)}(\mathbf{r}^n)$ are defined by the probability density of finding n particles $(n \leq N)$ of the system with coordinates in the volume element $d\mathbf{r}^n$ of Gibbs space regardless of the positions of the $N - n$ remaining particles $\rho_N^{(n)}(\mathbf{r}^n)d\mathbf{r}^n$. It results from integration on the whole volume V that:

$$\int \rho_N^{(n)}(\mathbf{r}^n)d\mathbf{r}^n = \frac{N!}{(N-n)!} \quad (5)$$

We note that the Gibbs space is usually a $6N$ space, $3N$ coordinates and $3N$ velocities or momentums in which a point corresponds to a state of the system. In this study, we focus on the localization of particles and the above definitions are obtained by summing on all the possible velocities.

Since the particles are identical, $\frac{N!}{(N-n)!}$ is the ratio of permutations between N and the $N - n$ particles. The sum of the probability of placing n particles among N shows all the possibilities of permuting all the N particles and also the remaining $N - n$.

From equation (5) we can write:

$$\int \rho_N^{(1)}(\mathbf{r})d\mathbf{r} = N \quad (6)$$

The single particle density of a homogeneous system is then equal to the overall number density:

$$\rho_N^{(1)}(\mathbf{r}) = \frac{N}{V} = \rho \quad (7)$$

In the special case of a uniform low density (without interaction) system of particles, the pair density becomes:

$$\rho_N^{(2)} = \rho^2\left(\frac{N-1}{N}\right) \quad (8)$$

The second particle density being $\rho\left(\frac{N-1}{N}\right)$.

The particle densities can also be defined in terms of δ-functions of position. The ensemble average $< \delta(\mathbf{r} - \mathbf{r}_1) >$ is a function of the coordinate $\mathbf{r}$ but is independent of the particle label ($n = 1$). Summing over all the N particles is then equal to N times the contribution from any single particle and we have:

$$\rho_N^{(1)}(\mathbf{r}) = \langle \sum_{i=1}^{N} \delta(\mathbf{r} - \mathbf{r}_i) \rangle \tag{9}$$

Which implies that the probability density of finding one particle at $\mathbf{r}$ and one at $\mathbf{r}'$ is:

$$\rho_N^{(2)}(\mathbf{r}, \mathbf{r}') = \langle \sum_{i=1}^{N} \sum_{j=1}^{N} \delta(\mathbf{r} - \mathbf{r}_i)\delta(\mathbf{r}' - \mathbf{r}_j) \rangle \tag{10}$$

With $i \neq j$.

From equation (10) we have:

$$\langle \frac{1}{N} \sum_{i=1}^{N} \sum_{j=1}^{N} \delta\big(\mathbf{r} - \mathbf{r}_j + \mathbf{r}_i\big) \rangle = \frac{1}{N} \int \rho_N^{(2)}(\mathbf{r}' + \mathbf{r}, \mathbf{r}') d\mathbf{r}' \tag{11}$$

Actually :

$$\langle \frac{1}{N} \sum_{i=1}^{N} \sum_{j=1}^{N} \delta\big(\mathbf{r} - \mathbf{r}_j + \mathbf{r}_i\big) \rangle = \langle \frac{1}{N} \int \sum_{i=1}^{N} \sum_{j=1}^{N} \delta\big(\mathbf{r}' + \mathbf{r} - \mathbf{r}_j\big)\delta\big(\mathbf{r}' - \mathbf{r}_i\big) d\mathbf{r}' \rangle$$

In the next section, equation (11) will allow a representation of the radial distribution function (equation (15)).

I-2-2 The n -particle distribution functions

In the case of N identical particles, the n −particle distribution function is an easier and less time costly representation of the system than the n −point probability function S_n **Hansen and McDonald (2006)** .

The n −particle distribution function $g_N^{(n)}(\mathbf{r}^n) = g_N^{(n)}(\mathbf{r}_1, \dots, \mathbf{r}_n)$ is defined in regards to the corresponding densities of particles by:

$$g_N^{(n)}(\mathbf{r}^n) = \frac{\rho_N^{(n)}(\mathbf{r}_1,\dots,\mathbf{r}_n)}{\prod_{i=1}^{n} \rho_N^{(1)}(\mathbf{r}_i)} \tag{12}$$

Where $\prod_{i=1}^{n} \rho_N^{(1)}(\mathbf{r}_i)$ is the probability of placing n particles among N.

When particles are randomly placed one by one according to a Poisson law in which each position within the volume is equiprobable, $\prod_{i=1}^{n} \rho_N^{(1)}(\mathbf{r}_i)$ is the probability of placing a first one times the probability of placing a second and so on till $i = n$ and $\rho_N^{(1)}(\mathbf{r}_i)$ becomes independent of position $\boldsymbol{r}_i$ so $\rho_N^{(1)}(\mathbf{r}_i) = \rho$ and equation (12) reduces to:

$$\rho^n g_N^{(n)}(\mathbf{r}^n) = \rho_N^{(n)}(\mathbf{r}^n) \tag{13}$$

The particle distribution function measures the deviation of a system from utter randomness. Unlike the n −point probability function S_n , the n −particle distribution function $g_N^{(n)}$ is only used to statistically describe systems of identical particles.

In the case of homogeneous systems of particles, the pair distribution function $g_N^{(2)}(\boldsymbol{r}_1, \boldsymbol{r}_2)$ depends only on the distance between two particles $\boldsymbol{r_{12}} = |\boldsymbol{r}_1 - \boldsymbol{r}_2|$. Moreover, if these systems are isotropic, the pair distribution function is reduced to the radial distribution function $g(r)$ (**Rdf**) by a simple angular integration in the cross-plane section in which $\boldsymbol{r_{12}}$ can be replaced by the distance $r = |\boldsymbol{r_{12}}|$.

So,

$$\mathrm{g_N^{(2)}(r_1, r_2) = g(r)} \tag{14}$$

From equations (11) and (13), $g(r)$ can be expressed in terms of δ functions:

$$g(r) = \frac{1}{\rho}\left\langle \frac{1}{N} \sum_{i=1}^{N} \sum_{j=1}^{N} \delta\left(\mathbf{r} - \mathbf{r}_j + \mathbf{r}_i\right) \right\rangle \tag{15}$$

The simplest form possible of Rdf assumes that no correlation exists between particles which could be the case for non-interacting penetrable or, in the dilute limit, impenetrable particles giving:

$$g(r) = 1$$

In statistical mechanics, the radial distribution function $g(r)$ of a system of particles (atoms, molecules, etc.), describes how the system's density ρ varies as a function of the distance r from a reference particle. Rdf is the easiest two-point correlation function and was initially introduced for pairwise additive interactions in liquids. However, as any spatial correlation function, $g(r)$ could be used to describe both spatial distributions of moving or unmoving bodies.

A simple physical interpretation of $g(r)$ is the number of fiber centers located in a volume dr at a distance r from a test fiber, divided by the number of fibers given by a uniformly distributed fiber field. $g(r)$ can then be defined as:

$$g(r) = \frac{n_c}{n_p} \tag{16}$$

Where n_c is the number of fiber centers within the area of the circle (blue disks in figure I-3) and n_p is the number of fiber centers within the circle's area following a Poisson law as shown in figure I-3.

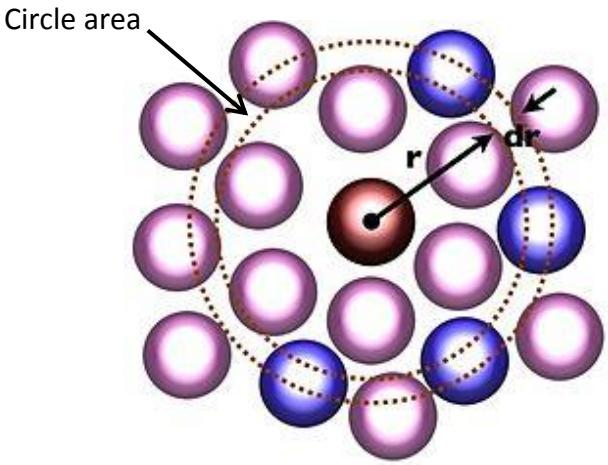

Figure I-3. Illustration of pair distribution function $g(r)$ in which the blue particles are those which contribute to the value of $g(r)$

In any case, particles separated by a large distance, much larger than the range of particle interactions, can be expected to have no influence on one another's position (figure I-3) and therefore approach the ideal-gas limit $g(r) = 1 \ \forall r$ when r is higher than the interaction range:

$$g(r) = 1 \tag{17}$$

Rdf is directly related to the local density around a single particle (equation (16)). Though its physical interpretation could let think that Rdf bears resemblance with inter-fiber spacing probability, they are fundamentally different as it will be shown in chapter 6. Actually, Rdf contains relevant information about how particles interact.

Lu and Torquato (1990b) have introduced a generalized formula of S_n based on the n −body distribution functions g_n of identical particles as follows:

$$S_n(\boldsymbol{x^n}) = 1 + \sum_{k=1}^{\infty} \frac{(-1)^k \rho^k}{k!} \int \dots \int g_k(\boldsymbol{r^k}) \times \prod_{j=1}^{k} \left[\left[1 - \prod_{i=1}^{n} \left[1 - I(\boldsymbol{x_i} - \boldsymbol{r_j}) \right] \right] \right] d\boldsymbol{r_j} \quad (18)$$

Where $\mathbf{r}^N \equiv \{\mathbf{r}_1, \dots, \mathbf{r}_N\}$ are the center-of-mass coordinates specifying the positions of particles.

This relation allows both the n −body distribution function g_n and the n −point probability function S_n to be deduced from each other.

In the case of identical particles, g_n provides as much information about the microstructure of the random system as S_n, while being an easier statistical characterization tool to determine and requiring less computational time. That is why, in our case, we chose to work with g_n that is going to be detailed in the next section.

For the sake of numerical convergence accuracy, our work will be limited to $n = 2$ for both functions.

I-3 Equilibrium systems

Equilibrium systems are systems in which the particle distribution leads to minimal energy. These systems are those observed in nature, for instance: molecules of ideal gases and liquids. Their typical radial distribution functions are sketched in figure I-4.

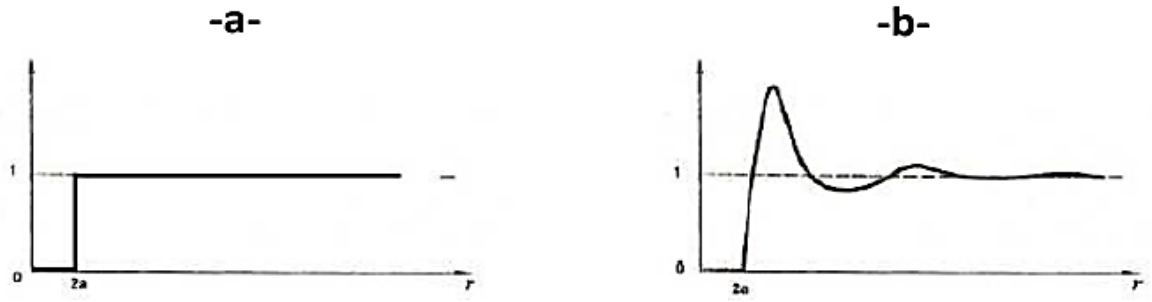

Figure I-4. Pair distribution function $g(r)$ for a monoatomic: **(a)** ideal gas and **(b)** liquid

Perfect gases are theoretically composed of many randomly moving point particles whose only interactions are perfectly elastic collisions and $g(r) = 1$ while for liquids, $g(r)$ is the result of the balance between molecular attraction and repulsion such as the forces derived from the Leonard-Jones potential. For both cases, $g(r) = 0$ at very short distances (molecular diameter) due to the Pauli Exclusion Principle which is equivalent to a non-overlapping condition for solid particles.

When particles interact through an ensemble of forces that derive from an interaction potential $U(r)$, this potential can be built with successive contributions of two-body interaction and many-body interactions (figure I-5):

$$U(r) = \sum_{i,j} u_{i,j}(r) + many - body\ interactions \quad (19)$$

Where $u_{i,j}$ is the direct interaction potential between particles i and j.

All $u_{i,j}$ are identical for homogeneous and isotropic systems: $u_{i,j} = u$

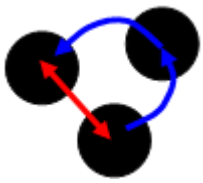

Figure I-5. Two-body interaction (red) and many-body interactions (blue)

For equilibrium systems, Ornstein-Zernike suggested similar decomposition for correlation functions in which the total correlation function $h(r) = g(r) - 1$ is defined by:

$$h(r) = c(r) + b(r) \tag{20}$$

Where $c(r)$ is the direct correlation function between two single particles and $b(r)$ is a convolution product that represents the many-body interactions:

$$b(r) = \rho \int c(r - r')h(r')dr' \tag{21}$$

Due to screening effect, the direct correlation function $c(r)$ is at short range while $b(r)$ can be at long range depending on the interaction potential. The influence of $c(r)$ is often greater than that of $b(r)$. In order to determine $h(r)$ or $g(r)$, the Ornstein-Zernike equation

requires an additional closure relation such as the well-known **Percus-Yevick (PY) (1958)** approximation:

$$c(r) = g(r)\left[1 - e^{[-\beta u(r)]}\right] \tag{22}$$

In the case of hard spheres of diameter d, the two-particle interaction potential is:

$$\begin{cases} u(r) = 0 & for\ r > d \\ u(r) \to +\infty & for\ r < d \end{cases} \tag{23}$$

The first evaluation of $c(r)$ for hard spheres was given by Percus and Yevick by determining local density fluctuations leading to a minimal energy of the system.

For 3-dimensional systems of particles:

$$c(r) = 0 \qquad for\ r > d$$

$$c(r) = \frac{-\left(1 + 2V_f\right)^2}{\left(1 - V_f\right)^4}\left(\frac{V_f}{2}r^3 + 1\right) + 6V_f\frac{-\left(1 + \frac{V_f}{2}\right)^2}{\left(1 - V_f\right)^4}r \qquad for\ r < d$$

$g(r)$ can then be calculated by Fourier or Laplace transforms of (20) and (21).

For 2-dimensional systems, the calculations are similar but with no analytical solutions, and the corresponding $g(r)$ is sketched on figure I-6.

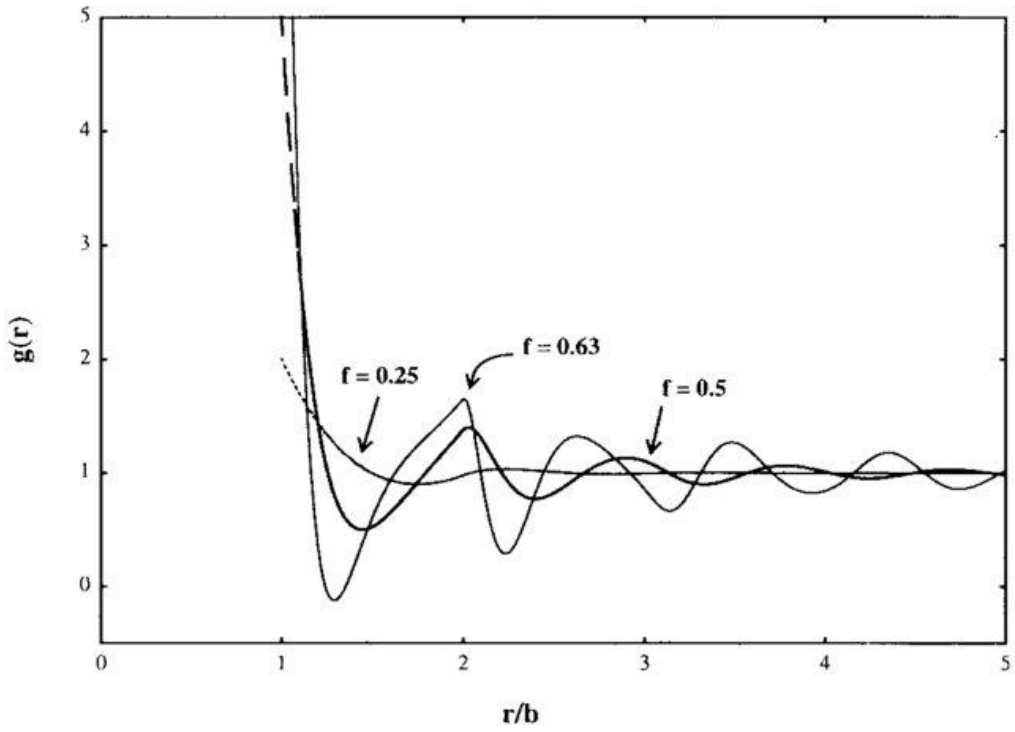

Figure I-6. Percus-Yevick pair distribution function for volume fractions $V_f = 63\%$, $V_f = 50\%$ and $V_f = 25\%$ **John R. and Kamal (1990)**

In this work, equilibrium systems will be solutions of the Ornstein-Zernike equation supplemented by PY approximation.

I-4 Systems of disks (2-Dimensional systems)

In cross-sections of parallel fiber reinforced media, the morphologies are similar to 2D disk systems which can either be overlapping (fully penetrable disks) or non-overlapping (hard disks). Their microstructures can be described with the aforementioned morphological descriptors applied in a 2D plane.

I-4-1 Radial distribution function

Rdf is the easiest two-point correlation function that can be rapidly extracted from both simulated and practical samples. In case of dispersion in fiber sizes, the covariance or S_2 is more suitable than Rdf, however for identical ones, it does not contain more information and is very time costly in terms of computations

For isotropic systems built with parallel fibers of identical circular section, the radial distribution function $g(r)$ is given by:

$$g(r) = \frac{1}{\rho N} \sum_i \sum_{j \neq i} \delta(|\mathbf{r} - \mathbf{r}_{ij}|) \tag{24}$$

Where r_i is the position of fiber centers in a transverse plane perpendicular to the fiber direction.

$\rho = \frac{N}{S}$ is the number N of fibers per unit transverse surface S of the specimen and $\boldsymbol{r}$ the dimensionless position vector such as $|\boldsymbol{r}|$ is equal to 1 at contact between fibers.

As long as the fiber distribution is not structured by n −fiber groups ($n > 2$) such as clusters (figure I-7), the radial distribution function is known for its skill to capture all principal information on microstructure **Rintoul and Torquato (1997)**.

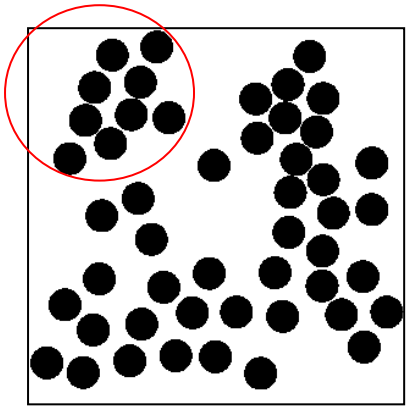

Figure I-7. Examples of n −fiber groups (clusters) : 9 −fibers group surrounded by the red circle

For overlapping fibers, the equilibrium system follows a Poisson law and all the n −particle distribution functions $g_N^{(n)}$ are equal to 1 for all values of r, especially $g(r) = 1 \quad \forall r$. Non-overlapping fiber equilibrium systems are equivalent to the full hard disk fluid problems for which full solutions have been determined. Among these solutions, the Percus-Yevick approximation is one of the most used in order to evaluate Rdf.

Many have carried out the work, **Boyer *et al.* (1995)**, by solving the Ornstein-Zernike the PY approximation for various dimensions D.

Unlike for rods $(D = 1)$ and spheres $(D = 3)$, there are no analytical solutions for systems of disks $(D = 2)$ and only numerical solutions are available in literature (figure I-8).

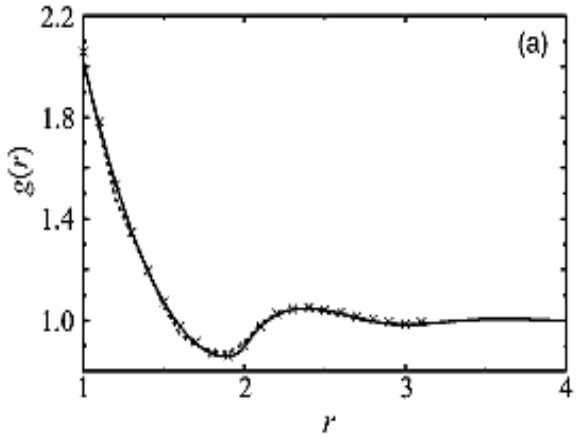

Figure I-8. The correlation function g(r) computed from the PY equation for $V_f = 36.29\%$ **Adda-Bedia *et al.* (2008)**

For dispersion in fiber sizes or shapes, which will not be the case in this work, the Rdf is not fully suitable for it only takes into account the fiber centers coordinates but fails to identify the nature of the inclusions. In this case, the 2 −point probability function S_2 is more useful. However S_2 is generally time costly in terms of computations.

I-4-2 The 2 −point probability function S_2

The 2 −point probability function S_2 is equivalent in nature to the central covariance function defined with the relation:

$$\mathrm{C_I}(\mathbf{r}) = < \big(\mathrm{I}(\mathbf{x}).\mathrm{I}(\mathbf{x}+\mathbf{r})\big) > \tag{25}$$

Where $\mathrm{I}(\mathbf{x})$ is the characteristic function.

From equation (2) we have:

$$\mathrm{C_I}(0) =< \big(\mathrm{I}(\mathbf{x}).\mathrm{I}(\mathbf{x})\big) > = \mathrm{V_f} \tag{26}$$

When $\mathbf{r} \to \infty$ the solution is obtained by introducing:

$$J = I - \langle I \rangle \tag{27}$$

$\langle J \rangle = 0$ so C_J is an autocorrelation function , hence : $C_J(r \to \infty) = 0$ and:

$$C_J(\boldsymbol{r}) = \langle J(\boldsymbol{x}).J(\boldsymbol{x}+\boldsymbol{r}) \rangle \tag{28}$$

$$C_J(\boldsymbol{r}) =< (I(\boldsymbol{x}) - < I >)(I(\boldsymbol{x}+\boldsymbol{r}) - < I >) > \tag{29}$$

We can then deduce that for isotropic systems:

$$C_I(r \to \infty) = C_J = V_f^2 \tag{30}$$

The $2-$point probability function $\mathrm{S_2}$ can be linked to the covariance $\mathrm{C_I}$ and C_J.

It is proportionate to C_J :

$$S_2(r) = k_1.C_J(r) \tag{31}$$

$\mathrm{S_2}$ being a probability function, the value of k_1 is determined by the normalization condition:

$$\int_0^\infty S_2(x)dx = 1 \tag{32}$$

and naturally:

$$\lim_{r\to\infty} S_2(r) = 0 \tag{33}$$

For overlapping fibers, S_2 can be determined through equation (18) introduced above, with all $g_N^{(n)}(r) = 1$ and is given by **Lu and Torquato (1990)** plotted in figure I-9.

$$S_n(x^n) = \exp[-\rho V_n(x^n)] \tag{34}$$

Where $V_n(x^n)$ is the union volume of n identical particle centered at x^n .

And especially for $n = 2$ we have:

$$S_2(r) = \exp(-\rho V_2(\boldsymbol{r})) \tag{35}$$

Where $V_2(\mathbf{r})$ is the union volume of two fibers whose centers are separated by a distance r**.**

$$V_2(r) = \frac{\pi D^2}{2} - \frac{D^2}{2}\left[\cos^{-1}\frac{r}{D} - \frac{r}{D}\sqrt{1-\frac{r^2}{D^2}}\right]H(D-r) \tag{36}$$

Unlike $g(r)$, $S_2(\boldsymbol{r})$ does not contain connectedness information **Torquato (1998).**

With r being the distance between two observation region centers, D the fiber diameter and $H(x)$ the Heaviside step function.

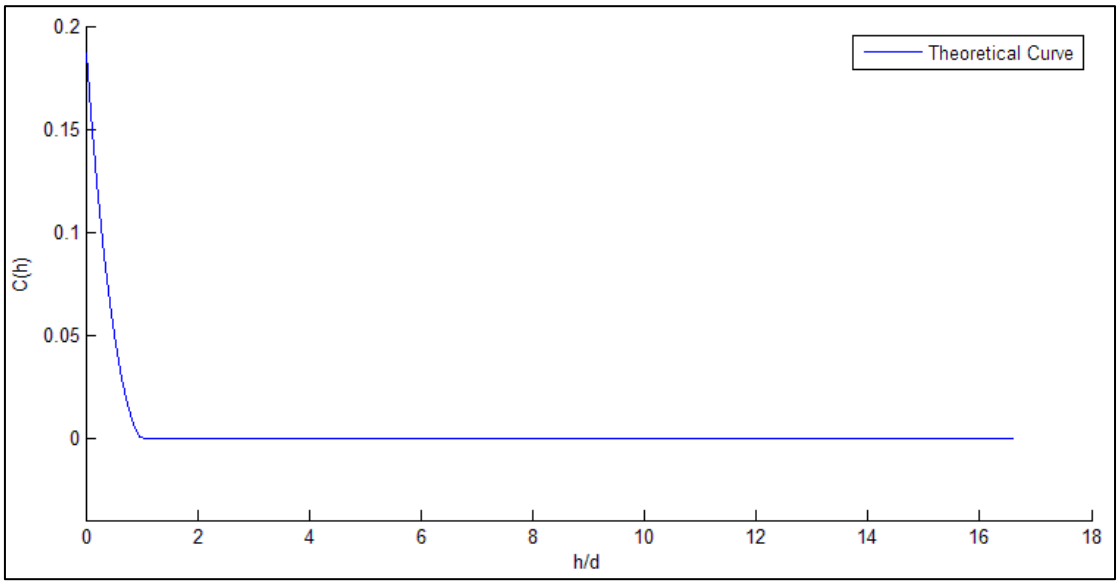

Figure I-9. The theoretical $2-$point probability function $S_2(\boldsymbol{r})$ for $V_f = 25.18\%$ for overlapping disks plotted from **Lu and Torquato (1990)**

While for non-overlapping fibers, the $g_N^{(n)}(r)$ are difficult to determine for $n > 2$, therefore, an analytical expression of S_2 is unknown.

II- Sample generation

The virtually generated numerical image samples representing the real heterogeneous media have saved tremendous time and money. In order to give satisfying and usable results, these numerical samples and the microstructures under study must have similar morphological descriptors. It could be based on real microstructures **Sanei *et al.* (2017)** or purely numerical samples as it was the case throughout this work.

II-1 Microstructure samples

The generated 2D samples synthetically represent the cross-sections of composite materials built with continuous longitudinally arranged parallel and identical fiber inclusions. This allowed the study to be reduced to a two-dimensional one. The disks were randomly distributed within a lattice of square cross-section in order to control the volume fraction V_f. These samples were referred to as the framed samples.

Two kinds of image samples were built with regard to chosen statistical distributions: systems of fully penetrable disks (overlapping) and others of hard disks (non-overlapping) as depicted in figure I-10.

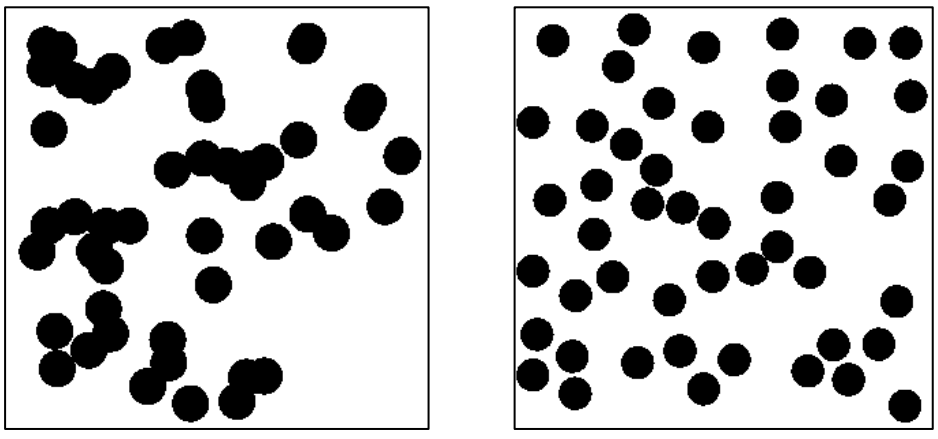

Figure I-10. (a) Overlapping and **(b)** Non-overlapping samples

II-1-1 Overlapping microstructures

The overlapping samples were generated by simply distributing the fiber centers according to a Poisson law for which each position within the square is equiprobable. The difficulty in such method is to reach the wanted volume fraction.
Typically two processes are used to better approach the wanted V_f value : one where fibers keep being added until the final V_f is the closest to the desired one and a second in which the number of fibers is previously deduced from the rate of overlapping **Lu and Torquato (1990)**. The first method is suitable for samples with a large enough number of inclusions to which adding an inclusion does not significantly increase V_f. The second method is used in the case of smaller samples where ensemble averaging leads to the right value of V_f.

If the inclusion diameter is not relevant, the exact volume fraction can easily be obtained by adjusting the fiber diameter.

As the inclusions centers are distributed following a Poisson law so the n −body distribution functions are all equal to 1:

$$g_N^{(n)}(\mathbf{r^n}) = 1 \ \forall n \tag{37}$$

Especially the radial distribution function:

$$g(\mathbf{r}) = 1 \ \forall \mathbf{r} \tag{38}$$

For example, for a volume fractions of 30%, 25 samples of 49 inclusions were generated and the resulting averaged $g(r)$ plotted on figure I-11 shows a good agreement with the expected value of 1.

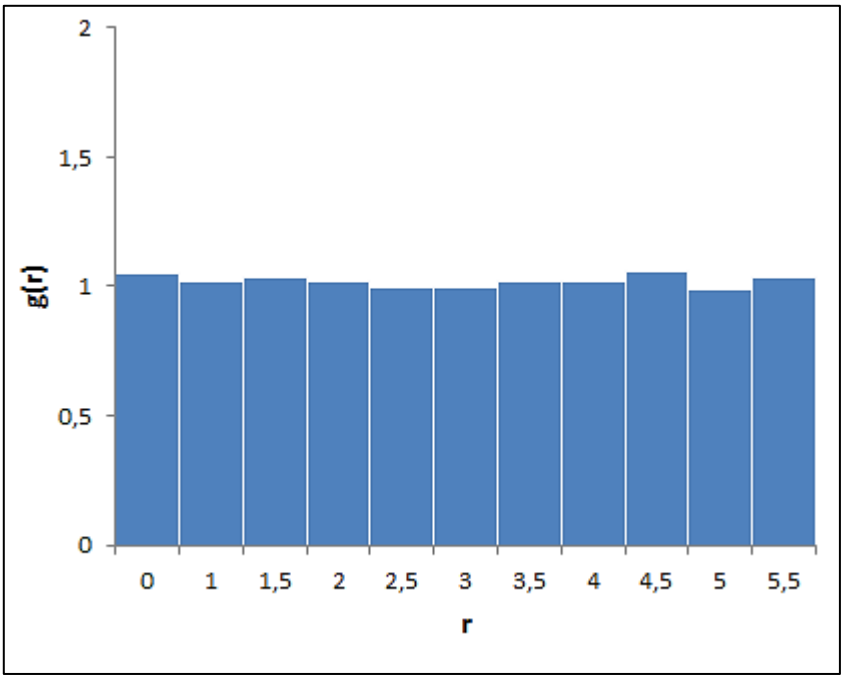

Figure I-11. Pair distribution function for overlapping systems

As all $g_N^{(n)}$ are equal to 1, according to equation (18), the n −point probability functions S_n are fully determined and depend only on volume fraction for overlapping random samples. This is confirmed by figure I-12 presenting the correlation functions of the characteristic function of the fiber phase for two different numbers of inclusions namely $N = 200$ and $N = 400$ and hence two distinct fiber diameters at the same volume fraction. These numbers of fibers allow to reach the convergence of S_2.

In this case of overlapping fibers at a given volume fraction, the obtained covariance values with regard to a dimensionless abscissa $(\frac{r}{d})$, are always identical independently of the fiber diameter or else the number of fibers.

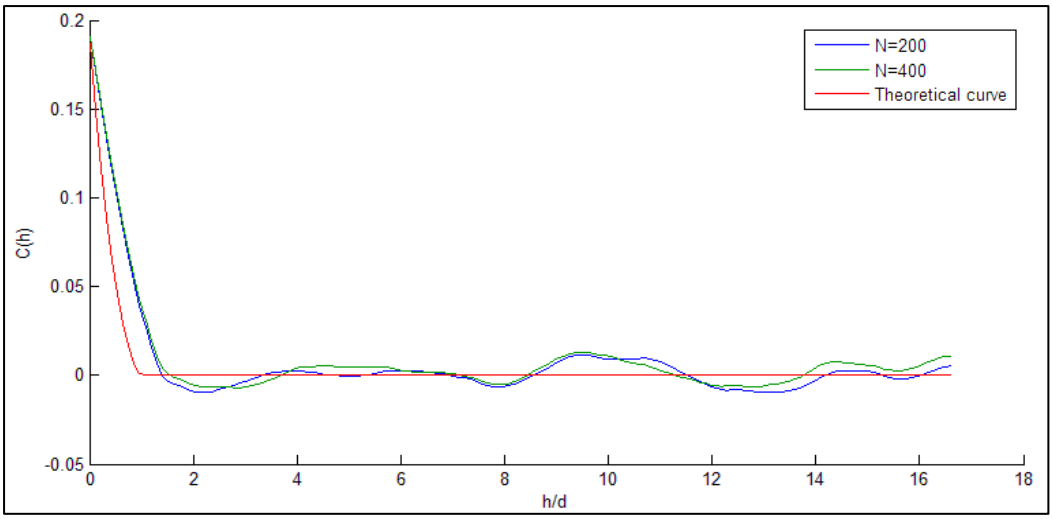

Figure I-12. Correlation functions of the characteristic function of the fiber phase for $N = 200$ and $N = 400$ compared to theoretical 2 point probability function $S_2(\boldsymbol{r})$ for $V_f = 25.18\%$

The numerical results are also compared to the theoretical correlation function deduced from the $2-$point probability function $S_2(\boldsymbol{r})$ given by **Lu and Torquato (1990)** in equations (35) and (36). The observed discrepancies are due to edge effect on our small samples of 49 inclusions.

II-1-2 Non-overlapping microstructures

The non-overlapping microstructures were built following a process in which particles were sequentially and randomly introduced, subjected to a condition of non-overlapping up to the desired volume fraction or number of particles. The non-overlapping condition is based on a repulsion criterion $|r_{ij}| > 1$ where r is the dimensionless position vector such as $|r_{ij}|$ is equal to 1 at contact between fibers i and j.

To take account of this repulsion criterion while in a random fiber-distribution process, the classical method is the Random sequential adsorption (RSA). It refers to a process where particles are one by one introduced into the system. First, a random point in the volume is chosen where a first hard disk is placed. A second point is then randomly chosen where a second hard disk is placed if not overlapping on the first, otherwise it gets rejected and a new point is again chosen following the same process until the desired number of particles within the volume is reached.

The RSA method was first studied for one-dimensional models such as the attachment of pendant groups in a polymer chain by **Flory (1969)** and the car-parking problem by **Rényi (1958).** For higher dimensions $(D \geq 2)$, **Widom (1966)** demonstrated that the RSA method is fundamentally different from the random cases generated following a Poisson law

(overlapping) for same densities. He also showed that the density at which the RSA systems become jammed is lower than that of agitated non-overlapping random systems. This limitation in density appears with occurrence of gaps that are about the size of the disks. For high densities, these gaps considerably reduce the jamming limit in comparison to agitated systems where all the space is filled until no significant gap is left. This puts a restriction on the volume fraction that can be attained **M. R. Islam (2016)**.
These limits are shown in Table 1.

		Jamming Limit	RSA Limit
V_{fmax}	**D=1**	1	0.75
	D=2	0.83	0.55
	D=3	0.64	0.38

Table I-1. Comparison of the maximal volume fraction V_f limit for equilibrium and RSA systems **Torquato (2002)**

Later works discussed the geometrical properties of the RSA configuration **Hinrichsen *et al.* (1986)**. Many other systems have been studied by computer simulation, including in 2D disks, randomly oriented squares, rectangles, ellipses, and various other shapes **Ricci *et al.* (1992).** Systems generated by RSA are in a nonequilibrium state except at very low density **Torquato (2002).**

The inherent gaps in RSA systems are clearly revealed by the covariance on the characteristic function $I(x)$ (figure I-13) where unlike overlapping systems, negative values appear around the abscissa $h/d = 1$ denoting an increase in the rate of finding two points separated by a distance h in two different phases.

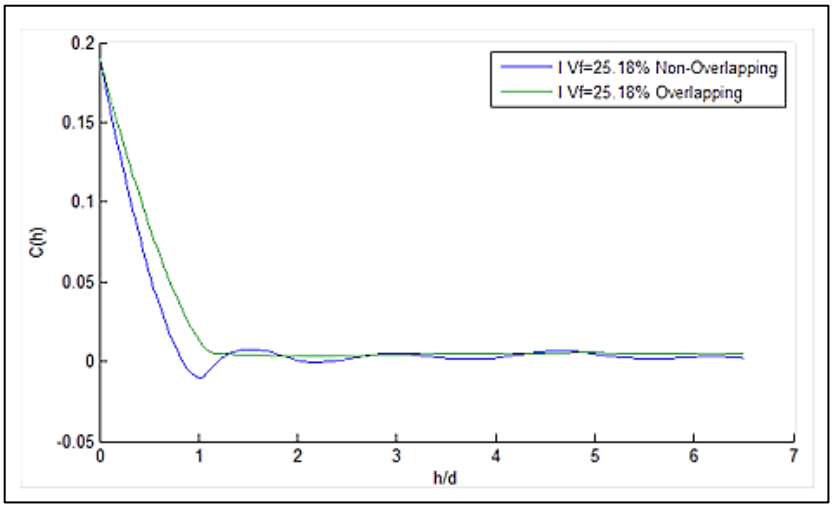

Figure I-13. Covariance on I for overlapping and non-overlapping composites

II-2 Modification of microstructure: Simulated annealing

The aim of the heuristic method presented in this section is to bring a random distribution of fibers to another one according to a chosen microstructure. Among the optimization methods developed for solving combinatorial minimization problems, the simulated annealing (SA) is especially well suited for reaching microstructures described by given Rdfs **Rintoul and Torquato (1997)**. Actually, the microstructure of a composite can be considered as a frozen picture of a dynamic system of particles driven by a potential energy directly related to their Rdf by the means of the canonical probability that will be introduced by equation (40).

SA consists of rearranging particles in order to evolve toward a desired new configuration. It mimics the process of atoms rearrangements or annealing during steel production and naturally corresponds to a stationary state of energy. Unlike purely statistical methods such as the Monte-Carlo method, with a suitable energy criterion, SA converges heuristically to the desired state. This method initially developed by **Metropolis *et al.* (1953), Kirkpatrick *et al.* (1983), Bertsimas and Tsitsilis (1993)** can be applied to any systems driven by random variables and allows them to remain in a state of equilibrium after the modification of their microstructures. Recent work by **Erchiqui (2017)** aiming to optimize heaters during the thermoforming process has proven the SA technique to be a very efficient optimization tool.

Technically, the ensemble of fibers is assimilated to a canonical ensemble where the energy fluctuates around a constant mean value. The fibers are moved in order to minimize their virtual inter-fiber interaction potential $U(r)$. A randomly chosen fiber is displaced by a random distance Δr in a random direction, both provided by a Poisson law. The maximum value of Δr is adjusted to optimize the efficiency of the global process by never exceeding the value of the mean free path in statistical physics. At each move of a fiber, a change in energy of the system ΔU is evaluated and calls on a probabilistic law of accepting the move (ΔU) :

$$P(\Delta U) = \begin{cases} 1, & \Delta U \leq 0 \\ e^{-\beta \Delta U}, & \Delta U > 0 \end{cases} \tag{39}$$

In which β is the Boltzmann factor.

As this process was purely numerical, both ΔU and $1/\beta$ are not necessarily real energies and no physical forces had to be derived from ΔU .

The values of Δr and β are manually adjusted to optimize the efficiency of the global process. Δr has to be large enough not to slow the evolution. The adjustment of β values is more sensitive. Actually, when β becomes large, the system evolves faster toward the wanted state but can be out of equilibrium.

The process is repeated until the desired state is reached. Naturally, the choice of the potential depends on this state.

For instance, in the special case of pairwise additive energy potential, the canonical probability of a state in the Gibbs space provides a simple relation between Rdf and the potential:

$$g(r) = e^{[-\beta U(r)]} \tag{40}$$

Which leads to:

$$U(r) \infty - ln[g(r)] \tag{41}$$

Such type of potential allows a RSA system to evolve toward a PY one as illustrated on figure I-14.

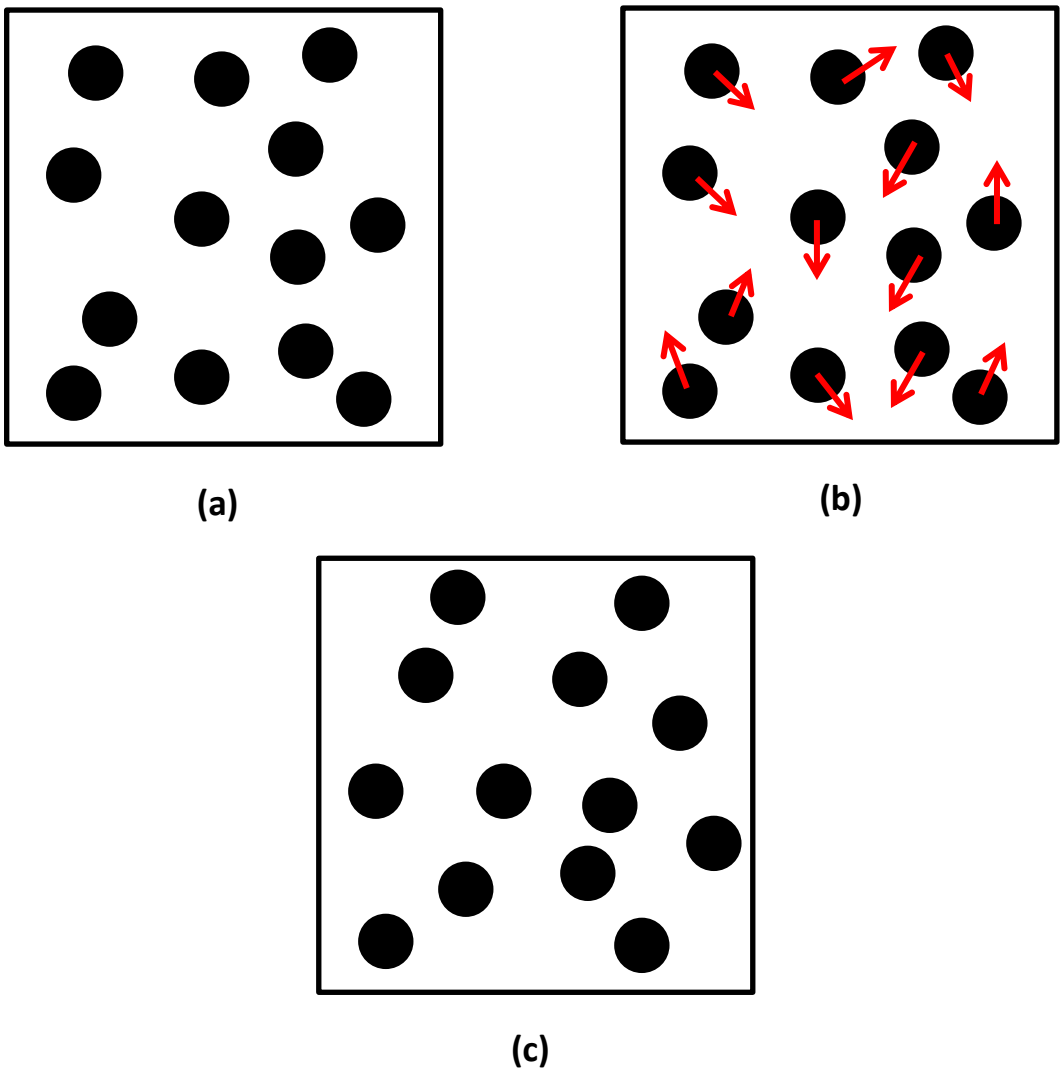

Figure I-14. Representation of a system of hard particles: **(a)** generated according to a RSA process, **(b)** under agitation by SA and **(c)** in equilibrium

Using different potentials throughout this work, the SA method will allow to build various microstructures such as clusters, sticky disks, etc..

Validation of the simulated annealing method

In order to validate the accuracy of our SA method, we compared our results to systems for which correlation functions are known. As the focus is on non-overlapping systems, the knowledge of correlation functions is reduced to PY solutions so SA was used to bring the non-equilibrium RSA samples to equilibrium PY systems. We then compared our Rdf results to those of PY solutions available in literature.

Five large samples of $N = 500$ particles were generated with $V_f = 36.30\%$, a volume fraction for which a numerical two dimensional solution of the PY equation for randomly distributed hard disks exists in literature **Bravo and Santos (1993)**. Other solutions for higher volume fractions are also available in literature **Adda-Bedia *et al.* (2008)**, however, they were not chosen due to hardware limitations (figure I-15).

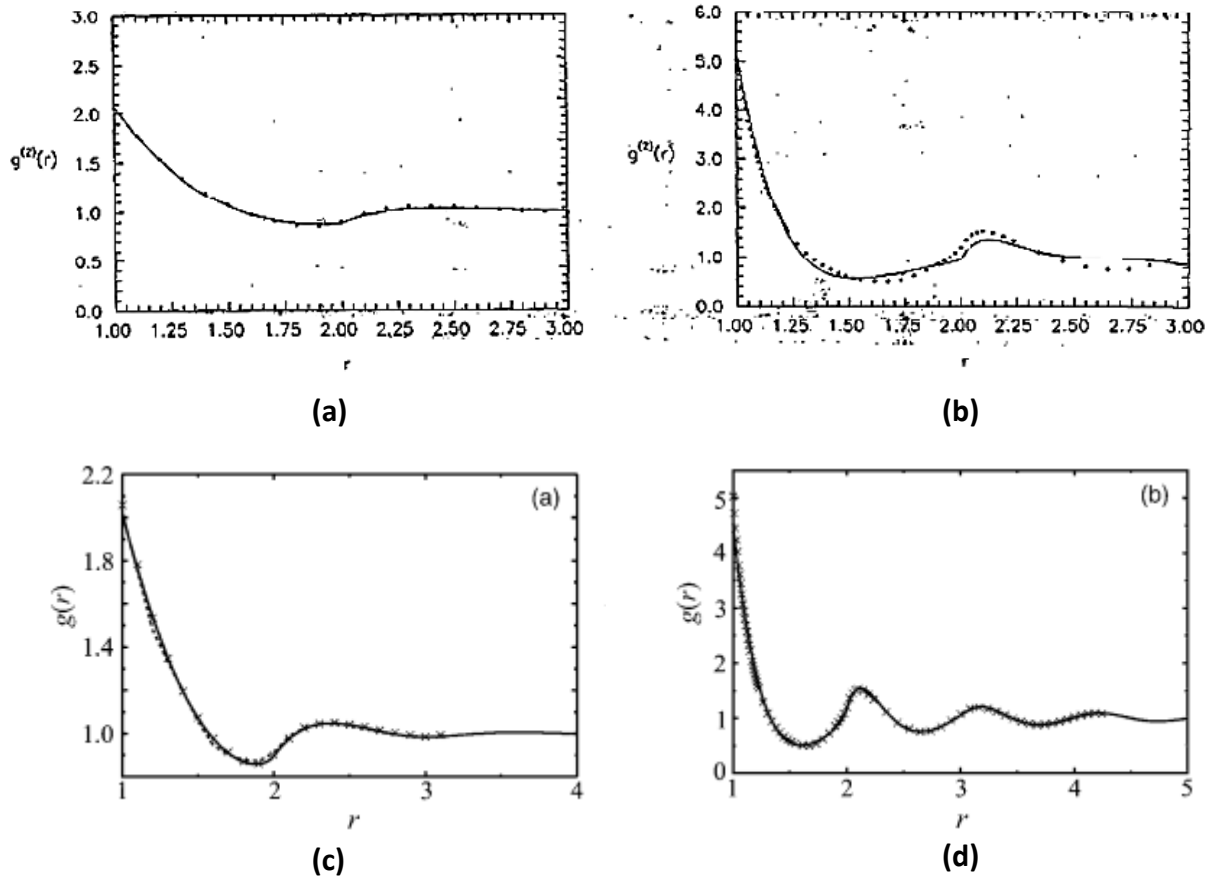

Figure I-15. The correlation function $g(r)$ interpolated between the PY distribution functions for hard spheres for **(a)** $V_f = 36.30\%$, **(b)** $V_f = 54.4\%$, **(c)** $V_f = 46.20\%$ and **(d)** $V_f = 79.40\%$, **Bravo and Santos (1993)** and **Adda-Bedia *et al.* (2008)**

Figure I-16 shows an example of a sample's initial and final states before and after applying SA.

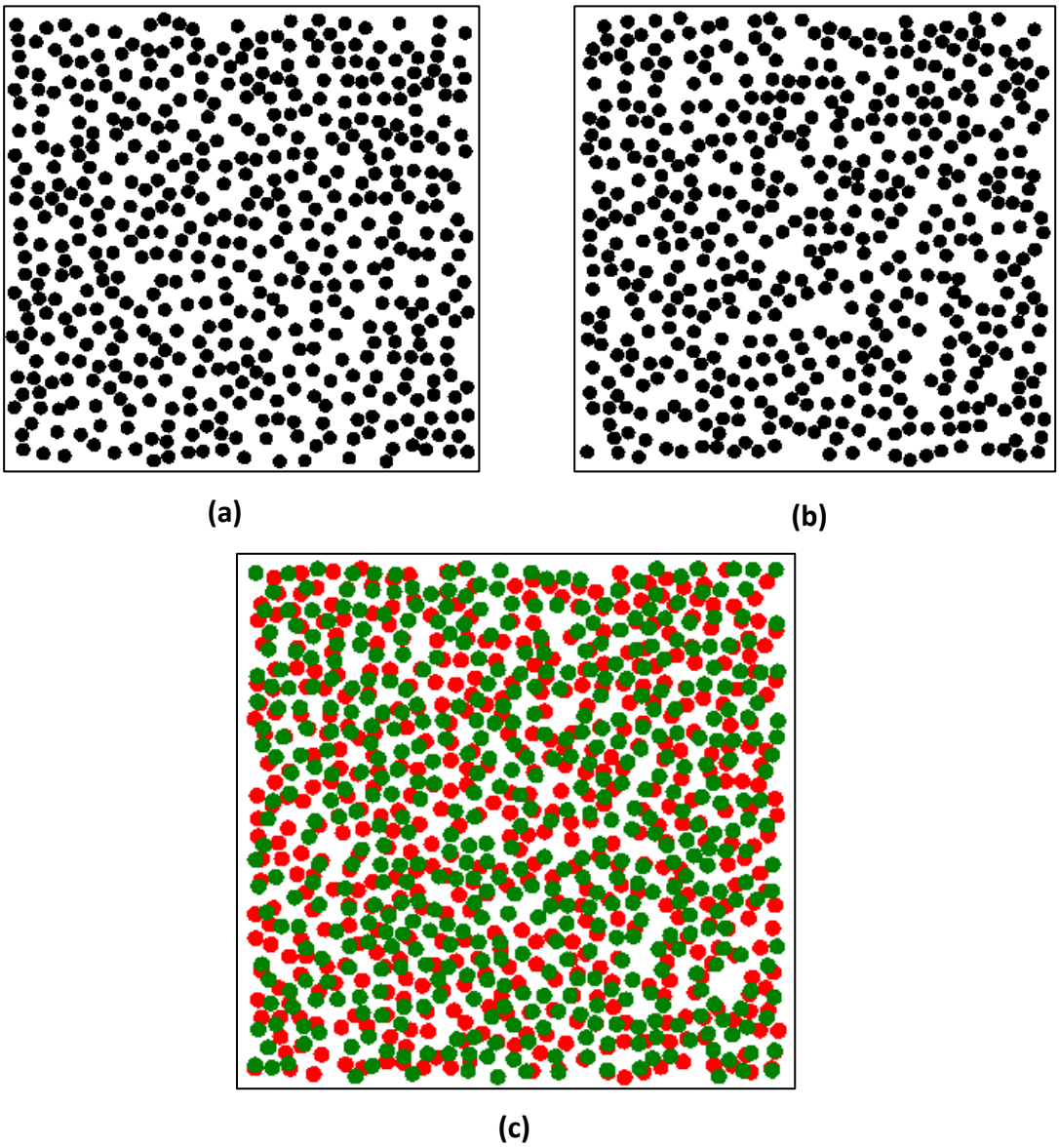

Figure I-16. Non-overlapping samples of $V_f = 36.30\%$: **(a)** Initial state (before SA), **(b)** final state (after SA) and **(c)** superposition of (a) **(red)** and (b) **(green)**

Here, the desired state is reached by increasing the values of $g(r)$ within the range of $1 < r < 1.5$ and the potential is as follows:

$$U \infty - ln[g(1 < r < 1.5)]$$

It was noticed that by adjusting this peak value, the remaining values of $g(r)$ for $r > 1.5$ converge toward the Percus-Yevick Rdf by simple agitation.

Figure I-17 shows a comparison between our Rdf results and those available in literature for $V_f = 36.30\%$.

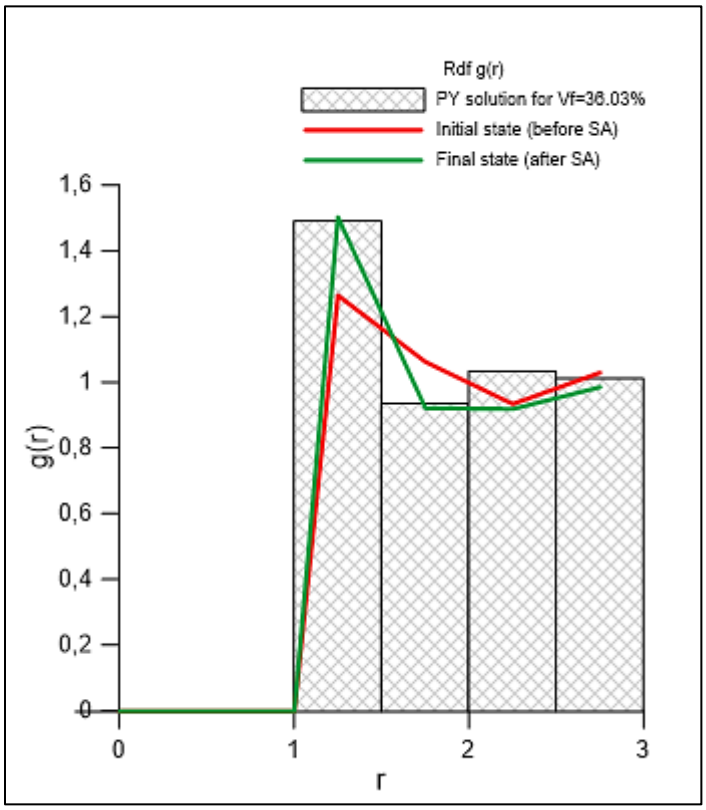

Figure I-17. Comparison of Rdf results between literature (histogram) and the generated numerical sample, before (red curve) and after (green curve) SA for $V_f = 36.30\%$

Figure I-16 above shows that the Rdf averaged on the five final samples Rdf results, calculated after applying SA, is in very good agreement with the PY solution plotted from literature **Bravo and Santos (1993)** as a histogram. Despite averaging on the 5 images samples of 500 disks, $g(r)$ converged hardly, so the histogram steps were set at a value of 1 (roughly the inclusion diameter). The corresponding values of $g(r)$ for PY were obtained by integration on curve (a) in figure I-14. The sample building method by SA is well validated by the obtained results as the distribution of fiber centers on these samples accurately fits the expected $g(r)$, nevertheless, the samples can slightly deviate from a PY distribution due to the heuristic nature of SA which does not take into account higher order correlations.

In the following chapters, all samples were built with RSA and adjusted by SA with the suitable potential.

Chapter 2

Homogenization method and bounds determination

In engineering mechanics and applied physics, the materials used for structural applications are rarely homogeneous, thus, the knowledge of elastic and thermal effective properties of heterogeneous or composite media is of high importance. The focus here was on the influence of microstructures rather than complex behavior laws. The small deformations hypothesis was considered and both elastic and thermal behaviors were presumed linear for predicting the deformations and internal stresses within a heterogeneous material under a given set of external strains such as pure shear, pure compression or heat fluxes under a temperature gradient.

The aim in this chapter is to predict the effective properties of heterogeneous materials using homogenization techniques. This can be done either analytically or numerically. However, only analytical homogenizations issued from literature will be presented in the course of this chapter as the specifications of numerical homogenizations used in this work to evaluate the influence of microstructure on effective properties will be detailed in the upcoming chapter.

Several considerations and assumptions regarding the physics of the studied media are required in order to apply the homogenization methods to each phase.

In case of elasticity, the effective coefficients are elastic bulk and shear moduli for isotropic materials while for heat transfer it is the thermal conductivity.

To introduce the notation, this chapter will begin with a brief reminder of linear elasticity and thermal conductivity.

I- Basics of physical behaviors

I-1 Linear elasticity

Let us consider a homogeneous material (single phase) with a linear elastic respond to a homogeneous mechanical loading on its outer contour.

In a linear elasticity framework, the law of behavior relation is expressed locally for each phase using the generalized Hooke's law:

$$\underline{\sigma} = \underline{\underline{c}} : \underline{\varepsilon} \tag{1-a}$$

with $\underline{\varepsilon}$ second-order symmetric strain tensor, $\underline{\underline{c}}$ fourth-order tensor of elastic moduli, also known as the elastic stiffness tensor and $\underline{\sigma}$ the second-order symmetric Cauchy stress tensor.

The strain can be expressed as a function of stress using the compliance tensor $\underline{\underline{s}}$ defined as the inverse of equation (1-a) :

$$\underline{\varepsilon} = \underline{\underline{s}} : \underline{\sigma} \tag{1-b}$$

On a macroscopic level, the set of equations (1) can be written as follows:

$$\Sigma = \underline{C_h} : \boldsymbol{E} \tag{2-a}$$

And

$$\boldsymbol{E} = \underline{S_h} : \Sigma \tag{2-b}$$

Where Σ and $\boldsymbol{E}$ represent the macroscopic strain and deformation and the index h denotes the homogenized tensors.

The elastic potential energy stored in a material is:

$$U_E = \frac{1}{2}\int_V \sigma_{ij}\, \varepsilon_{ij}\, dV \tag{3}$$

And with Hill-Mandel's lemma:

$$U_E = \frac{1}{2}\, \boldsymbol{E}.\Sigma$$

I-2 Thermal conductivity:

In the case of thermal conductivity of homogeneous materials, let us consider $\boldsymbol{q}$ the heat flux and $\boldsymbol{\nabla} T$ the gradient of temperature. We assume that heat transfer takes place within the material and the local thermal linear behavior of the heterogeneous medium can be defined according to Fourier's law:

$$\boldsymbol{q} = -\underline{\lambda} \,.\, \boldsymbol{\nabla} T \tag{4}$$

Where λ is the thermal conductivity.

Both the microscopic local gradients of temperature and local heat fluxes can be related to the macroscopic gradient of temperature G and heat flux Q by means of localization tensors that contain all the geometrical information.

The thermal potential energy is given by:

$$U_T = -\boldsymbol{q}.\boldsymbol{\nabla} T \tag{5}$$

II- Effective physical properties of heterogeneous media

To determine the effective properties of heterogeneous media based on the properties of their various elementary components, namely, the behavior of the matrix and that of inclusions in the case of two-phased composites, a set of averaging operations are used. The general idea behind this process called homogenization is to substitute the inhomogeneous material with a fictional equivalent homogeneous one called the homogeneous equivalent material (HEM) by taking a closer look at the local behavior variations of the heterogeneities.

Random microstructured materials are described by two main scales: the micro scale which is the size of inclusions and the macro scale which is the size of the sample.

Supposing a full separation of micro and macro scales, the HEM takes all the heterogeneities into account and has the same overall macroscopic response to loadings as the initial heterogeneous material. This method could be applied to many problems in physics such as thermal conductivity, linear elasticity, plasticity, visco - plasticity, electromagnetism, etc.

Figure II-1. shows a simplified illustration of the transitioning method from a heterogeneous medium to the HEM using the homogenization technique.

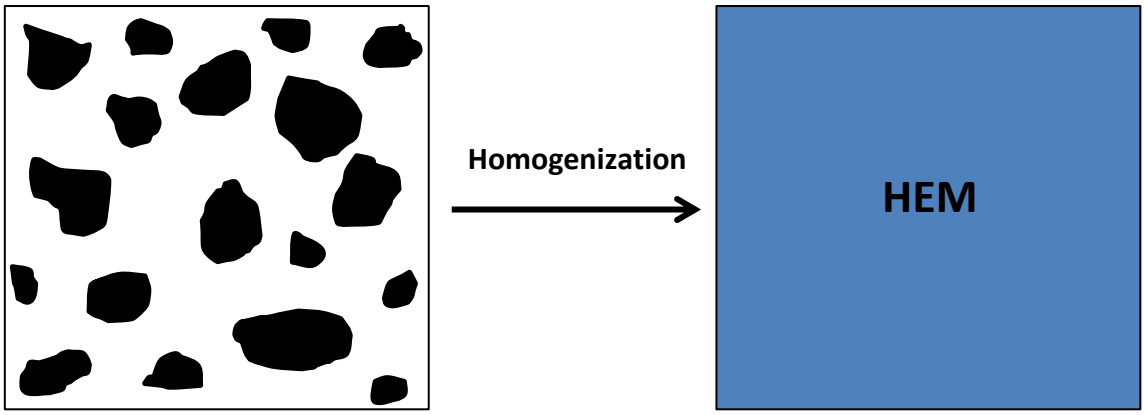

Figure II-1. The homogenization principle for a heterogeneous microstructure

In order to obtain reliable homogenized values, the macro scale has to be large enough to be representative of the whole microstructure and the sample is referred to as the representative volume element (RVE).

II-1 Homogenization

This method has first been developed in various fields of science and technology for periodic spacial distributions for which the problems and calculations are facilitated and reduced to analytical solutions for a single elementary cell **Eshelby (1957)**. However, in the course of the last decades, this technique has been improved considerably and has extended to random morphologies of materials. It has since been applied to all kinds of disordered media and not just restricted to the periodic cases.

The issue with transitioning from heterogeneous media to their fictional equivalent homogeneous ones lies in the capacity of capturing all the different heterogeneities within. For a homogeneous material, we assume the outer constraint as uniform while in practice, it is the sum of all the constraints applied on the surface:

$$\frac{F}{S} = N_i = \frac{1}{S}\iint_S \sigma_{ij} n_j dS \tag{6}$$

Where N_i is the total tension.

Unless this first mandatory step is mastered, no effective properties of the composite material can be deduced. When of a set of external strains such as pure shear or pure compression or a difference of temperature is applied on the outer boundary of a domain, the heterogeneities within the volume are hidden which makes it difficult to take them into account and the accurate effective properties of the material are therefore impossible to determine (figure II-2).

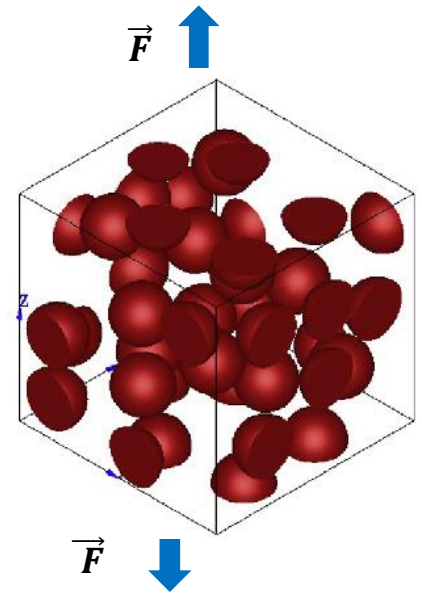

Figure II-2. A 3D sample of a composite material under traction $\vec{F}$

However, external strains are mathematically linked to local internal behaviors through an equality between the integral on the outer surface of the material and a volume one**,** as shown in the equation (6). This allowed to quantify the local behavior at the heterogeneities level and constitutes the base of the homogenization as we know it today.

$$< \sigma_{ij} >= \frac{1}{V} \iiint_V \sigma_{ij} dV = \frac{1}{S} \iint_S \sigma_{ij} dS \quad (7)$$

The homogenization process seeks an average formulation of the properties of inhomogeneous media starting with a microscopic description and evolving toward a macroscopic, also called effective, one. This operation is known as the Micro-Macro passage.

Many have taken interest in the subject, namely **Eshelby (1957)** in his early works that have later inspired many others.

In this way, homogenization can be regarded as a highly advanced version of the averaging methods. In case of elasticity, the effective parameters are the ratio of the spatial average

stresses to the spatial average strains within the medium when subjected to forces of pure mechanical nature on its outer boundary and in case of thermal conductivity, the ratio of heat fluxes to temperature gradient.

Throughout this work, all the following quantities will be supposed linear hence additive and their effective values can be determined by spatial average:

- Lengths, surfaces and volumes

- Strain, stress, forces and displacement fields

- Heat flux and temperature fields

For microstructures with simple geometries, the averaging process can be done analytically while for more complex geometries, the only way is to homogenize effective properties from numerical results. Analytical methods were the first homogenization techniques to be developed for estimating the properties of heterogeneous materials and they can be categorized into two distinct types: analytical models when the microstructure is well-known and bounds when the microstructure is much less obvious, with an unknown behavior that can only be approached. Analytical methods often involve a variety of assumptions regarding the studied microstructures **Buryachenko (2006) .**

Our study was limited to the case of two-phased materials: a phase i of volume fraction V_f and a phase m of volume fraction $1 - V_f$.

Let us consider an elastic medium composed of two isotropic phases characterized by compression moduli K_i and K_m and shear moduli μ_i and μ_m or Young's moduli E_m and E_i and Poisson ratios υ_m and υ_i.

A large range of analytical methods is available in literature. However, the choice of a given method over others is highly related to the properties of the medium and the morphology of the microstructure. For linear behavior, these methods are essentially governed by the geometrical conditions of the medium, the contrast C between the properties of both phases and the volume fraction V_f and are often asymptotic estimations for very specific microstructures. For instance, for cylindrical, ellipsoidal or plane fibers within an isotropic matrix, analytical models were introduced by **Mori-Tanaka (1973).** A wide range of other empirical models exists, namely the **Halpin and Tsai (1967)** one that takes the fiber length

effect on the elastic properties of composites into account and the **Maxwell (1873)** and **Bruggeman (1935)** models for the thermal properties. For high volume fractions, there is usually a divergence between analytical models which is directly linked to the decrease of spacing hence the increase of interactions between inclusions. These exact analytic models are therefore not suitable for higher volume fractions or more complex configurations.

II-2 Representative Volume Element

The RVE can be defined as the smallest volume V for which the integral (7) reaches convergence, in other words, its value remains constant with an increasing V. The choice of samples is always bound to how representative they are of the material under study. For homogeneous materials, the samples can be of any size, they will still show the same properties and responses as the initial material. For the heterogeneous ones however, the heterogeneities make the choice of a representative size more difficult. This is why the size of the samples must be large enough to separate micro and macro scales in order to take into account the heterogeneities that influence the properties of materials and allow an accurate estimation of their macroscopic behaviors.

In literature, this size is called RVE, Representative Volume Element and has numerous definitions. Several of these definitions are found in **Gitman *et al.* (2007).**

One of the classical definitions was given by **Hill (1963)** where the RVE of a given material is introduced as a structurally typical sample of the whole microstructure, containing enough heterogeneities for the macroscopic properties to be independent of boundary conditions.

A later definition by **Sab (1992)** stated that the previous definition only stands when the RVE's properties tend towards those of a periodic medium and are independent of boundary conditions. **Ostoja-Starzewski (1998)** added later on that the RVE should only be defined in the case of a periodic unit-cell or a non-periodic cell containing an infinite number of heterogeneities. **Drugan and Willis (1996)** also gave a definition of the RVE as being the smallest volume element of the composite for which the apparent properties of the microstructure converge.

Many definitions have also appeared in literature over the years, **Hashin (1983)** , **Terada *et al.* (2000)** etc. One of the latest is purely statistical and numerical and was introduced by **Kanit *et al.* (2003)** where it is stated that size is closely related to: statistical parameters such as the absolute error on effective values, morphological parameters such as volume fraction V_f, and mechanical properties : the contrast between phases for linear behavior.

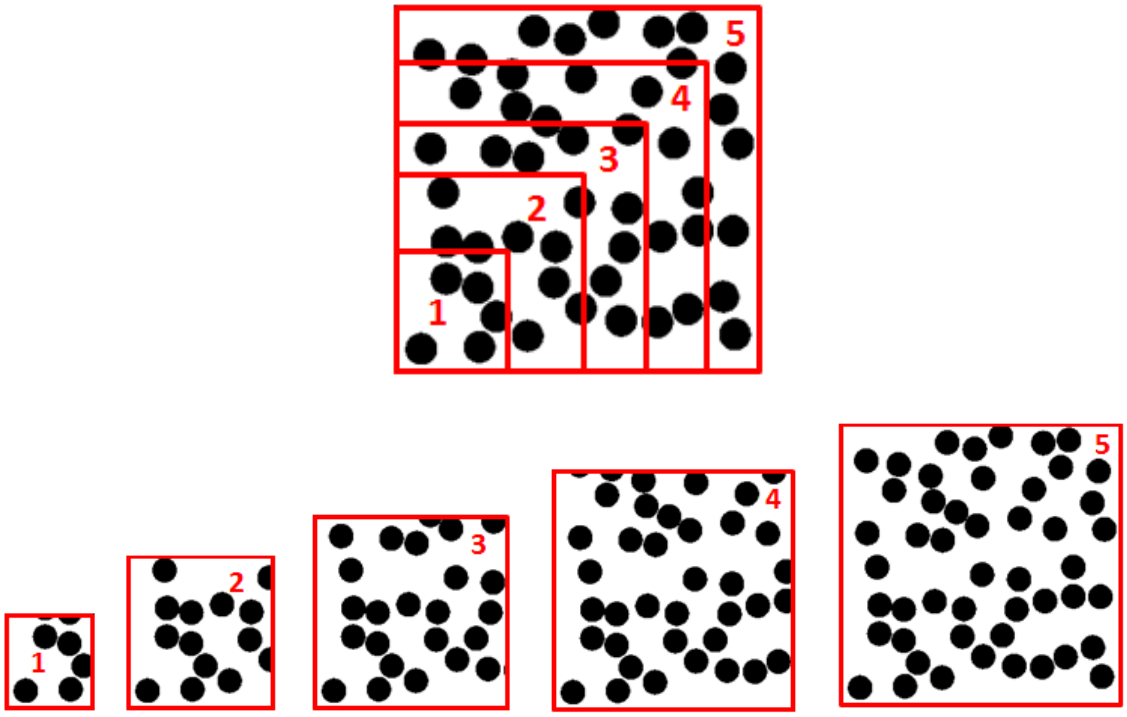

Figure II-3. Different sub-volumes sizes of the microstructure

As illustrated on figure II-3, the different sub-sizes ranging from 1 to 5 are a result of the increase in the side length from one sample to the other.

Figure II-4 emphasizes the evolution of a given apparent property towards convergence depending on the chosen sample size. The apparent property starts converging around sample 4. Therefore, it can be said that sample 4 is a good RVE that gives accurate effective properties of the represented microstructure.

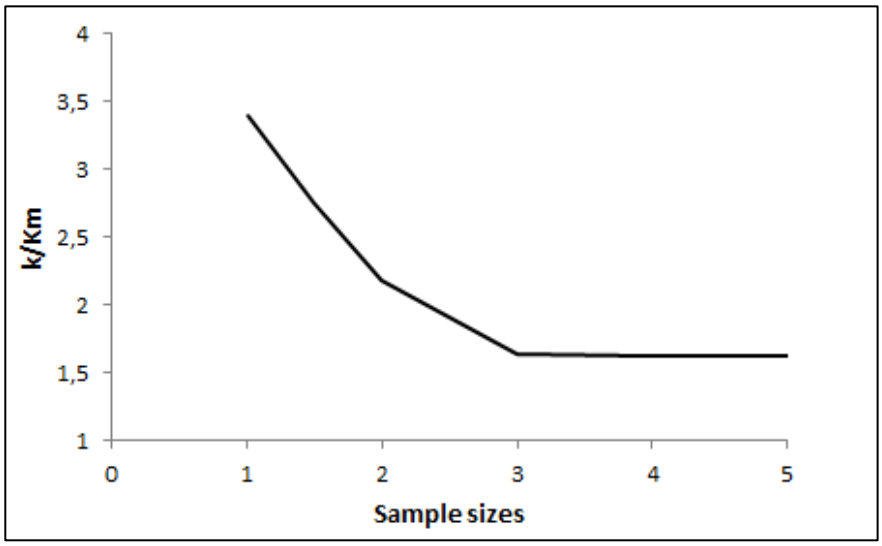

Figure II-4. Evolution of $\frac{k}{K_m}$ for the different sample sizes shown in figure II-3.

For the numerical study of heterogeneous materials, the RVE is a highly important parameter that ensures accurate calculation of their properties. The samples should be neither too small thus compromising the accuracy of homogenization nor too big acquiring longer calculation time or introducing larger errors on the local values.

III- Bounds on physical moduli

The geometric details are usually the most difficult to know or measure, in which case, the only available option is to estimate upper and lower bounds on the moduli within which all microstructures are included.

Naturally, the largest and perhaps most obvious bounds for a heterogeneous material with a compression moduli k and a shear moduli μ composed of inclusions within a matrix are the compression moduli K_m and K_i and shear moduli μ_m and μ_i . They are called 0 order bounds and are expressed as follows:

$$min(K_i, K_m) < k < max(K_i, K_m) \tag{8}$$

$$min(\mu_i, \mu_m) < \mu < max(\mu_i, \mu_m)$$

Given that one phase is stiffer than the other, the homogenized elasticity modulus k and shear modulus μ are then bounded by the moduli of the hardest phase as an upper bound and that of the softest as a lower one.

The bounds of order 0 do not take volume fraction into account and do not provide an estimation of the effective properties. They rather frame the elastic moduli, only providing a maximum and a minimum value of the actual properties.

Therefore, such bounds are of limited interest since they fail to give any useful estimation of the homogenized properties and any tighter and more useful bounds require information about the microstructure.

III-1 First order bounds

The well-known classic examples are **Voigt (1889),** and **Reuss (1929)** bounds. They are associated to a strictly empirical basis defining a power law average for a given property of each phase of a heterogeneous medium to obtain the resulting effective one. This is commonly referred to as the law of mixtures.

Let φ be a given effective property of a heterogeneous medium composed of the two phases i and m. The bounds are defined by:

$$\varphi^{\alpha} = V_f \varphi_i^{\alpha} + (1 - V_f)\varphi_m^{\alpha} \, , \alpha \in [-1,0[\cup]0,1] \tag{9}$$

The negative and positive values of α define respectively lower and upper bounds.

$\alpha = 1$ corresponds to the upper bound (**Voigt**) and -1 to the lower bound (**Reuss**).

The first order bounds match the arithmetic and harmonic means of the two phases' properties, pondered by the volume fraction V_f.

If φ_c is any resulting linear behavior property of the composite, then:

$$\left(\frac{V_f}{\varphi_f} + \frac{(1-V_f)}{\varphi_m}\right)^{-1} \leq \varphi_c \leq V_f \varphi_f + \left(1 - V_f\right)\varphi_m \tag{10}$$

These first order bounds do not presume any information about the microstructure and only require knowledge of the volume fractions of each of the phases. In this way, they are an improved version of the bounds of order 0 aforementioned.

The Voigt and Reuss bounds are ratios of the averaged stress and strain applied to a heterogeneous material. For complex microstructures, the stress and strain are usually unknown and are unlikely to be uniform. Voigt's upper bound was built upon the assumption that the strain field is homogeneous throughout the medium, while Reuss's lower bound presumed the stress field uniform everywhere in the medium.

The geometrical interpretation of Voigt's bound corresponds to a parallel model of laminated materials (axial loading) for which the deformations are supposed homogeneous (figure II-5).

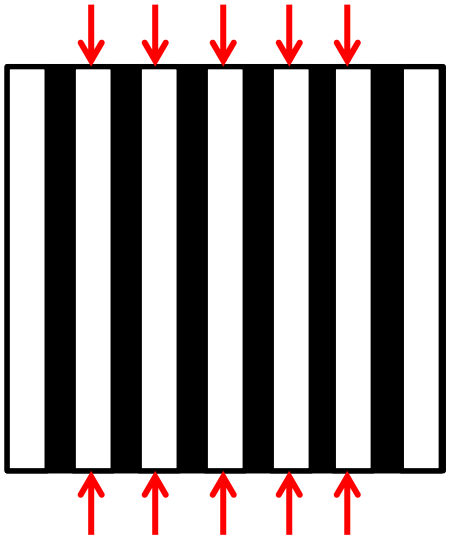

Figure II-5. Voigt's uniform strain

We have the generalized Hooke law:

$$\underline{\sigma} = \underline{\underline{C}} : \underline{\varepsilon} \tag{11}$$

Where $\underline{\sigma}$ and $\underline{\varepsilon}$ are second order strain and deformations tensors, and $\underline{\underline{C}}$ the fourth order elastic behavior tensor.

It follows from Hooke's generalized law and the uniform strain assumption that:

$$\underline{\underline{C}} = \sum V_{fi}.\sigma_i : \underline{\varepsilon} = \sum V_{fi}.(\underline{\varepsilon}.E_i) : \underline{\varepsilon} \tag{12}$$

And we have:

$$\underline{\underline{C}} = \sum V_{fi}.E_i \tag{13}$$

Reuss's bound corresponds to a geometrical model in series for laminated materials (transverse loading) and for which the stress field is presumed uniform throughout the medium (figure II-6).

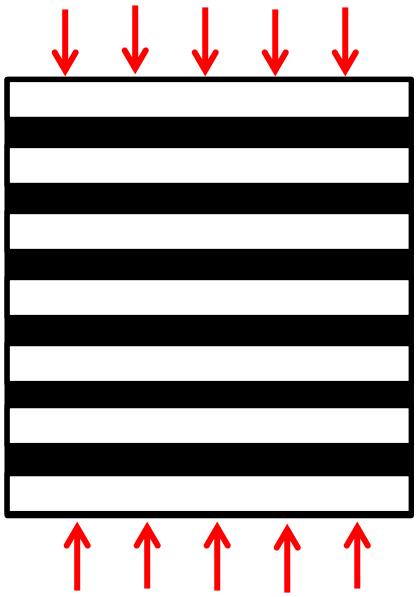

Figure II-6. Reuss's uniform stress model

And we have again:

$$\underline{\underline{C}} = \underline{\sigma} : \left(\sum V_{fi} \, . \, \underline{\varepsilon_i} \right) = \underline{\sigma} : \left(\sum V_{fi} \, . \, (\underline{\underline{\frac{\sigma}{E_i}}}) \right) \tag{14}$$

So,

$$\underline{\underline{S}} = \sum \frac{V_{fi}}{E_i} \tag{15}$$

III-2 Bounds of Hashin-Shtrikman

The first bounds on elastic coefficients tighter than those of Voight and Reuss were introduced by **Hashin-Shtrikman (1962) (1963)** following Brown's work on the electrical permittivity of solid mixtures **Brown (1955)**.

Hashin-Shtrikman (HS) and **Walpole (1966)** for shear modulus are the tightest bounds of effective elastic moduli that do not call for any assumptions on the geometry of the materials (geometrically independent bounds) and necessitate the sole knowledge of the volume fraction V_{fi} of both phases i. These "second order" bounds are physically interesting as they emphasize the frame of improvement in the effective properties of composite media as a result to the variation of their structures. It is also noticeable that the aforementioned Voigt and Reuss first order bounds are wider than HS.

Hashin and Shtrikman have defined second order bounds for both bulk and shear moduli, respectively k and μ based on the general theory of energy minimization for linear elasticity.

These calculations will be detailed below as they are the basics of any bound calculations.

Let an elastic homogeneous and isotropic medium of arbitrary geometry be subjected to surface tractions associated to a homogeneous stress tensor (figure II-7.).

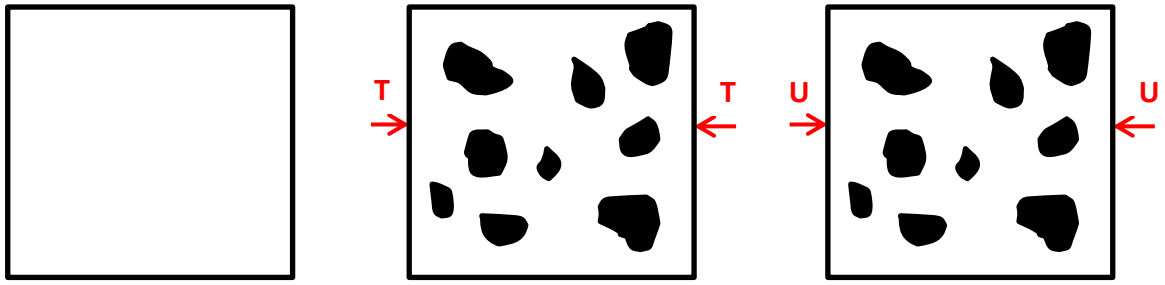

Figure II-7. (1) Reference state (pure matrix), **(2)** Strains applied to a homogeneous material, and **(3)** Displacements applied to the same material

The strain energy U is given by the following integral:

$$U = \frac{1}{2}\int_{(S)} T_i . u_i dS \tag{16}$$

Where:

$T_i = \sigma_{ij} . n_j$ are the components of the surface stress vector with σ_{ij} constant stresses and n_j the components of the normal to the outer surface.

$u_i = \varepsilon_{ij} . n_j$ are the elastic displacements.

Using the equation (7) that links the integral of surface to that of volume, applied to the case of energy, we can write:

$$U = \frac{1}{2}\int_{(V)} \sigma_{ij} . \varepsilon_{ij} dV \tag{17}$$

The strain energy density may then be written as follows:

$$w = \frac{1}{2}\,\sigma_{ij}.\,\varepsilon_{ij} \tag{18}$$

$$w = \frac{1}{2}\,(\mathrm{k\,trace}(\varepsilon) + 2\mu \mathrm{e_{ij}}.\,\mathrm{e_{ij}}) \tag{19}$$

Where e_{ij} is the deviatoric part of the stress tensor.

Hook's law introduces: $\sigma = 3k\varepsilon$ and $\mathrm{s_{ij}} = 2\mu \mathrm{e_{ij}}$

$$w = \frac{1}{2}\left(\frac{\sigma^2}{9\mathrm{k}} + \frac{\mathrm{s_{ij}}.\mathrm{s_{ij}}}{2\mu}\right) \tag{20}$$

Where $\mathrm{k} = \lambda + \frac{2}{3}\mu$ is the bulk modulus of the medium and μ its shear modulus.

The differences of energy between the 3 cases shown in figure II-7 above are then evaluated:

$$\delta U_2 = U_2 - U_1 \text{ and } \delta U_3 = U_3 - U_1 \tag{21}$$

Stationary solutions for δU_2 and δU_3 answering the principle of least action, also called the principle of stationary action (Fermat's principle in optics) are sought. This variational principle applied to our case aims to minimize the two energy differences.

In the case of two-phased materials subjected to surface tractions (stress approach), it has been proven by **Eshelby (1956) (1957)** that the difference of elastic energy stored in the two cases is given by:

$$\delta U_2 = \frac{1}{2}\int_{(\bar{S})}(T_{1i}\overline{u_i} - \overline{T_i}u_{1i})dS \tag{22}$$

Where $\bar{S}$ is the surface of an inclusion and $\overline{T_i}$ and $\overline{u_i}$ the stress and displacement vectors on its surface. This formula is general and applies to any inclusion geometry and boundary tractions.

Another form of the above mentioned equation has also been given by Eshelby. It has been reduced to the volume of an inclusion and calls for the bulk and shear moduli of the composite's two phases as well as the stresses:

$$\delta U_2 = \frac{1}{2}\int_{(\bar{V})}\left[\frac{K_m - K_i}{9K_mK_i}\sigma_1\sigma + \frac{\mu_m - \mu_i}{2\mu_m\mu_i}S_{1ij}s_{ij}\right]dV \quad (23)$$

With $\bar{V}$ being the volume of an inclusion.

When surface displacements are prescribed to the medium (displacement approach), Eshelby's formula is written as follows:

$$\delta U_3 = -\frac{1}{2}\int_{(\bar{S})}(T_{1i}\overline{u_i} - \bar{T}_i u_{1i})dS \quad (24)$$

Minimizing δU_2 gives an upper bound for the bulk modulus $K^{(HS^+)}$ while minimizing δU_3 provides a lower bound $K^{(HS^-)}$.

To determine minima of equations (23) and (24), assumptions had to be made regarding the medium. In the simplest one, the homogeneous matrix contains a number of inclusions large enough to obliterate the anisotropies within. The material was therefore presumed homogeneous and isotropic with $\varepsilon_{ij} = 0$.

The calculations then lead to easier formulas:

For the stress approach:
$$\frac{1}{k^{(HS^+)}} = \frac{1}{K_m} + \frac{\delta U_2}{\frac{\sigma_0^2}{18}V} \quad (25)$$

For the displacement approach:
$$k^{(HS^-)} = K_m + \frac{\delta U_3}{\frac{\varepsilon_0^2}{2}V} \quad (26)$$

Let us consider a composite medium which consists of n different elastic phases and which may be regarded as quasi-homogeneous and quasi-isotropic.

These assumptions allow for easier calculations and so the solutions to the formulas (25) and (26) are presented for the bulk and shear moduli as follows:

For the bulk modulus k, $k^{HS^-} < k < k^{HS^+}$ and:

$$k^{(HS^-)} = k^1 + \frac{A_1}{1+\alpha_1 A_1} \tag{27}$$

$$k^{(HS^+)} = k^n + \frac{A_n}{1+\alpha_n A_n} \tag{28}$$

Exponents 1 denote the lowest moduli while exponents n denote the highest. Thus, it is assumed that $k^{n-1} < k^n$ and $\mu^{n-1} < \mu^n$.

And we have:

$$\alpha_1 = -\frac{3}{3k^1 + 4\mu^1} \tag{29}$$

$$\alpha_n = -\frac{3}{3k^n+4\mu^n} \tag{30}$$

$$A_1 = \sum_{i=2}^{n} \frac{A_A^i}{\frac{1}{k^i-k^1}-\alpha_1} \tag{31}$$

$$A_n = \sum_{i=1}^{n-1} \frac{A_A^i}{\frac{1}{k^i-k^n}-\alpha_n} \tag{32}$$

With A_A^i the surface fraction of phase i in $2D$ and V_f^i the volume fraction of the same phase in $3D$.

For the shear modulus μ, $\mu^{HS^-} < \mu < \mu^{HS^+}$ and:

$$\mu^{HS^-} = \mu^1 + \frac{B_1}{2(1+\beta_1 B_1)} \tag{33}$$

$$\mu^{HS^+} = \mu^n + \frac{B_n}{2(1+\beta_n B_n)} \tag{34}$$

Where B_1, B_n, β_1 and β_n are defined by:

$$\beta_1 = -\frac{3(k^1+2\mu^1)}{5\mu^1(3k^1+4\mu^1)} \tag{35}$$

$$\beta_n = -\frac{3(k^n+2\mu^n)}{5\mu^n(3k^n+4\mu^n)} \tag{36}$$

$$B_1 = \sum_{i=2}^{n} \frac{A_A^i}{\frac{1}{2(\mu^i-\mu^1)}-\beta_1} \tag{37}$$

$$B_n = \sum_{i=1}^{n-1} \frac{A_A^i}{\frac{1}{2(\mu^i-\mu^n)}-\beta_n} \tag{38}$$

In the case of two-phased materials in $2D$, the Hashin-Shtrikman bounds formulas for both bulk and shear moduli are:

$$k^{(HS^-)} = K_m + \frac{V_f}{\frac{1}{K_i-K_m}+\frac{3(1-V_f)}{3K_m+4\mu_m}} \tag{39}$$

$$k^{(HS^+)} = K_i + \frac{1-V_f}{\frac{1}{K_m-K_i}+\frac{3V_f}{3K_i+4\mu_i}} \tag{40}$$

$$\mu^{(HS^-)} = \mu_m + \frac{V_f}{\frac{1}{\mu_i-\mu_m}+\frac{6(1-V_f)(K_m+2\mu_m)}{5\mu_m(3K_m+4\mu_m)}} \tag{41}$$

$$\mu^{(HS^+)} = \mu_i + \frac{1-V_f}{\frac{1}{\mu_m-\mu_i}+\frac{6V_f(K_i+2\mu_i)}{5\mu_i(3K_i+4\mu_i)}} \tag{42}$$

When the information on the microstructure is reduced to the volume fraction, the finest bounds are those of Hashin and Shtrikman, their typical microstructures are illustrated on figure II-8.

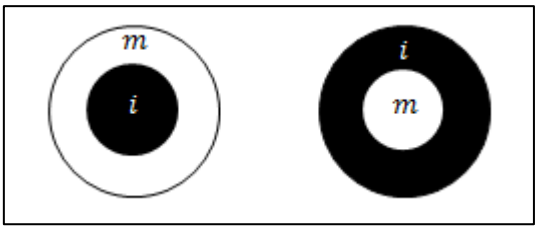

Figure II-8. Microstructures for HS bounds: lower (left) and upper (right)

At high contrasts however, these bounds are less suitable because of the divergence of the upper one. If more details on the microstructures are known, tighter bounds can be expected.

Similar bounds were obtained by **Hill (1963)** by a slightly different method.

III-3 Tighter bounds for 2D fiber reinforced composites

At this point, in order to obtain better bounds, it is necessary to introduce information about the geometry of inclusions: shape and distribution. Improved bounds including finer microstructures were given by **Beran (1965)**, **Beran and Molyneux (1966)**, **Miller (1969)**…and were reviewed by **McCoy (1970).**

The work of **Miller (1969)** introduced a shape factor in the expression of his bounds for 3D microstructures. The schematic form of these bounds presented here for bulk modulus is as follows. The shape factor is introduced through the functions A and B of material properties and geometry.

$$K^{+} = \left(\langle k \rangle - \frac{\langle k'^{2} \rangle}{A}\right) \tag{43}$$

$$K^{-} = \left(\left\langle \frac{1}{k} \right\rangle - \frac{\left\langle \frac{1}{k'^{2}} \right\rangle}{B}\right)^{-1} \tag{44}$$

In which :

$\langle k \rangle = V_f K_i + \left(1 - V_f\right) K_m$ is the Voigt bound

$\left\langle \frac{1}{k} \right\rangle = V_f \frac{1}{K_i} + \left(1 - V_f\right) \frac{1}{K_m}$ is the Reuss bound

$\langle k'^2 \rangle$ and $\langle \frac{1}{k'^2} \rangle$ are respectively the variance of the local bulk modulus and its inverse generally approximated **Brown (1955)** by $V_f(1-V_f)(K_i - K_m)^2$ and $V_f(1-V_f)\left(\frac{1}{K_i} - \frac{1}{K_m}\right)^2$.

According to **Brown (1955)** and **Beran (1965),** this estimation of the local variances is only relevant for composite media with a very low contrast $C = \frac{k_i}{k_m}$.

Figure II-9 shows the importance of this factor in the intrinsic behavior of bounds.

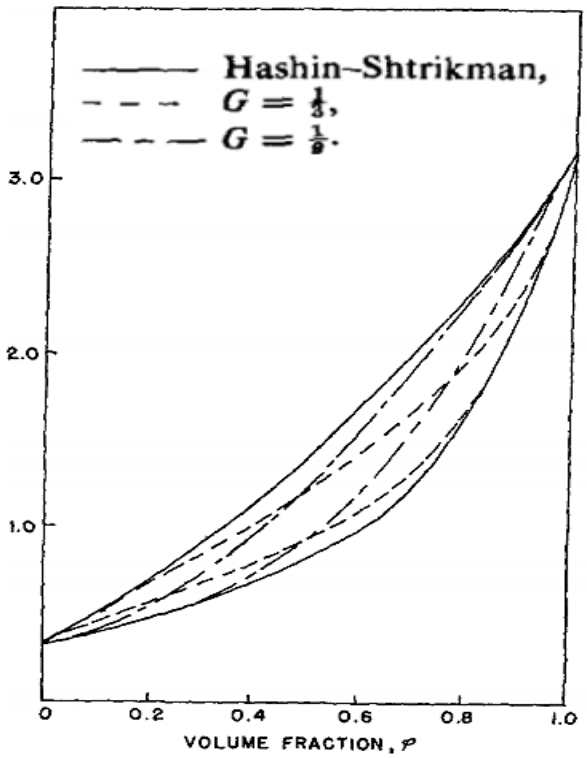

Figure II-9. Bounds on effective bulk modulus for a symmetric-cell material where the shape factor $G = \frac{1}{3}, \frac{1}{9}$ is respectively for plates and spheres **Miller (1969)**

The specific geometry of 2D fiber reinforced composites was first introduced into bound calculations by **Beran and Silnutzer (1971)** including fiber shape and distribution factors. Similar bound calculations were carried out for thermal conductivity **Corson (1974)**. As their determination uses exactly the same mathematics as those of shear modulus **(Hashin 1970)** the former will not be detailed in the next sections and results will be presented in this work when necessary.

In the case of homogeneous and isotropic distribution of non-overlapping disks, a pure random distribution corresponds to the lower bound while the upper one was suspected to be related to the formation of clusters. This supposition was confirmed by **Elsayed and**

McCoy (1973) who showed the influence of clustering through a packing coefficient. Later, **Milton (1982)** formulated exact expressions of these shape and distribution factors up to the third order for elasticity moduli and fourth order for electrical permittivity. These bounds are suitable for any microstructure with known n −point probability functions S_2, S_3 and even S_4 for the electrical permittivity. For the upper bound, he showed that the dominant shape factor was independent of the cluster's localization.

These bounds, which will be called "Milton bounds" throughout this manuscript, were later interpreted for elasticity of aligned fiber reinforced materials. The difficulties were to obtain suitable expressions of S_2, S_3 for realistic materials. They were evaluated for:

- Overlapping fibers, using a Poisson distribution or "fully penetrable cylinders" by **Joslin and Stell (1986)** and **Torquato and Beasley (1986)**.

- Non-overlapping inclusions, using a distribution of fibers driven by a PY approximation by **Torquato and Lado (1988)** and **Miller and Torquato (1991)**.

The simplified expressions of these bounds are expressed as follows:

For the bulk modulus k :

$$K^+ = \left(\langle k \rangle - \frac{V_f(1-V_f)(K_i-K_m)^2}{\langle \widetilde{K} \rangle + \langle \mu \rangle_\xi} \right) \tag{45}$$

$$K^- = \left(\langle \frac{1}{K} \rangle - \frac{V_f(1-V_f)\left(\frac{1}{K_i}-\frac{1}{K_m}\right)^2}{\langle \frac{1}{\widetilde{K}} \rangle + \langle \frac{1}{\mu} \rangle_\xi} \right)^{-1} \tag{46}$$

With $K^- \leq k \leq K^+$

For the shear modulus μ :

$$\mu^+ = \left(\langle \mu \rangle - \frac{V_f(1-V_f)(\mu_i-\mu_m)^2}{\langle \widetilde{\mu} \rangle + \Theta} \right) \tag{47}$$

$$\mu^- = \left(\langle \frac{1}{\mu} \rangle - \frac{V_f(1-V_f)\left(\frac{1}{\mu_i}-\frac{1}{\mu_m}\right)^2}{\langle \frac{1}{\widetilde{\mu}} \rangle + \Phi} \right)^{-1} \tag{48}$$

With $\mu^- \leq \mu \leq \mu^+$

And :

$$\Theta = \frac{2\langle k\rangle_\xi \langle \mu\rangle^2 + \langle k\rangle^2 \langle \mu\rangle_\eta}{\langle k + 2\mu\rangle^2}$$

$$\Phi = 2\langle \frac{1}{k}\rangle_\xi + \langle \frac{1}{\mu}\rangle_\eta$$

Here we define the following:

$$\langle b\rangle = V_f b_i + \big(1 - V_f\big) b_m$$

$$\langle \tilde{b}\rangle = \big(1 - V_f\big) b_i + V_f b_m$$

$$\langle b\rangle_\xi = b_m \xi_1 + b_i \xi_2$$

$$\langle b\rangle_\eta = b_m \eta_1 + b_i \eta_2$$

The transverse bulk modulus of a phase i can be expressed in terms of the isotropic phase moduli as:

$$k_i = K_i + \frac{\mu_i}{3} \tag{49}$$

The parameters $\xi_2 = 1 - \xi_1$ and $\eta_2 = 1 - \eta_1$ are integrals over the two and three-point probability functions $S_2(r)$ and $S_3(r, s, t)$.

In these bounds, the first terms $< k >$, $< 1/k >$, $< \mu >$ and $< 1/\mu >$ are similar to the Reuss and Voight first order ones. The second terms or correction terms are the ratio of an estimation of the local variances of $< k >$, $< 1/k >$, $< \mu >$ and $< 1/\mu >$ by a function of the microstructure's parameters S_2 and S_3. The local variances were estimated by the same expressions as in equations (43) and (44).

As the contrast C increases, the upper bounds diverge including Voigt bounds.

According to **Joslin and Stell (1986)** for the fully penetrable (overlapping) inclusions and **Miller and Torquato (1991)** for the non-overlapping (N-O) inclusions as previously mentioned, the coefficients for the Milton bounds are shown in figure II-10:

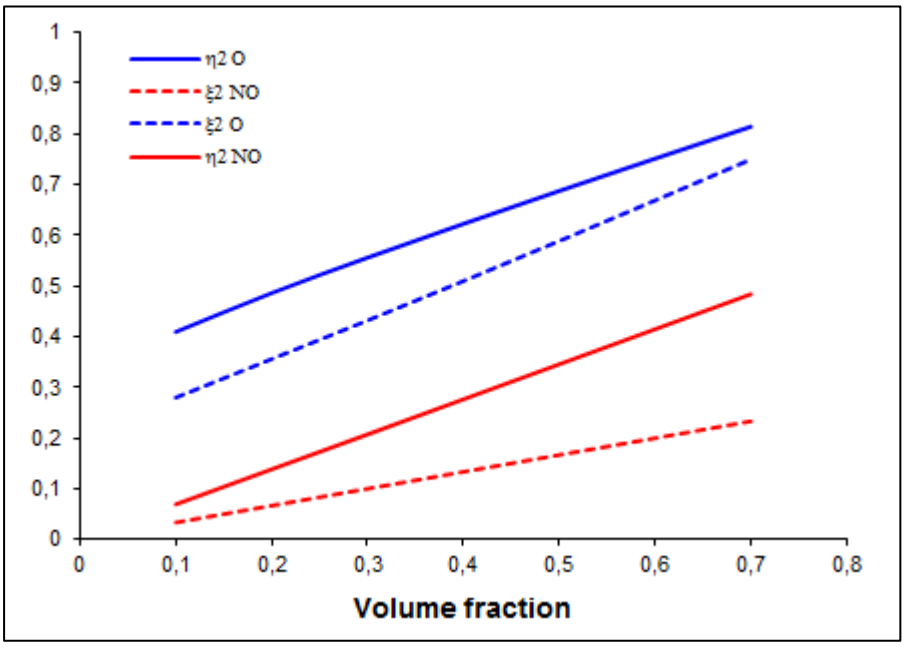

Figure II-10. The Milton bounds parameters with regard to volume fraction for overlapping (O) and non-overlapping (NO) cases

The third order bounds take into account the microstructure details through the two and three-point probability functions S_2 and S_3 hence the difference in formulas for the overlapping and non-overlapping microstructures as shown below for $V_f = 25\%$ and various contrasts. Our evaluations of these coefficients have shown very little differences between the S_3 estimations by **Torquato and Lado (1988)** and **Miller and Torquato (1991)**.

Figure II-11 depicts the Hashin and Shtrikman and Milton bounds kM and µM for bulk and shear moduli k and µ for overlapping and non-overlapping cases.

These bounds for both overlapping and non-overlapping samples are relevant to very specific ensembles of microstructures, however, they become wide for high volume fractions and/or contrasts between physical properties of matrix and fibers.

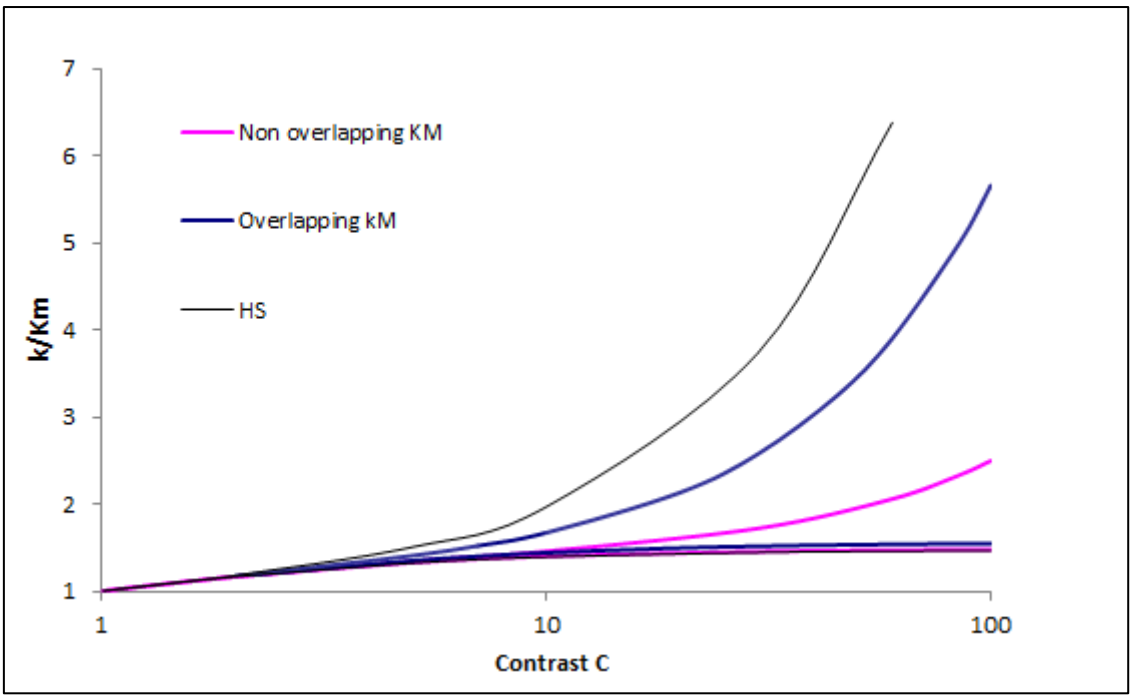

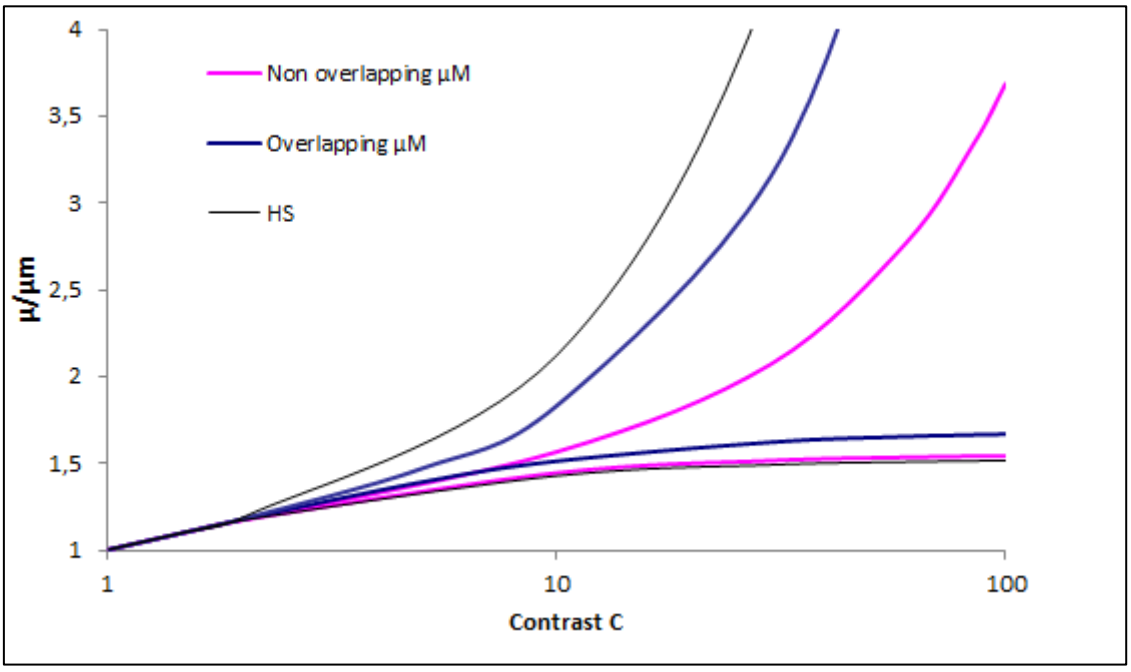

Figure II-11. Milton bounds for $\frac{k}{K_m}$ and $\frac{\mu}{\mu_m}$ for overlapping and non-overlapping for $V_f = 25.18\%$ and varying contrasts C

The lower bounds for non-overlapping are very close to HS^-. Actually, for stiffer fibers than the matrix at a given volume fraction, the geometry of fiber reinforced composites are very similar to the HS^- geometry sketched in figure II-8 (left).

The upper bounds were not built with suitable microstructures but by an “inversion” of the lower bounds through the variational process. The upper bounds could be significantly more accurate based on their real microstructures but can hardly be analytically calculated due to the complexity of the geometry. Other methods of homogenization by numerical approaches are required; they will be the main topic of the next chapter.

Chapter 3

Numerical methods and their validation

The ever growing interest for composite materials in industrial, technological and scientific fields in the course of the last century has led to the significant development of a large variety of computational homogenization techniques in order to precisely establish the effective properties of heterogeneous media. Today, digital homogenization has become one of the strongest tools for determining these properties especially being a method applicable to any type of composites and characterized by its fast and highly accurate results. One of the most commonly used numerical homogenization methods, also the one chosen for this work, consists of applying finite element calculations (FEM) on numerical samples built by image processing. These samples have to be of a sufficient size to better represent the full microstructure and mimic its response to various loadings. For this purpose, the knowledge of the Representative Volume Element (RVE) is crucial for determining the effective properties of heterogeneous materials.

In this chapter, the numerical homogenization by finite elements using RVE for parallel, circular fiber reinforced composites will be detailed, starting with a brief presentation of the FEM simulations followed by validation of our numerical results. These simulations were carried out using an existing FEM code however all post processing was developed as a part of this work using the Matlab software.

I- Finite element method

For homogenization of effective properties, both elastic and thermal, the knowledge of respectively stress and displacement fields and temperature and heat flux fields is necessary.

The usual numerical method to calculate these fields is FEM which is based on the weak formulation and can be interpreted as the virtual work principle for a deformable body.

I-1 Boundary conditions

Three types of classical boundary conditions are usually considered to be prescribed on the boundary of the domain. In the case of linear elasticity, these conditions are: static uniform boundary conditions (**SUBC**) in which a traction vector is applied at the boundary of the sample, kinematic uniform boundary conditions (**KUBC**) and periodic conditions (**PBC**).

Convergence of the results is faster for KUBC and PBC, therefore the focus in this chapter was on these boundary conditions which will be detailed below.

In the thermal case, similar boundary conditions are commonly used, namely: uniform heat flux (**UHF**), uniform gradient of temperature (**UGT**) and the thermal periodic conditions (**PBCT**). Similar to the SUBC, the UHF will not be used within our framework.

The size of the RVE is known (**Kanit *et al.* (2003)**) to be sensitive to boundary conditions and comparison of results under different boundary conditions, KUBC and PBC or UGT and PBCT, allows verifying the convergence of effective properties.

I-1-1 Mechanical boundary conditions

The applied boundary conditions used in our computations in the case of linear elasticity are strains. The displacement could either be uniform KUBC or periodic PBC.

V denotes the surface of the considered domain in a 3D case.

- KUBC is described by imposing the displacement $\mathbf{u}$ at a point $\mathbf{x}$ which belongs to the boundary ∂V (figure III-1.):

$$\mathbf{u} = \underline{E}\,\mathbf{x} \quad \forall \mathbf{x} \in \partial V \tag{1}$$

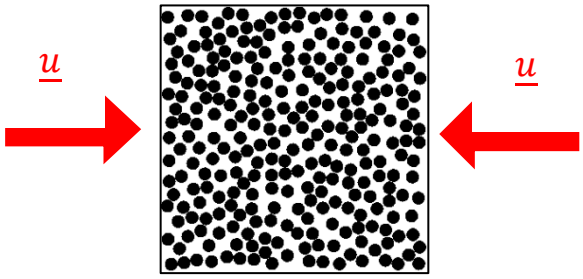

Figure III-1. Uniform displacement applied on ∂V

where $\underline{E}$ is a symmetrical second-order tensor independent of $\mathbf{x}$ which implies:

$$\underline{E} = \langle \underline{\varepsilon} \rangle = \frac{1}{V} \int_V \underline{\varepsilon}\, dV \tag{2}$$

The macroscopic stress tensor is defined by the spatial average:

$$\underline{\Sigma} = \langle \underline{\sigma} \rangle = \frac{1}{V} \int_V \underline{\sigma}\, dV \tag{3}$$

- PBC has the same displacement field as KUBC but a periodic fluctuation $\boldsymbol{\upsilon}$ is added into the equation. The particularity with the PBC is that the fluctuation takes the same values at two homologous points on opposite edges of the microstructure (figure III-2.):

$$\mathbf{u} = \underline{E}\,\mathbf{x} + \boldsymbol{\upsilon} \quad \forall \mathbf{x} \in \partial V \tag{4}$$

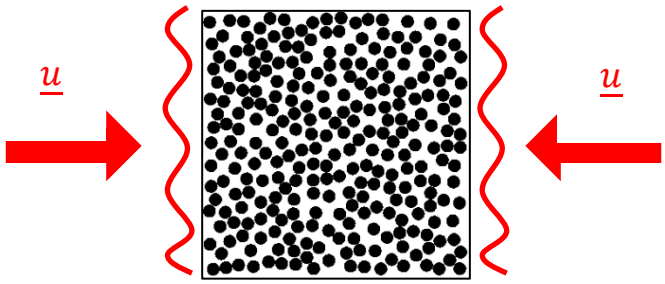

Figure III-2. Periodic displacement applied on ∂V

It should be noted that in this work, calculations are strictly linear elastic with a plane strain hypothesis. This implies that for each boundary condition, only a single solution is admitted.

To determine the apparent mechanical properties, strain tensors $\underline{E}$ are defined for the calculation of each elastic modulus. For both KUBC and PBC, these macroscopic strain tensors are applied as follows for 2D:

$$\underline{E^k} = \frac{1}{2}\begin{pmatrix}1 & 0 & 0\\ 0 & 1 & 0\\ 0 & 0 & 0\end{pmatrix} \qquad \underline{E^{\mu}} = \frac{1}{2}\begin{pmatrix}0 & 1 & 0\\ 1 & 0 & 0\\ 0 & 0 & 0\end{pmatrix} \tag{5}$$

Then homogenization of apparent macroscopic plane bulk and shear moduli k and μ can be obtained from the elastic stress field using the Hell-Mandel lemma:

$$k = \langle\underline{\sigma}\rangle : \underline{E^k} = \frac{1}{2}\left[trace(\langle\underline{\sigma}\rangle)\right] \text{ and } \mu = \langle\underline{\sigma}\rangle : \underline{E^{\mu}} = \langle\sigma_{12}\rangle \tag{6}$$

Where $\langle \quad \rangle$ brackets indicate volume averaging of macroscopic $\langle\underline{\sigma}\rangle$ and local stress $\underline{\sigma}$.

I-1-2 Thermal boundary conditions

Following Fourier's law, the thermal flux vector $\mathbf{q}$ is related to the temperature gradient by means of the thermal conductivity tensor as follows:

$$\mathbf{q} = -\underline{\lambda}\,\boldsymbol{\nabla} T \tag{7}$$

With T the temperature and $\boldsymbol{\nabla} T$ its gradient.

-In the case of the Uniform Gradient of Temperature at the boundaries (UGT), a uniform temperatures T_1 and T_2 are applied on two opposite outer sides of the volume V linked by a uniform gradient $\boldsymbol{\nabla} T$ on the adjacent sides (figure III-3) :

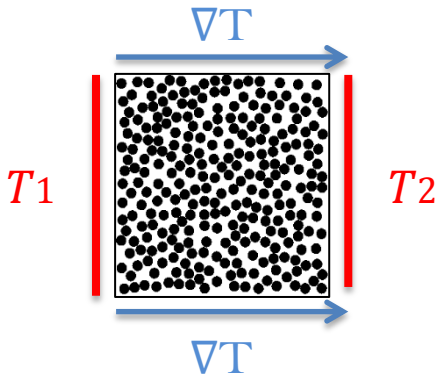

Figure III-3. Uniform gradient of temperature applied on ∂V

The vector of macroscopic heat flux is defined by the surface average that can be replaced by a volume average as follows:

$$\mathbf{Q} \widehat{=} \langle \mathbf{q} \rangle = \frac{1}{V} \int_V \mathbf{q}\, dV \tag{8}$$

-The Periodic Boundary Conditions (PBCT) are similar to UGT with temperatures $T_1 + t$ and $T_2 + t$ instead of T_1 and T_2, where t is a temperature fluctuation (figure III-4.):

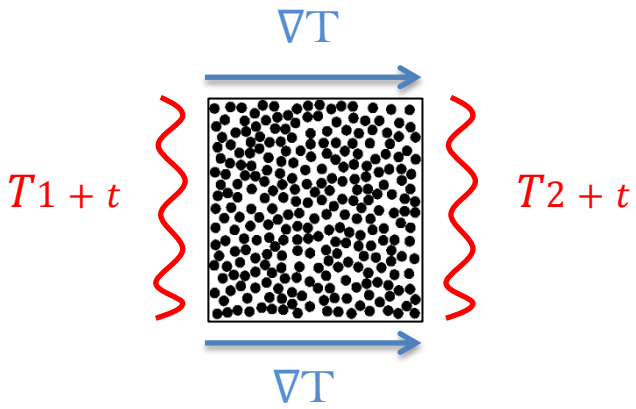

Figure III-4. Periodic boundary conditions applied on ∂V

In the upcoming chapters, only the uniform boundary conditions for both the mechanical and thermal behaviors are going to be used, given the very slight differences between the uniform and periodic boundary conditions shown by the results in the following sections.

I-2 Meshing

After generating the 2D image samples described in chapter 1, the meshing process is carried out using the multi-phase element technique that consists of superposing square element grids with 8 nodes on microstructure image samples instead of triangular ones since it requires less finite elements to reach the convergence of elastic properties. The proper phase property is then allocated to each integration point of the mesh. This meshing technique was chosen for simplicity and time saving purposes.

With this meshing technique, there are no degrees of freedom at the interface between phases which denotes a perfect adhesion or a continuity of stress and displacement fields hence the study of inter-fiber contacts was not necessary. To ensure accurate results, even in high stress gradient situations, the mesh was of 500^2 quadratic finite elements.

Previous works have shown that from a macroscopic perspective, the properties obtained while using the multi-phase meshing technique are similar to those for which the free meshing (Delaunay triangle elements) is used **Kanit *et al.* (2003).** However**,** the two techniques show slight local field discrepancies where the free meshing technique happens to be more accurate **Lippmann *et al.* (1997).** Still, in our case of macroscopic properties, this difference is not of great importance.

The application of periodic boundary conditions (PBC) on boundaries of the domain also calls for the use of square elements that ensure regular node distributions on the mesh edges rather than triangular ones for which this condition is not sure to be fulfilled, hence securing a uniform distribution and the proper functioning of the PBC.

An example of a multiphasic meshed image sample with a square grid is shown in figure III-5.

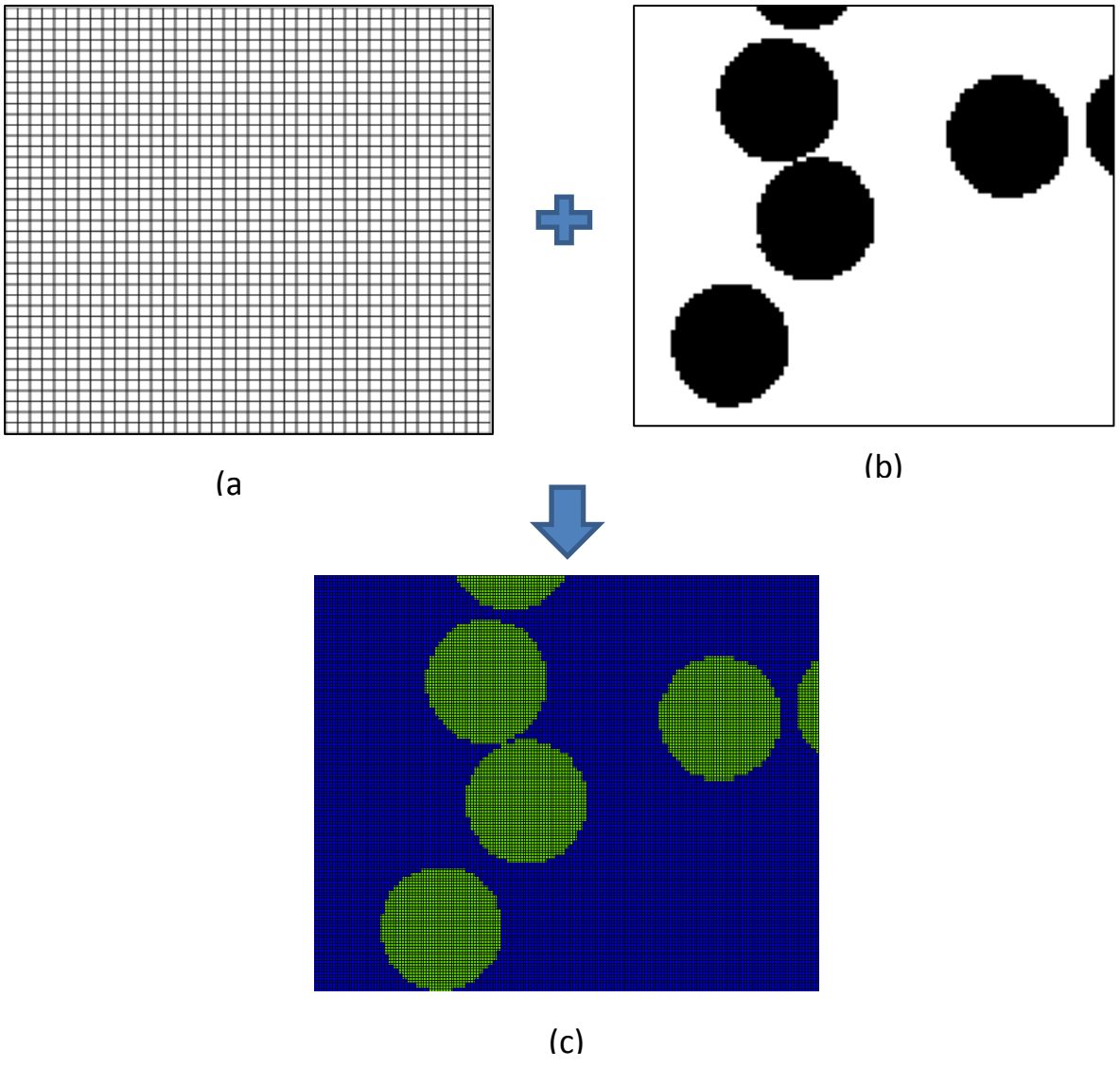

Figure III-5. Description of the multi-phase meshing technique: **(a)** Square meshing grid applied to **(b)** image sample and **(c)** the final meshed image sample

The mesh quality was also verified by controlling the final volume fraction of the meshed sample.

II- Validation of simulations

In this section, only the validation of the samples will be presented. Actually, the FEM code used to obtain the numerical results is known to be highly accurate (ref. Kanit ???) yet the ratio between the characteristic sizes of inclusions and the mesh, the typical size of the RVE and the edge effect on the effective values had to be quantified.

II-1 Mesh density

With the multiphase mesh technique, the possibility of having two different phases in the same finite element is a disadvantage that can skew the results. Thus, to ensure accuracy, even in high stress gradients situations, the finite element mesh must be fine enough to avoid dependence of results on mesh scales. It is then mandatory to study the different mesh resolutions. For this matter, a wide range of increasing mesh grids were tested for the same non-overlapping microstructure, namely here: 50^2, 100^2, 150^2, 200^2, 250^2, 300^2, 400^2 and 500^2. The bulk modulus was calculated on the previous different mesh grids for a volume fraction $V_f = 30\%$ until the convergence stabilized as shown in figure III-6.

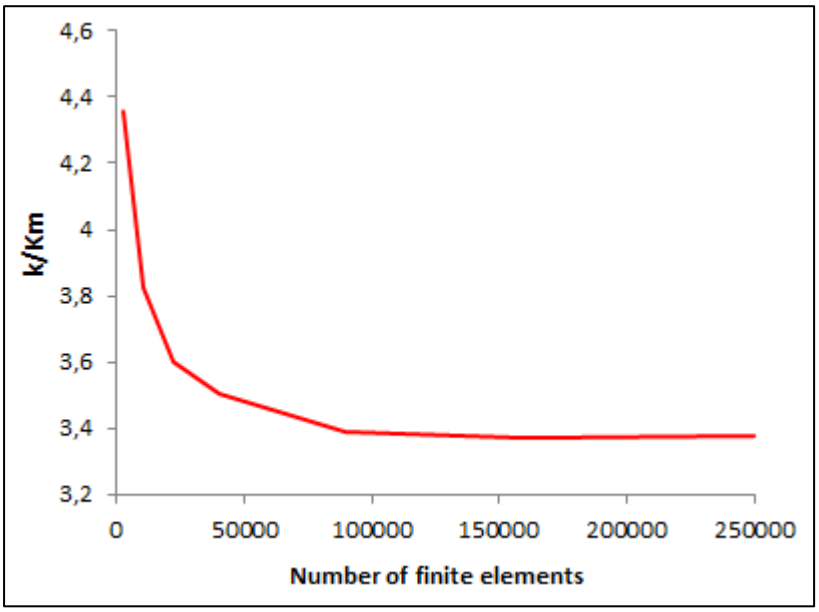

Figure III-6. Evolution of the bulk moduli as a function to the number of finite elements for $V_f = 30\%$

It is noticed that the bulk modulus tends to stabilize for large node densities, starting at the 300^2 mesh grid.

The study was conducted on the bulk moduli because shear modulus is known to converge faster.

The mesh density used for all the studies conducted and presented in this manuscript was that of 500^2 finite elements ensuring an accurate representation of the geometry.

II-2 Study of RVE

In the following work, a study to determine the representative volume element RVE of our microstructures has been conducted on 3 generated overlapping image samples of different sizes (figure III-7) where N is the number of inclusions.

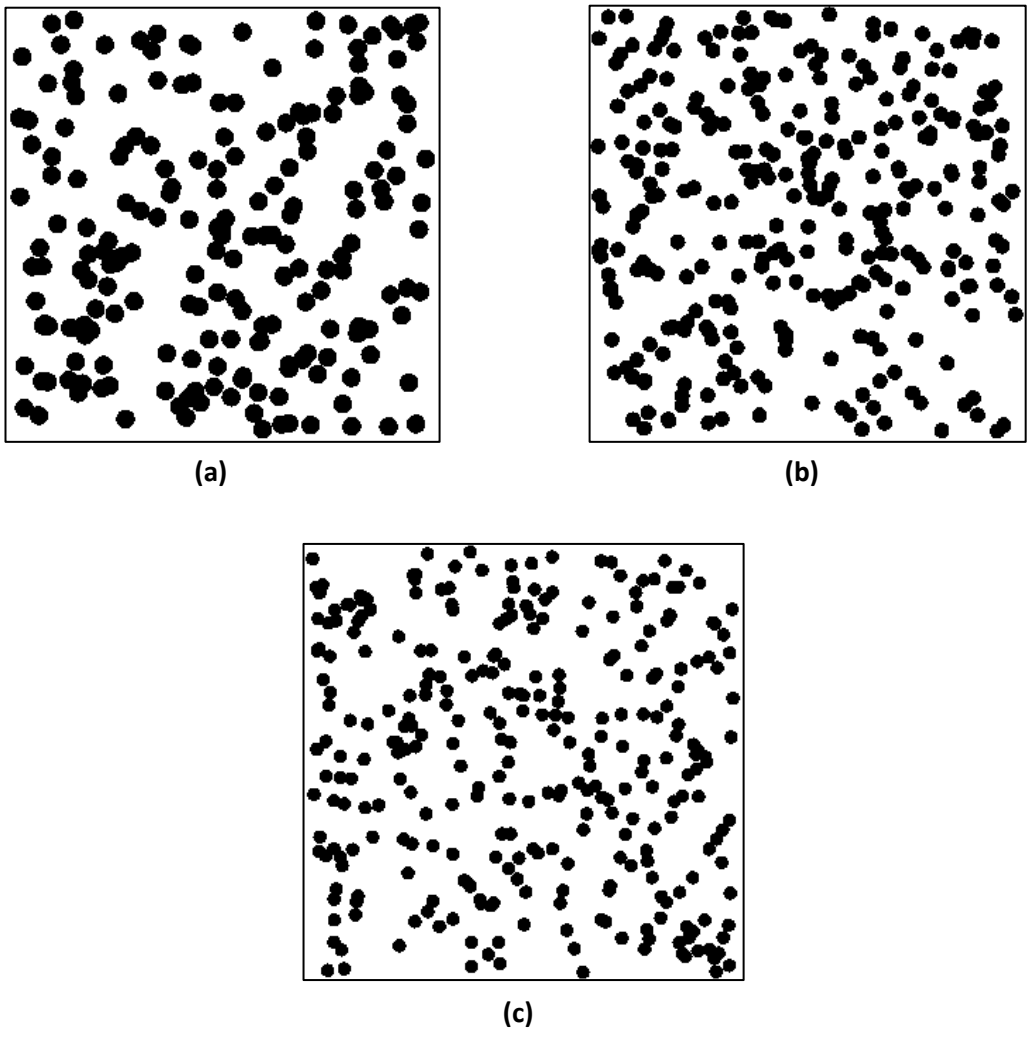

Figure III-7. Different overlapping sample sizes **(a)** $N = 200$, **(b)** $N = 300$ and **(c)** $N = 400$

As an example, the following table 1 summarizes the numerical results for a volume fraction $V_f = 30\%$ with Young moduli $E_m = 10\ GPa$, $E_i = 1000\ GPa$ and Poisson ratio $\upsilon_m = \upsilon_i = 0.3$ and thermal conductivity $\lambda_i = 1000\ Wm^{-1}K^{-1}$ and $\lambda_m = 10\ Wm^{-1}K^{-1}$.

	Bulk		Shear		Thermal Conductivity	
N	KUBC	PBC	KUBC	PBC	UGT	PBCT
200	15.8	15.62	6.85	6.68	19.95	19.63
300	15.73	15.59	6.91	6.78	20.61	20.21
400	14.04	13.94	6.02	5.91	17.64	17.26

Table 1. Results under different boundary conditions for the 3 overlapping image samples in GPa

Table 1 shows that for $N = 200$, we reach a good convergence of the results and the discrepancy between uniform and periodic boundary conditions is generally less than 2%.

This sample size can be considered an RVE and used for later work.

In the upcoming studies, and due to computer hardware limitations (the previous calculations were carried out on a more performant computer), the samples will be limited to $N = 49$ fiber inclusions beyond which the results lose precision and become inaccurate and the simulations will be studied under KUBC boundary conditions.

To overcome this limitation, the results presented in this work, for any given physical property, were averaged on 25 different samples that were necessary to reach convergence of the overall elastic and thermal properties. Thus the numerical accuracy and the precision of calculations were preserved.

However, with samples $(N = 49)$ significantly smaller than the RVE $(N = 200)$ the issue of boundary conditions also referred to later as the edge effect becomes highly relevant and necessitates a closer study which is going to be the subject of the next section.

II-3 Edge effects

Because the RVE is not reached on the scale of a single image of $N = 49$, local effects in the zones adjacent to borders could affect the effective properties and were to be looked at closely.

On plane samples where the centers of inclusions were randomly generated following a Poisson law, some inclusions can be truncated on the edges of the sample as figure III-8 shows.

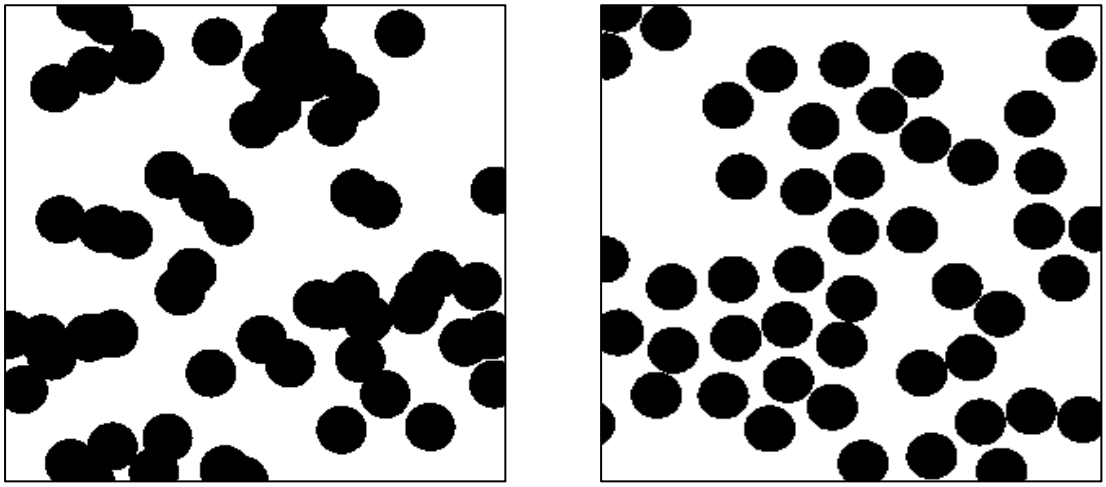

(a) **(b)**

Figure III-8. Plane **(a)** overlapping and **(b)** non-overlapping

Another way to create samples is to impose an additional condition of staying strictly within the frame for the fibers. They are referred to as framed samples (figure III-9).

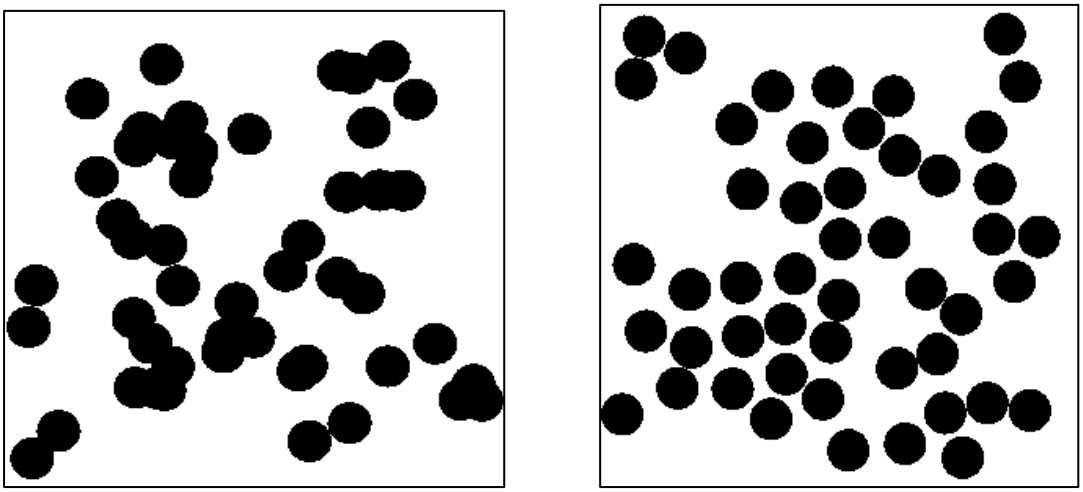

(a) **(b)**

Figure III-9. Framed **(a)** overlapping and **(b)** non-overlapping samples

The plane samples were not considered in this work due to difficulties in controlling the volume fraction and only the framed samples were studied.

To characterize the edge effects on numerical results, the study was only carried on the bulk elastic property case, which is representative of the problem. For this, partial samples of the original ones were generated in order to compare the results for both samples.

The original 300^2 pixels sample was cropped by $L = 26.5$ pixels as sketched on figures III-10 and III-11 which corresponds to the diameter of an inclusion and then cropped by $L = 30$ pixels for the second sample that aims to go a little further into the structure and would help determine the limits of these edge effects. The error on V_f was always kept lower than 1%.

The presented results were averaged on 3 image samples for both overlapping ($V_f = 25.7\%$ $N = 49$) and non-overlapping ($V_f = 30\%$ $N = 49$) examples.

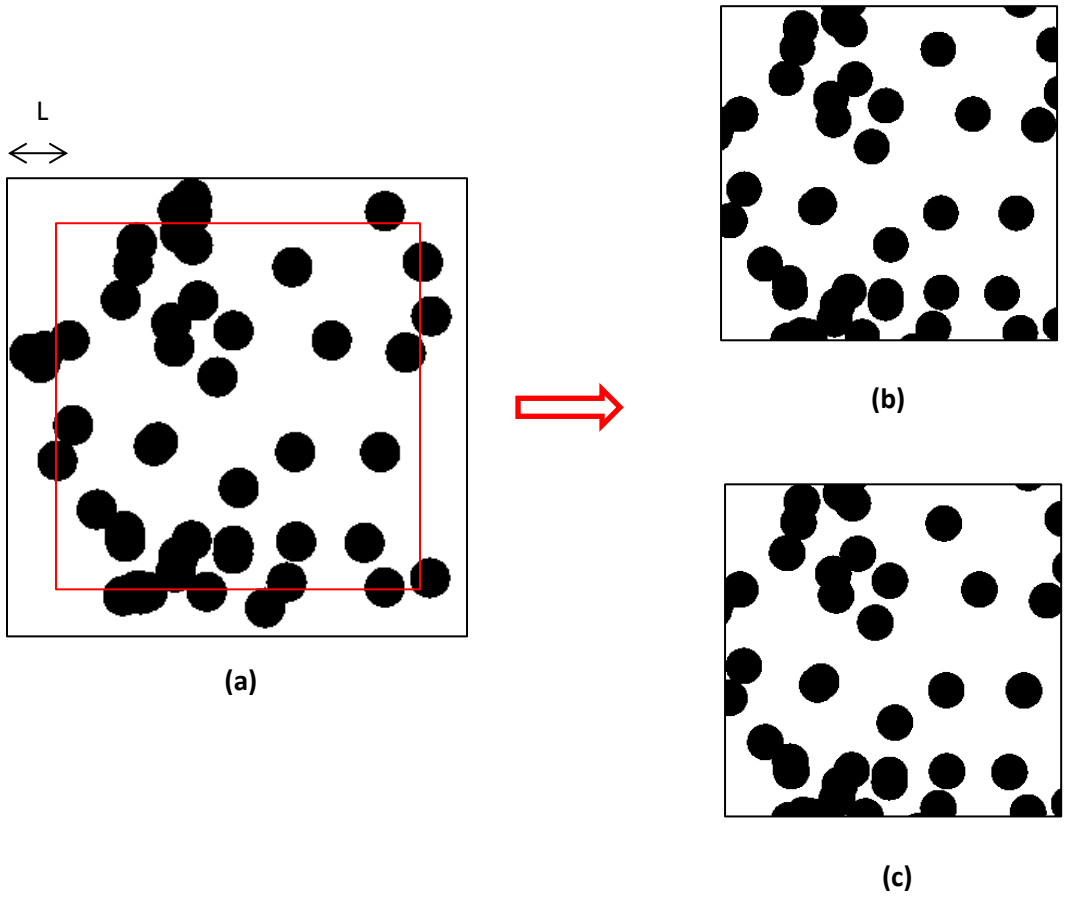

Figure III-10. Overlapping: **(a)** Initial sample, **(b)** Embedded sample ($L = 26.5$) and **(c)** Embedded sample ($L = 30$)

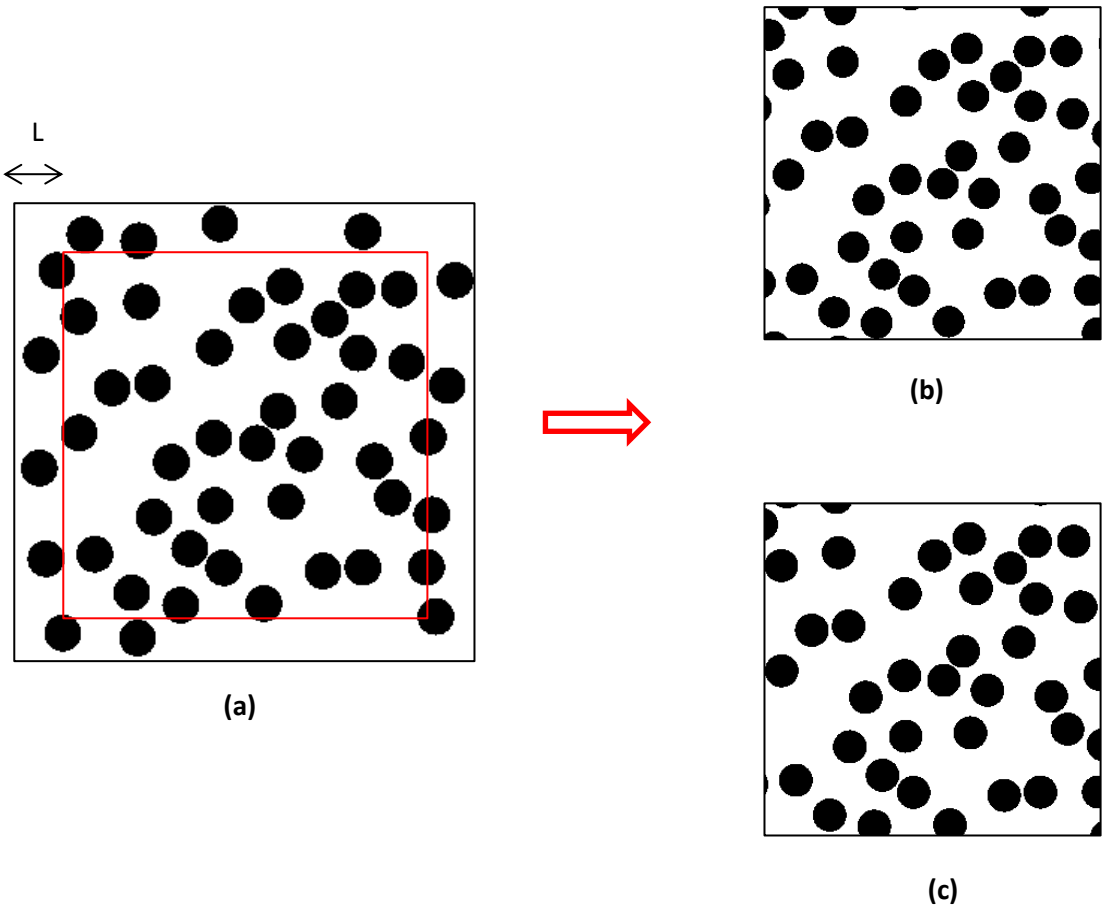

Figure III-11. Non- overlapping: **(a)** Initial sample, **(b)** Embedded sample $(L = 26.5)$ and **(c)** Embedded sample $(L = 30)$

The following table 2 summarizes the obtained results:

		Overlapping	Non-Overlapping
		Bulk	**Bulk**
Framed sample		15.53	15.81
Partial samples	**L=26.5**	22.73	20.84
	L=30	22.79	20.68

Table 2. Results for bulk modulus for overlapping $V_f = 25.7\%$ and non-overlapping $V_f = 30\%$ samples

The comparison of the two partial samples shows that edge effects are of very low influence on effective bulk moduli. The relative discrepancies are of same order than those of volume fraction (less than 1%). However, the behavior of the framed samples is significantly different with effective bulk moduli 30% lower due to the absence of inclusions on the boundaries.

The results of Part 2 will all be obtained on framed samples that are more representative of materials in real applications in which all fibers are located within the matrix.

Part 2

Chapter 4

Characterization of samples

The aim of this chapter is to characterize the microstructures of the 49 inclusion samples which will be used for non-overlapping aligned fiber reinforced composites.

Two main results stand out:

- The influence of inclusions on bulk modulus is at longer range for RSA samples than for PY ones for which stresses are minimized.

- For well-defined microstructures, the RVE minimum size is reduced to less than 49 inclusions.

As in the previous chapter, the overlapping case will be used as a reference given its trivial fiber distribution following a Poisson law.

All the results are presented for a contrast between fibers and matrix Young moduli $C = \frac{E_i}{E_m} = 100$. This contrast is the same for bulk and shear moduli as the Poisson ratios for both phases were chosen equal.

I- Integral range

As mentioned in chapter 1, contrary to $g(r)$, the two-point correlation function S_2 alone contains little information. Nevertheless, S_2 allows a measure of the characteristic length scales of the variation of physical quantities such as bulk modulus called the integral range.

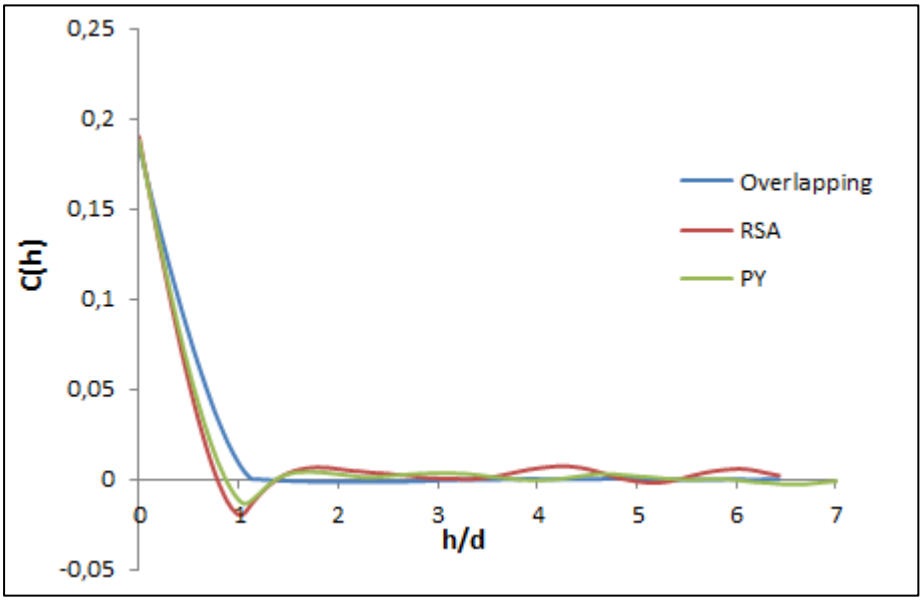

Figure IV-1. Covariance on I for overlapping and non-overlapping composites for $V_f = 25.18\%$ and $C = 100$

Figure IV-1 shows the covariance on the characteristic function I for overlapping, RSA and PY samples. These results were obtained by ensemble averaging on 25 samples of 49 inclusions. Covariance is equivalent to S_2 but is summable with null values at long distance. Negative values appear around the abscissa h/d=1 for the non-overlapping systems denoting an increase in the rate of finding two points separated by a distance h in two different phases unlike for the overlapping ones in which the probability of finding two points in the same phase is higher, especially in the inclusion phase for volume fractions less than 50%.

PY and RSA covariance curves are very similar so $C(h)$ or S_2 are not suitable tools to compare different non-overlapping structures, higher $n-$point probability functions are required (at least S_3 as it was the case in Milton bound calculations). Therefore, in this study of non-overlapping composites, Rdf will be favored as the second order correlation.

An efficient tool to measure the discrepancies between characteristic functions is the integral range **Jeulin (2016)** that is the sphere of influence through the characteristic

functions of the considered physical quantity. For two dimensional problems, the sphere is reduced to a circle.

Let C be the covariance of these functions in 2D:

$$A = \frac{1}{C(0)} \iint_S C\left(\sqrt{x^2 + y^2}\right) dxdy \quad (1)$$

Which becomes in cylindrical coordinates:

$$A = \frac{2\pi}{C(0)} \int_0^{+\infty} C(h)\, h\, dh \quad (2)$$

For the covariance on figure IV-1, the integral ranges on the characteristic function are respectively $A = 0.71\mathrm{d}^2$ and $A = 0.97\mathrm{d}^2$ for PY and overlapping samples. The highest value denotes connectedness between fibers.

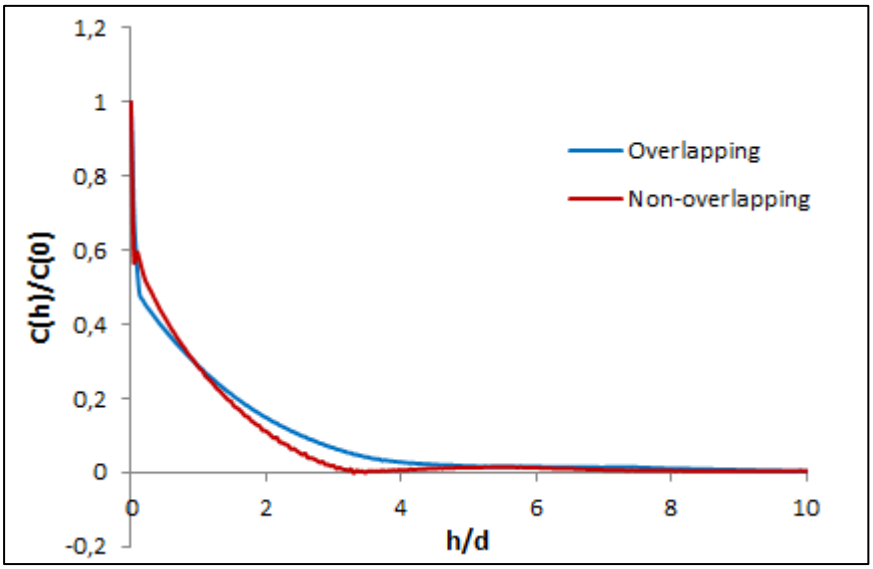

Figure IV-2. Covariance on bulk modulus k for overlapping and non-overlapping PY samples for $V_f = 25.18\%$ and $C = 100$

As for covariance on I, covariance on k shows a higher value for overlapping than non-overlapping cases (figure IV-2). The corresponding integral ranges are $A = 8.72d^2$ and

$A = 3.74d^2$, denoting again the connectedness of the overlapping system.

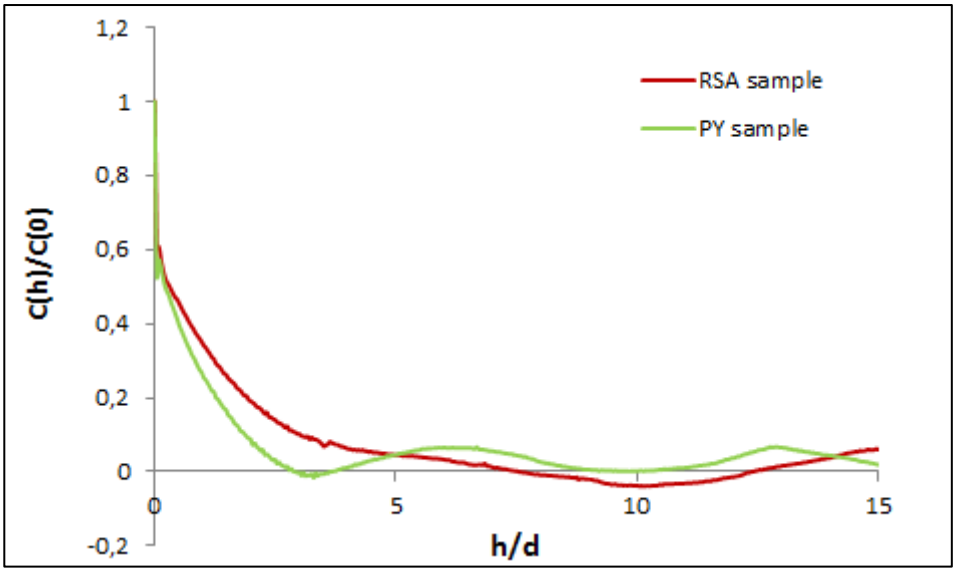

Figure IV-3. Covariance on bulk modulus k for non-overlapping PY and RSA samples for $V_f = 25.18\%$ and $C = 100$

The integral range evaluated from figure IV-3 for PY and RSA are respectively $A = 3.7\ d^2$ and $A = 11.7\ d^2$ denoting larger areas of high stresses around fibers for RSA sample due to occurrence of fiber close-together as it is confirmed by the Rdf on figure IV-4.

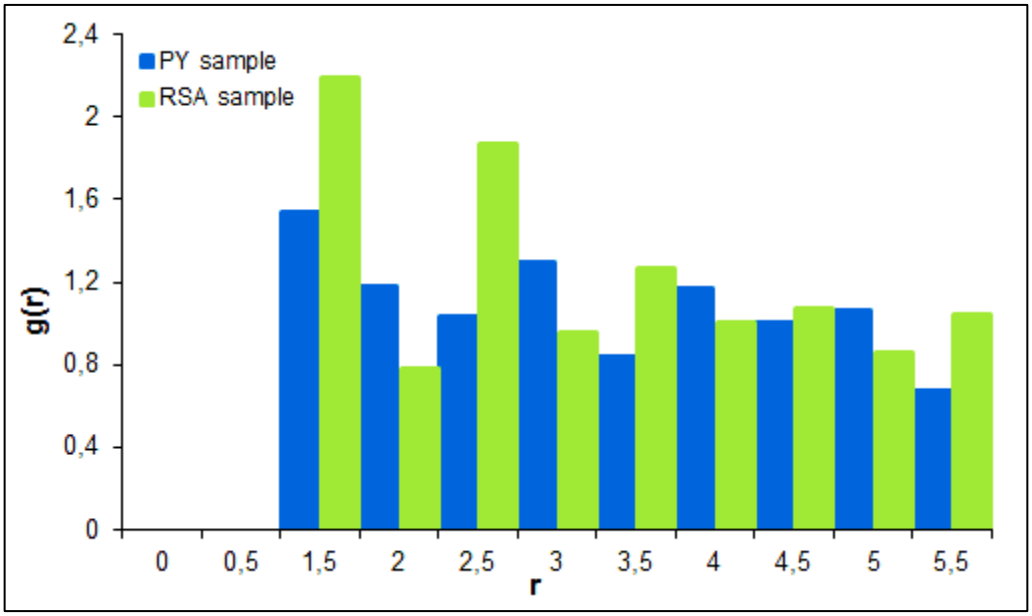

Figure IV-4. Rdf for PY and RSA samples of $V_f = 25.18\%$

The peak $g(1 < r < 1.5)$ is 1.5 times higher for RSA than PY and denotes the formation of chains of fibers where higher stresses occur.

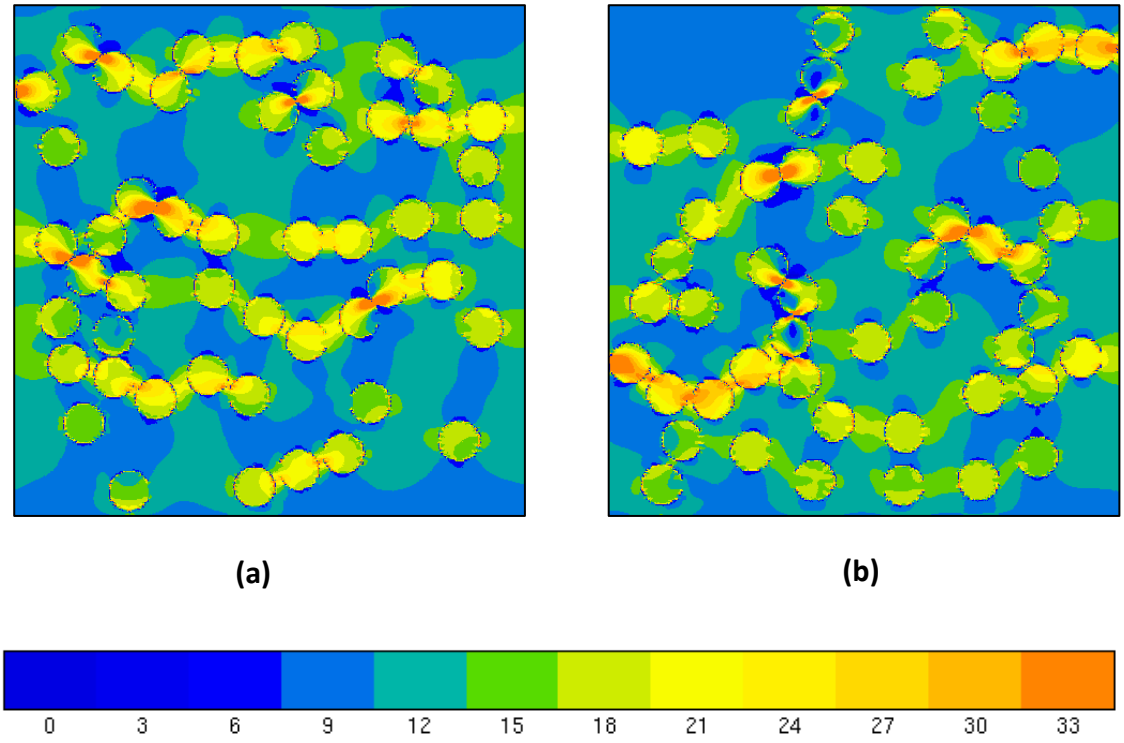

Figure IV-5. Normal stress σ_{11} maps for **(a)** PY and **(b)** RSA samples (GPa) for $C = 100$ and $V_f = 25.18\%$

Figure IV-5 confirms the previous deduction from $g(r)$. For PY, high stresses appear only between pairs of fibers while for RSA, these high stresses form line segments aligned in the direction of the strain. The PY sample is more homogeneous than the RSA one where large areas of matrix characterized by low stresses occur but are still insufficient to compensate for the high stress chains. The effective values for RSA are higher than those of PY of about 10%.

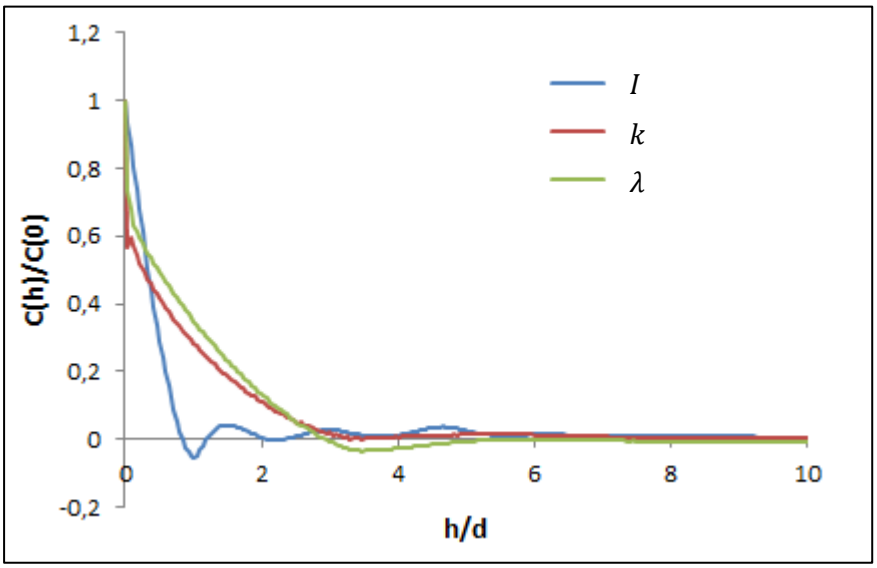

Figure IV-6. Covariance on the characteristic function I, bulk modulus k and thermal conductivity λ for non-overlapping PY samples for $V_f = 25.18\%$ and $C = 100$

For each of the random variables I, k and λ, the shape of the covariance curves on the PY samples is different indicating different integral ranges (figure IV-6). For I, $A = 0.71d^2$ which is close to the surface area of inclusions $\frac{\pi d^2}{4}$ while for k and λ, we have respectively $A = 3.74d^2$ and $A = 4.32d^2$ which corresponds to a diameter slightly higher than $2d$. The integral range of the thermal conductivity is higher than that of bulk modulus, however, there is a large uncertainty on the integral range due to integration with cylindrical coordinates that amplifies the small fluctuations at long distance. The variation in elasticity damps more rapidly than in thermal conductivity.

The shear stress corresponds to a "rotation" within the solid so covariance on shear modulus is irrelevant and was not studied.

II- Homogeneity of samples

At the scale of a chosen sample, the macroscale, the volume fraction is well defined while at smaller scales, ranging from those of inclusions (microscale) to intermediate ones (mesoscale), the local volume fraction may fluctuate. On small samples of only 49 inclusions, these fluctuations might significantly affect physical effective properties unlike samples of RVE size where local fluctuations are overshadowed by the large number of inclusions.

A measure of these fluctuations was introduced by **Lu and Torquato (1990)** by means of an adimensioned standard deviation $\sigma_{V_{f1}}$ of the local volume fraction called coarseness C_{S_1}.

Let S_1 be the area of a sliding window swept across the whole surface S of the sample, a local volume fraction V_{f1} is associated to each $\boldsymbol{x}$ position of $S_1(\boldsymbol{x})$:

$$V_{f1}(\boldsymbol{x}) = \frac{1}{S_1} \iint_{S_1} I(\boldsymbol{x}) d\boldsymbol{x} \tag{3}$$

The coarseness is defined by:

$$C_{S_1} = \frac{\sigma_{V_{f1}}}{V_f} \tag{4}$$

Where N_1 positions were chosen depending on the size of the window:

$$\sigma_{V_{f1}} = \sqrt{\frac{1}{N_1} \sum_{i=1}^{N_1} \left(V_{f1i} - V_f\right)^2} \tag{5}$$

And with the properties of the characteristic function $I(\boldsymbol{x})$:

$$\sigma_{V_{f1}} = \sqrt{\frac{1}{N_1} \sum_{i=1}^{N_1} {V_{f1i}}^2 - V_f^2} \tag{6}$$

Typical examples of coarseness are presented in figure IV-7.

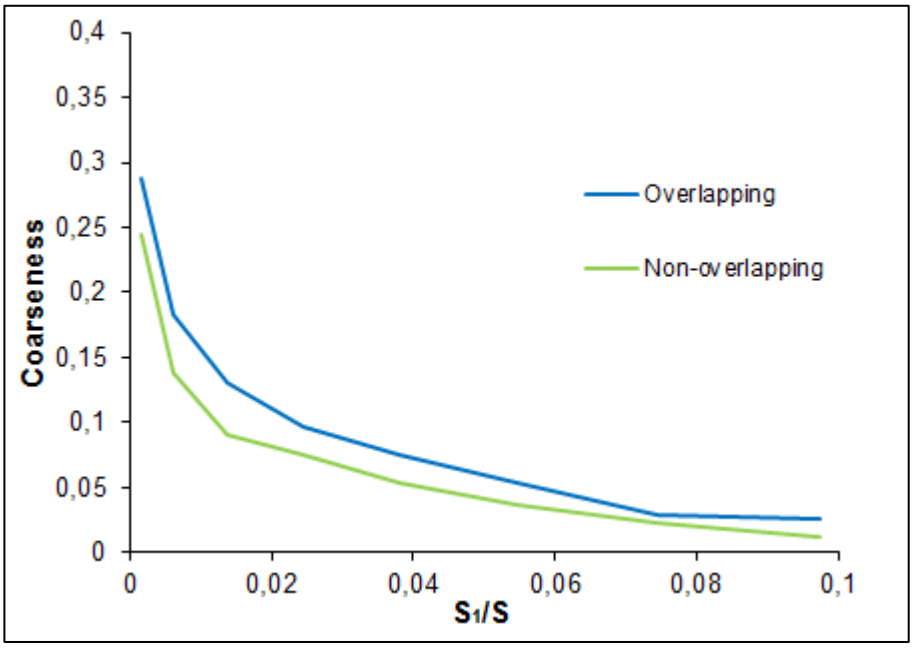

Figure IV-7. Typical coarseness curves for overlapping and non-overlapping PY samples for $V_f = 25.18\%$

Naturally for small windows, the coarseness is high with frequent changes of phase. As window size increases, C_{S_1} decreases down to zero for $S_1 = S$. Thus, very small and very large window sizes with regard to inclusion size are not relevant.

The following results are presented for three windows of sizes:

$S_1 = 1.2\, S_{Incl} = 0.0062\, S$, $S_1 = 5.0\, S_{Incl} = 0.0257\, S$ and $S_1 = 11.2\, S_{Incl} = 0.0576\, S$

As it will be shown in chapter 6, the peak of $g(1 < r < 1.5)$ is a significant parameter for determining the values of the effective properties, therefore, figure IV-7 are phase diagrams between coarseness and $g(1 < r < 1.5)$.

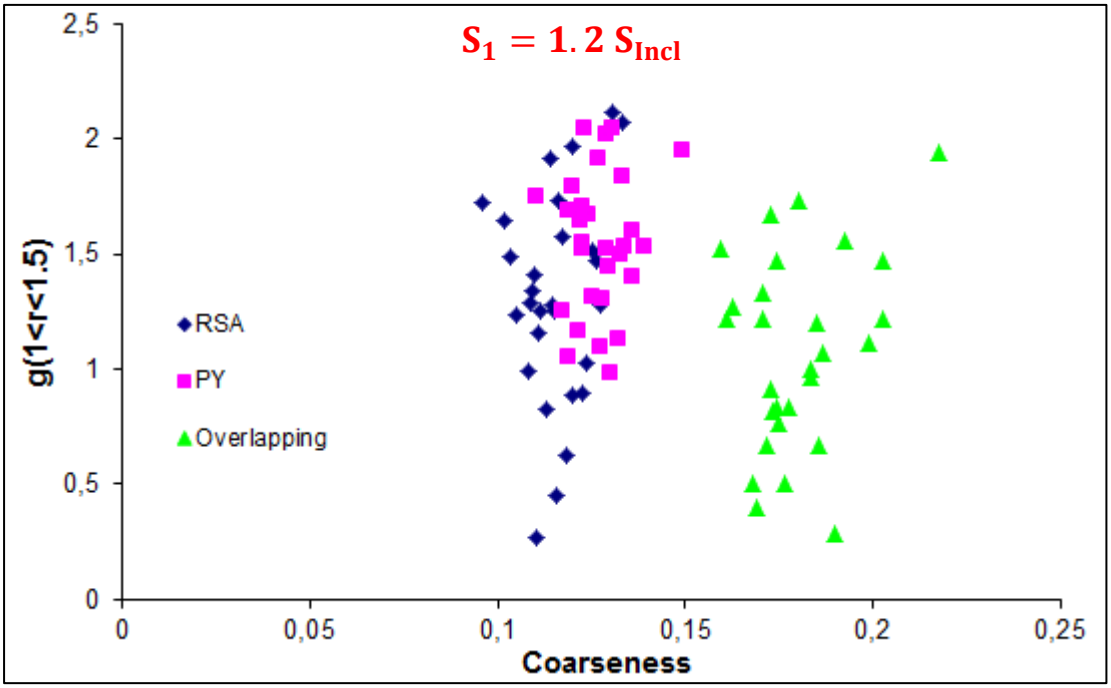

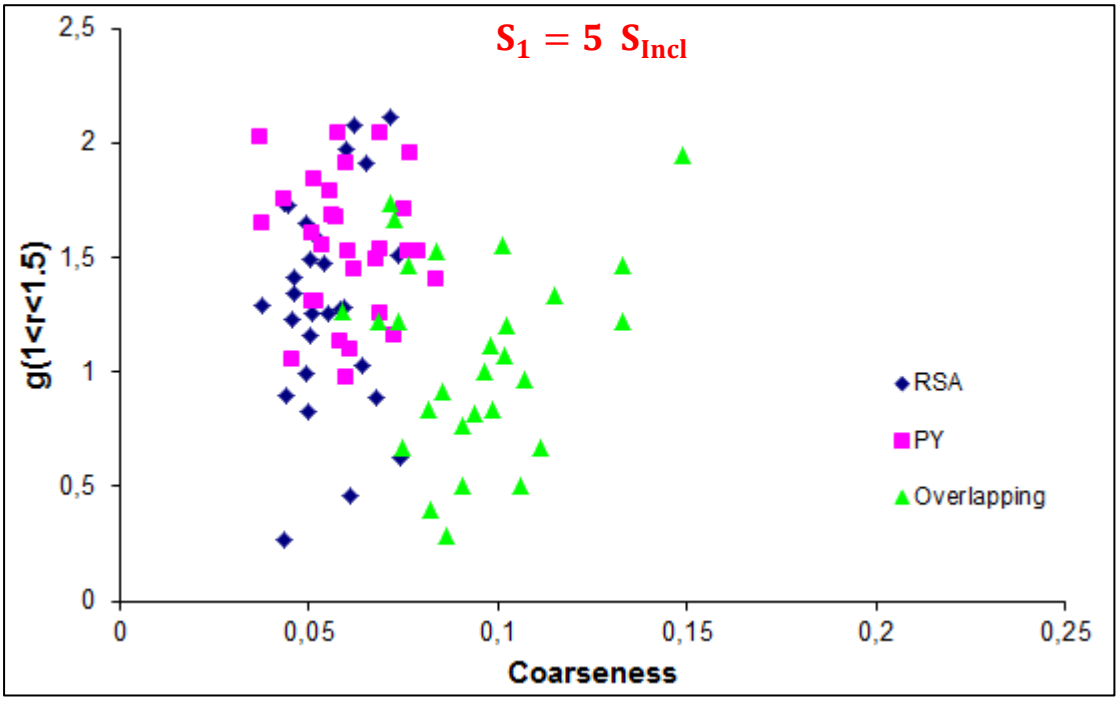

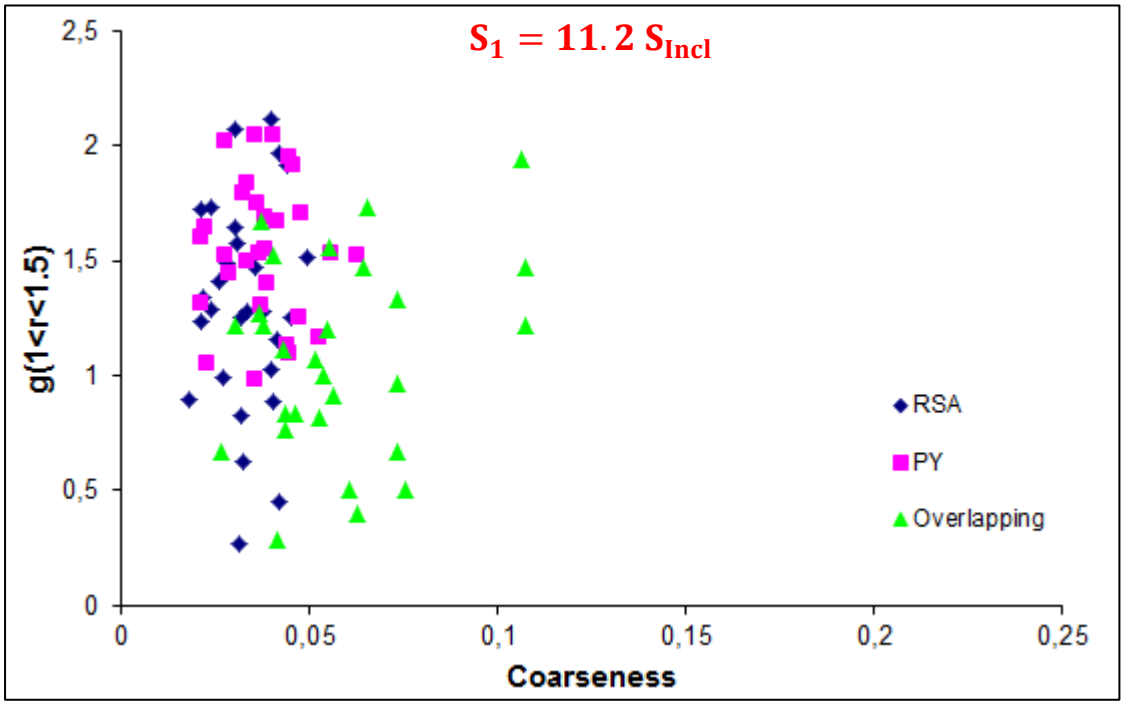

Figure IV-8. Peak of Rdf with regard to coarseness for three window sizes: $S_1 = 1.2\ S_{Incl}$, $S_1 = 5.0\ S_{Incl}$ and $S_1 = 11.2\ S_{Incl}$ for $V_f = 25.18\%$

On figure IV-8, the whole ensemble of points are scattered indicating that coarseness is uncorrelated with the peak of Rdf and could be a complementary tool to characterize influence of microstructure on homogenization.

Naturally for the small window $S_1 = 1.2\ S_{Incl}$, the overlapping and non-overlapping populations are clearly distinct due to connectedness of fibers in the former. As the window size increases, the two populations merge and even at mesoscale $S_1 = 11.2\ S_{Incl}$, the overlapping samples are still more inhomogeneous. From $S_1 = 1.2\ S_{Incl}$ to $11.2\ S_{Incl}$, the coarseness evolves from respectively 12 and 18% for non-overlapping and overlapping to about 5% for both which denotes an expected change in the shape of the probability density of the local volume fraction as sketched on figure IV-8.

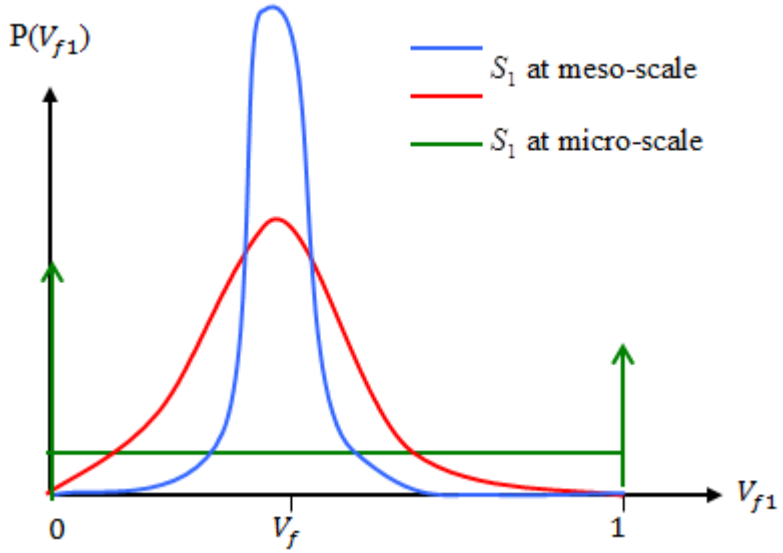

Figure IV-9. Schematic probability density frequencies $P(V_{f1})$

For windows at microscale $S_1 < S_{Incl}$, the probability density frequencies of V_{f1} exhibits two Dirac distributions for $V_{f1} = 0$ and $V_{f1} = V_f$ corresponding respectively to the windows in the matrix and the inclusions. When both matrix and inclusion phases are within the window, a continuous probability density frequencies between the two peaks is expected, schematically represented in figure IV-9 by a straight line. This window size does not provide new information on microstructures and will not be used for the study of coarseness influence on effective values. Actually, the inhomogeneity in volume fraction can only be revealed at mesoscales.

For large windows at mesoscale, the probability density frequencies of V_f behaves as a maxwellian distribution centered on V_f with decreasing widths as the window size increases (from the red curve to the blue).

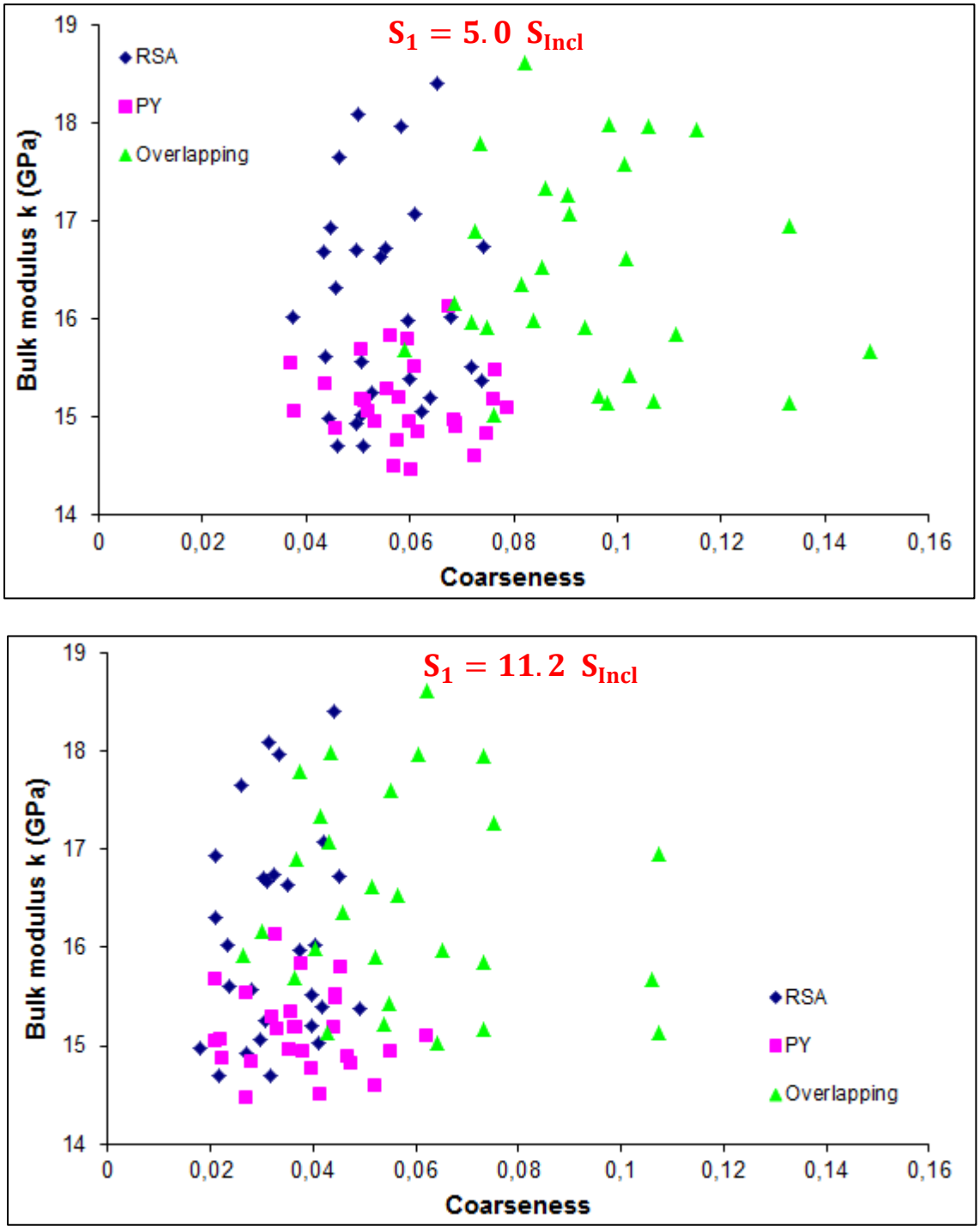

Figure IV-10. Bulk modulus with regard to coarseness for two window sizes: $S_1 = 5.0\ S_{Incl}$ and $S_1 = 11.2\ S_{Incl}$ for $V_f = 25.18\%$

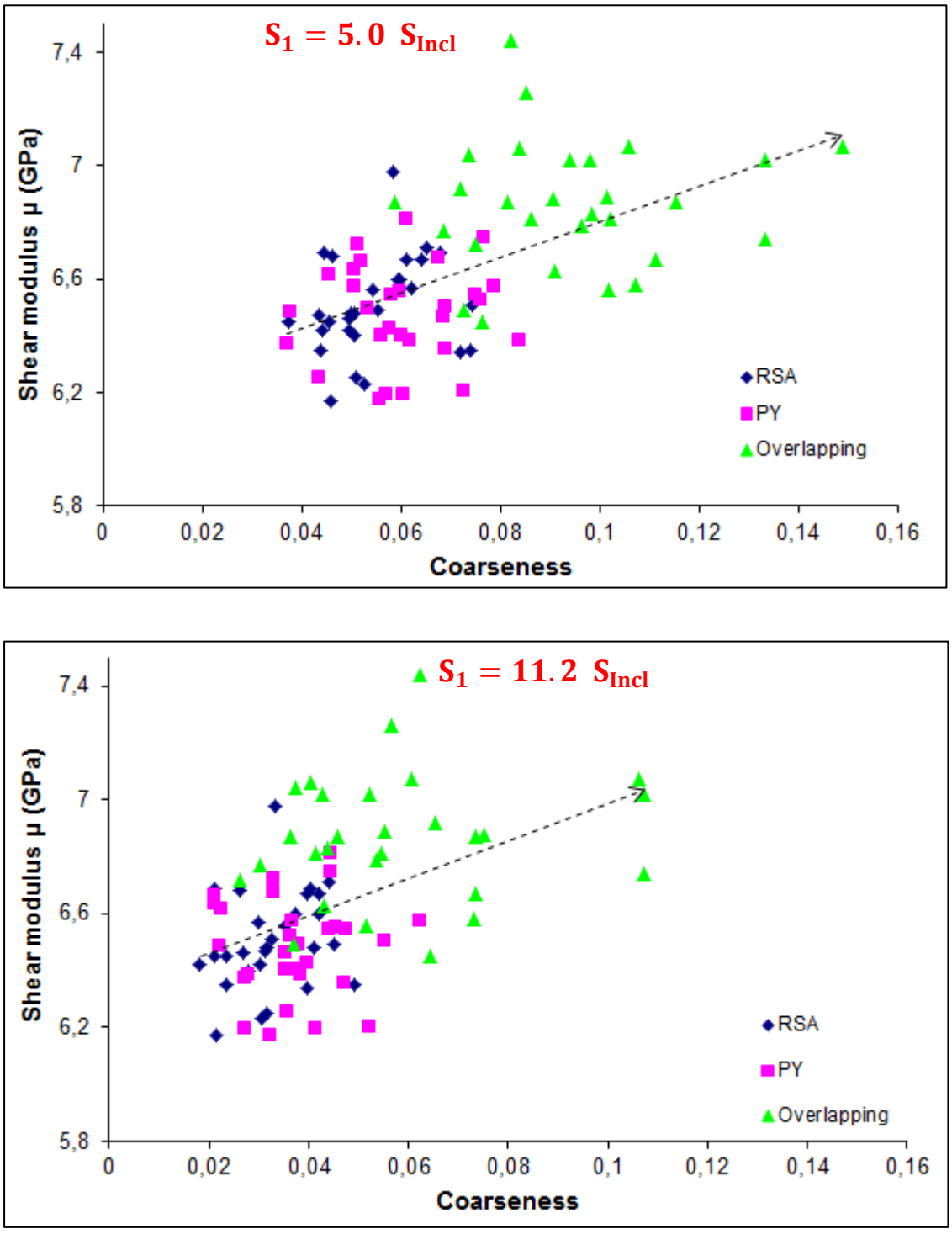

Figure IV-11. Shear modulus with regard to coarseness for two window sizes: $S_1 = 5.0\ S_{Incl}$ and $S_1 = 11.2\ S_{Incl}$ for $V_f = 25.18\%$

The homogenized values of bulk moduli are uncorrelated with coarseness as figure IV-10 shows. Coarseness is not able to capture the relevant inhomogeneities that affect the bulk effective values. However, shear moduli clearly increase with coarseness as illustrated on figure IV-11 by the tendency arrows evaluated with the help of least square regression but the reason why shear is more sensitive than bulk to local density inhomogeneity is still not explained.

For both window sizes, this tendency is significant enough to be taken into account in modelization of microstructures for homogenization of shear stresses.

III- RVE minimum size

For bulk modulus the PY values, shown on figure IV-10, are less dispersed than those of RSA. The extreme PY values deviate by 5% from the mean value while those of RSA deviate by 15% due to a better control of microstructures on PY systems. The shear stress seems less sensitive to dispersion in microstructures as RSA and PY values on figure IV-10 show. Thus, for bulk modulus, it is expected that a controlled microstructure leads to a smaller RVE.

The PY samples in this study were built with a SA that only controlled the peak $g(1 < r < 1.5)$. Their second order correlations can slightly differ from those of real PY microstructures. That explains the above mentioned dispersion of their bulk moduli.

Among the 25 samples built according to a PY distribution with $V_f = 25.18\%$, three were selected and are sketched on figure VI-12. The **(a)** sample has a bulk modulus close to the value averaged on the 25 samples while for **(b)** and **(c)** samples, the bulk moduli are respectively higher and lower, both deviating from the average value by 5%.

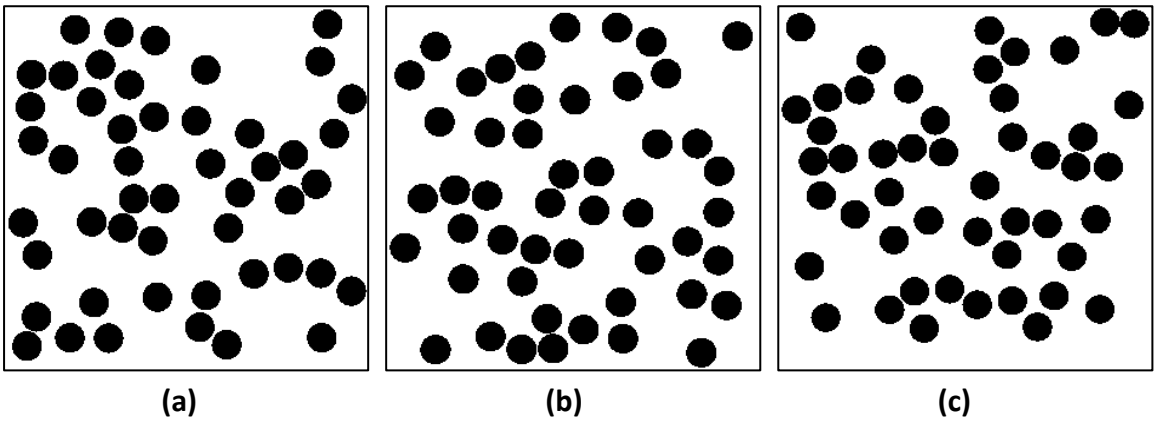

Figure IV-12. Three PY samples: **(a)** with a bulk modulus close to the mean value and **(b)** and **(c)** samples with bulk moduli respectively higher and lower.

At mesoscale, all three samples seem to present inhomogeneity characterized by large voids so their coarseness was evaluated (figure IV-13).

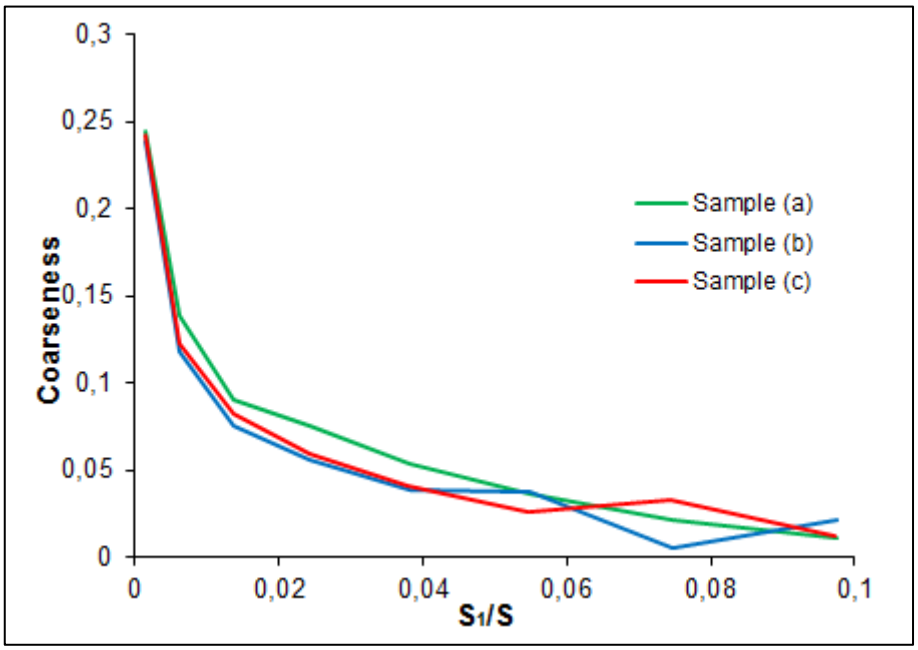

Figure IV-13. Coarseness on the three PY samples **(a)**, **(b)** and **(c)** for $V_f = 25.18\%$

No significant differences between the three samples are observed but surprisingly, slightly higher coarseness values for sample (a). For a family of samples that already tends toward a PY distribution, the coarseness is not a relevant tool hence the study of their Rdf (figure IV-14).

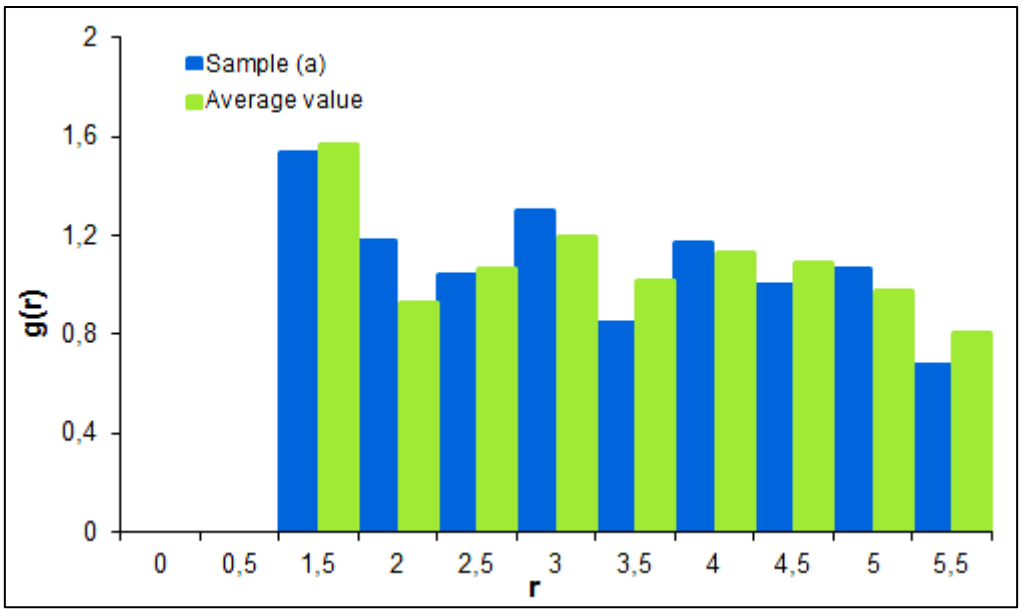

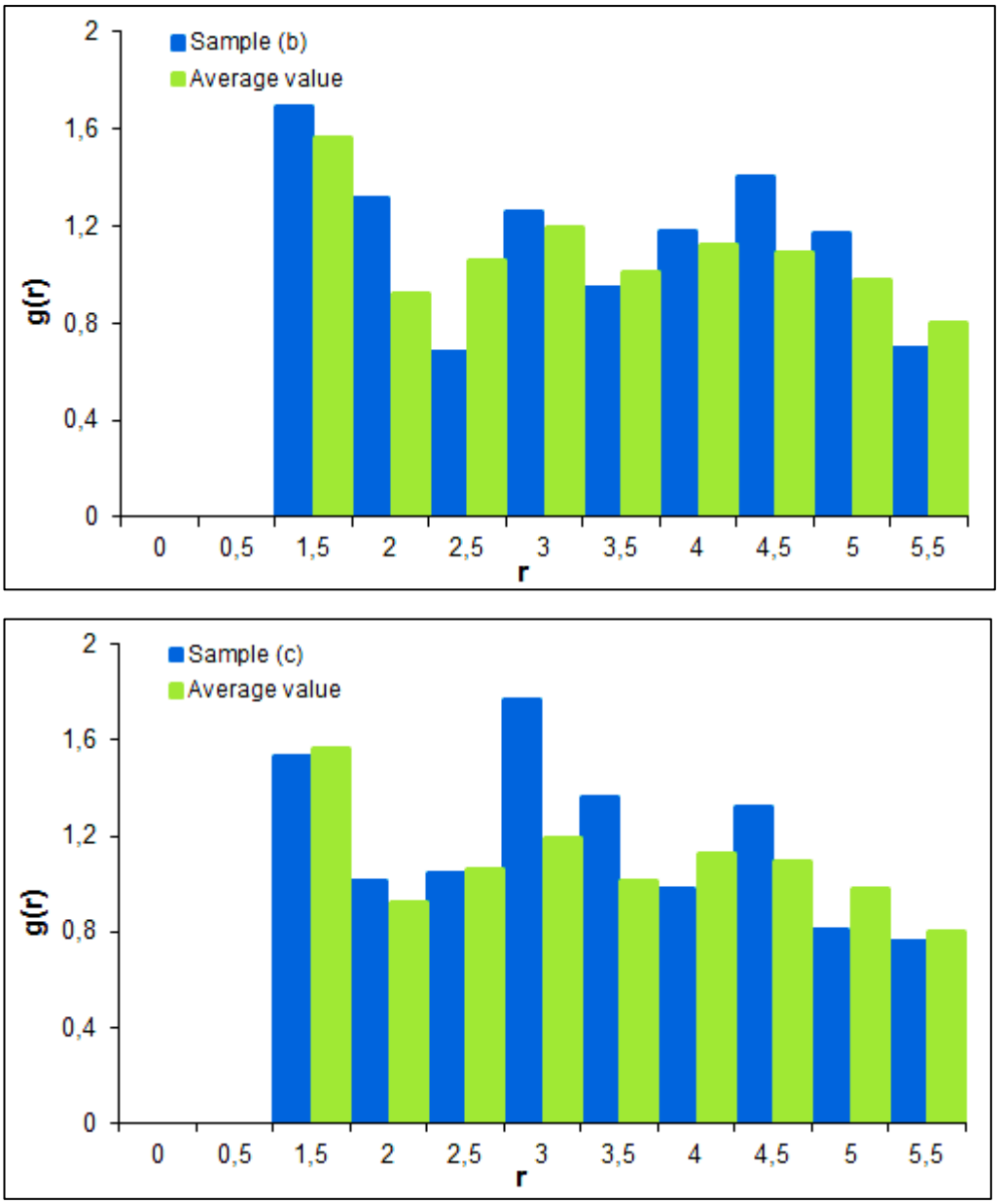

Figure IV-14. Comparison between the mean Rdf and Rdfs of the three PY samples **(a)**, **(b)** and **(c)** for $V_f = 25.18\%$

Rdf on sample (a) suits very well the mean values that are those of the RVE. For samples (b) and (c), Rdf values are respectively too high at a very short distance less than two diameters and larger distances around three diameters. For sample (b), local areas of high stresses appear while for sample (c) high stresses are avoided.

A sample of 49 non-overlapping inclusions with an efficient control of its Rdf such as sample (a) allows to reach RVE according to a high enough precision to observe fluctuations lower than 1% while the usual (without fine Rdf control) RVE sizes for RSA samples are around 300 inclusions, 6 times larger. This confirms the efficiency of Rdf to describe and control microstructures of fiber reinforced composites. It could be expected that reaching RVE could

require even smaller samples if higher order correlations such as $g_N^{(n)}$ with $n > 2$ are controlled as well. In the following chapters, all random samples will be built according to the PY Rdfs.

Chapter 5

Contrast

In terms of contrast C, the elastic behavior of reinforced composites is not trivial: the matrix cushions the deformation of inclusions. The two simple situations of $C = 1$ and $C \to \infty$ lead to easy interpretation, respectively the obvious homogeneous elastic behavior and displacements of rigid bodies. One can expect the field of stresses at infinite contrast to mathematically behave as the characteristic function I, meaning, only two discrete values of local elastic coefficients are observed, one in the matrix and the other within the inclusions.

Generally, the homogenized elastic coefficients k and μ could be expected at first order to be given by simple arithmetic or harmonic averaged values, respectively:

$$k = V_f K_i + \left(1 - V_f\right) K_m \qquad or \qquad \mu = V_f \mu_i + \left(1 - V_f\right) \mu_m$$

And

$$\frac{1}{k} = V_f \frac{1}{K_i} + \left(1 - V_f\right) \frac{1}{K_m} \qquad or \qquad \frac{1}{\mu} = V_f \frac{1}{\mu_i} + \left(1 - V_f\right) \frac{1}{\mu_m}$$

In reality, these expressions are only valid for laminated composites with stresses and deformations in the plane aligned with the composites layers for the arithmetic average (**Voigt (1889)**) and perpendicular to the layers for the harmonic one (**Reuss (1929)**). Obviously, when $C \to \infty$, these expressions are respectively: $k = K_i$ and $k = \frac{K_m}{\left(1 - V_f\right)}$.

For more complicated materials such as fiber reinforced composites, the influence of microstructure cannot be overlooked and additional information is required. It will be shown again that the two-point probability function S_2 or similarly the covariance $C(h)$ that provide a first knowledge of the geometry, for instance, the distinction between overlapping and non-overlapping systems (figure I-12) are still not sufficient when describing elastic behavior at high contrasts.

In this chapter, the focus will be on identifying the elastic and rigid body behaviors. In overlapping situations, the connection between fibers creates large rigid areas that reduce the elasticity of the composite especially at high contrasts. Therefore, a comparison between overlapping and PY non-overlapping systems will also be carried out.

I- Effective elastic values with regard to contrast

Effective values of bulk and shear moduli with regard to contrast are presented on figure V-1 below. These results were obtained by ensemble averaging on 25 samples.

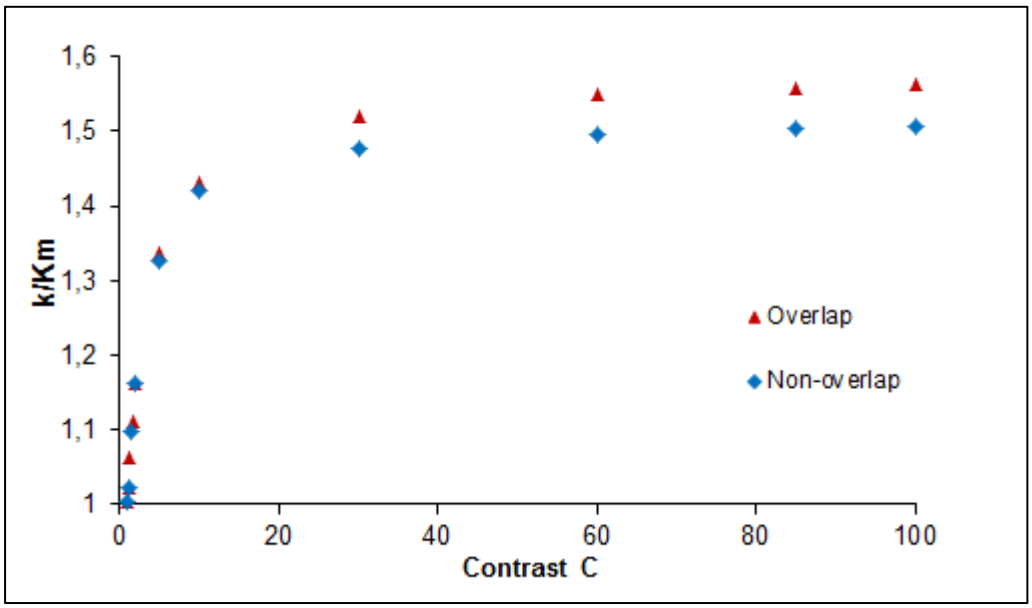

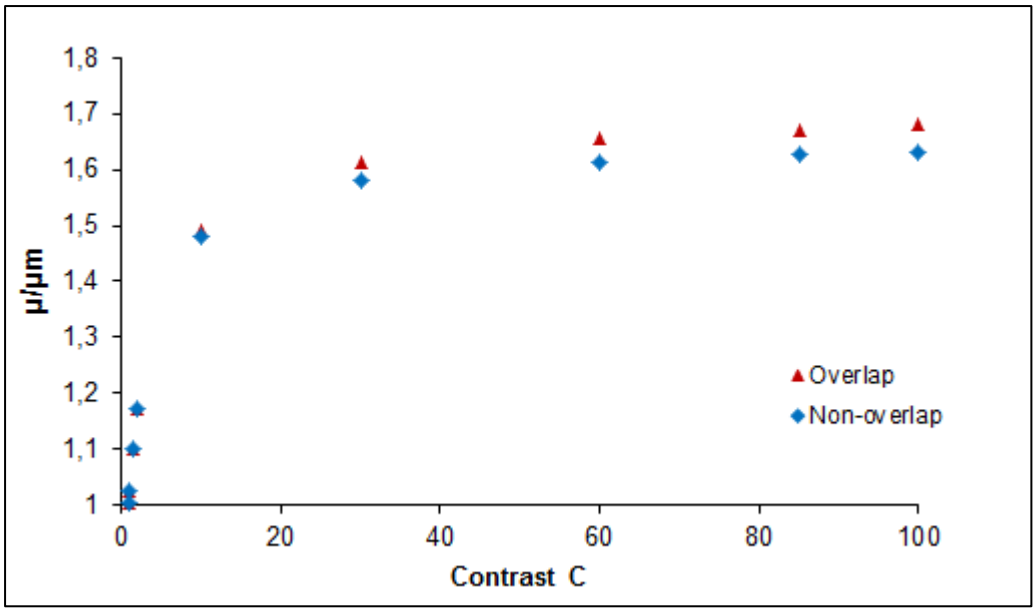

Figure V-1. $\frac{k}{K_m}$ and $\frac{\mu}{\mu_m}$ with regard to contrast for overlapping and non-overlapping fibers for $V_f = 25.18\%$

Figure V-1 shows similar tendencies for both bulk and shear moduli: a continuous increase of effective values. For contrasts ranging from 1 to 5 where it is assumed that the behavior is purely elastic, effective values increase very rapidly with contrast. Above $C = 30$, effective values seem to stabilize.

Figures V-2 and V-3 present the same curves as figure V-1 with a more suitable logarithmic abscissa compared to the Milton lower bounds for bulk and shear moduli. For all contrasts, the homogenized values fit very well with the lower Milton bound kM^- for the overlapping cases whereas for non-overlapping ones, these values slightly deviate (2% at $C = 100$) from the lower bounds.

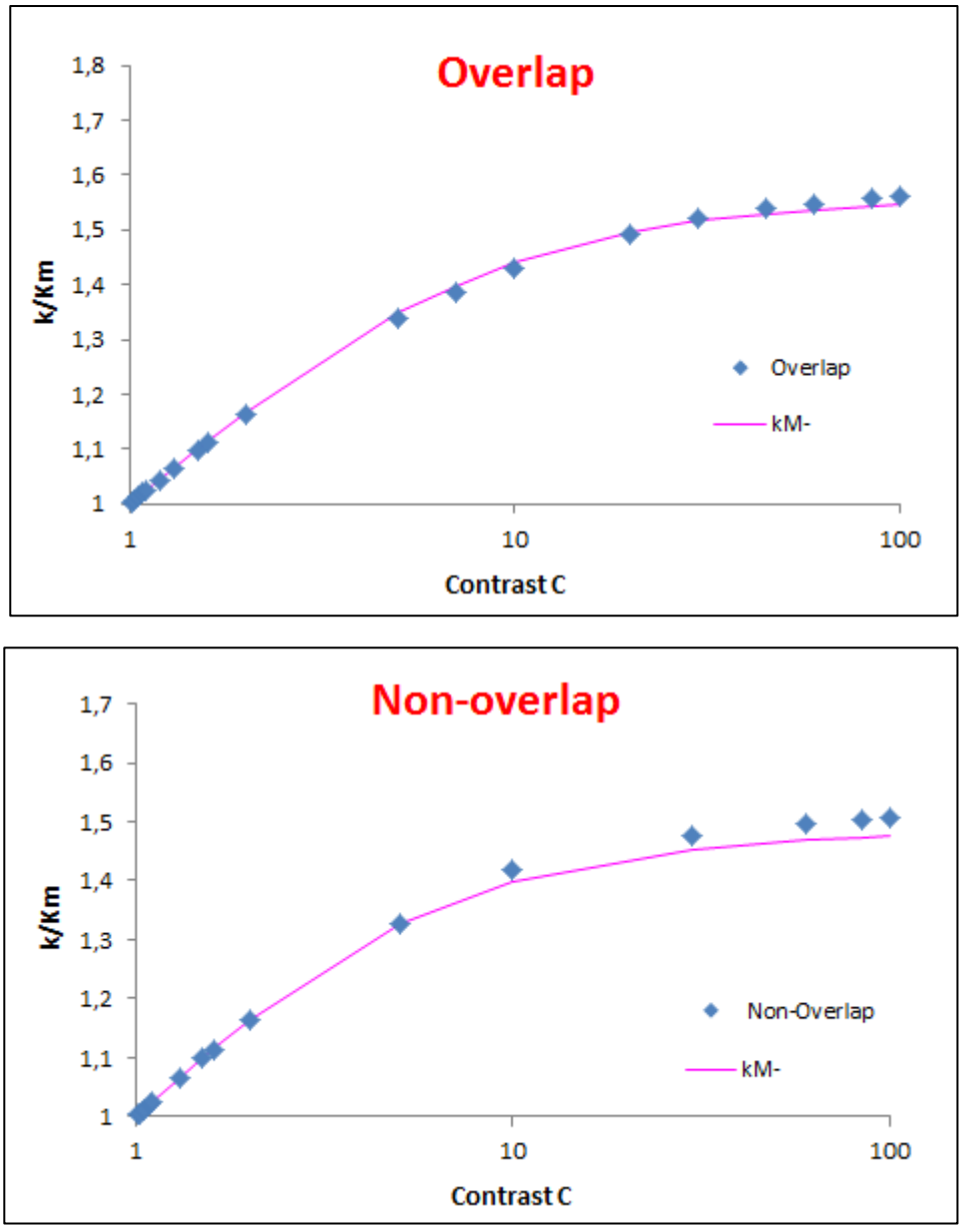

Figure V-2. Milton lower bounds and bulk modulus with regard to contrast for overlapping and non-overlapping systems for $V_f = 25.18\%$

Just like bulk stresses, shear stresses fit very well with the lower Milton bound μM^- for overlapping systems while for non-overlapping ones, the discrepancies between effective values and μM^- can reach 18% at $C = 100$.

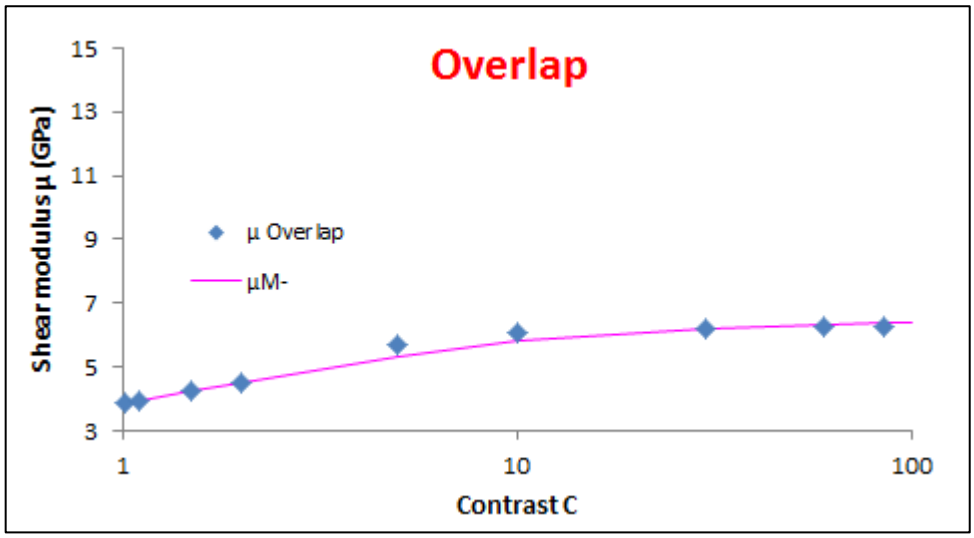

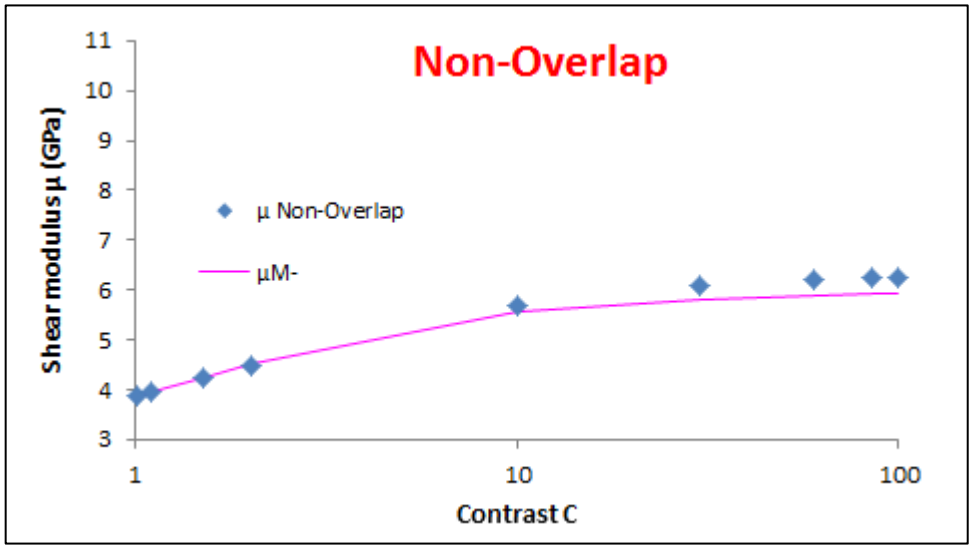

Figure V-3. Milton lower bounds and shear modulus with regard to contrast for overlapping and non-overlapping systems for $V_f = 25.18\%$

The logarithmic abscissa plots prove that the stabilization of effective values around $C = 30$ was an artifact especially for non-overlapping samples.

Further simulations for higher contrasts have shown no evolution of k and μ values for contrasts over $C = 100$ while micro scale physical processes continue to evolve as the following observations of stress distributions within samples will demonstrate.

Compared to the commonly admitted threshold for pure rigid body behavior of fibers in industrial applications, these contrast values are surprisingly high as it will be shown on Table V-1.

The first tool used to closely detail the stress distributions is their histograms or probability density frequencies (figure V-4).

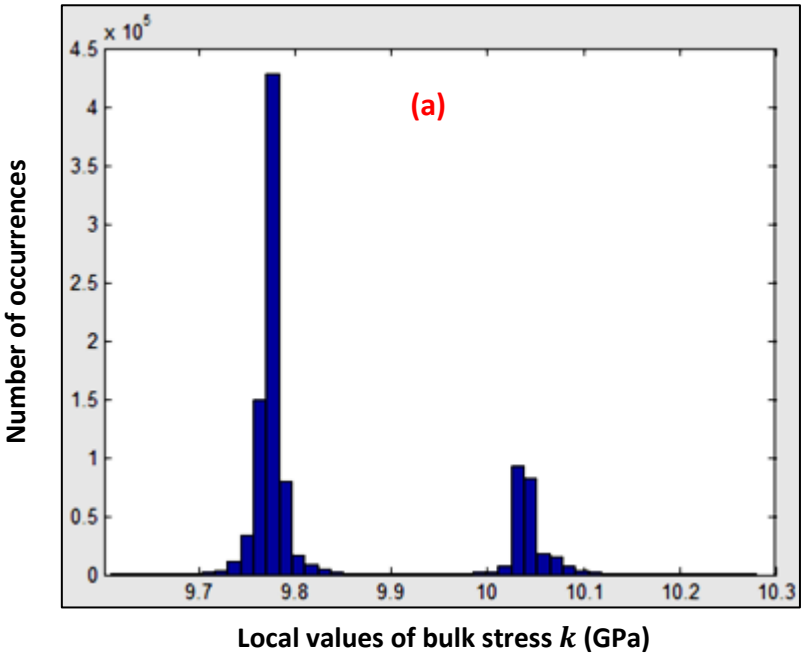

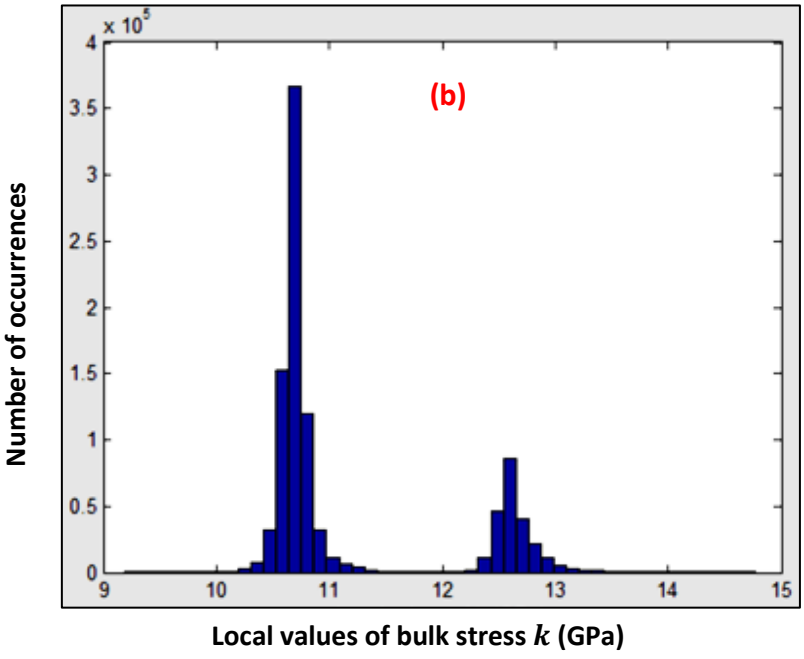

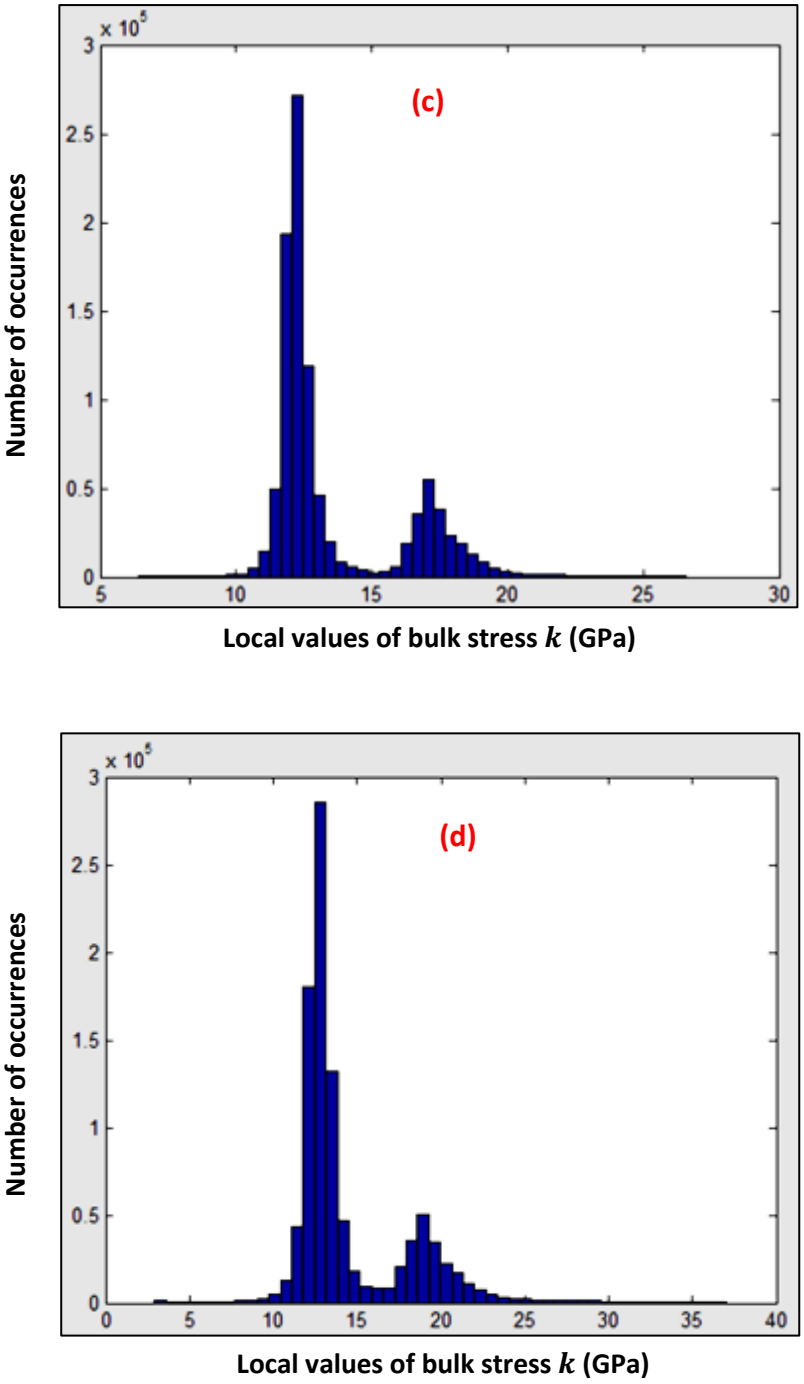

Figure V-4. Histograms of local values of bulk modulus for **(a)** $C = 1.1$, **(b)** $C = 2$, **(c)** $C = 10$ and **(d)** $C = 100$ for $V_f = 25.18\%$

All histograms of local values of bulk stress in figure V-4 exhibit two peaks. These two peaks correspond to the values $k_m = 9.615\, GPa$ and $k_i = C\, k_m$ of bulk moduli of matrix and inclusions but only at the very low contrast of $C = 1.1$.

Let us consider KL the most probable value of the lower peak and KU that of the upper one and they are plotted on figure V-5.

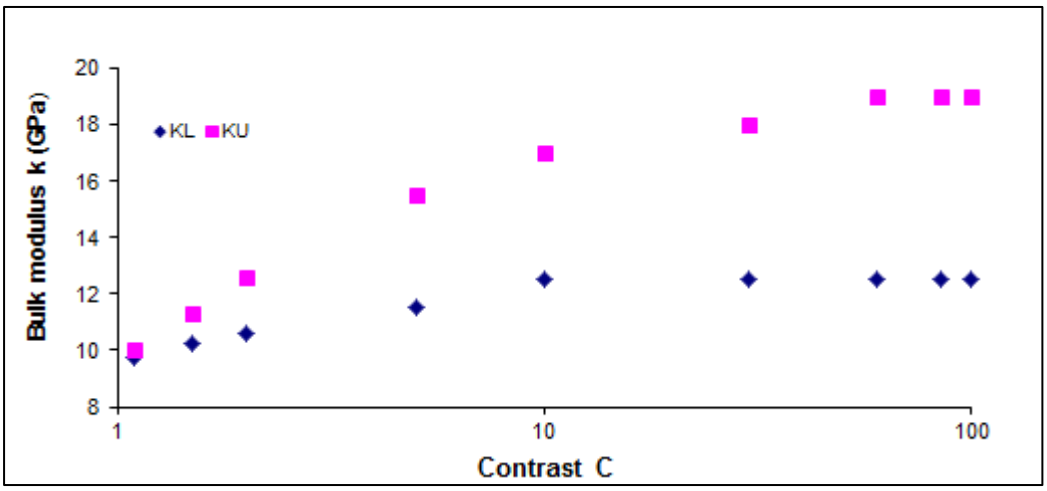

Figure V-5. Most probable values KL and KU (GPa) with regard to contrast C for $V_f = 25.18\%$

Naturally, the gap between KL and KU tends toward 0 as the contrast tends towards 1 and increases. It can be assumed, as shown on stress maps of figure V-7 that KL and KU are respectively the relevant elasticities of the matrix and the inclusions. Rapidly at $C = 10$, KL stabilizes suggesting that the matrix behaves as if surrounding rigid bodies.

The values of KL and KU in themselves are not significant unless compared to K_i and K_m as plotted in figure V-6.

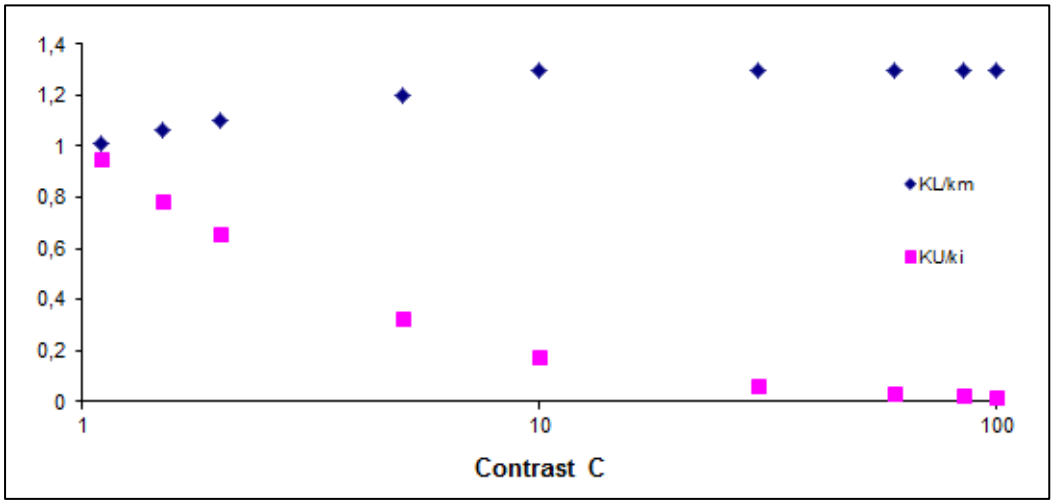

Figure V-6. $\frac{kL}{k_m}$ and $\frac{kU}{k_i}$ as a function of the contrast C for $V_f = 25.18\%$

For inclusions, the rigid body behavior seems to occur at $C = 60$ where KU becomes constant. These observations are confirmed by the curves on figure V-6.

KL stabilizes at $1.3\,k_m$ and so denotes higher rates of deformation of the matrix which correspond exactly to the expected $\frac{K_m}{(1-V_f)}$.

$\frac{kU}{k_i}$ tends toward 0 for high contrasts denoting that the local stresses are not strong enough to deform the inclusions and confirming pure rigid body motions. The comparison between KU and k_i suggests that these motions occur around $C = 30$ rather than $C = 60$ but it is difficult to determine a real threshold.

On the maps of figure V-7 that compare bulk stresses at $C = 30$ and $C = 100$, discrepancies are still noticeable.

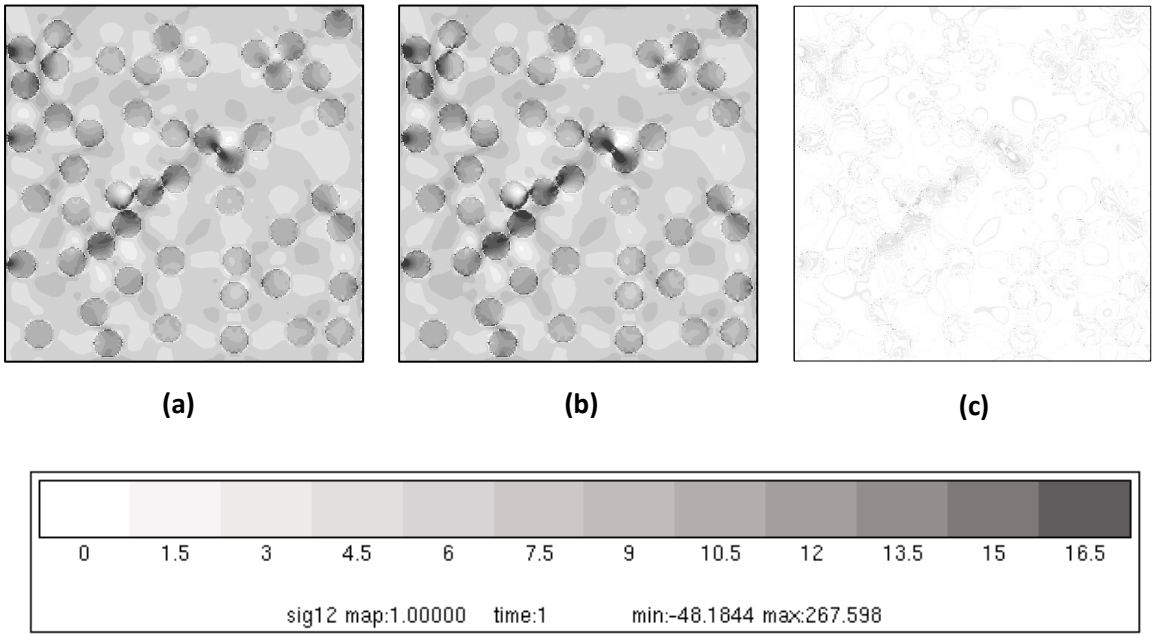

Figure V-7. Bulk stress maps: **(a)** for contrasts of 30 **(b)** for contrasts of 100 and map **(c)** of the differences between maps **(a)** and **(b)** for $V_f = 25.18\%$

The differences of bulk stresses between contrasts of 30 and 100 shown on map (c) can reach 18% of the local stress. The same map comparison for $C = 60$ and $C = 100$ gives insignificant differences and were not presented.

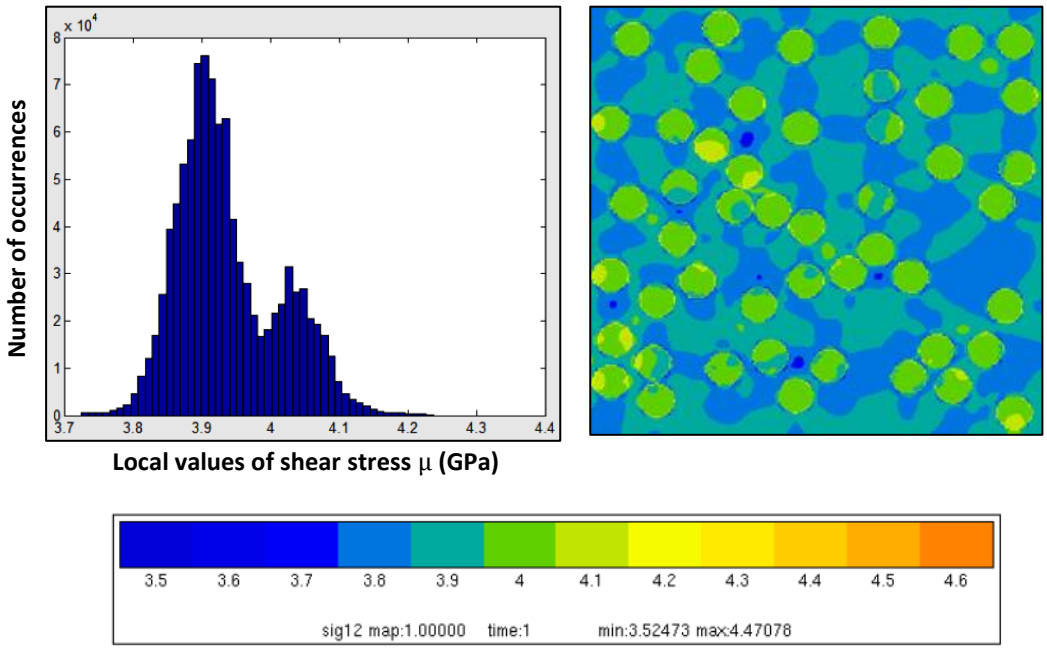

(a)

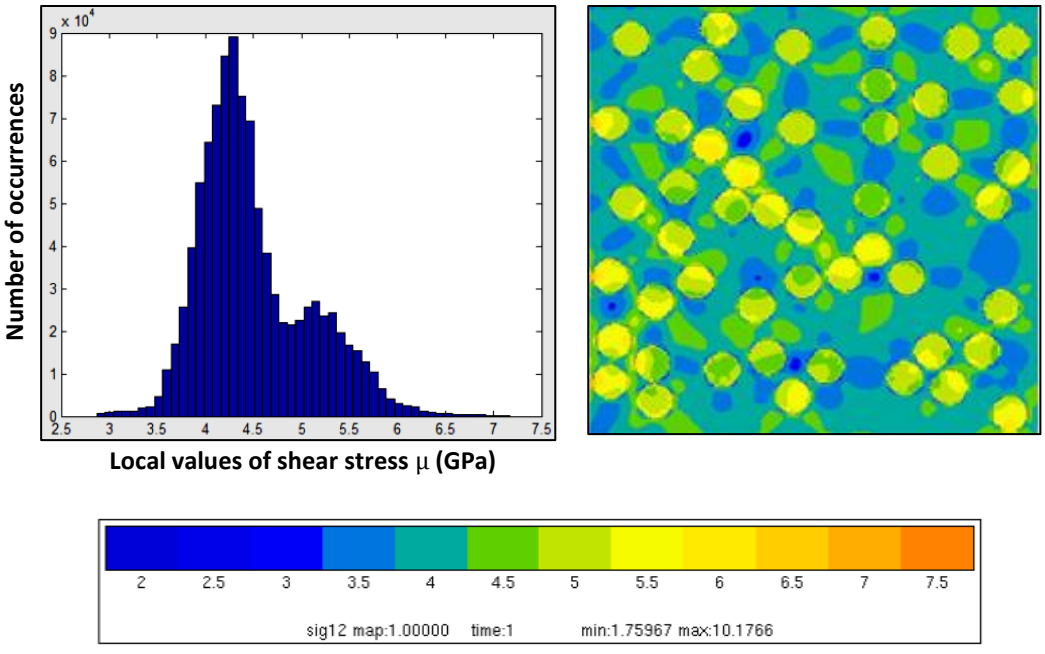

(b)

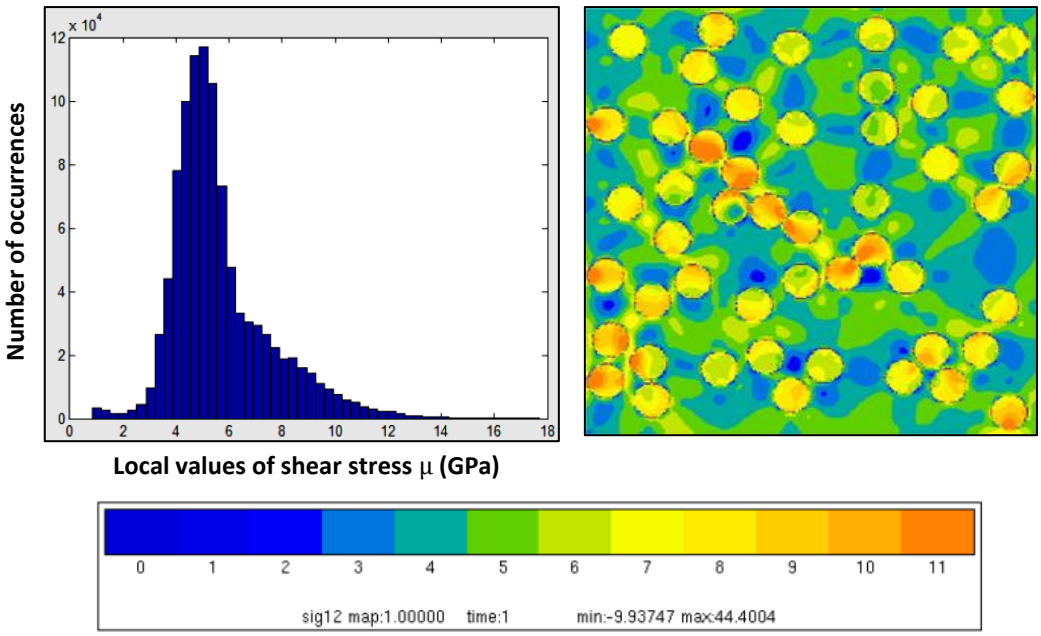

(c)

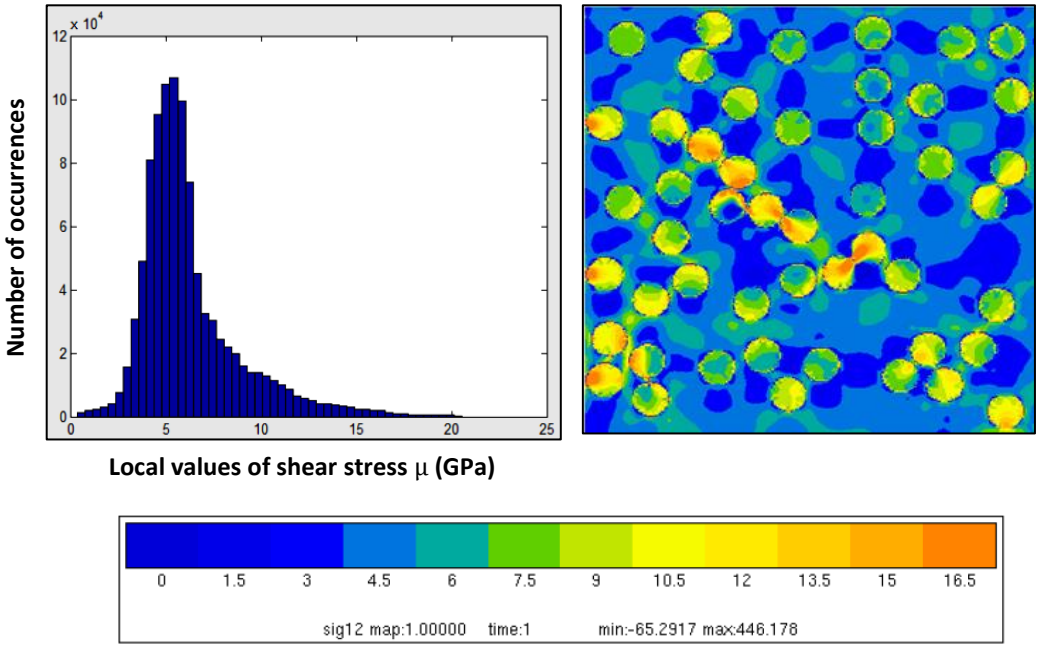

(d)

Figure V-8. Histograms of local values of shear stress and their corresponding stress maps on σ_{12} for **(a)** $C = 1.1$, **(b)** $C = 2$, **(c)** $C = 10$ and **(d)** $C = 100$ for $V_f = 25.18\%$

At low contrasts, the histograms of figure V-8 on shear modulus show two peaks of most probable values close to $\mu_m = 3.84\ GPa$ for the lower peak and always lower than μ_i for the upper one. Rapidly for higher contrasts $C > 2$, a single mode of deformation is observed.

This is suggesting two behavior modes with transitions that occur for $2 < C < 10$ rather than $30 < C < 60$ for bulk stress.

The common contrast, around $C = 10$, for a transition from elastic deformation to rigid body motion seems to be relevant for shear stress but highly unsuitable for normal deformation (traction-compression).

II- Local variance C(0)

A usual measure of histogram ranges is the square root of the local variance noted $C(0)$, namely the standard deviation. Its knowledge is of great importance in modelization as it appears in the basic expressions of every bound of high order.

$C(0)$ is extracted from each of the N_G FEM Gauss points providing local values of the effective property under consideration.

$$C(0) = \frac{1}{N_G}\sum_{i=1}^{N_G}(a_i - \langle a \rangle)^2 \quad (1)$$

In which a is the physical property under study.

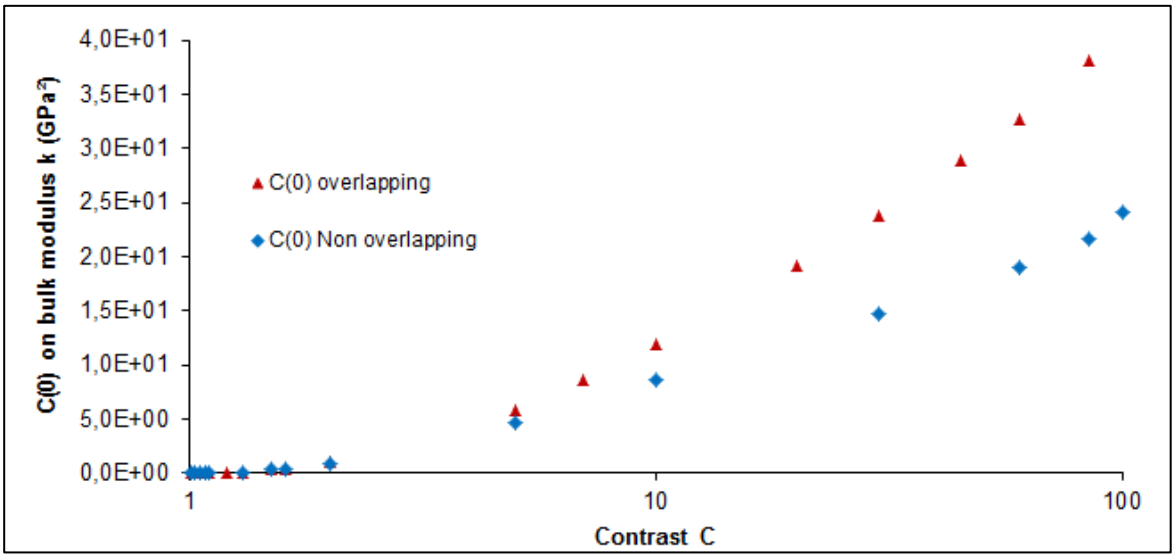

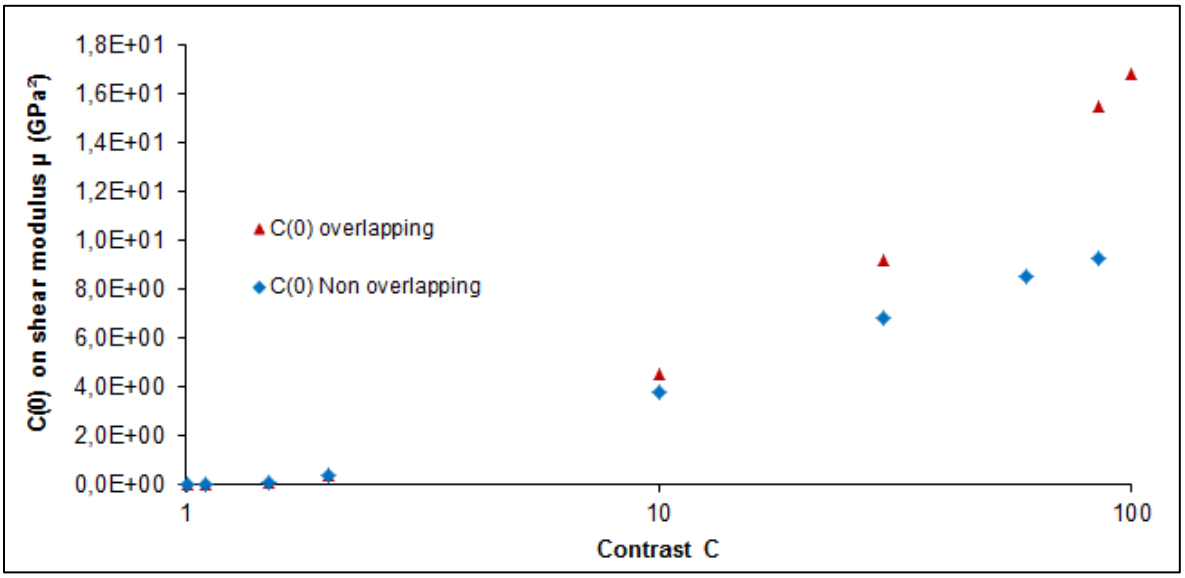

Figure V-9. Local variance $C(0)$ on bulk and shear moduli in (GPa^2) with regard to contrast with a log abscissa for $V_f = 25.18\%$

Up to $C = 2$, the fiber deformations occur continuously along with those of the matrix and a low dispersion of the local values is observed. For higher contrasts, $C(0)$ increases abruptly and no asymptotic behaviors are noticed as it was the case for effective bulk and shear moduli.

Further studies were carried out for higher contrasts in order to determine the threshold at which the local variance stabilizes (Table 1).

	Overlapping		Non-Overlapping	
	C(0) (GPa²)			
Contrast	k	μ	k	μ
100	40.8	16.87	23.04	9.36
200	54.91	24.55	30.04	10.7
50000	124.18	72.79	56.55	14
100 000	124.6	73.34	56.7	14.01
200 000	124.84	73.28	56.76	14.02
300 000	124.87	73.34	56.79	14.02

Table 1. Local variance $C(0)$ on bulk and shear moduli for different contrasts for overlapping and non-overlapping cases for $V_f = 25.18\%$

$C(0)$ stabilizes for a contrast around $C = 50000$, a surprisingly high value.

A detailed study of this phenomenon was carried out on the following sample in figure V-10.

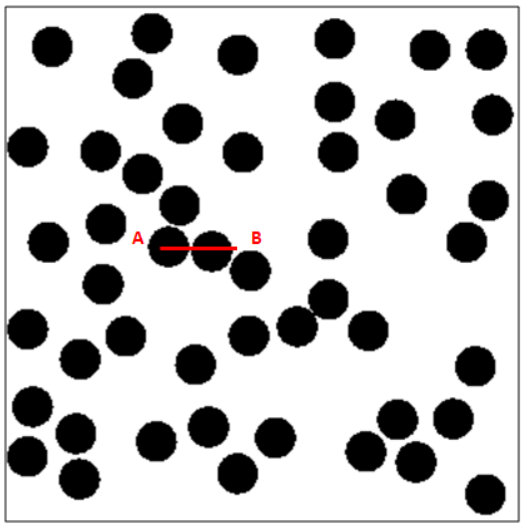

Figure V-10. Localization of the segment [AB]

The local normal stresses $(\sigma_{11} + \sigma_{22})/2$ along the segment [AB] are plotted for different contrasts on figure V-11.

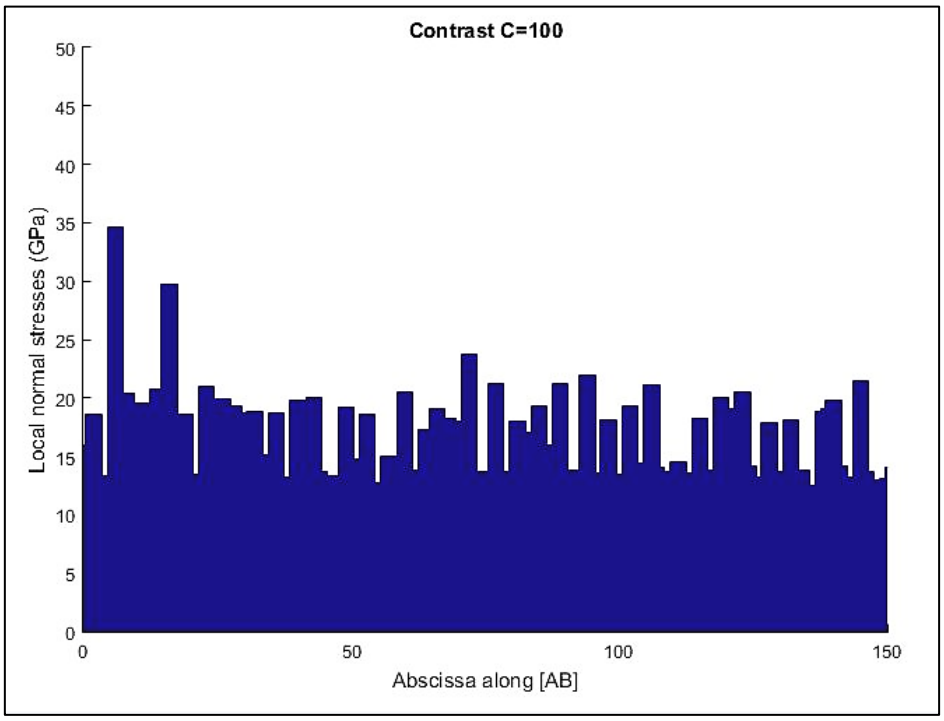

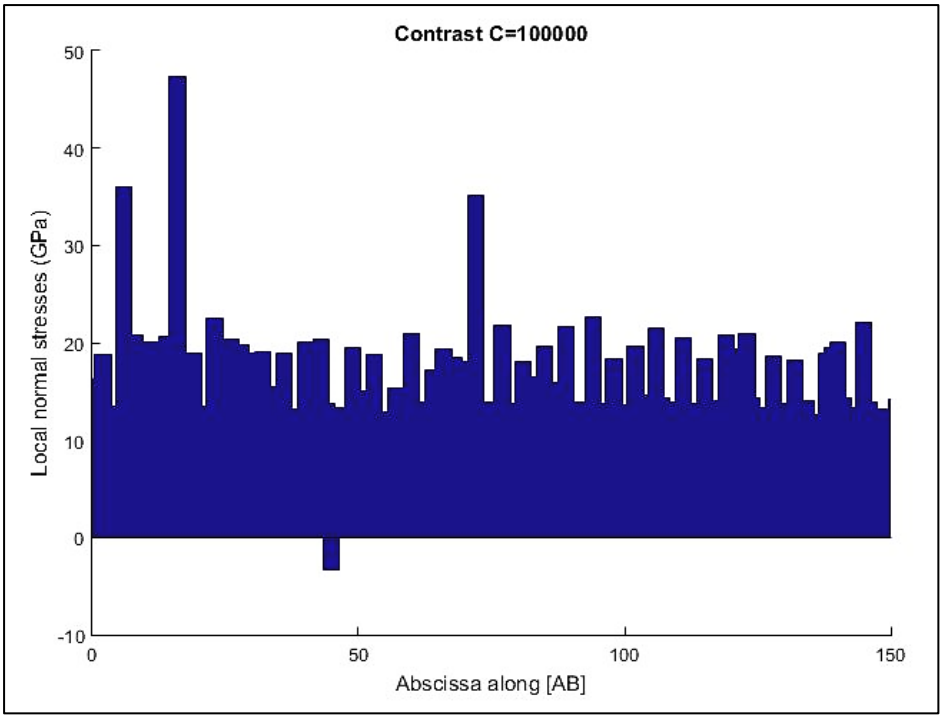

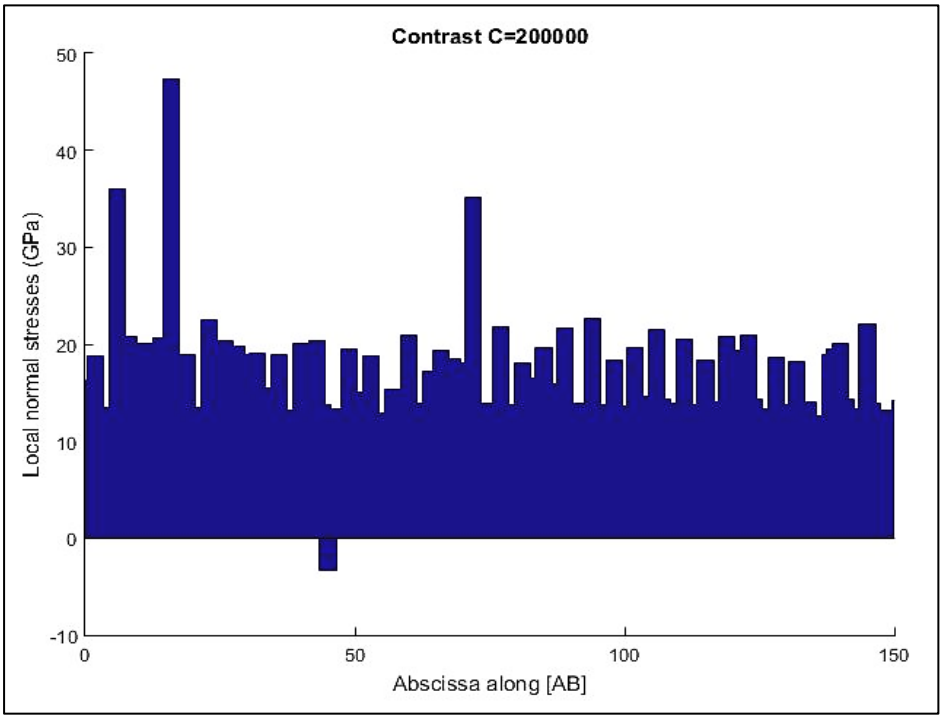

Figure V-11. Local normal stresses along segment [AB] in GPa for different contrasts

Though effective values stabilize around $C = 60$, the local normal stresses continue to slightly evolve from $C = 100$ to $C = 100000$ and then no change is observed between $C = 100000$ and $C = 200000$. As small as they are, the inclusion deformations still cushion the occurrence of very high local stresses at C= 100: the highest peak at abscissa 18 increases from $35\,GPa$ at $C = 100$ to $48\,GPa$ at $C = 100000$ for which also appear negative stresses at abscissa 44. The first peak is very likely to have appeared due to the presence of the inclusion right above the segment [AB] while the negative one occurred in the small area of matrix between the two inclusions on [AB].

As long as the cushioning is able to even the local stresses, the local variance $C(0)$ increases with contrast.

Despite being very high, these values are always significantly lower than the usual theoretical values of $C(0) = V_f(1 - V_f)(k_i - k_m)^2$ for bulk modulus and $C(0) = V_f(1 - V_f)(\mu_i - \mu_m)^2$ for shear modulus. These asymptotic expressions are known to be valid only for very low contrasts **Brown (1955), Milton (1982)** and quickly diverge with increasing contrasts. The comparisons are presented on figure V-12 in which the ordinates are in log scale in order to capture the differences at high contrasts.

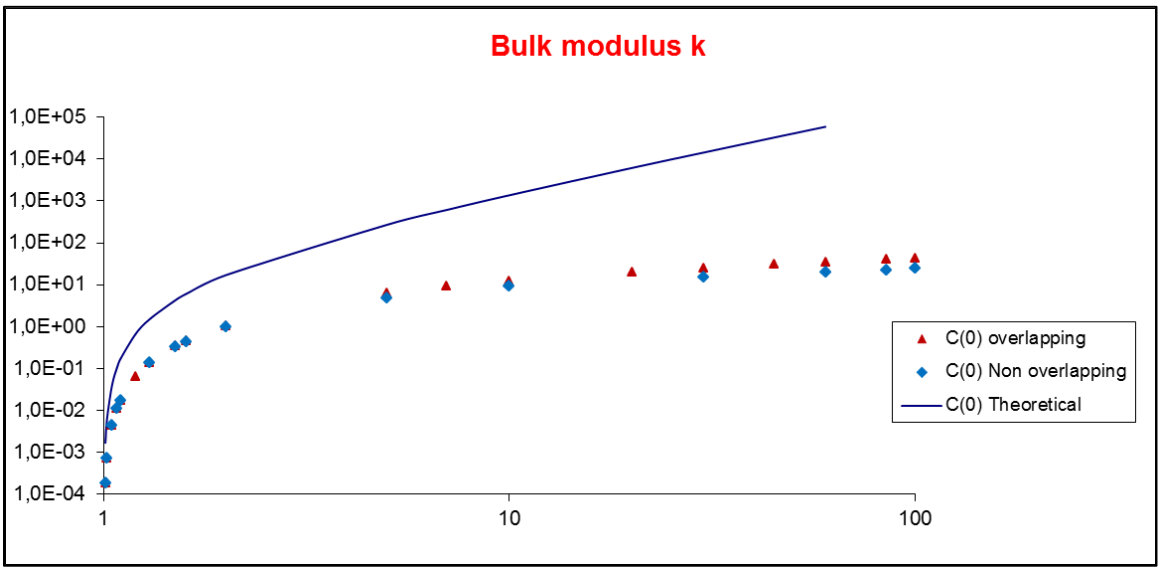

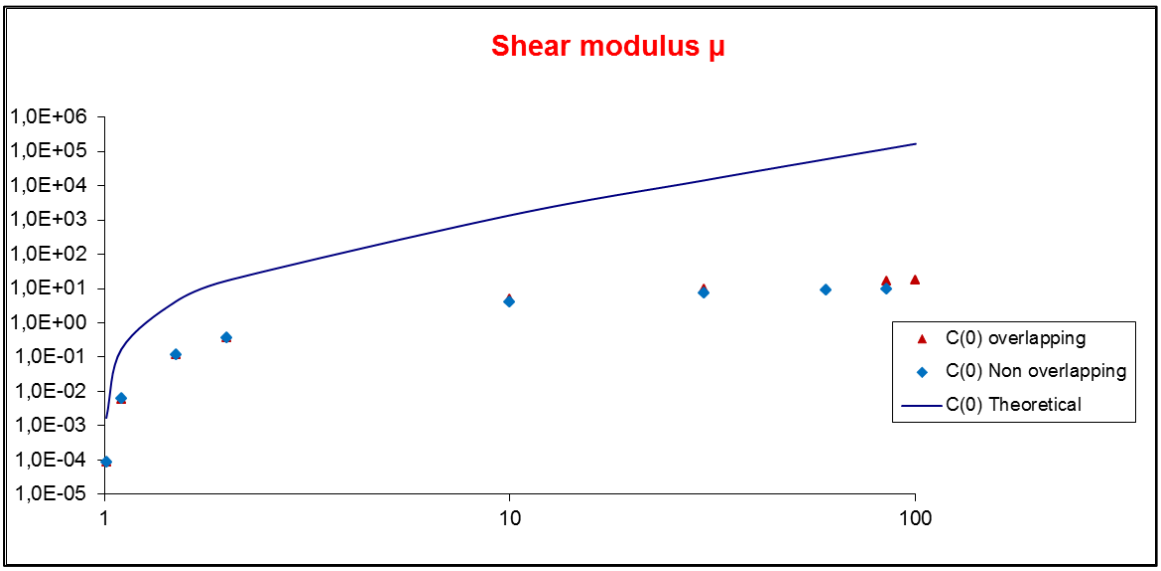

Figure V-12. Local variance $C(0)$ as a function of bulk and shear moduli for overlapping and non-overlapping versus the theoretical $C(0)$ for $V_f = 25.18\%$

The discrepancies between the numerical and theoretical values of $C(0)$ are very significant and appear at a surprisingly low contrast: at $C = 1.1$, the ratio between these values is already higher than 30. This theoretical formulation of local variance that is efficient for the characteristic function is not valid for effective elastic coefficients. It could be explained by the previously observed differences between real moduli KL and KU and the properties of matrix K_m and inclusions K_i. A substitution of K_m and K_i by KL and KU in the theoretical formula of $C(0)$ was tested and remained higher than the simulation values.

The well-fitting Milton lower bounds and effective values on figures V-2 and V-3 are surprising especially at high contrasts knowing that the expressions of Milton bounds call for this theoretical approximation of $C(0)$.

Chapter 6

Influence of the radial distribution function

For a fine comprehension of the microphysical behavior of materials, non-overlapping samples with statistically controlled microstructures are required **Melro *et al.* (2008), Romanov *et al.* (2013)** and **Knight *et al.* (2003)**. The first difficulties in building theoretical models for random distributions of fibers occur with the non–overlapping condition that deviates the fiber distribution from a Poisson distribution **Ohser and Mücklich (2000).** At low volume fractions, a random material built with fibers stiffer than the matrix fits very well with the classical lower bound HS^- of **Hashin and Shtrikman (1962)** but discrepancies appear with increasing volume fraction. According to **Beicha *et al.* (2016),** on the elastic bulk modulus, this discrepancy can reach more than 25% at $V_f > 30\%$ especially for high Young moduli contrasts. However, Milton lower bounds calculated with a PY distribution of fibers fit very well with samples of the same distribution.

The shear modulus is subject to similar observations but the discrepancy seems less sensitive.

In the upcoming studies, the focus will only be cast on elastic bulk and shear moduli from which thermal conductivity can be deduced.

The aim of this chapter is to characterize the influence of Rdf on effective elastic properties of non-overlapping fiber reinforced materials. As the characteristic peak of Rdf increases, effective values increase as well. This process can be taken further as it will be seen in chapter 7 with the formation of clusters.

The results presented in the next two sections were initially published in **Lakhal *et al.* (2019)** in International Journal of Modern Physics C.

I- Generation and morphology of samples

The studied microstructures were an arrangement of non–overlapping parallel identical fiber inclusions randomly located by RSA within the frame of a square matrix.

On figure VI-1, typical shapes of Rdf worked out on RSA samples of various volume fractions are represented as histograms with abscissa steps of width $\Delta \mathrm{r} = 0.5$. The number of steps is reduced to 6 for $V_f = 30\%$ and 5 for $V_f = 50\%$ due to the increasing diameters in dimensionless r abscissa. At $V_f = 10\%$, Rdf (except for $\mathrm{r} < 1$) is like that of ideal gas. At higher volume fractions, the non-overlapping constraint induces higher values of $g(r)$ for r between 1 and 1.5 fiber diameters. These values increase with V_f denoting frequent occurrences of close-together fibers. According to **Knight *et al*. (2003)** and **Baouane *et al.* (2016)** this rise of near neighbor occurrences can increase the stiffness of the materials.

On the results obtained for RSA samples, the peaks are always higher than those of a Percus-Yevick distribution. The discrepancies in Rdf peaks increase with V_f. For low volume fractions such as $V_f = 10\%$, the results are almost similar while for high volume fractions, RSA results stray considerably from the PY ones.

RSA samples are non-equilibrium systems but will be used in this chapter for the sole purpose of quantify the influence of Rdf shapes.

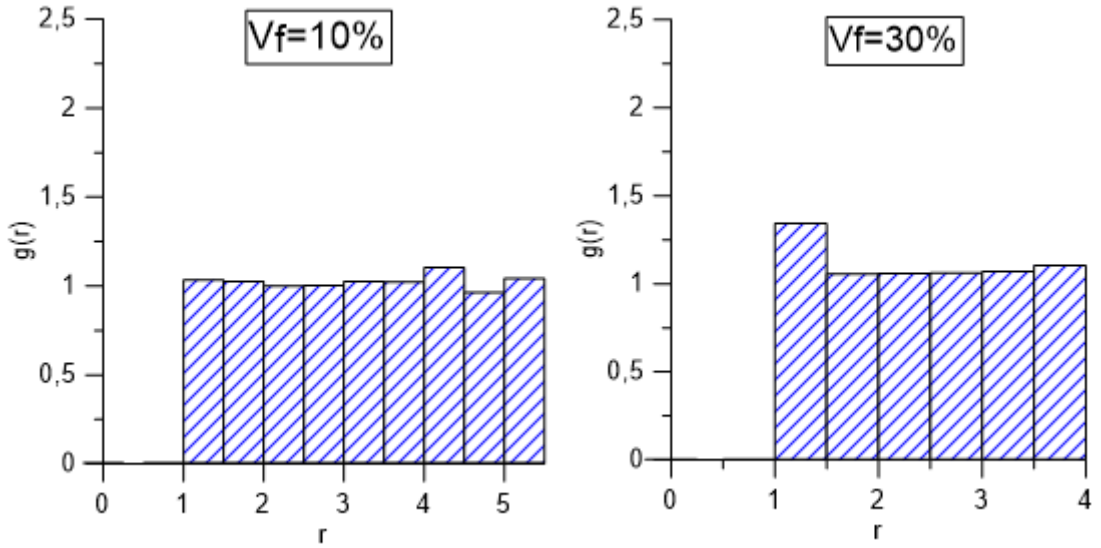

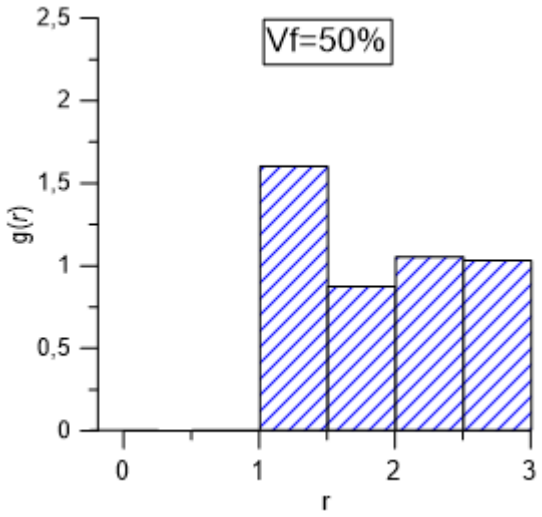

Figure VI-1. Values of $g(r)$ for $V_f = 10\%$, 30% and 50%

The composite samples microstructures were transformed using the SA method in order to change the shape of Rdf by increasing the peak of $g(r)$ within the range of $1 < r < 1.5$.

To reach the desired states, the fiber-center locations were rearranged with SA under the following potential:

$$U\infty - \ln[g(1 < r < 1.5)]$$

For $V_f = 30\%$, the highest number of moves was limited to 20000 for which clusters started to form, as it clearly appears on Figure VI-2 (c) and the overall uniform and random aspect of the samples was lost.

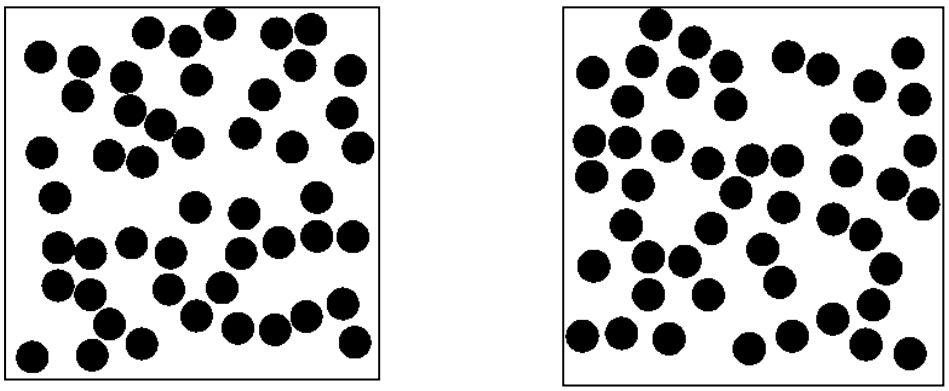

(a) (b)

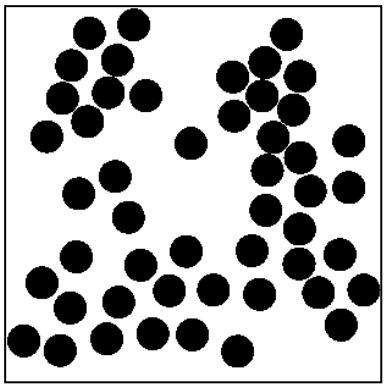

(c)

Figure VI-2. (a) Initial image sample, **(b)** same image after 4000 moves, **(c)** image after 20000 moves for $V_f = 30\%$

At $V_f = 50\%$, the clusters occurred after 4000 displacements as depicted in figure VI-3.

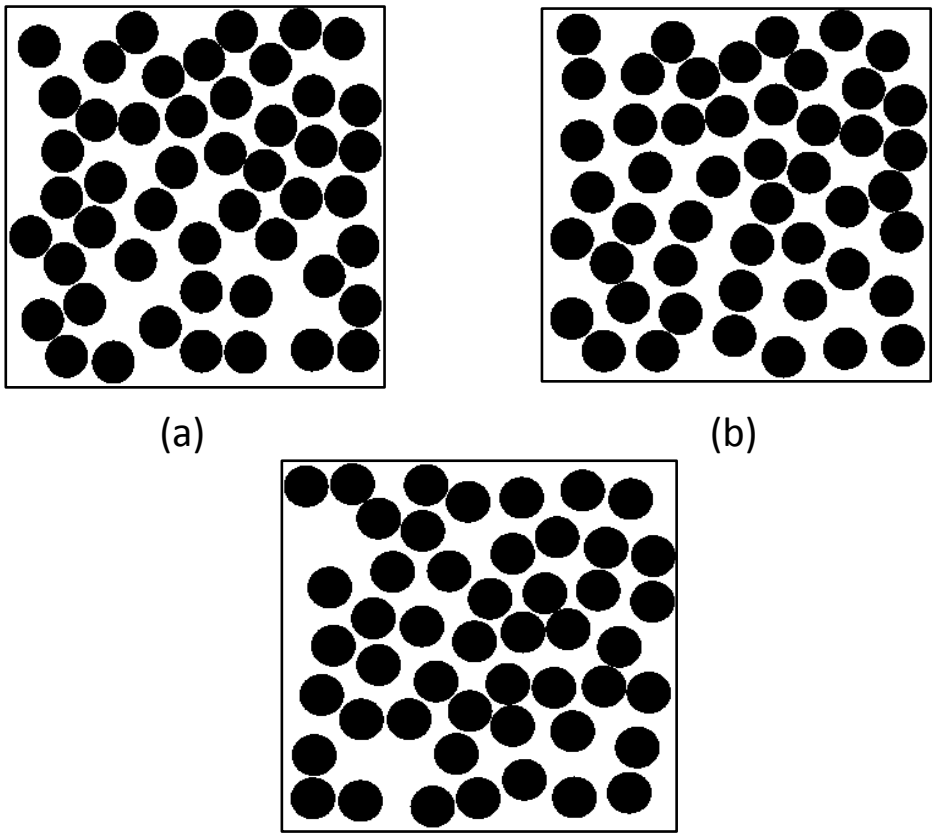

(a) (b)

(c)

Figure VI-3. (a) Initial image sample, **(b)** same image after 4000 moves, **(c)** image after 15000 moves for $\mathrm{V_f} = 50\%$

Beyond this number of fiber displacements, the general shapes of the samples such as their radial distribution function became unchanged at a constant Boltzmann factor. But it is still possible to accentuate the fiber aggregation by increasing Boltzmann factor or decreasing the amplitude Δ*r* of the displacement, however the final microstructure would not necessarily correspond to an equilibrium state in which statistical properties are well known.

For both volume fractions $V_f = 30\%$ and $V_f = 50\%$ the Rdf of figures VI-4 (a) and VI-5 (a) result from ensemble averaging on 25 samples. The fiber distributions of each sample were then rearranged by SA providing new microstructure whose Rdf are sketched figures VI-4 (b), VI-4 (c), VI-5 (b) and VI-5 (c).

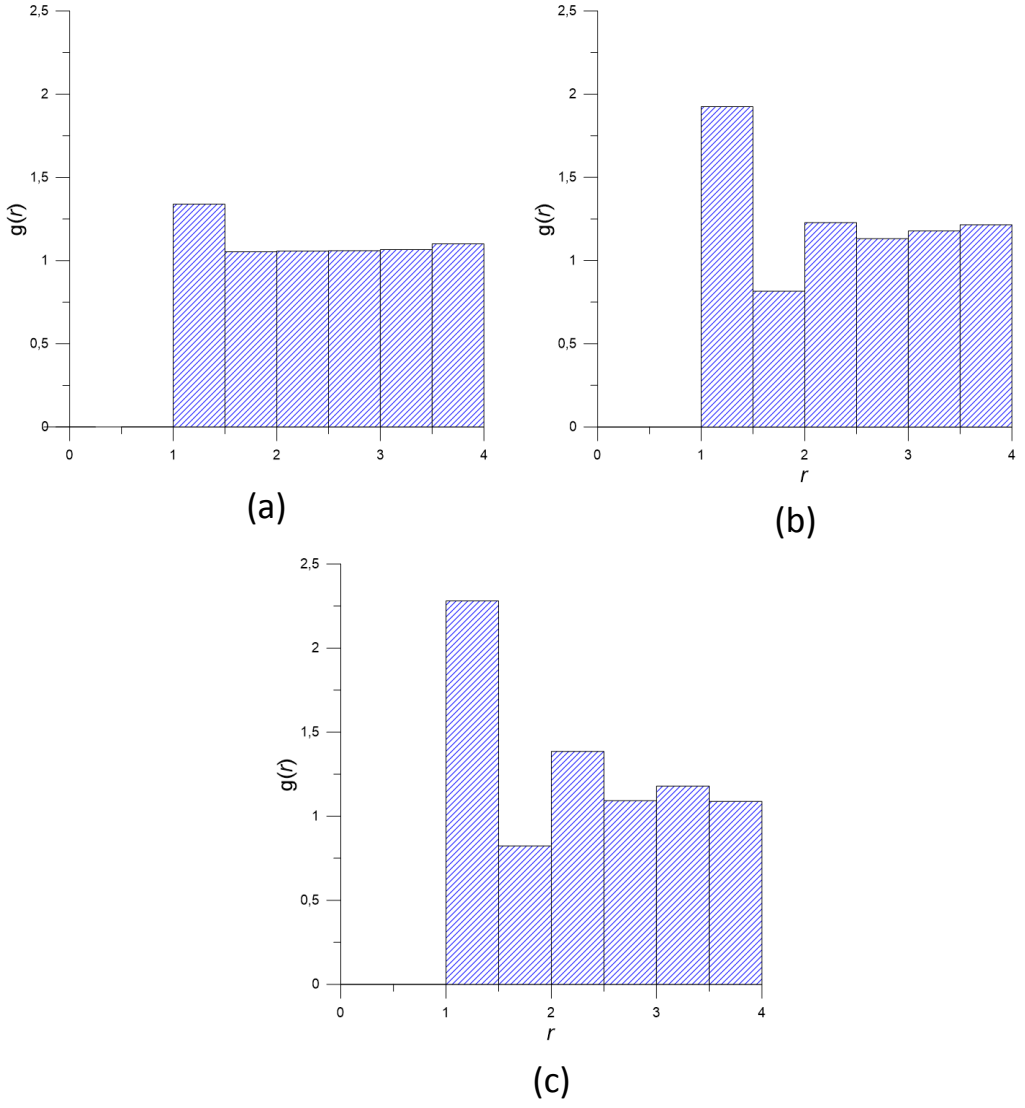

Figure VI-4. Values of g(r) for $V_f = 30\%$ at **(a)** initial state, **(b)** after 4000 moves and **(c)** after 20000 moves

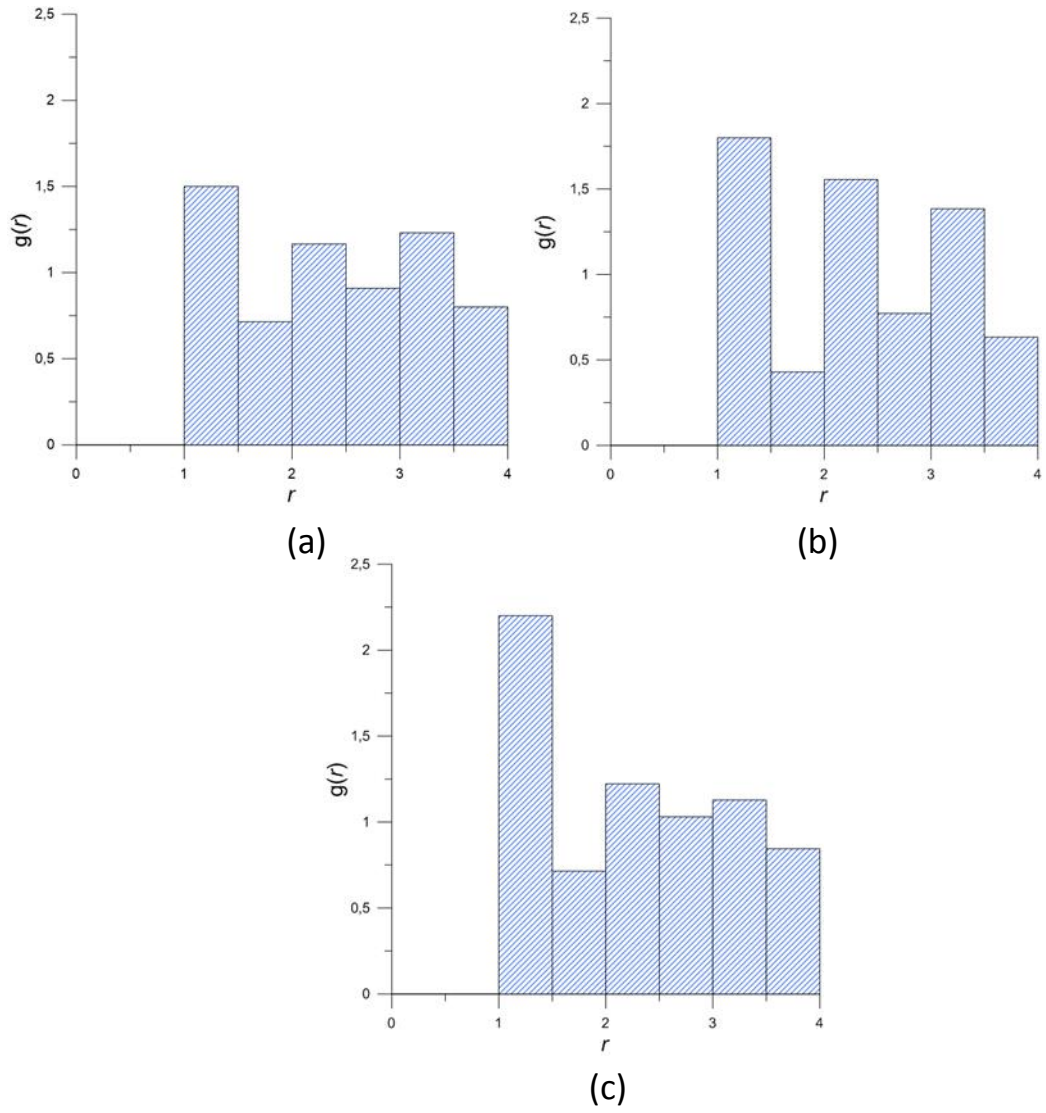

Figure VI-5. Values of g(r) for $\mathrm{V_f} = 50\%$ at (a) initial state, (b) after 4000 moves and (c) after 15000 moves

As expected, figures VI-4 and VI-5 show the increase of the values of $\mathrm{g}(1 < \mathrm{r} < 1.5)$ with the number of moves for both volume fractions. This increase is of the same order as the difference of $\mathrm{g(r)}$ values between RSA and PY distributions.

A direct consequence of higher concentration of fibers close together is the apparition of a larger voids at a short range distance, characterized by a deficient of the Rdf around $r = 1.75$.

The same tendency is observed on the probability of inter-fiber spacing at a short range $1 < r < 1.5$ for $V_f = 30\%$ but at $V_f = 50\%$, the microstructure started to aggregate after

only 4000 displacements and reached a state of saturation for higher numbers of moves (figure VI-6).

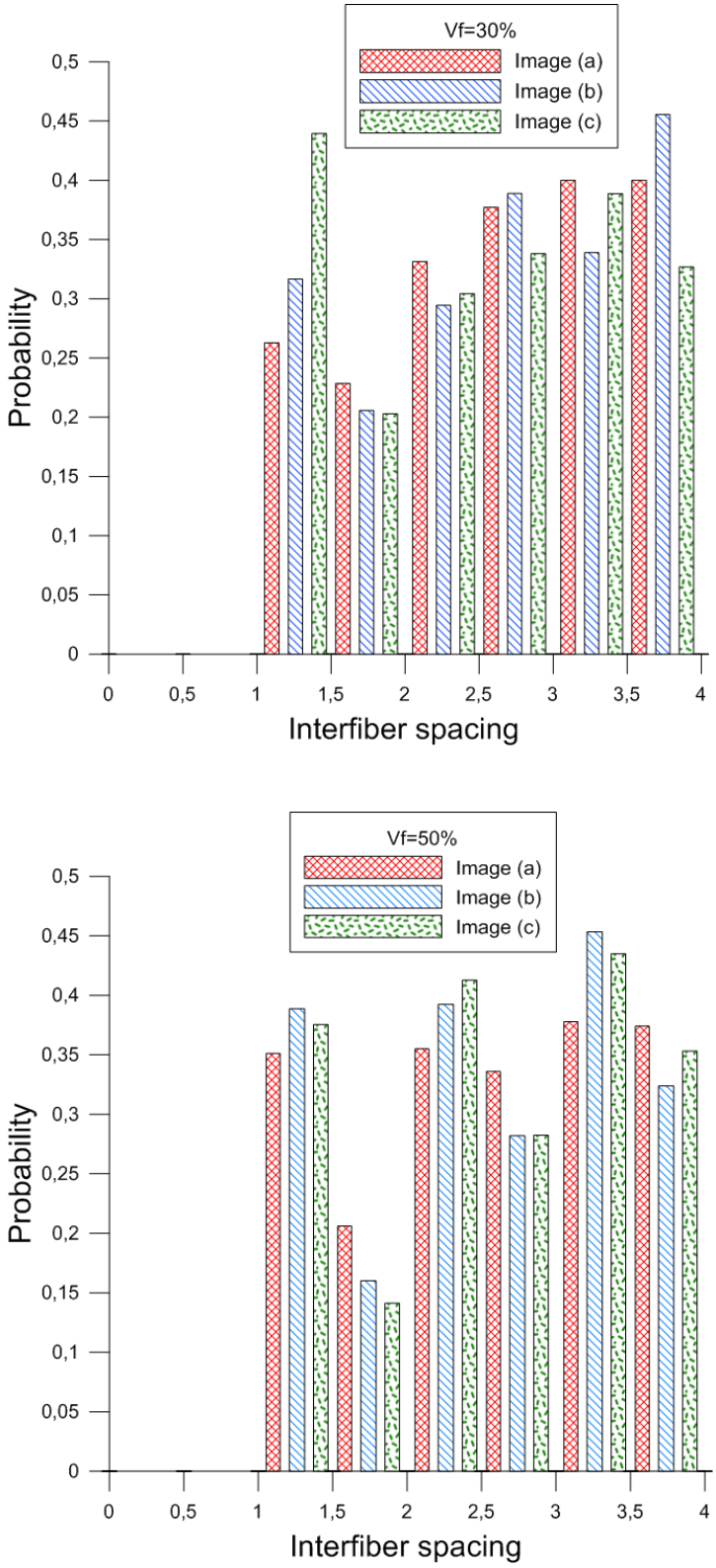

Figure VI-6. Probability of inter-fiber spacing at short range for **(a)** initial state, **(b)** after 4000 moves and **(c)** after 20000 moves for $V_f = 30\%$ and respectively 4000 and 15000 moves for $V_f = 50\%$

Although inter-fiber spacing captures less information about microstructures compared to Rdf or the covariance, it can still provide a useful length scale for physical modeling.

Like previous observations at a volume fraction of 50% **Seyed Hamid Reza *et al*. (2017)**, the probability of nearest neighbors is uncorrelated with $g(r)$ as shown in figure VI-7. It could be assumed that it was due to a fiber density too close to the jamming limit. Whereas at a volume fraction of 30%, the fiber mobility allowed a significant effect of the $g(1 < r < 1.5)$ values on the occurrence of nearest neighbors, that in average, increases of 19% from case (a) to case(c).

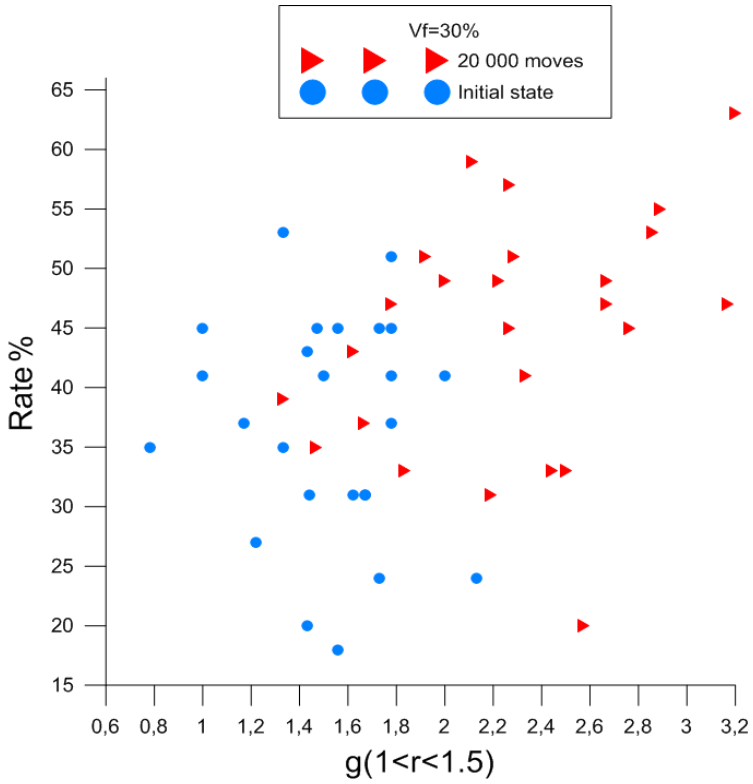

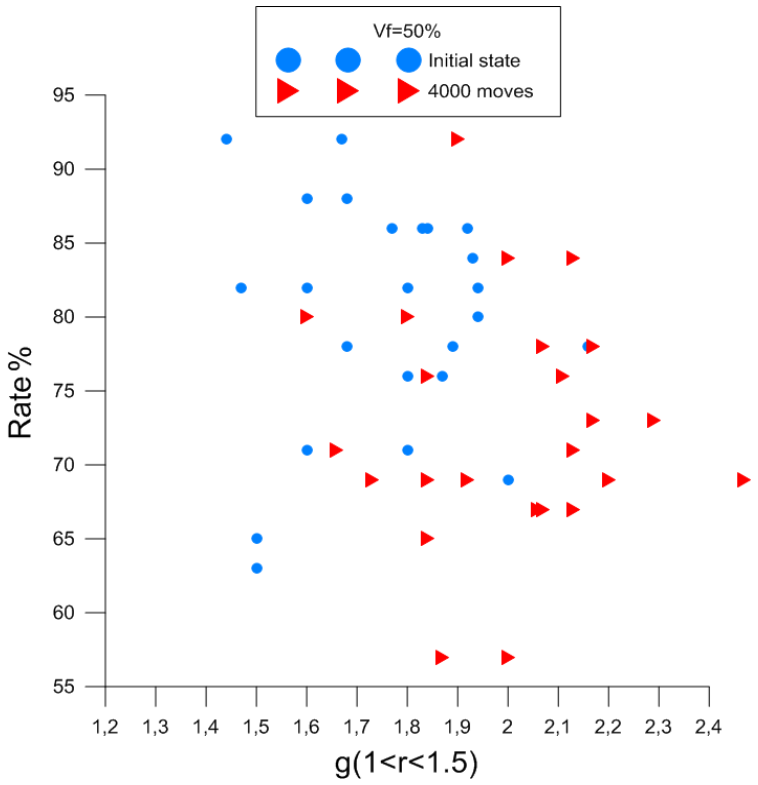

Figure VI-7. Probability of the 1st nearest neighbor distances as function of $g(1 < r < 1.5)$ values for $V_f = 30\%$ and $V_f = 50\%$

For the remainder of this work, particular attention will be cast on the same 3 cases characterized by (a) $g(1 < r < 1.5) = 1.5$, (b) 1.9 and (c) 2.3 at $V_f = 30\%$.

II- Elasticity and thermal conductivity

In order to verify the similarity of behavior with elastic properties as the cross-property linking conductivity and elastic moduli suggests, the results for thermal conductivity will be presented along with those for bulk and shear moduli.

The first rigorous cross-property bounds were first obtained by **Milton (1984), Berryman and Milton (1988)** and **Torquato (1991)** and later improved upon by Gibiansky and Torquato (**Gibiansky and Torquato, 1993, 1994, 1995, 1996a**).

The images samples studied contained 49 inclusions at a volume fraction of 30%. Young's moduli, Poisson's ratios and thermal conductivities were respectively for the matrix and the fibers:

$$E_m = 10GPa,\ E_i = C\,E_m\ , \upsilon_m = \upsilon_i = 0.3,\ \lambda_m = 10\ W/mK \text{ and } \lambda_i = C\,\lambda_m \text{ with } C = 100$$

Contrast is the only significant parameter for linear elasticity and thermal conductivity. At low contrasts, the bounds on effective properties such as HS bounds are very narrow and no significant evolution of effective properties with microstructure can be expected. Therefore, the present contrasts were set at 100 even if it is a relatively high value in practical applications.

Figure VI-8 describes the evolution of the effective values of bulk moduli, shear moduli and thermal conductivity with regard to the values of Rdf $g(1 < r < 1.5)$ for $V_f = 30\%$. The coordinates of each point of the curves correspond to the value of $g(1 < r < 1.5)$ and their physical properties obtained by FEM homogenizations for a given number of moves. These results were averaged on the 25 samples.

These results always agree with the second order bounds of HS. As expected, results tend to be much closer to the lower bound HS^- that is known to well fit the behavior of common random fiber reinforced composites.

To check whether these increases in elastic coefficients and thermal conductivity are significant, it is interesting to compare them to the HS^- bounds.

For the bulk modulus the value $k = 17.67\ GPa$ obtained without any fiber displacement is equal to the values of HS^- bound for a volume fraction $V_f = 37\%$ instead of the real $V_f = 30\%$. Exactly the same observation 37% instead of 30% is observed on shear modulus whereas for thermal conductivity, the homogenized value remains very close to the lower bound HS^-.

In spite of a light dispersion, the overall evolutions on figure VI-8 clearly show an increase of effective physical properties with the height of $g(r)$.

From $g(1 < r < 1.5) = 1.5$ to $g(1 < r < 1.5) = 2.3$ the bulk modulus increases of 1.5%, the shear modulus of 2.6% and the thermal conductivity of 2.7%.

It is surprising that the thermal conductivity is more sensitive than the bulk modulus given the simple nature of thermal conductivity tensors. Actually, thermal conductivity is driven by first order tensor (heat fluxes are along temperature gradient) while elasticity by second order (elastic stresses are related to strain in all directions). However, the same tendencies are observed as suggested by cross-properties.

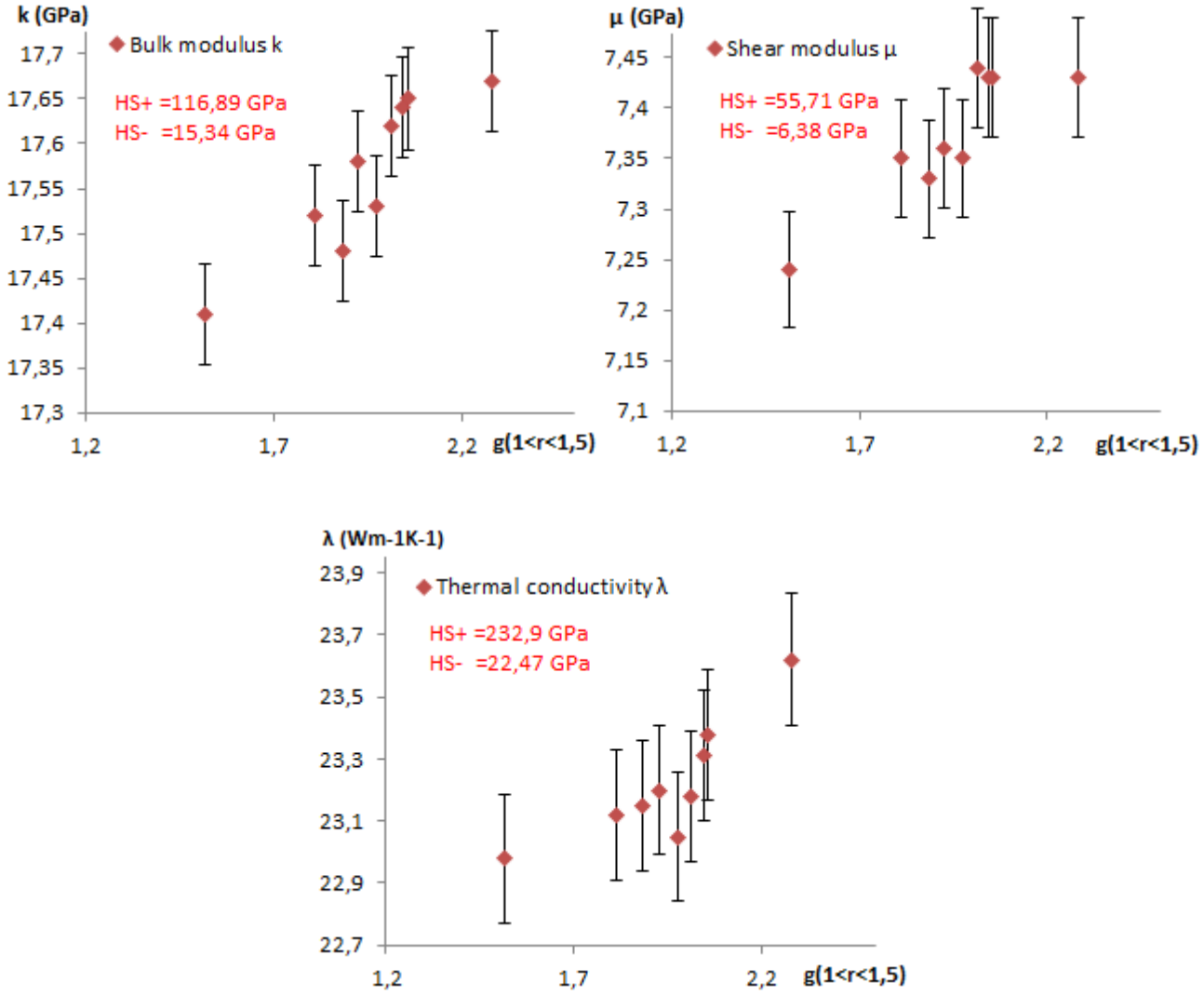

Figure VI-8. Evolution of macroscopic bulk modulus k, macroscopic shear modulus μ and macroscopic thermal conductivity λ with regard to $g(1 < r < 1.5)$

At, $V_f = 50\%$ the mobility of inclusions was restrained; hence, the study tackled only two values of $g(1 < r < 1.5)$: 1.6 for the initial sample and 2 after simulated annealing. At this volume fraction, no significant influence of $g(r)$ on the physical properties was observed. This could be linked to the minor evolution of the probability of nearest neighbors between the two states.

Sketched on figure VI-9 are the maps of normal stresses σ_{11} given by FEM. σ_{11} that are aligned with the imposed displacement are presented rather than σ_{22} because they are better fitted to depict the local physical behavior.

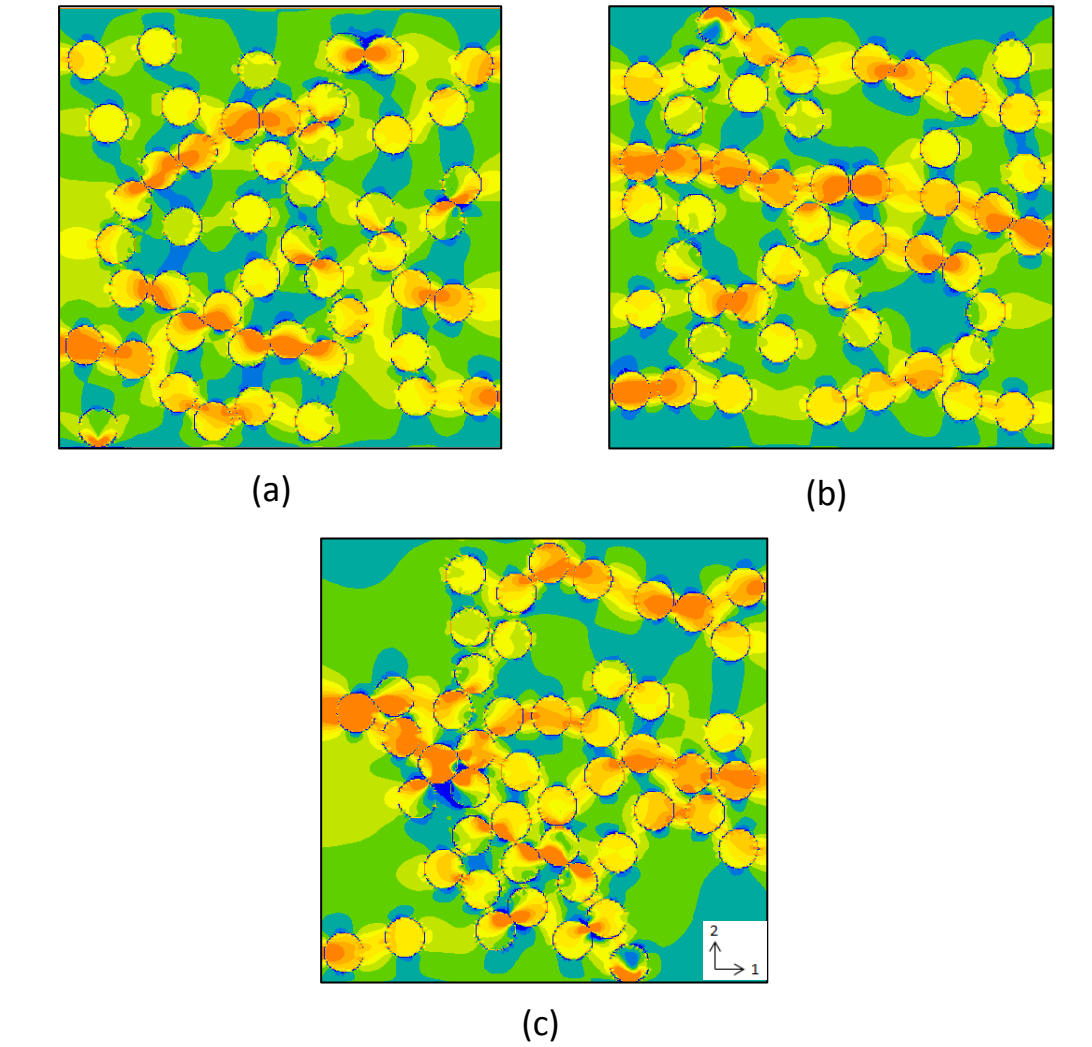

Scale depicting the colors on the stress maps according to the values of microscopic σ_{11}(GPa)

Figure VI-9. Normal stresses σ11 map for $g(1 < r < 1.5) = 1.5$ **(a),** 1.9 **(b)** and 2.3 **(c)**

The applied displacement fields were for each sample a same horizontal contraction. The paths of high stresses always form line segments aligned in the direction of stresses under consideration. These lines are built by succession of jumps from one fiber to the closest and generate high stresses not only in the stiff fibers but in the inter–fiber spaces as well. A simple look at the maps shows that the rates of high stresses increase with the values of $g(1 < r < 1.5)$ and consequently with the 19% increase of the number of near–touching fibers from case (a) to case (c). These observations are confirmed by the Probability Density Functions (P.D.F) of local stresses sketched on figure VI-10.

These P.D.F. are built from stresses collected on each node of a single sample of 49 fiber inclusions given the regular mesh used in FEM simulations. Histogram (a) is the initial sample ($g(1 < r < 1.5) = 1.5$), (b) the same sample after 4000 moves ($g(1 < r < 1.5) = 1.9$) and (c) after 20000 moves ($g(1 < r < 1.5) = 2.3$).

As a single sample does not allow reaching the RVE, these P.D.F. are roughly converged and provide only qualitative observations. Therefore the histograms were built with local values of normal stresses σ_{11} which are the dominant part of the bulk stress moduli as they are aligned with the main displacement. Even if the range increase is low from case (a) to case (b) and (c), the standard deviations remain appreciably constant. The only noticeable difference is an evolution of P.D.F. shapes from case (a) to (b).

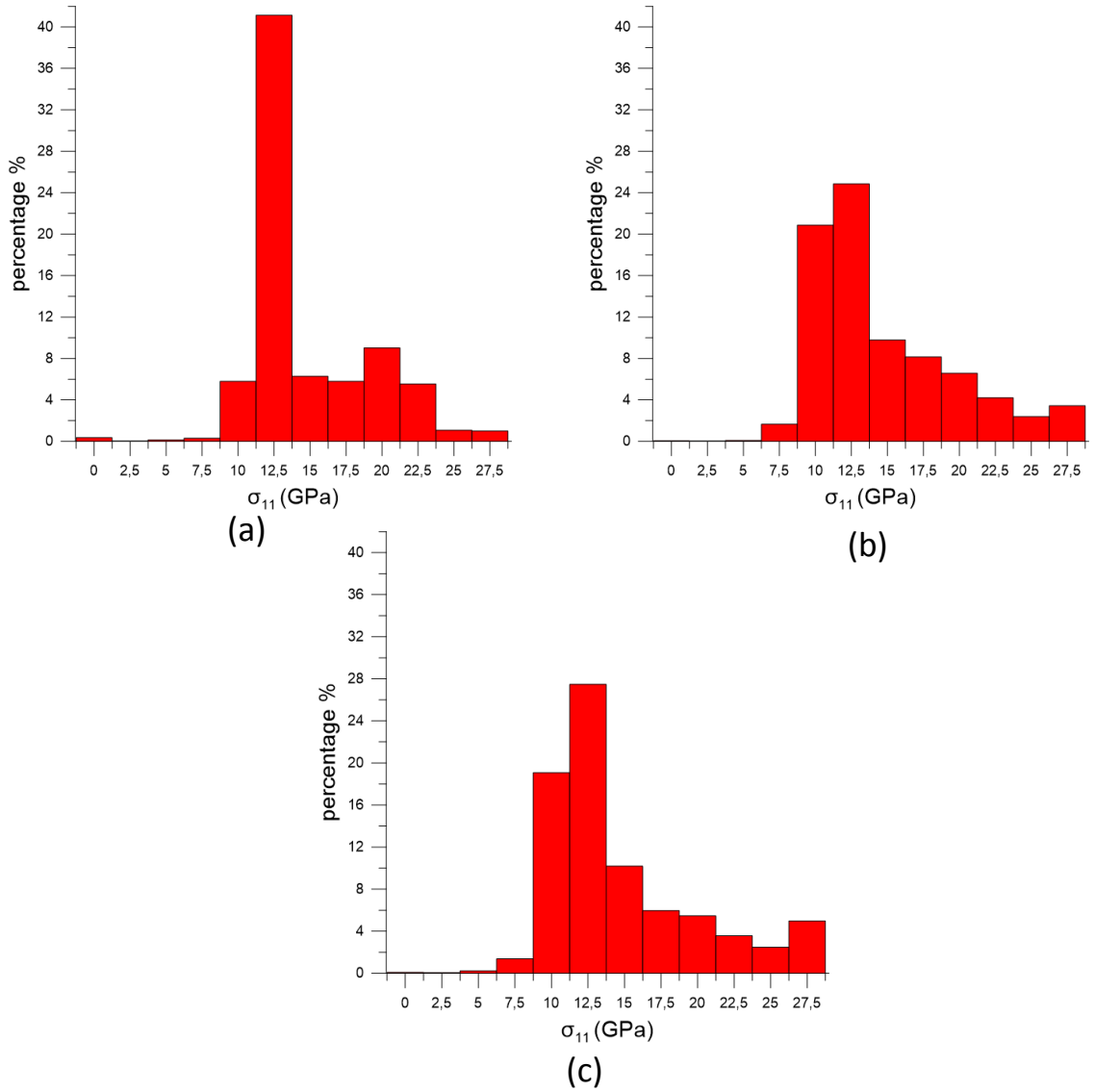

Figure VI-10. Probability density functions of local stresses for $g(1 < r < 1.5) = 1.5$ (a), 1.9 (b) and 2.3 (c)

The ratios of high stresses increase with $g(1 < r < 1.5)$, and even without any clue of fiber aggregation as in case (b), the occurrence frequencies of very high stresses (around $27.5\ \mathrm{GPa}$) is more than four times higher than in case (a). On another hand, the most probable stresses of the P.D.F (around $12.5\ \mathrm{GPa}$) decrease.

For case (a) with the smaller value of $g(1 < r < 1.5)$, the sample deformation is dominated by matrix effect while for cases (b) and (c) the collective effects between fibers occur resulting in high stress values. It is assumed that the appearance of these interactions between fibers is responsible for the increase in effective elastic properties.

Even if it does not strongly affect the effective behavior, another remark is that the probability of low stresses (around $10\ \mathrm{GPa}$) increases from case (a) to (b) corresponding to larger areas with no fibers. This formation of large pores might be included in modelization of materials characterized by high agglomeration of fibers. Similar observations have already been reported by **Botsis *et al.* (1994)** about strength. No noticeable differences are observed between case (b) and case (c), in which fibers begin to aggregate.

The SA method is a numerical process and so cannot be used in production of practical composites, such as fiber reinforced resins. However it is easy to extract Rdf from snapshot of real composite section by image processing **Sanei *et al.* (2017).** Then the values of $g(r)$ at short range $(1 < r < 1.5)$ could be a good indicator of the relative stiffness between different samples. 2 to 3% variations on effective properties are rather small compared to typical fabrication scatter and cannot be expected to optimize production processes. Nevertheless, in specific cases, Rdf could allow a selection among irregular samples.

III- The sticky-disk samples

To further investigate the increase of the Rdf peak on samples in which fibers are distributed on their whole sections, a new SA potential was introduced to connect non-overlapping fibers called the sticky-dicks (SD) **Rintoul and Torquato (1997).** Figure VI-11 presents an example of a SD sample.

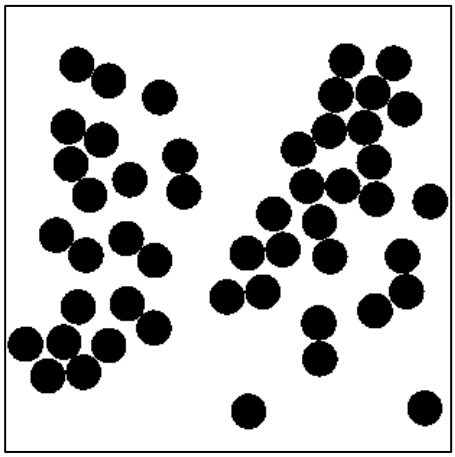

Figure VI-11. A sticky disks image sample

To generate the SD samples, the chosen energy in SA method was the adhesive potential of **Seaton and Glandt (1986)** defined as:

$$U = \begin{cases} \infty, & r < d \\ a, & d < r < d' \\ 0, & r > d' \end{cases}$$

Where $a = -\frac{1}{\beta}\ln(\frac{d'}{12\tau(d'-d)})$ and $(d' - d)$ is the thickness of the adhesive layer.

τ^{-1} the adhesiveness of the potential.

Despite accurate values of d' and τ, the SA fails to connect disks with this potential. For $r > d'$ the potential allows all the displacements as in highly agitated systems. Therefore, it is necessary to reduce the probability of ineffective displacements for which $r > d'$. The fibers then start to connect but the final system can be out of equilibrium.

The peak of Rdf for SD samples is higher than that of RSA samples, still, the value of $g(1 < r < 1.5)$ rarely reaches that of the previous section samples after 20000 displacements: the high values of Rdf for $r = 1$ is compensated by the redistribution of fibers within the sample. Nevertheless, it is interesting to compare effective values of SD samples to overlapping and non-overlapping ones in an attempt to explain the role of fiber connections. SD systems are expected to be an intermediate state in which fibers are connected but do not overlap. Actually, overlapping cases always exhibit a stiffer behavior than non-overlapping ones. At least at high enough volume fractions, this result was expected due to the fiber connections that build low deformation areas in overlapping samples.

On figure VI-12 are compared the homogenized values for bulk and shear moduli of overlapping, sticky and non-overlapping PY samples with regard to contrast.

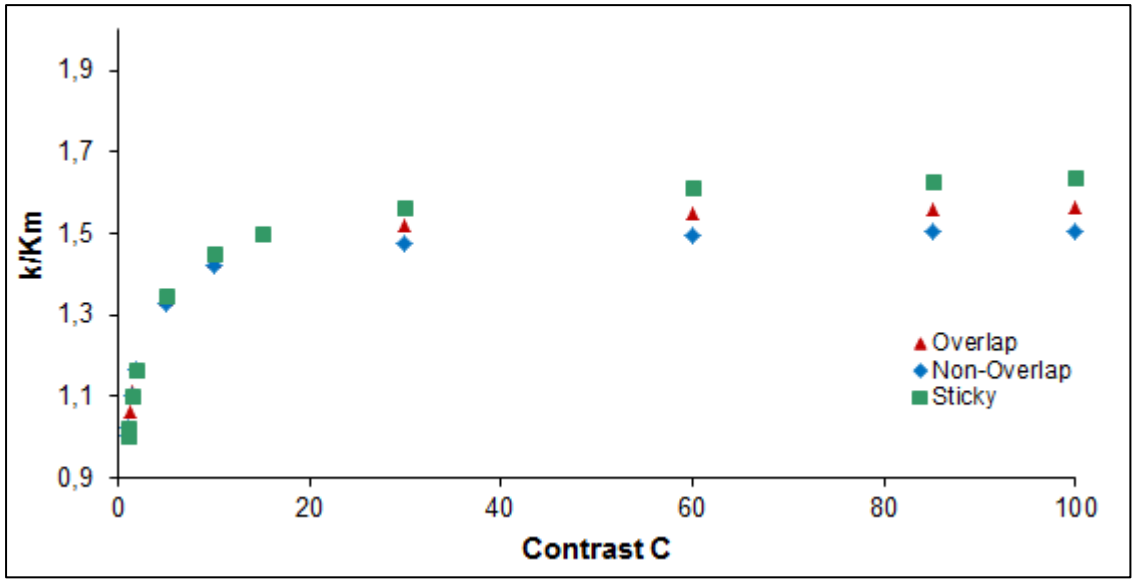

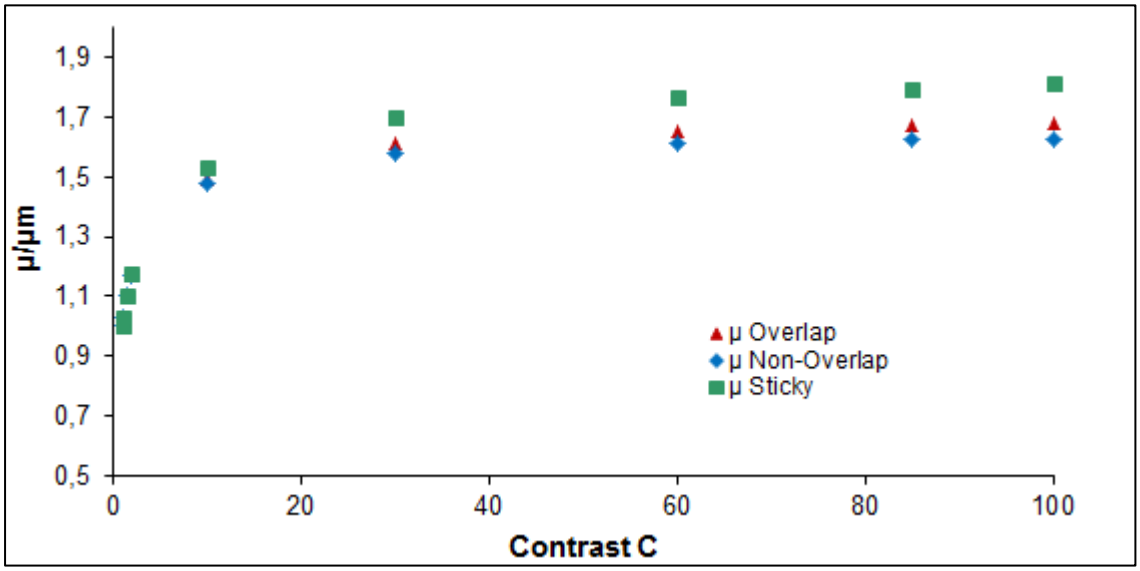

Figure VI-12. $\frac{k}{K_m}$ and $\frac{\mu}{\mu_m}$ with regard to contrast for overlapping, non-overlapping and sticky disks for $V_f = 30\%$

For both bulk and shear moduli, the effective values for the sticky disks are higher than those of non-overlapping PY samples. The Rdf peak increases with the rate of connected fibers leading to an increase of the homogenized elastic properties as expected from the results of the previous section. However, the SD systems were not the initially expected intermediate state as their effective values were also found higher than those of overlapping

samples. Therefore, fiber connection alone cannot entirely explain the differences of behavior between overlapping and non-overlapping systems.

The high effective values of the sticky disks samples suggest that for non-overlapping systems, the higher the rate of packed fibers the higher the elastic moduli.

As the SA method for sticky disks does not guarantee equilibrium, the results on effective values can be irrelevant compared to natural or industrials systems.

Chapter 7

Numerical bounds for non-overlapping equilibrium systems

In practical situations, microstructures of fiber reinforced composites and the exact values of their effective properties cannot be fully determined but only evaluated in the frame of bounds.

To determine tight and useful bounds for effective elasticity coefficients of any random aligned fiber distribution of reinforced composites, it is interesting to know what microstructures correspond to each of the upper and lower ones.

It was shown in chapter 4 that the integral range on bulk modulus is minimum for PY distributions preventing the occurrence of high stress areas and the lower bounds can coincide with equilibrium systems without interaction between fibers with correlation functions given by the PY approximation for non-overlapping systems.

It is confirmed by the spatial distribution of local elastic properties $\mathrm{k_i}$ and $\mathrm{k_m}$ or μ_i and μ_m that is similar in shape to the characteristic function I with discontinuities at the interfaces. For PY distributions, the hard-disk potential energy is minimum and the elastic energy is expected to reach a minimum as well.

This reasoning obvious for high contrasts might not apply for lower ones but it was found by **Torquato and Lado (1988)** and **Miller and Torquato (1991)** that the PY approximation provides the lowest bounds for random non-overlapping aligned fiber distribution of reinforced composites. Likewise, a Poisson distribution of fibers (fully penetrable cylinders) was found to correspond to the lower bound for overlapping systems by **Joslin and Stell (1986)** and **Torquato and Beasley (1986)**.

It is more difficult to conceive the upper-bound microstructures. Results from chapter 6 suggest that the effective values increase with the peak of $g(1 < r < 1.5)$ deviating from the lower bound. The sticky-disk cases suggest that the more in contact are the fibers the higher are the effective properties and for equilibrium systems, the upper bounds are likely to correspond to packed fiber samples as it was first suggested by **Beran and Silnutzer (1971)** and then shown by **Elsayed and McCoy (1973)**, the real difficulty being the determination of the type of clustering that leads to the highest effective values.

In the following sections, PY and clustered distributions will be studied in order to determine efficient microstructures for bounds tighter than Milton ones that include all the equilibrium systems. These bounds were finally obtained via FEM simulations.

I- Microstructures for the lower bound

The aim here is to generate fiber distributions similar to those given by the PY approximation with the hard-disk potential. Such fiber distribution cannot be directly provided by RSA (cf. Chapter I, section II-1-2.) but can easily be accurately approached with SA. In this case, SA consists of a simple agitation of fibers governed by the hard disk potential and controlled by second order correlations. However, for volume fractions close to the jamming limit (Chapter I, table 1.), typically $V_f > 50\%$, the fiber mobility is highly reduced and a repulsion criterion between fibers is required in order to accelerate the process. The resulting fiber distribution might slightly be out of equilibrium and necessitate successive checkings of the final state since the method is no longer heuristic. Examples are given in figure VII-1.

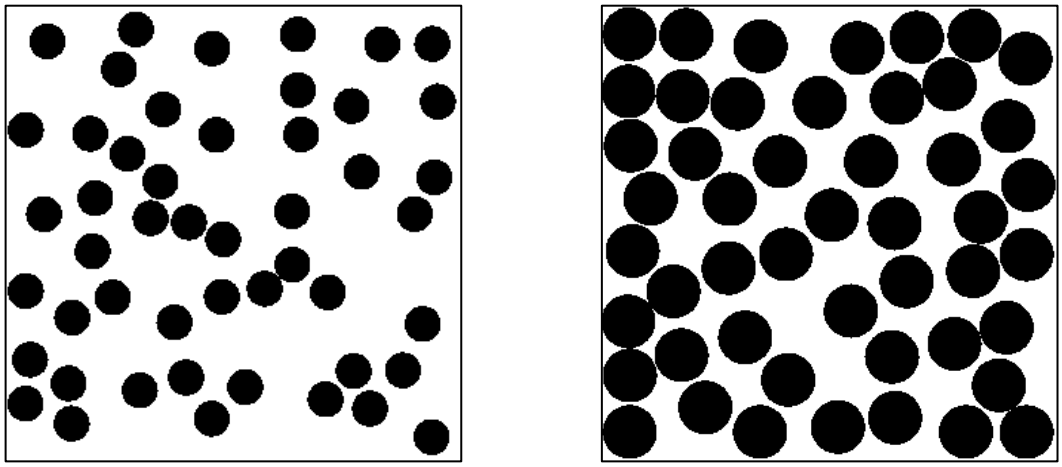

(a) **(b)**

Figure VII-1. PY image samples for **(a)** $V_f = 24.3\%$ and **(b)** $V_f = 54.4\%$

Due to FEM limitations, samples were reduced to 49 inclusions and Rdf are not fully converged and the comparison to the correlations given by the PY approximation available in literature has to result from an integration on a large enough distances r. However, the efficiency of SA has been previously proven on larger samples (cf. Chapter I, section II-2.).

This restriction calls for a statistical analysis of several samples with relevant peaks of Rdf in the range $1 < r < 1.5$ in order to select the one with the lowest effective values (figures VII-2 and VII-3).

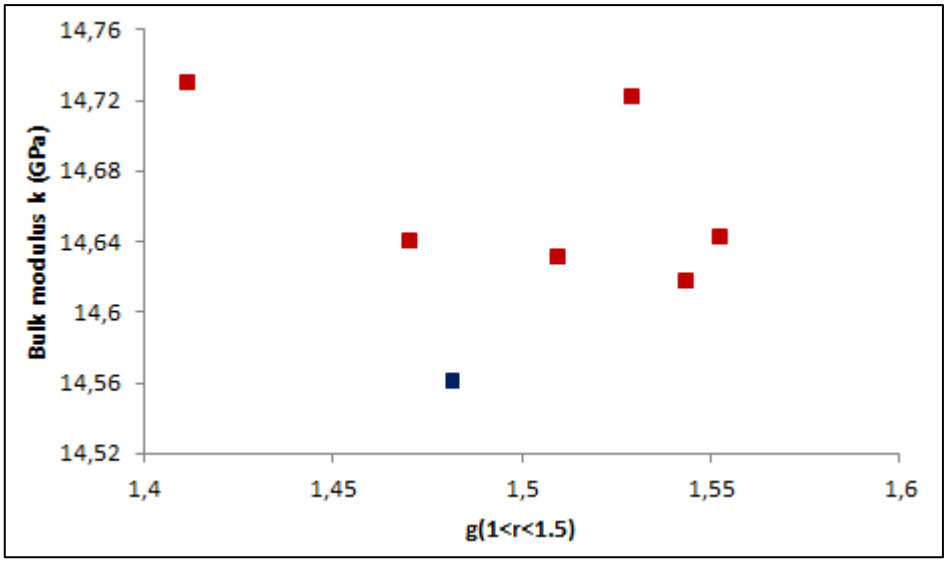

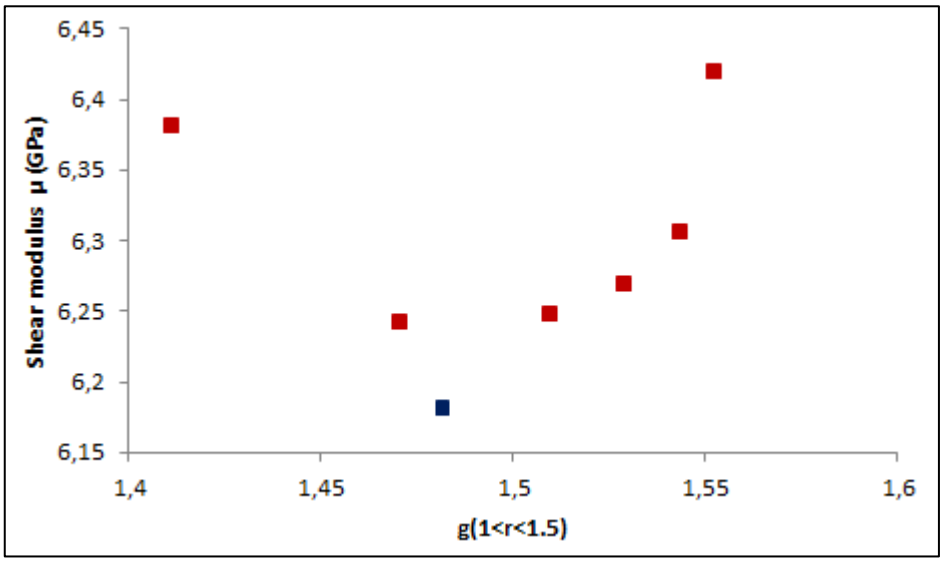

Figure VII-2. Bulk and shear moduli with regard to $g(1 < r < 1.5)$ for $V_f = 24.3\%$

Though the exact value of PY $g(1 < r < 1.5)$ for $V_f = 24.3\%$ is not available in literature, this value was estimated as just short of 1.55 which is the PY $g(1 < r < 1.5)$ for $V_f = 36.30\%$ (cf. Chapter I, section II-2).

For $V_f = 54.4\%$, PY $g(1 < r < 1.5)$ is available in literature and its value is of 1.7 (cf. Chapter I, section II-2).

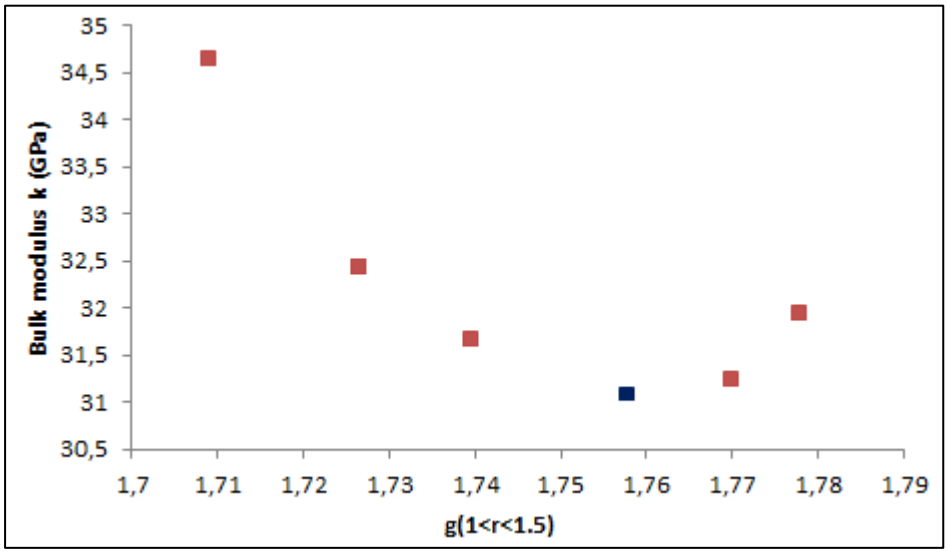

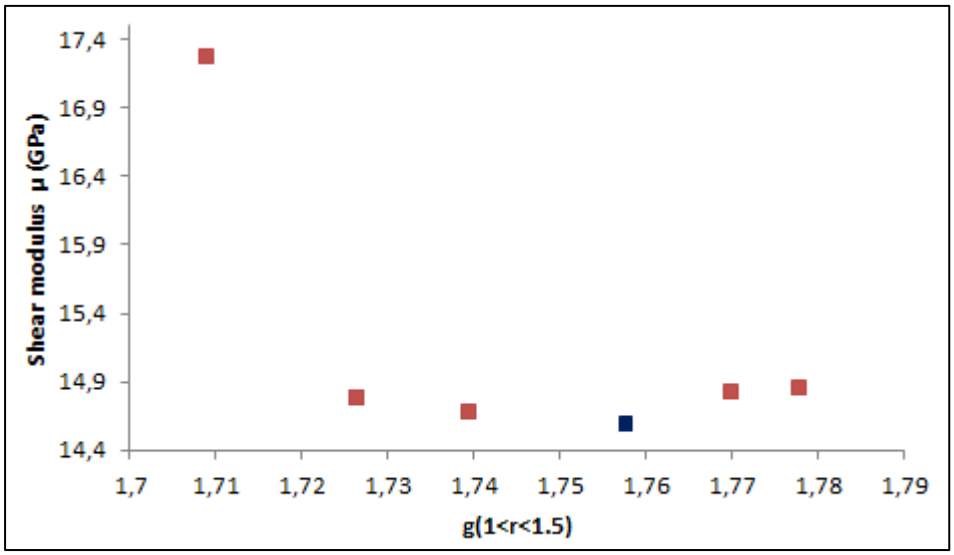

Figure VII-3. Bulk and shear moduli with regard to $g(1 < r < 1.5)$ for $V_f = 54.4\%$

All samples in figures VII-2 and VII-3 present a peak of $g(r)$ within an acceptable range to be the PY solution. The dispersion around the one with the lowest effective values was expected and confirms the relevance of a statistical analysis given the downsides of SA which does not take into account correlations of orders higher than 2 and is not fully converged on small samples of 49 inclusions.

The samples with the lowest effective values for both volume fractions were those selected to determine the lower bounds. The FEM simulations were carried out for various contrasts on bulk and shear moduli of matrix and inclusions.

II- Microstructures for the upper bound

The first bounds for non-overlapping aligned fiber reinforced composites were introduced by **Beran and Silnutzer (1971)** who suggested that the upper bounds corresponded to packing of fibers. This hypothesis was then confirmed by **Elsayed and McCoy (1973)** and then by **Milton (1982)** who also noticed that the values of the upper bounds are independent of the cluster positions.

Samples corresponding to the upper bounds can be regarded as infinite (very large) equilibrium homogeneous media where many clusters of, at this point, undetermined sizes are randomly scattered within the cross section. Such samples can be numerically represented a single cell surrounding a single cluster.

In order to determine numerical values of the upper bounds, samples with clusters were built and the primary step was to select the relevant clusters by studying their various sizes and compactness.

All these clusters were generated with the help of SA with an attraction potential:

$$U \equiv \begin{cases} +\infty, & x < d \\ -\frac{1}{x^n}, & x > d \end{cases} \quad (1)$$

In which $n > 1$

The exact value of n is not of great important because it is balanced out by the agitation energy in the probability of accepting the displacements. The difficulty with SA in such situations is that for a given value of n, the choice of the agitation energy will condition the internal microstructure of the cluster and other tools are required in order to select the optimal cluster.

Two examples are sketched on figure VII-4 .

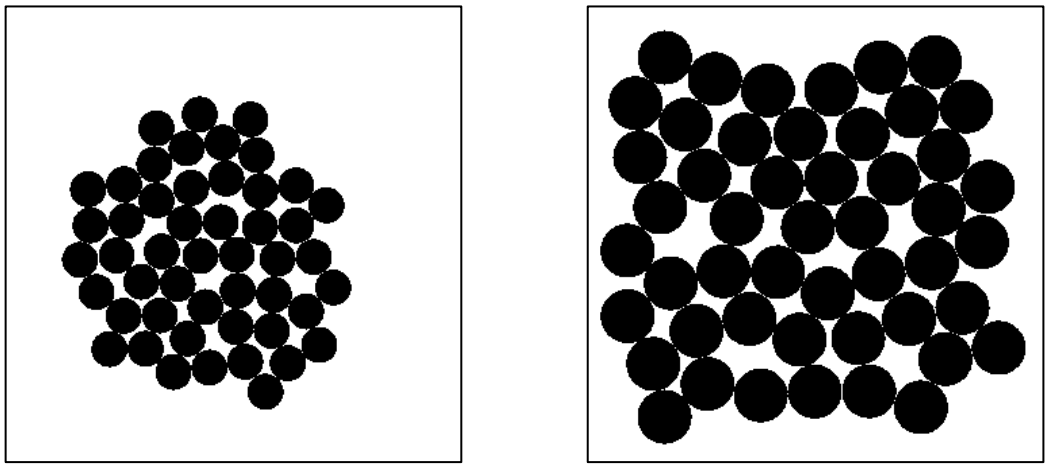

(a) **(b)**

Figure VII-4. Cluster image samples for **(a)** $V_f = 24.3\%$ and **(b)** $V_f = 54.4\%$

FEM simulations were performed on the generated cluster samples to determine the existence of a minimum size of clusters that allows reaching the upper bound for both k and μ.

To obtain clusters of various sizes on samples of 49 inclusions provided by RSA, the distribution of fibers was subjected to SA in which the agitation was applied to all fibers while the attractive potential was restricted to n fibers resulting in a $n-$ fiber cluster as shown in figure VII-5 below.

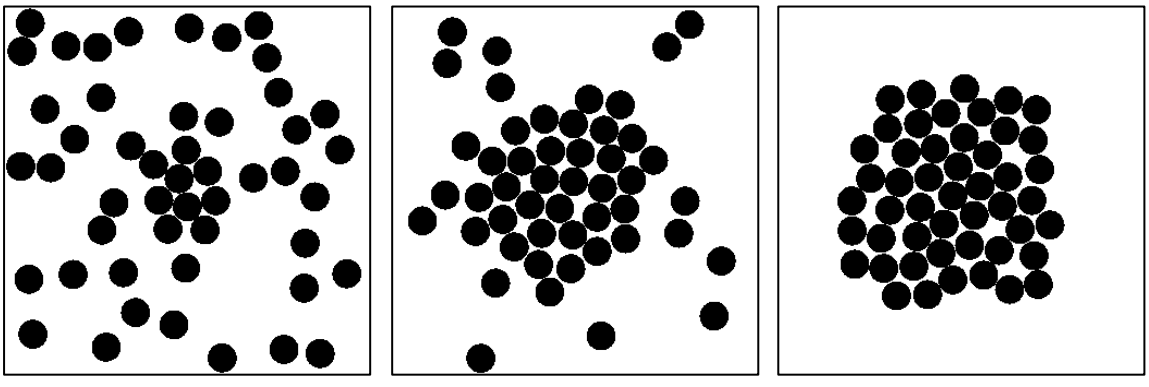

(a) **(b)** **(c)**

Figure VII-5. $n-$ fiber Clusters for **(a)** $n = 10$, **(b)** $n = 30$ and **(c)** $n = 49$

Naturally, due to the heuristic SA character, the n −fiber clusters exhibit various internal structures that lead to different effective values.

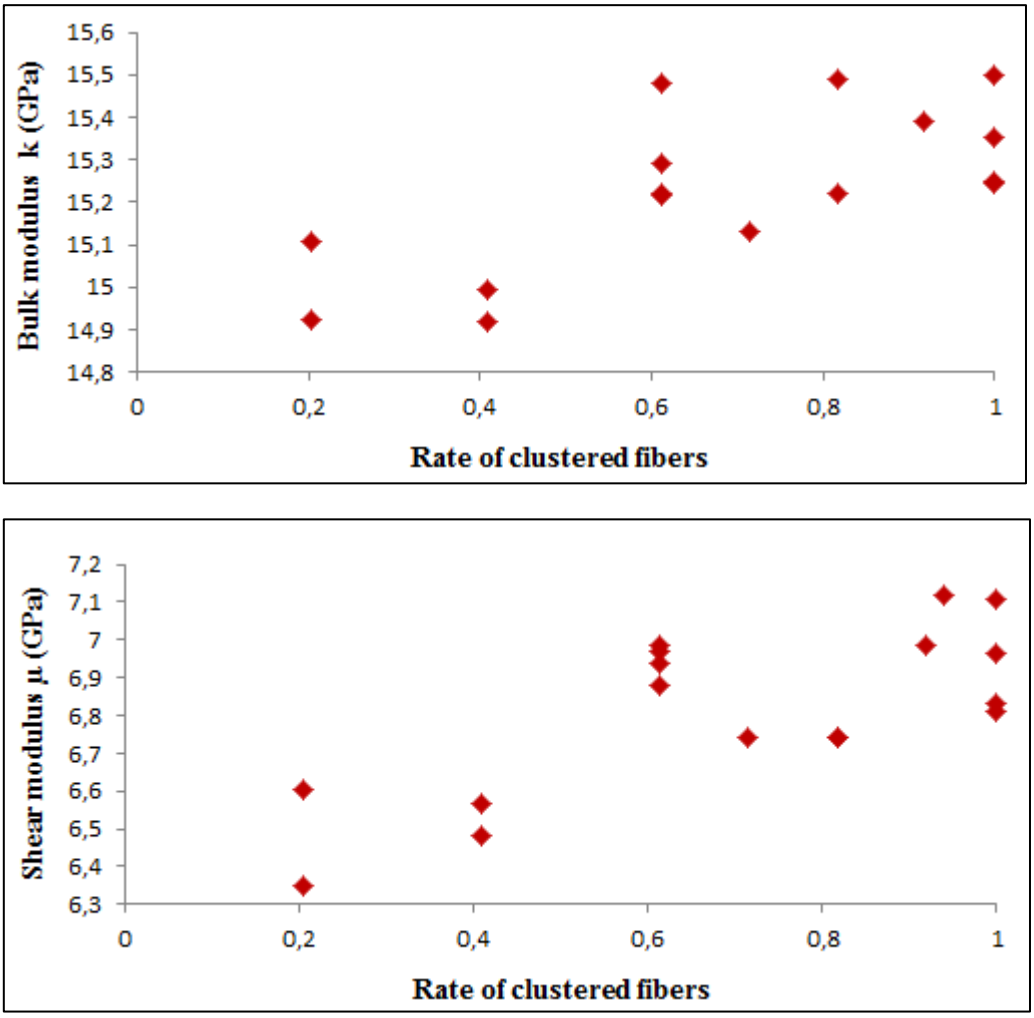

Figure VII-6. Bulk and shear moduli k and μ versus the rate of clustered fibers for $V_f = 24.3\%$ and $C = 100$

Figure VII-6 shows scatter points of effective values for different cluster sizes. This dispersion of results is due to different internal structures of clusters of same size. With no finer control over these fiber distributions, the RVE is not reached.

For rates of clustered fibers higher than 0.6 the bulk modulus of some clusters saturates. This rate of 30 to 49 fibers (30 −fiber clusters) is the minimum number of packed fibers required for the sample to fit for the upper bound. In the following sections, clusters of $N = 49$ inclusions, corresponding to a rate of 1, were arbitrary chosen for determination of the upper bound.

This cluster size criterion is not sufficient so the internal structure of clusters has to be investigated through compactness in order to select the optimal ones.

To evaluate the compactness of the clusters, we can either study their size or their RDF at short distance. The former tool is hardly accurate because of the irregularity in cluster shapes and the latter loses its classical significance when applied on inhomogeneous samples. Nevertheless, for a given volume fraction, it is expected that the highest peaks of $g(1 < r < 1.5)$ would lead to the upper-bound clusters.

However, when the clustering process is pushed to the limits of SA, with very short fiber displacements, the fibers start forming a hexagonal network which is known for lower effective elasticity values **Beicha *et al.*** (figure VII-7).

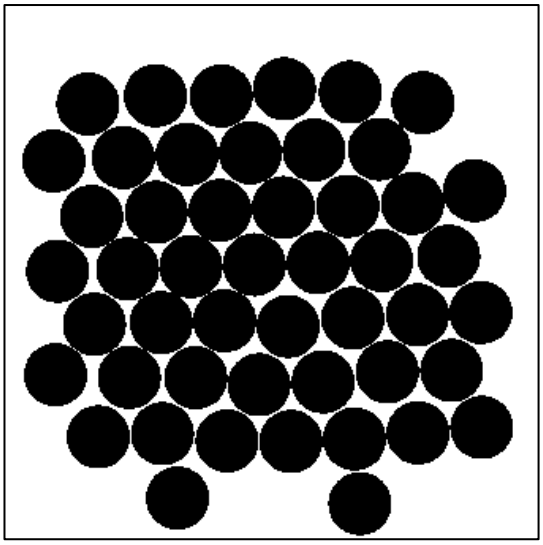

Figure VII-7. Hexagonal image sample obtained with SA for $V_f = 54.4\%$

The low effective values (k=14.683 GPa and μ=6.479 GPa) obtained for the artificially induced hexagonal structure on figure VII-8 confirm the results of Beicha's work.

A means to characterize hexagonal networks is the knowledge of $g(r)$ at very short distances ($r \approx 1$). The values of $g(r)$ cannot be accurately accessed due to convergence difficulties. To overcome this limitation, local volume fractions were measured using a sliding window method in which various sizes of windows can be swept across the whole image. For simplicity, squared windows were used. For this purpose, it was found that the optimal side length of the windows was five times the radius of fibers. Smaller windows gave disparate results while larger ones failed to capture the details of the microstructure. This optimal size is suitable for all volume fractions as long as the cluster size is large enough with regard to that of the sliding window.

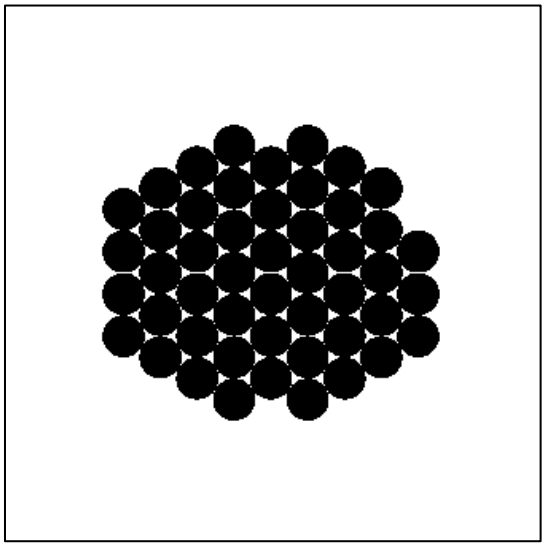

Figure VII-8. Artificial hexagonal image sample for $V_f = 24.3\%$

The most probable local volume fractions for random and hexa-structured clusters are respectively centered around 78% (percolation threshold) and 86%. Here, random refers to clusters without hexagonal structuration.

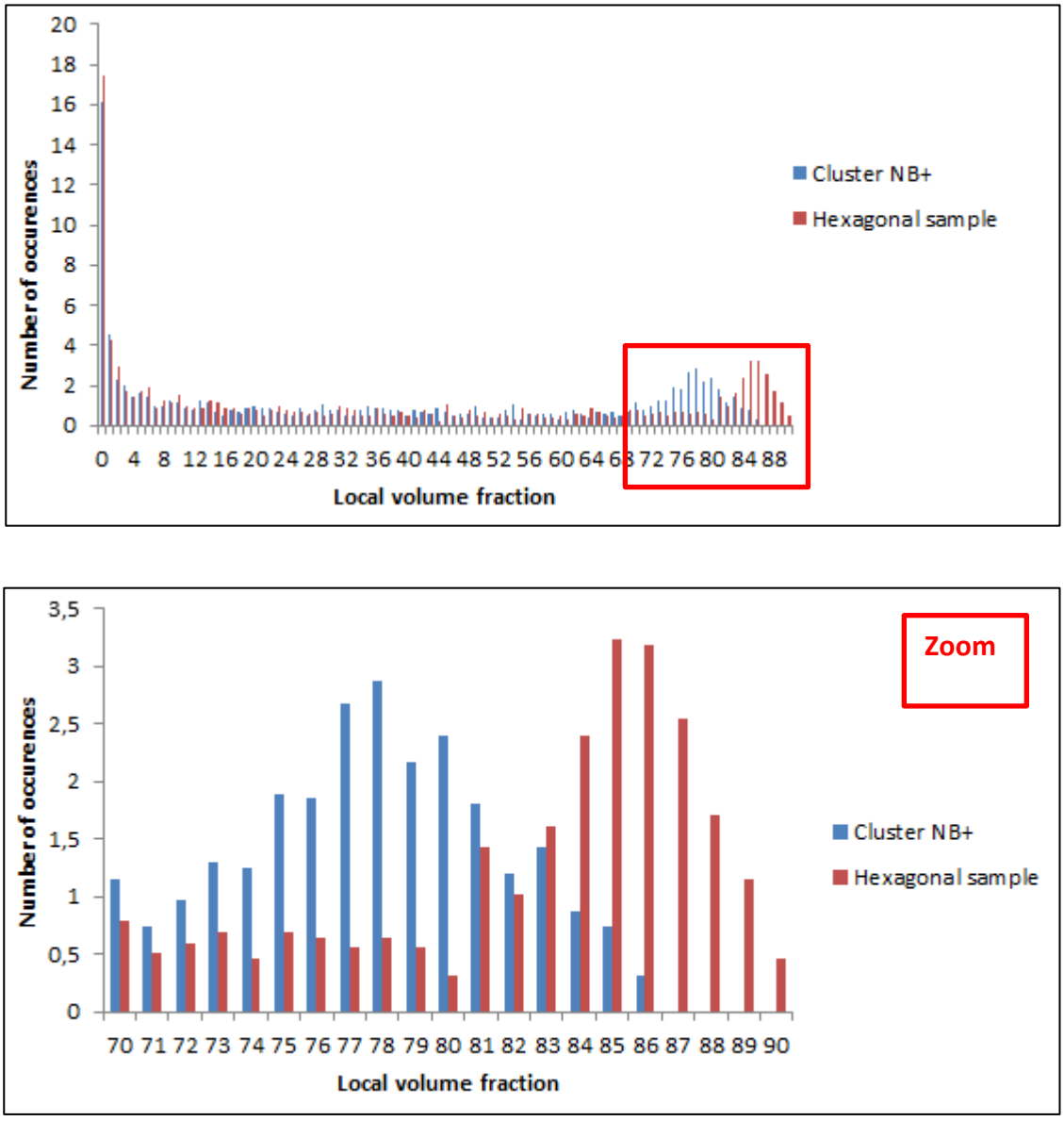

Figure VII-9. Histograms of number of occurrences as function of the local volume fractions (%) for the hexagonal sample versus the cluster NB+ for $V_f = 24.3\%$

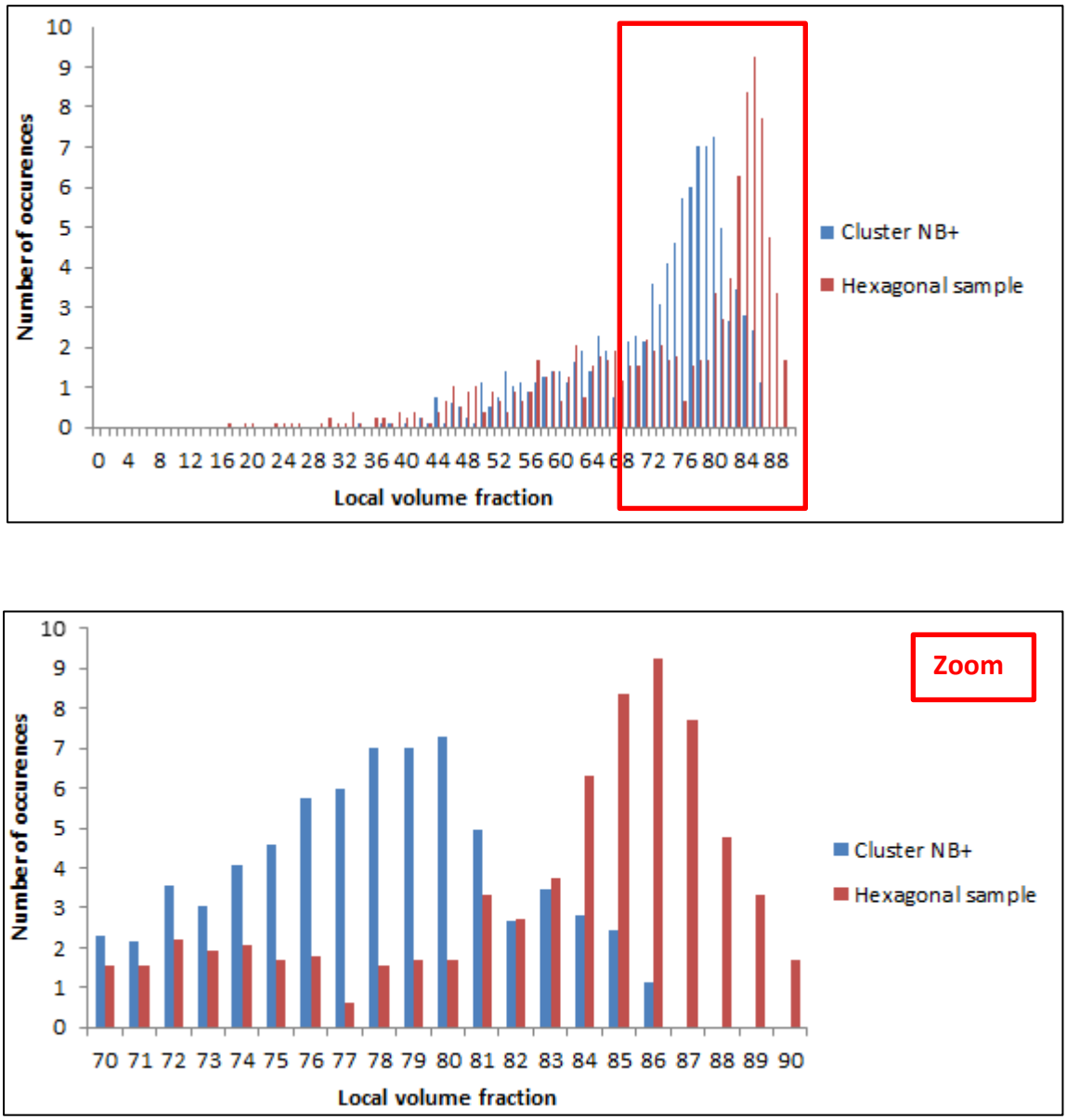

Figure VII-10. Histograms of number of occurrences as function of the local volume fractions (%) for the hexagonal sample versus the cluster NB^+ for

The histograms represent the number of occurrences of given local volume fractions determined by sliding the window over the whole image sample. For both random and hexa-structured clusters, unlike figure VII-10 for $V_f = 54.4\%$, figure VII-9 for $V_f = 24.3\%$ naturally exhibits numerous occurrences of very low local volume fractions due to larger areas of matrix on edge of the sample.

For both volume fractions, the focus on local volume fractions higher than 70%, figures VII-9 and VII-10 show two different behaviors. For random clusters, local volume fraction exhibit a

peak of occurrence at 78% and go up close to the jamming limit for two dimensional disordered media (83%, table 1. Chapter I) while for the hexa-structured clusters, the peak is situated around 86% with a wider range going up to 90% which is approximately the maximum volume fraction for hexagonal networks 90.7% $(\frac{\pi}{2\sqrt{3}})$.

Local volume fraction histograms are a relevant criterion for hexagonal structuration of a cluster and can be an efficient tool to select the optimal compactness of clusters.

On figures VII-11 and VII-12, the random clusters are sketched in green triangles and the hexa-structured ones in red squares.

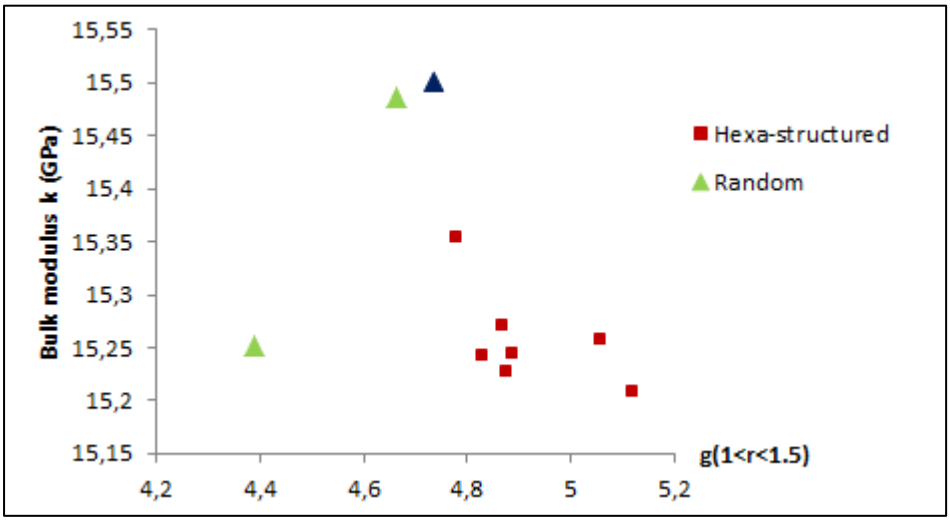

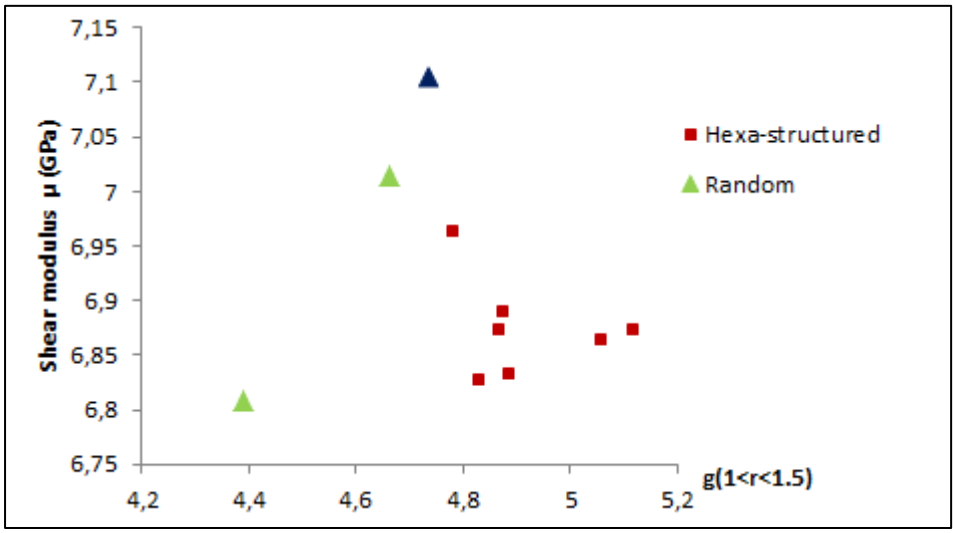

Figure VII-11. Bulk and shear moduli with regard to $g(1 < r < 1.5)$ for $V_f = 24.3\%$ and $C = 100$

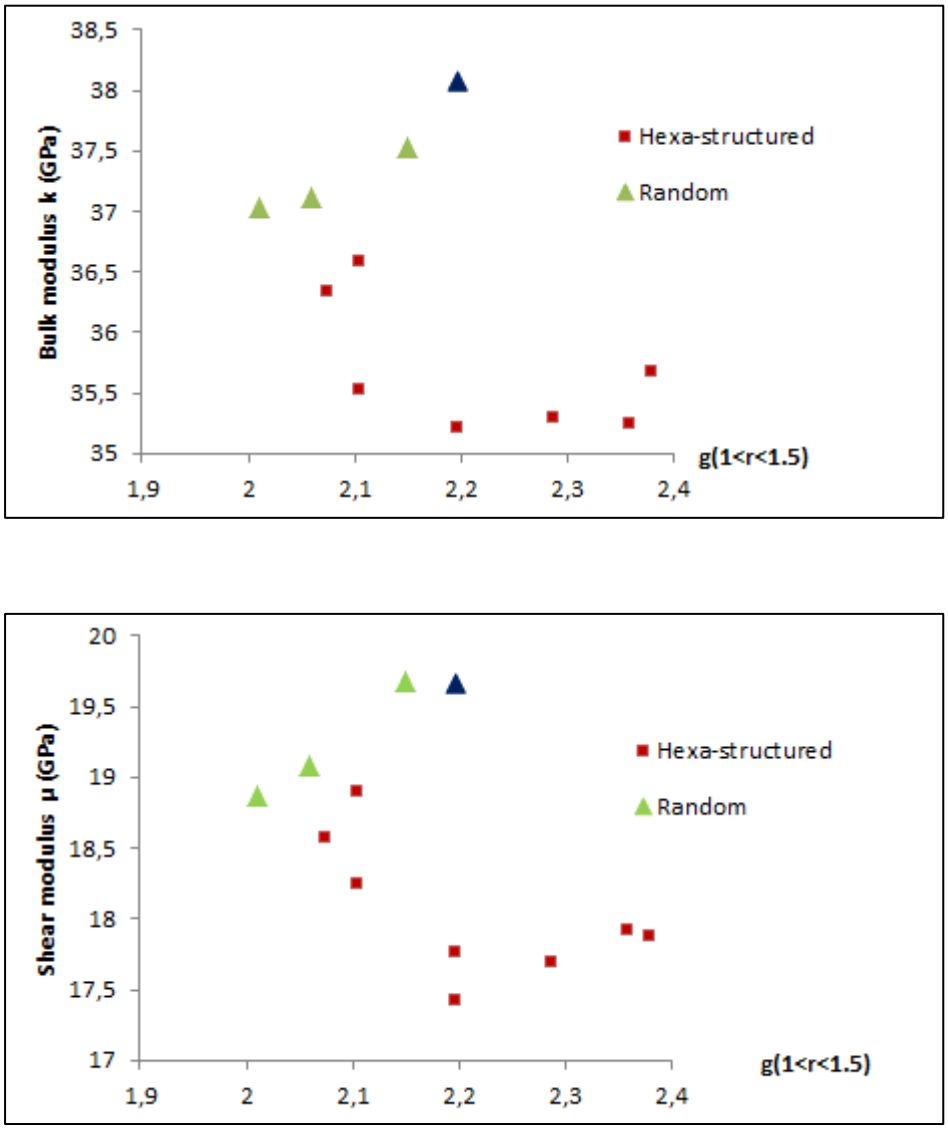

Figure VII-12. Bulk and shear moduli with regard to $g(1 < r < 1.5)$ for $V_f = 54.4\%$ and $C = 100$

Regardless of $g(1 < r < 1.5)$, the bulk and shear moduli for hexa-structured clusters are lower than those of random ones. This confirms the above mentioned results from literature.

Discarding the hexa-structured clusters, the highest $g(1 < r < 1.5)$ among the remaining ones is that of the optimal random cluster for the upper bound and will be the one used in the next section.

III- Comparison to existing bounds

The numerical NB^+ and NB^- bounds were evaluated with FEM simulations applied on the samples built with the above-mentioned microstructures. It is assumed that any equilibrium system in which the correlation functions are solutions to the Ornstein-Zernike equation is framed by NB^+ and NB^-.

Although Milton bounds were derivate from a single microstructure, the PY one, they are still wider than NB^+ and NB^- as shown on figures VII-13 and VII-14.

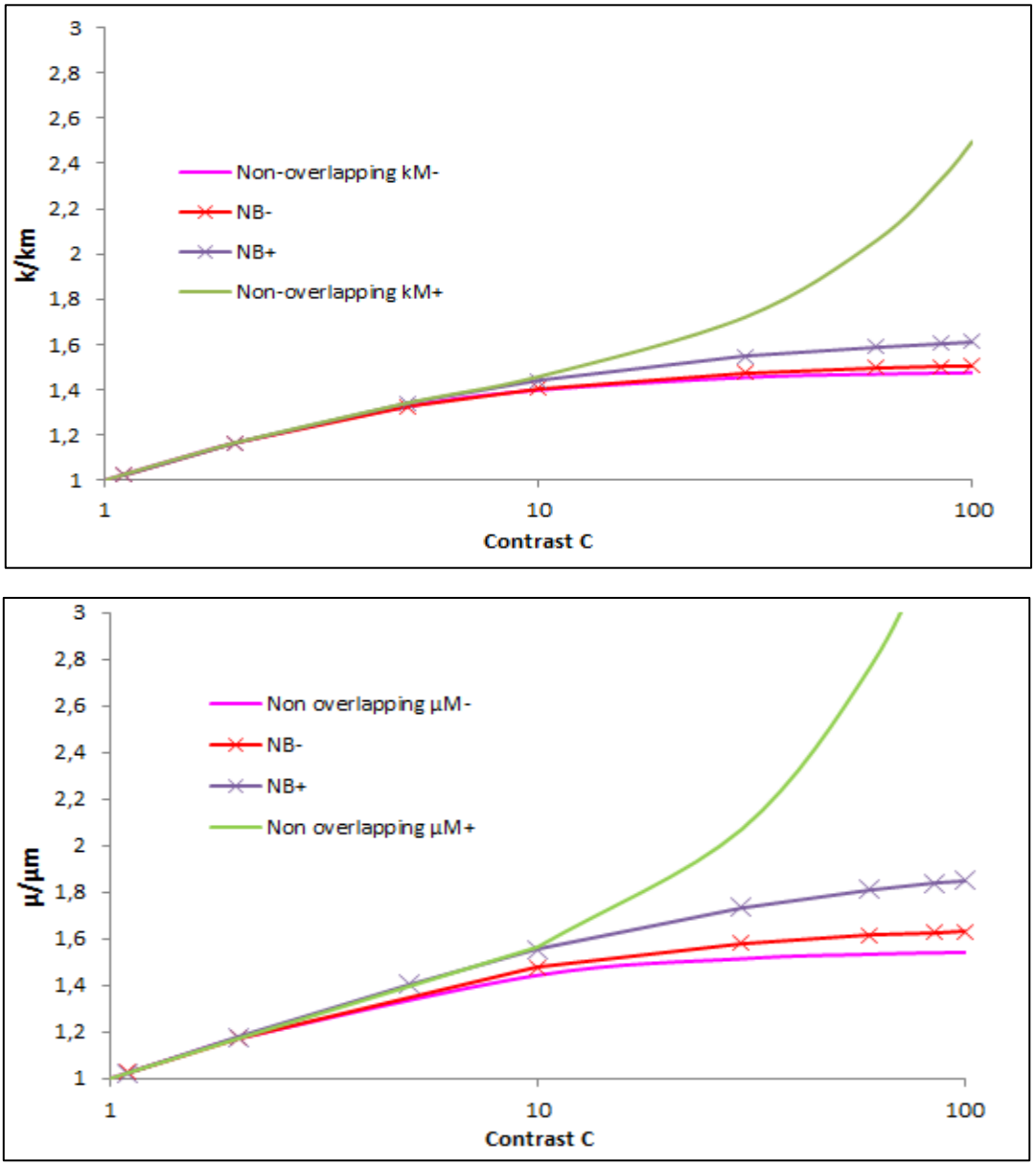

Figure VII-13. Numerical bounds for non-overlapping systems NB^- and NB^+ compared to Milton bounds for $\frac{k}{k_m}$ and $\frac{\mu}{\mu_m}$ with regard to contrast for $V_f = 24.3\%$

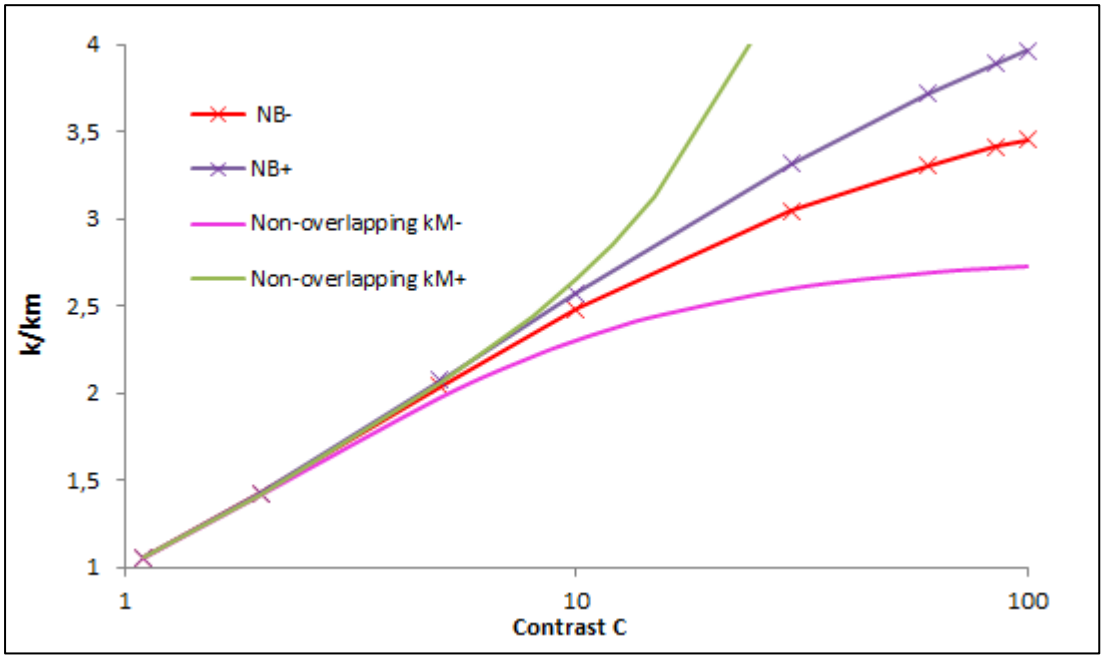

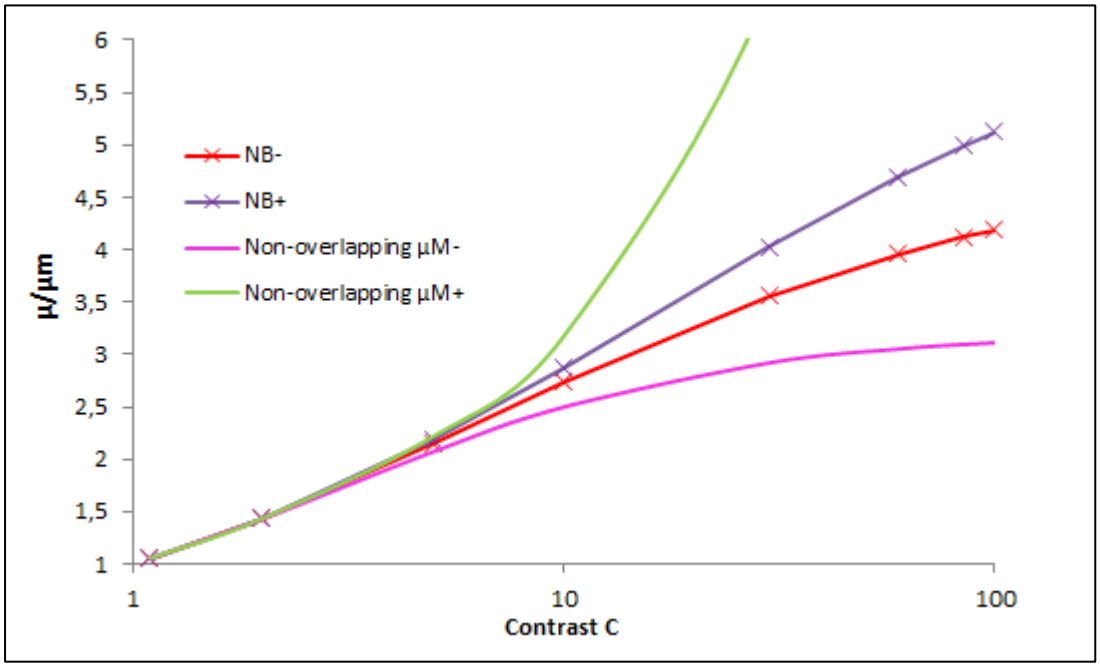

Figure VII-14. Numerical bounds for non-overlapping systems NB^- and NB^+ compared to Milton bounds for $\frac{k}{k_m}$ and $\frac{\mu}{\mu_m}$ with regard to contrast for $V_f = 54.4\%$

As expected, these bounds coincide at low contrasts $C < 5$, while at high contrasts, the upper Milton bounds (kM^+ and μM^+) diverge. Though the NB bounds are fit for a wide range of microstructures, they are still very tight and never diverge.

At $C = 100$, NB^+ is still increasing with contrast suggesting that the threshold for rigid-body models occurs for a higher contrast than the common expectation. This phenomenon could be explained by a collective effect of compressibility at the scale of the whole cluster where some fibers can roll around other ones.

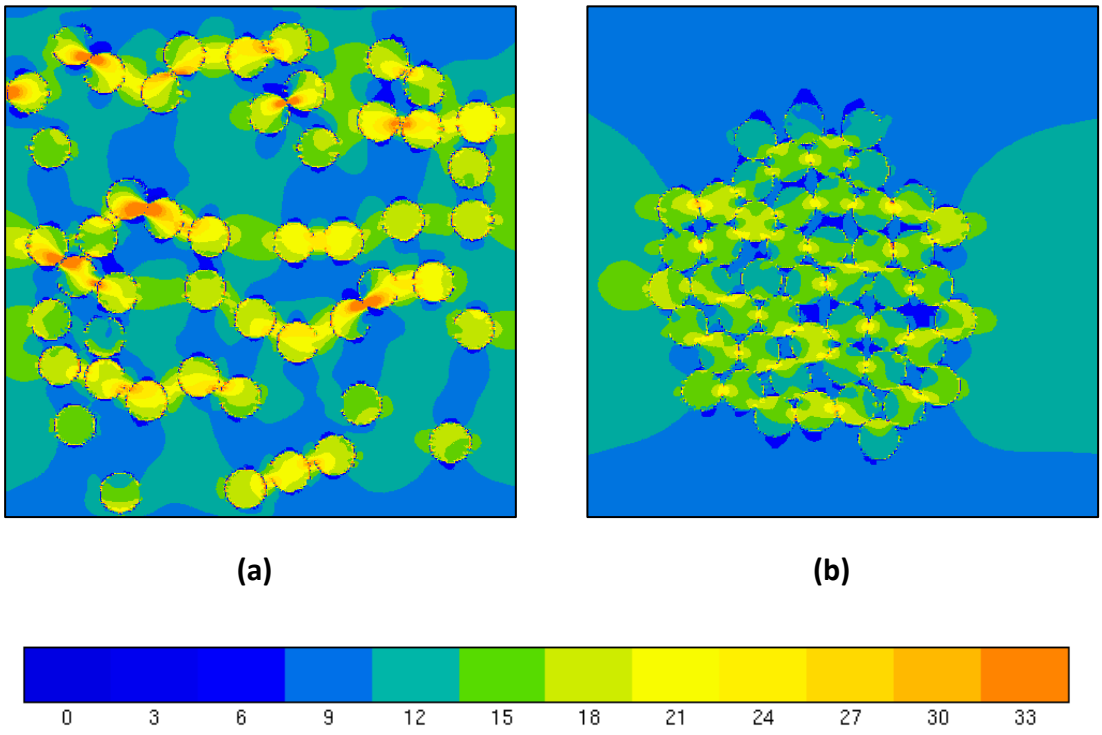

Figure VII-15. Normal stress σ_{11} maps for **(a)** PY sample and **(b)** cluster (GPa) for $C = 100$ and $V_f = 24.30\%$

Figure VII-15 allows a comparison between normal stresses σ_{11} on the lower **(a)** and upper **(b)** bounds. On these maps, it is not obvious that the effective values for case **(a)** are lower than those for case **(b)** as homogenization has shown. The cluster spatially structures the stresses along the strain for σ_{11} and perpendicular to σ_{22}(map not presented here) and forms a large horizontal strip of σ_{11} stresses that increases stiffness.

It is necessary to precise that these bounds do not all microstructures of aligned fiber reinforced composites. As mentioned before, NB^+ and NB^- are only fit for equilibrium systems which are expected to occur in any process of fiber arrangements without educated interventions. Effective values of non-equilibrium systems can be either within or out of NB^+ and NB^- bounds. Examples with effective values higher than NB^+ are shown below.

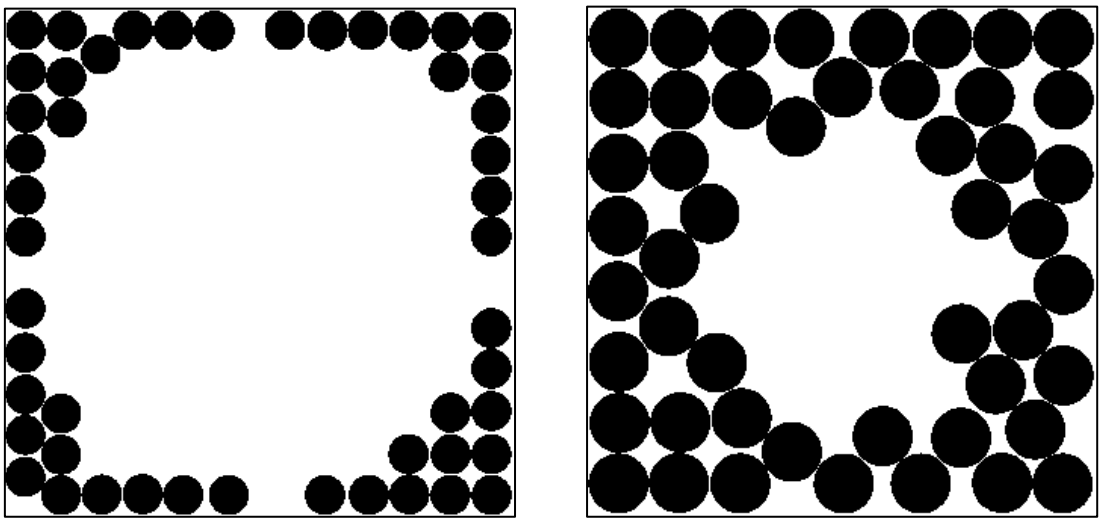

(a) **(b)**

Figure VII-16. First examples of non-equilibrium systems:

(a) $V_f = 24.3\%$ and **(b)** $V_f = 54.4\%$

The samples of figure VII-16 are easy to obtain with SA by introducing a repulsion potential between fibers without any agitation (out of equilibrium). The effective bulk moduli are respectively 40% and 42% higher than NB^+ for $V_f = 24.3\%$ and $V_f = 54.4\%$ and for the former volume fraction, it is also higher than Milton's upper bound by 12%. In this particular case, these results are not surprising given the aligned chains along the edges. Knowing that the applied displacement was horizontal, the chains along the upper and lower edges could be vaguely assimilated to the Voigt configuration.

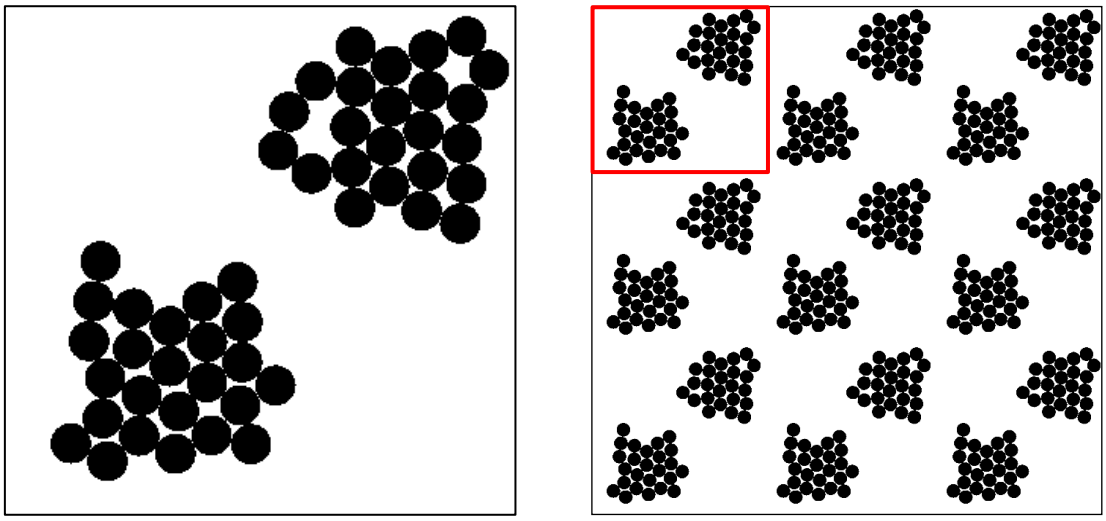

Figure VII-17. Second example of non-equilibrium systems for $V_f = 24.3\%$

(a) Elementary cell and **(b)** Periodic medium

The second example of figure VII-17 (a) contains two clusters that are individually close of the upper bound NB^+. However this artificially induced arrangement within the cell leads to a strong anisotropy on a periodic medium built by juxtaposition of this single cell (figure VII-16 (b)). The effective values of sample (a) are respectively for bulk and shear moduli 5 and 15% higher than NB^+.

Frequently, it is admitted that a large medium is equivalent to a periodic one built with an elementary RVE extracted from the initial medium **Sanei *et al.* (2017), Cavalcante and Pindera (2014).** The present example shows the limits of such method in which the elementary RVE has to remain isotropic and homogeneous.

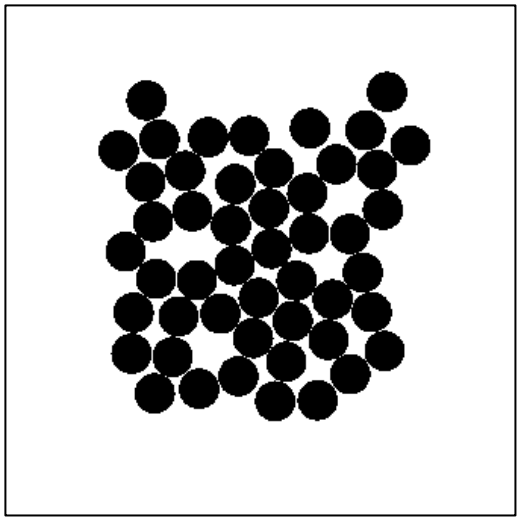

Figure VII-18. Second example of non-equilibrium systems for $V_f = 24.3\%$

The third example of less obvious non-equilibrium systems is sketched on figure VII-18. It is a cluster built with SA where the agitation energy was kept very low. Among all "low-agitation" clusters, some fall within the NB^+ and NB^- bounds and others do not. This is not fully predictable, however, visual observation can give hints on the effective properties. For this example, due to the low agitation energy, the lack of freedom in displacements of fibers leads to the formation of large voids within the cluster characteristic of non-equilibrium. In this case, the size of the area with a rigid behavior is enlarged increasing the homogenized values as would an increase in volume fraction.

Conclusion and perspectives

Throughout this work, the influence of microstructure of non-overlapping aligned fiber reinforced composites on macroscopic elastic properties has been quantified with the help of numerical homogenization on FEM simulations. Unusual tools in the field of mechanics were used both to characterize and generate microstructures: the radial distribution function and simulated annealing respectively provided by the theory of liquids and optimization processes. Rdf has proven to be the best second order correlation to describe spatial distributions of identical fibers.

The first main result is that effective elasticity increases with the peak of Rdf characteristic of non-overlapping conditions. Even a small fiber rearrangement by SA can increase stiffness. 2 to 3% variations on effective properties are rather small compared to typical fabrication scatter and cannot be expected to optimize production processes. However it is easy to extract Rdf from snapshots of real composite sections by image processing and in specific cases, it could be a good indicator of relative stiffness allowing selection among irregular samples.

The second main result has required several intermediate studies leading to the determination of new numerical bounds (NB) that frame any configuration of non-overlapping aligned fibers for equilibrium systems. These systems are observed in both nature and industrial processes; they result from natural arrangements under specific constraints and their correlation functions are solutions to the Ornstein-Zernike equation. With suitable potentials, any system will evolve toward equilibrium by SA rearrangement. Among equilibrium systems, following **Beran and Silnutzer (1971)** hints, it was found that packed fibers correspond to the upper bound NB^+ while Percus-Yevick PY distribution of fibers to the lower one NB^-. These bounds are tighter than the existing high order analytical ones called Milton bounds in this manuscript. Milton lower and upper bounds are built with the PY distribution hence the small discrepancies between NB- and the Milton lower bounds. The efficiency of NB bounds lies in the tightness of their upper bound compared to the existing ones. The NB^+ bound could be of great interest in production processes where fiber agglomeration is not always easy to avoid, increasing the composite's stiffness with effective elastic moduli closer to the upper bound. At high contrasts, the upper Milton bounds diverge and do not frame real composites. Actually, these bounds are built as a correction of Voight's expression that diverges as well. This correction is based on an asymptotic model of the local variance $C(0)$ that infinitely increases and is not sufficient to avoid this divergence. This model of $C(0)$ is only valid for contrasts close to 1 but surprisingly, the local variance evaluated by FEM keeps increasing up to C around 100000 while rigid body behavior occurs for contrasts lower than 100.

As the microstructures corresponding to NB bounds are well defined, obtaining effective values only required a small RVE of 49 inclusions.

The NB bounds can be used in various fields of physics **Torquato (1991)** not only elasticity and thermal conductivity as shown in chapter 6 but also electrical conductivity, magnetic and fluid permeability …

Perspectives

The study presented here can easily be extended to 3D situations in which fibers are replaced by spheres granted that hardware resources are sufficient. The radial distribution functions and simulated annealing remain suitable tools. Moreover, the Rdf of the required PY distributions for the lower bounds are analytical and can be obtained for any volume fraction.

It is expected that for both 2D and 3D situations, the microstructures corresponding to the upper and lower bounds are the same for any elastic behavior. The relevant elastic law only needs to be implemented in the FEM software.

For the visco-elastic behavior, the same final state is delayed by a relaxation time and again, for time stationary problems, the same microstructures are expected to be relevant.

As this study only dealt with time stationary strains applied on sample boundaries, an interesting continuation of the work can be an analysis of time-dependent elasticity (cycle loading). Actually, an efficient measure of liquid compressibility is the limit when the wave number k tends to 0 of the structure factor $S(k)$ (**Hansen and McDonald (2006)**): $\lim_{k\to 0} S(k)$ that is the Fourier transform of the total correlation function $h(r) = g(r) - 1$. **Jiang *et al.* (2010)** used $S(k)$ for macroscopic systems to measure the elastic response of suspension of particle in a fluid. For system of aligned fibers, as systems of particles in suspensions, $S(k)$ can easily be evaluated from direct position of fiber or particle centers r_i by:

$$S(k) = 1 + \langle \frac{1}{N} \sum_{i=1} \sum_{j \neq i} e^{-ik(r_j - r_i)} \rangle$$

The ensemble averaging is only necessary when the RVE is not reached.

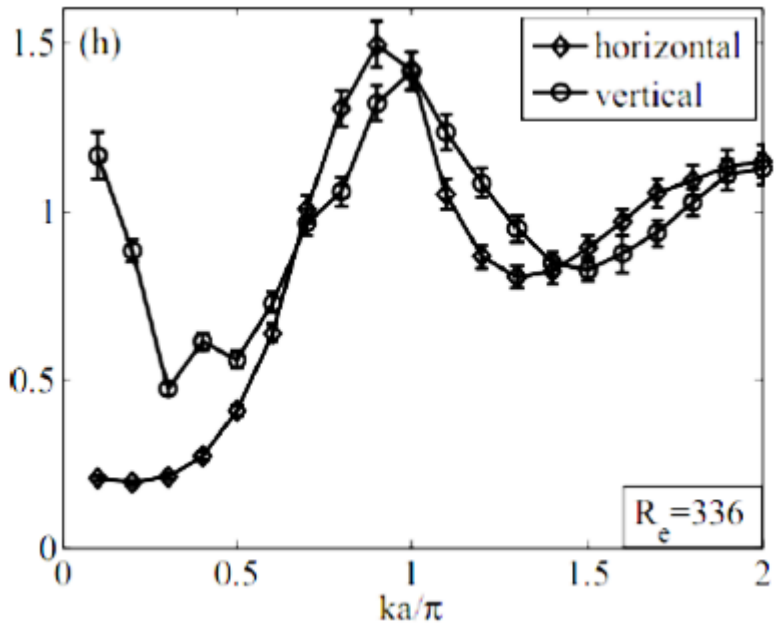

Typical example of structure factor $S(k)$ for an anisotropic suspension (**Jiang *et al.* (2010)**)

The lowest values of $S(k)$ are characteristic of the resonant frequencies $f = \frac{kC}{2\pi}$ in which C is the speed of sound in the medium. Similarly for solid composites, $S(0)$ is expected to be an indirect measure of elastic moduli and shapes of $S(k)$ could still indicate the resonant frequencies for cycle loading.

From a modeling perspective, the local behavior exhibited by stress maps and stress P.D.F. of chapter 6 suggests that pertinent scaling for fiber reinforced material stiffness cannot be reduced to the macroscopic scale (volume fraction) and has to be supplemented by a micro–scale such as the inclusion size or equivalently the nearest neighbors distance that is able to capture the occurrence of small area of high stresses.

This study was limited to equilibrium systems as defined by statistical physics (Ornstein-Zernike). The potentials driving the fiber distributions in industrial productions of composites can be very different from those used in this work and uncontrolled. In this case, local inhomogeneity could appear with areas of large voids between fibers (as shown on figure VII-18 for a non-equilibrium system) and an intermediate scale might be required for modelling the elastic behavior.

Appendices

Appendix 1

Appendix 1 : Coarseness

In this study, 25 examples of both overlapping and non-overlapping cases were studied and were necessary to reach convergence of previously introduced effective values. The aim of this appendix is to present the results on each sample.

A special attention was cast on the samples with extreme bulk moduli, either higher or lower than the mean value $k_{average}$ averaged on the results of the 25 examples.

These examples will be presented below for overlapping and non-overlapping, with a comparison of their evaluated coarseness to the averaged one (here referred to as “coarseness moyenne”).

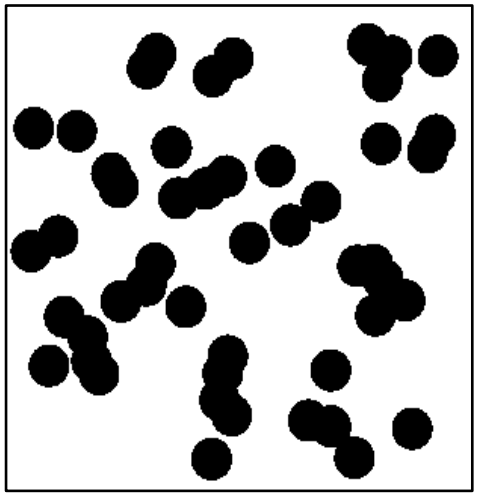

$\boldsymbol{k} = 16.16\ GPa$

$\boldsymbol{k_{average}} = 16.49\ GPa$

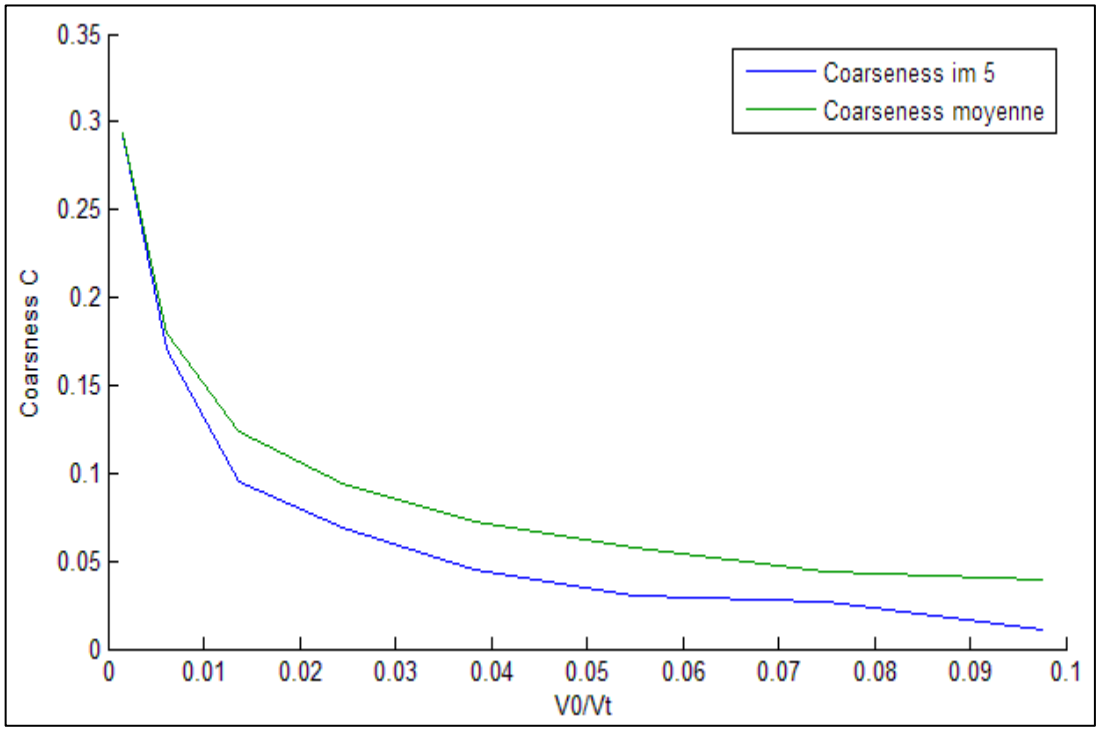

Appendix 1 : Coarseness for overlapping samples

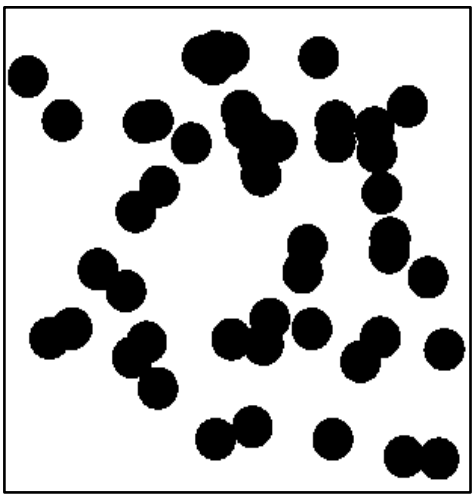

$\boldsymbol{k} = 15.02\ \ GPa$

$\boldsymbol{k_{average}} = 16.49\ \ GPa$

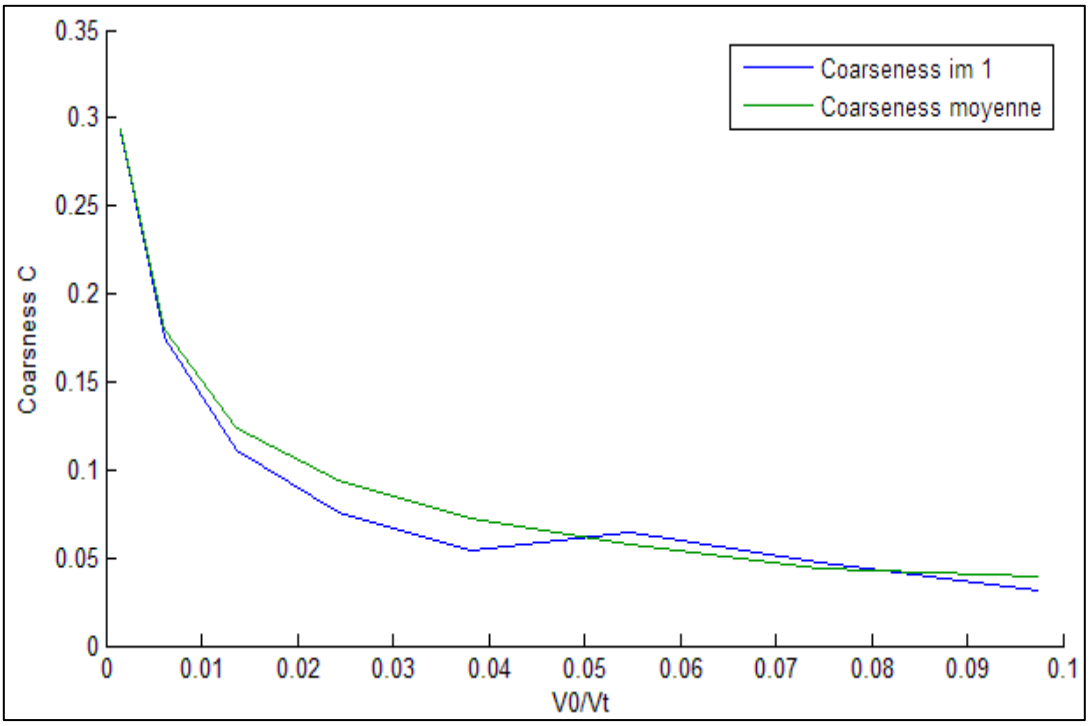

Appendix 1 : Coarseness for overlapping samples

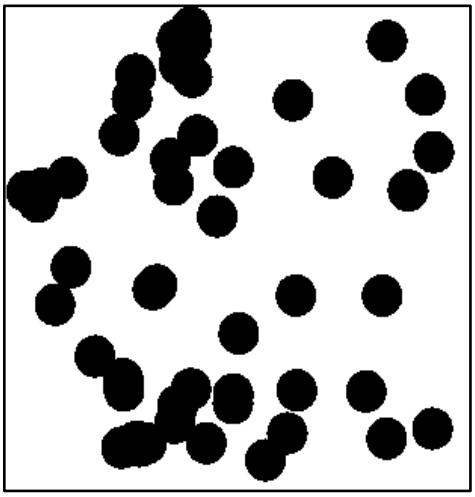

$\boldsymbol{k} = 15.22\ GPa$

$\boldsymbol{k_{average}} = 16.49\ GPa$

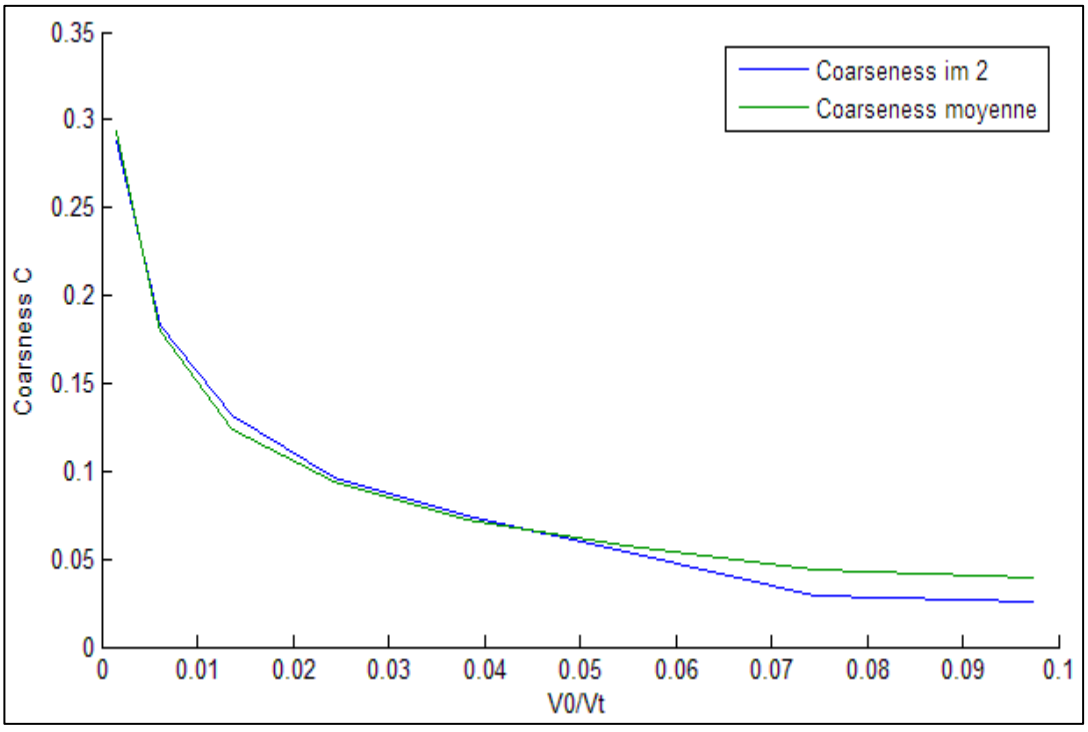

Appendix 1 : Coarseness for overlapping samples

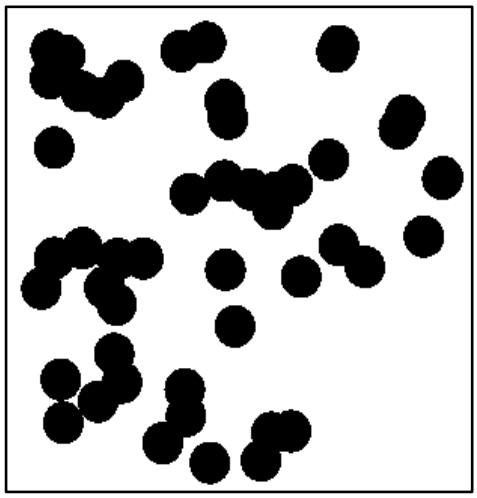

$\boldsymbol{k} = 15.16\ GPa$

$\boldsymbol{k_{average}} = 16.49\ GPa$

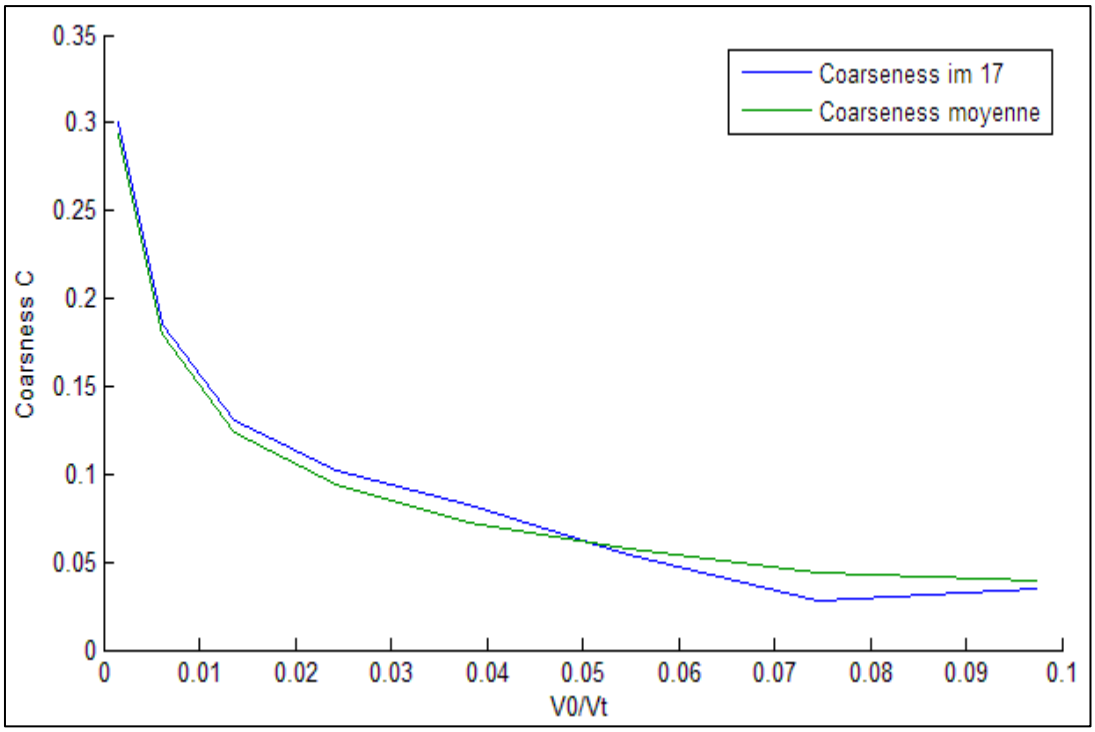

Appendix 1 : Coarseness for overlapping samples

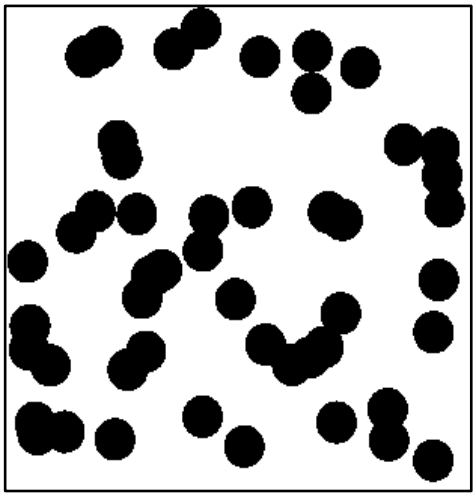

$\boldsymbol{k} = 15.43\ GPa$

$\boldsymbol{k_{average}} = 16.49\ GPa$

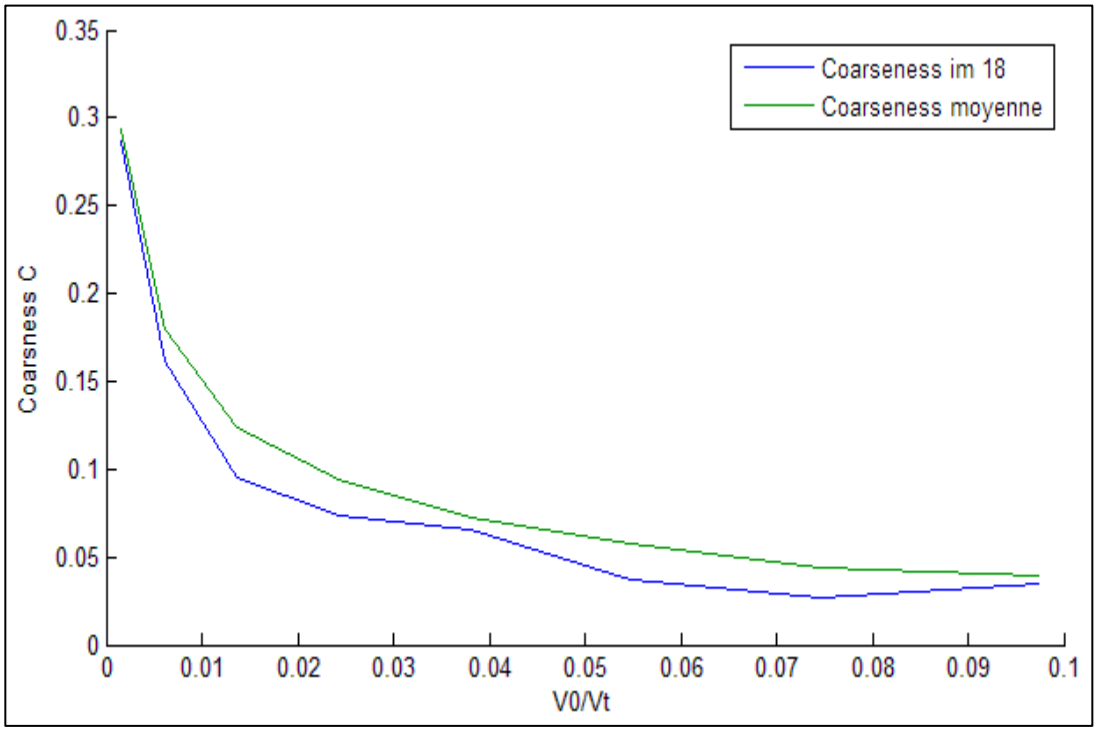

Appendix 1 : Coarseness for overlapping samples

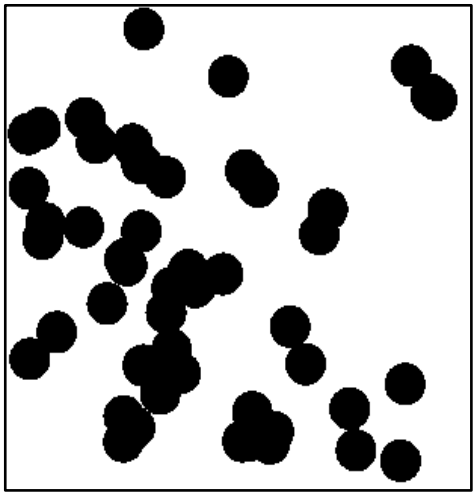

$\boldsymbol{k} = 15.14\ GPa$

$\boldsymbol{k_{average}} = 16.49\ GPa$

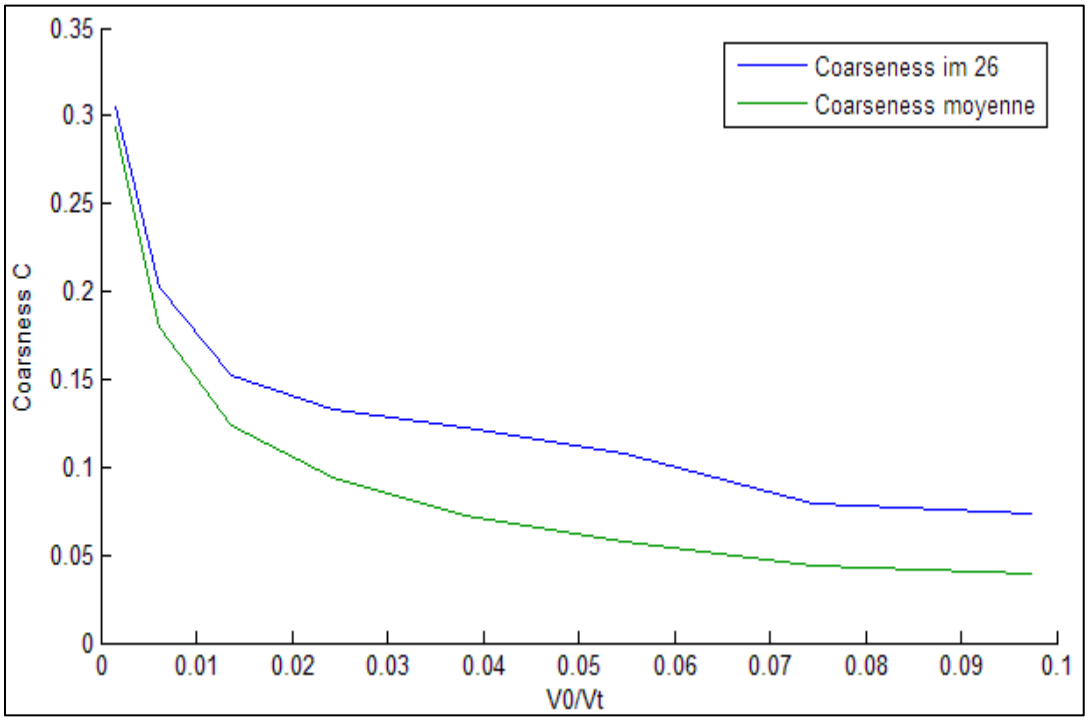

Appendix 1 : Coarseness for overlapping samples

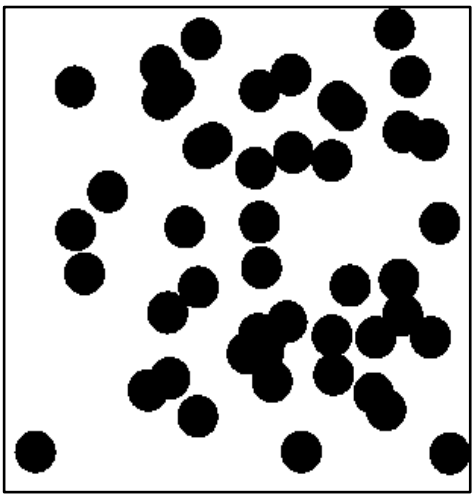

$\boldsymbol{k} = 17.94\ GPa$

$\boldsymbol{k_{average}} = 16.49\ \ GPa$

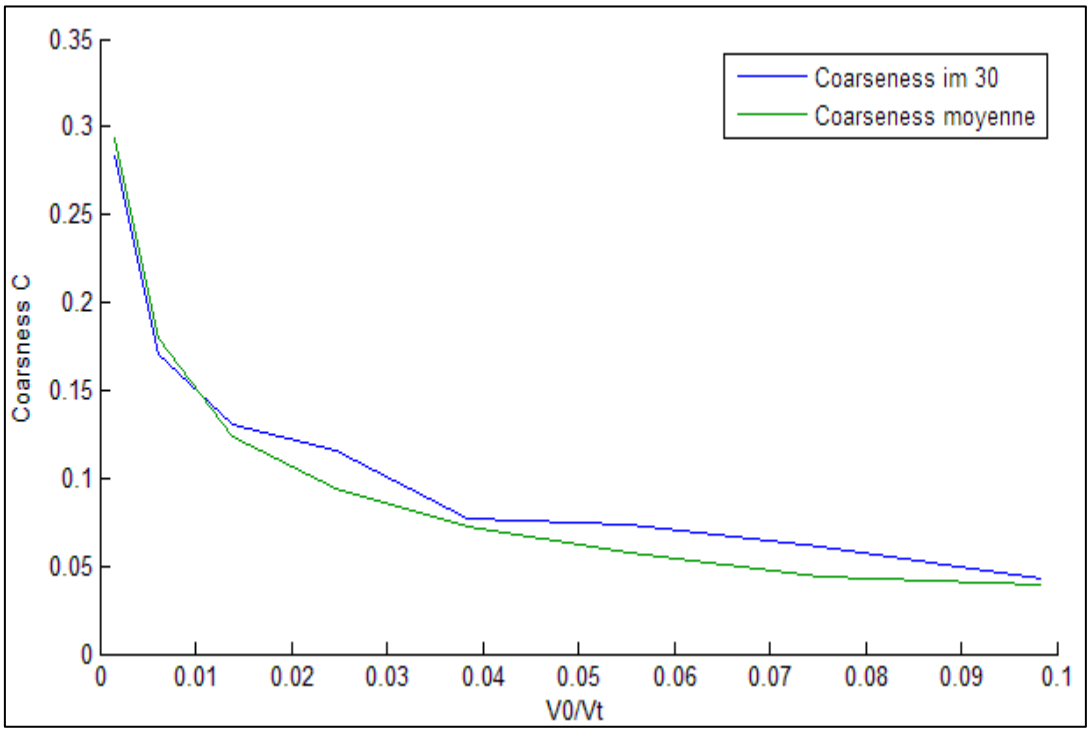

Appendix 1 : Coarseness for overlapping samples

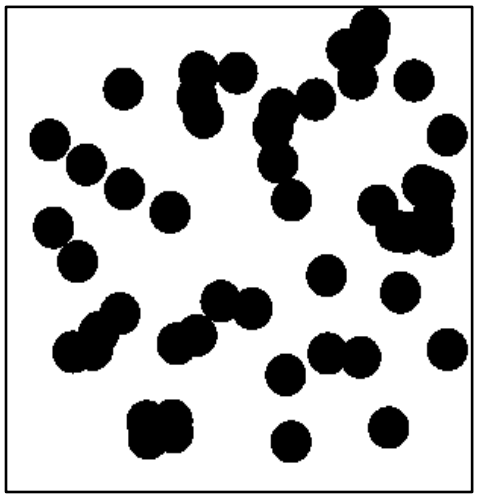

$\boldsymbol{k} = 17.97\ GPa$

$\boldsymbol{k_{average}} = 16.49\ \ GPa$

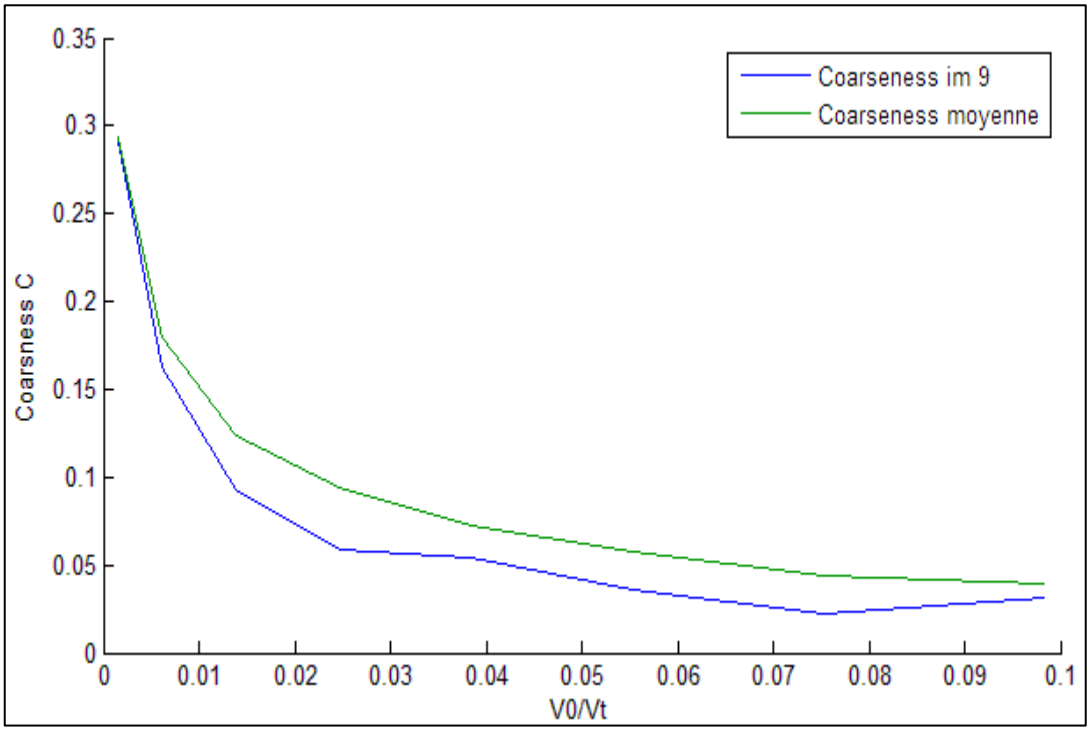

Appendix 1 : Coarseness for overlapping samples

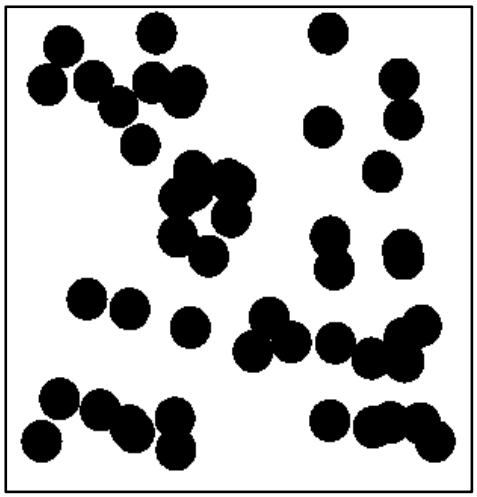

$\boldsymbol{k} = 17.59\ GPa$

$\boldsymbol{k_{average}} = 16.49\ \ GPa$

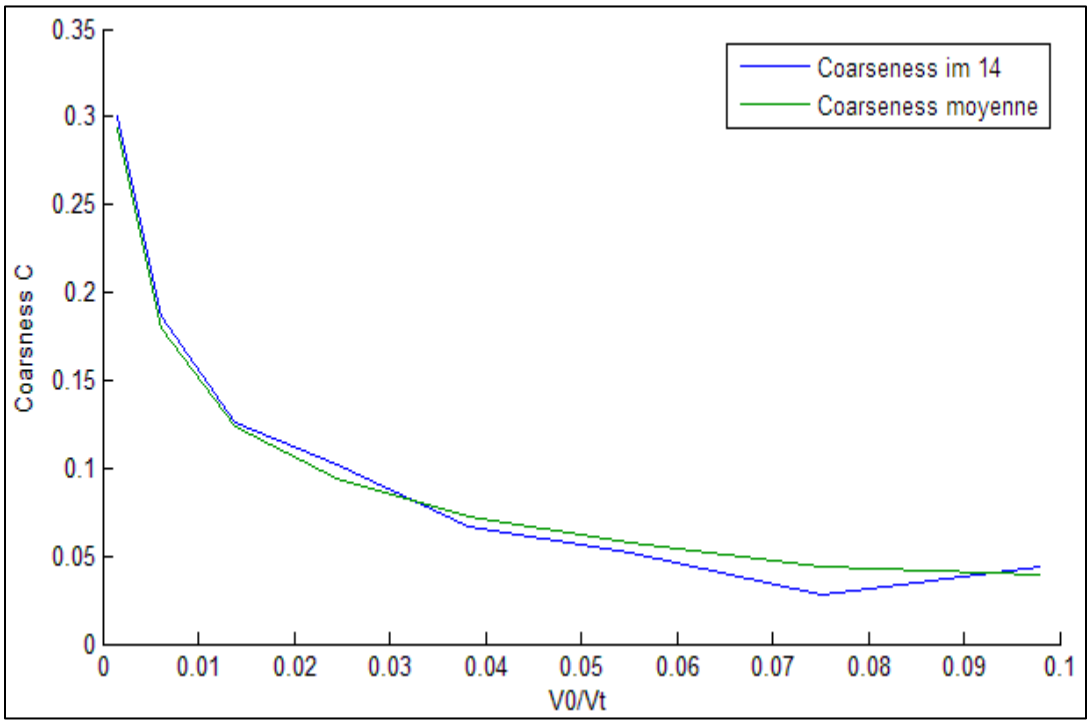

Appendix 1 : Coarseness for overlapping samples

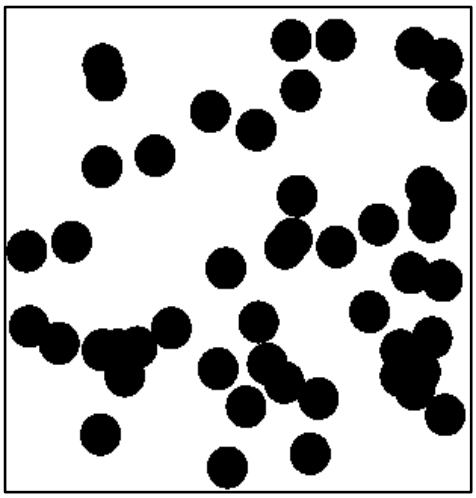

$\boldsymbol{k} = 17.79\ GPa$

$\boldsymbol{k_{average}} = 16.49\ \ GPa$

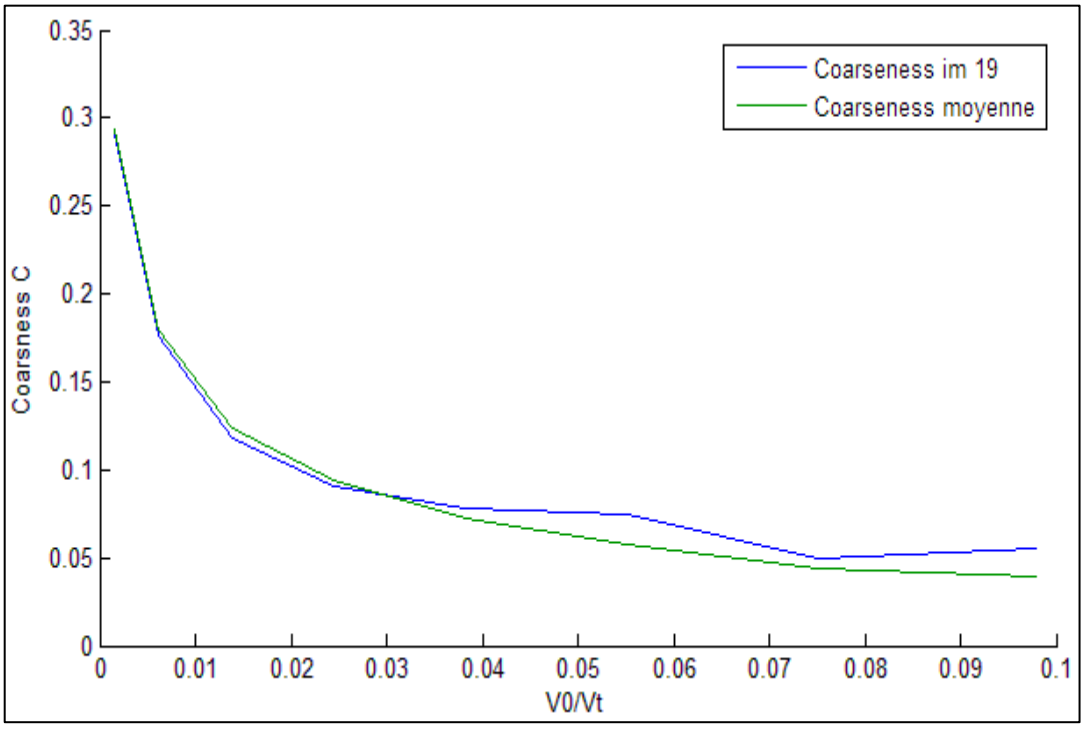

Appendix 1 : Coarseness for overlapping samples

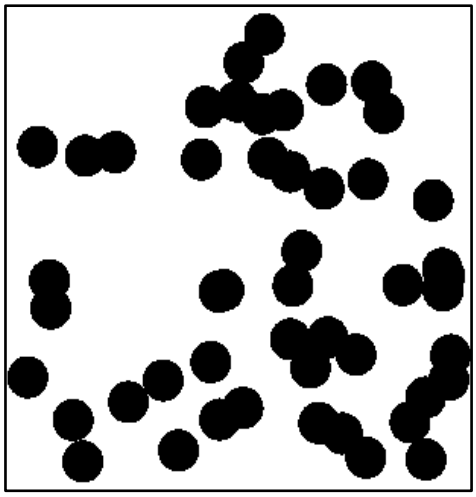

$\boldsymbol{k} = 18.61\ GPa$

$\boldsymbol{k_{average}} = 16.49\ \ GPa$

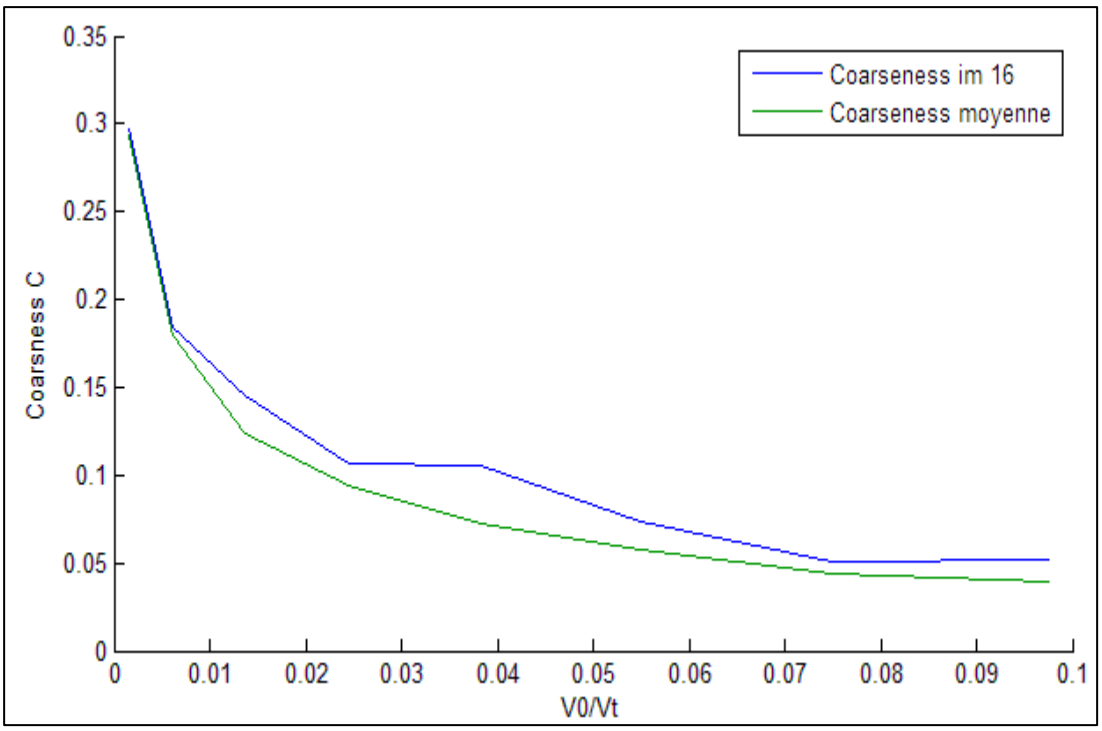

Appendix 1 : Coarseness for overlapping samples

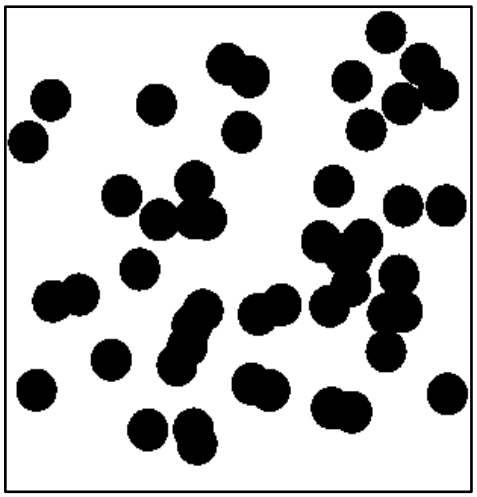

$\boldsymbol{k} = 17.99\ GPa$

$\boldsymbol{k_{average}} = 16.49\ \ GPa$

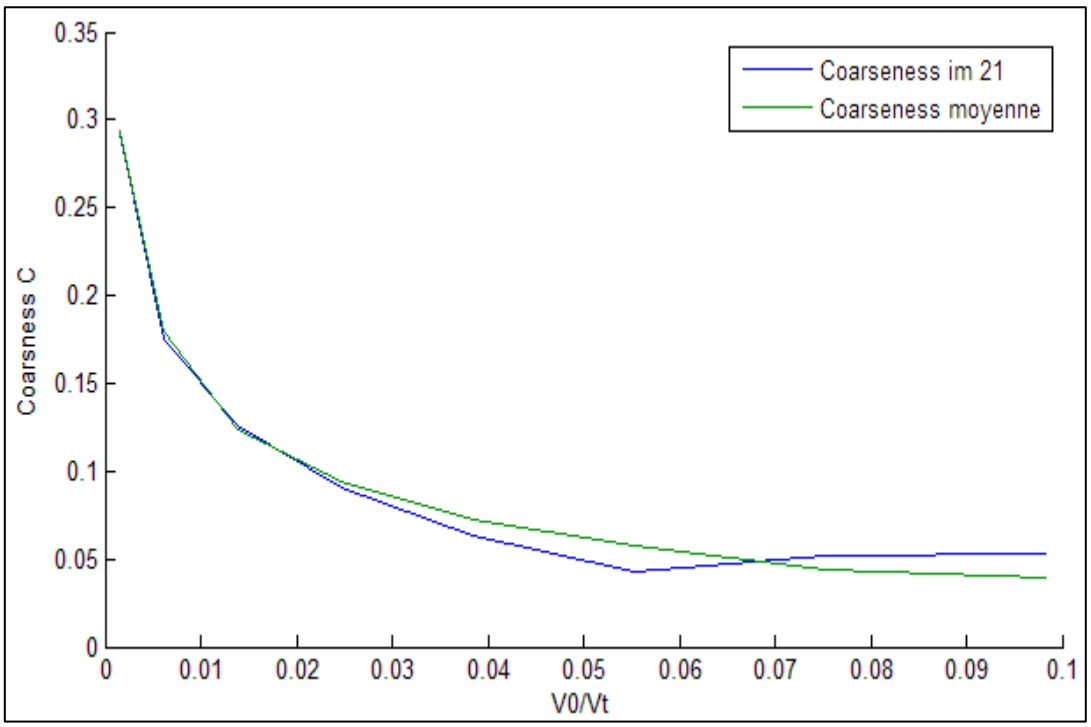

Appendix 1 : Coarseness for non-overlapping samples

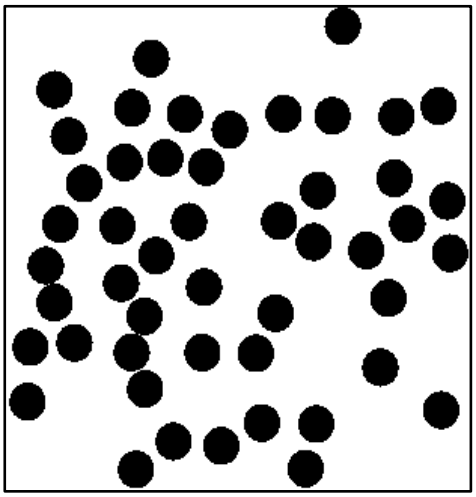

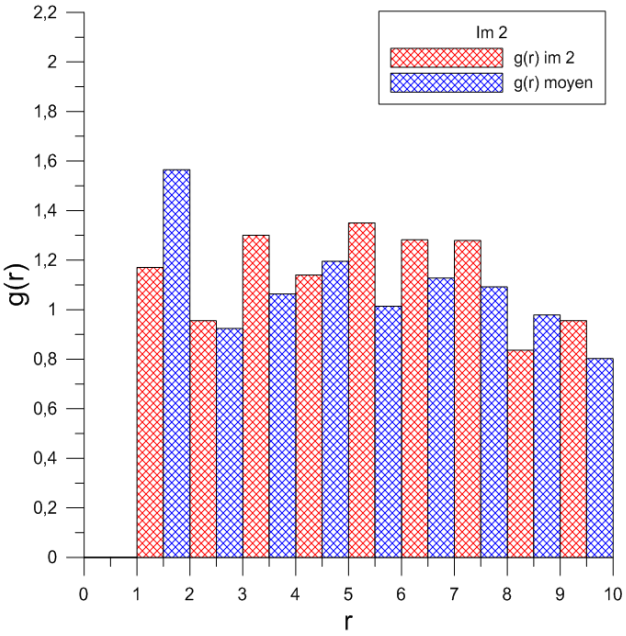

$\boldsymbol{k} = 14.61\ GPa$

$\boldsymbol{k_{average}} = 15.22\ \ GPa$

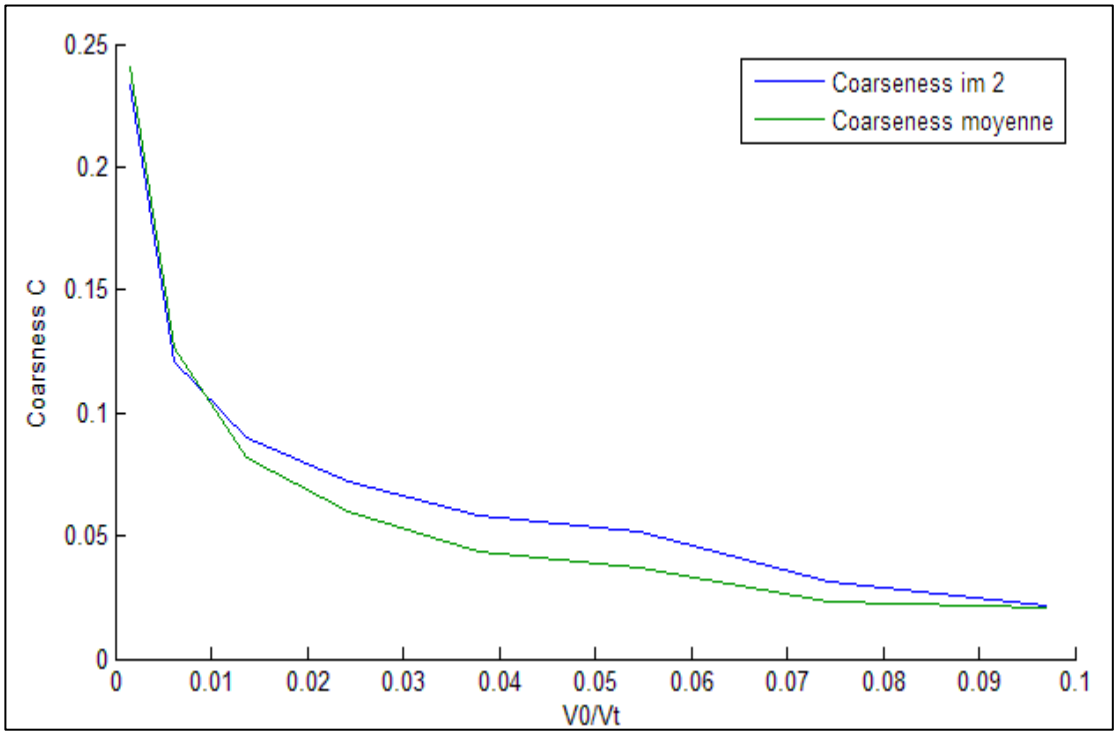

Appendix 1 : Coarseness for non-overlapping samples

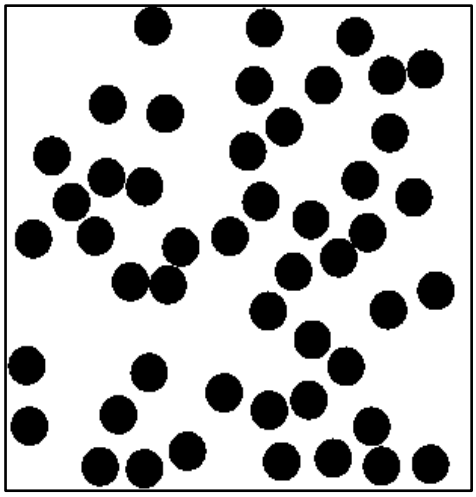

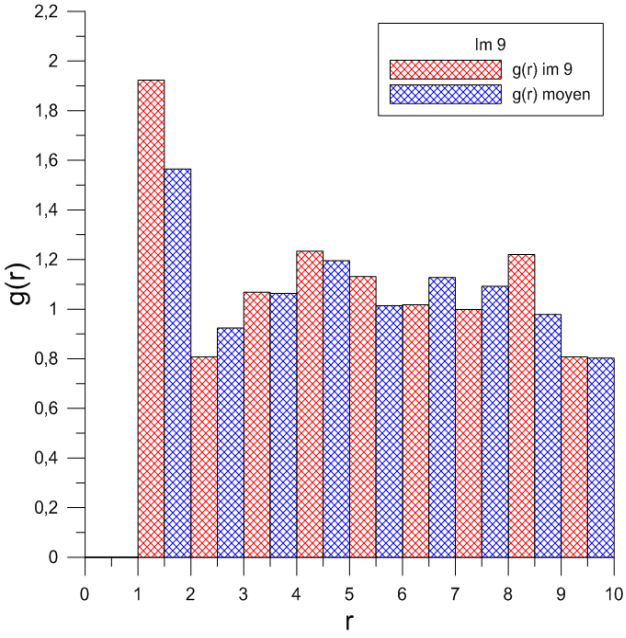

$\boldsymbol{k} = 15.81\ GPa$

$\boldsymbol{k_{average}} = 15.22\ \ GPa$

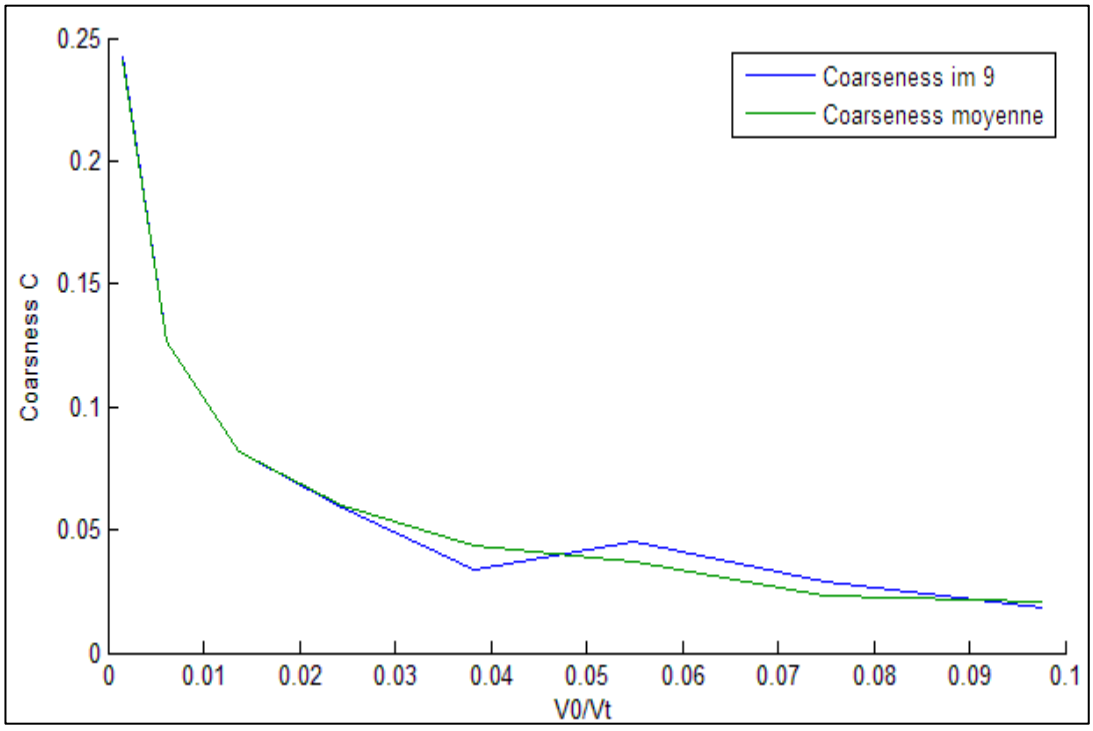

Appendix 1 : Coarseness for non-overlapping samples

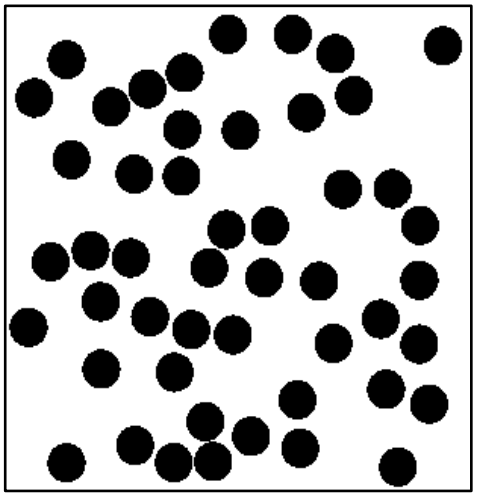

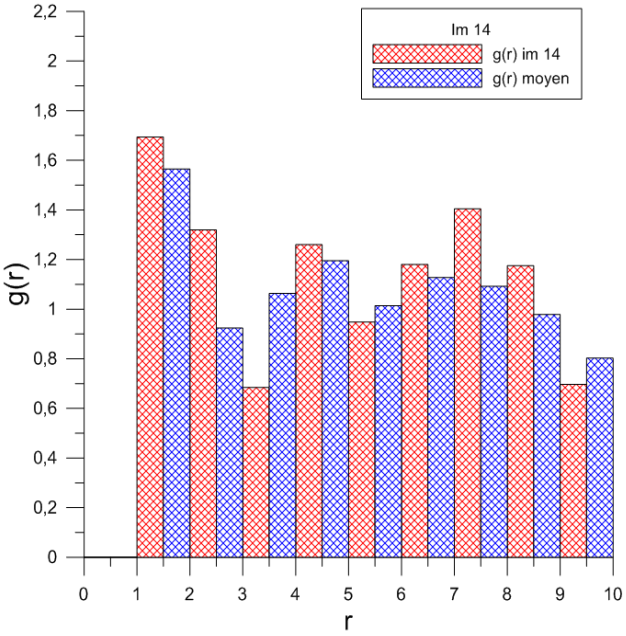

$\boldsymbol{k} = 15.85\ GPa$

$\boldsymbol{k_{average}} = 15.22\ \ GPa$

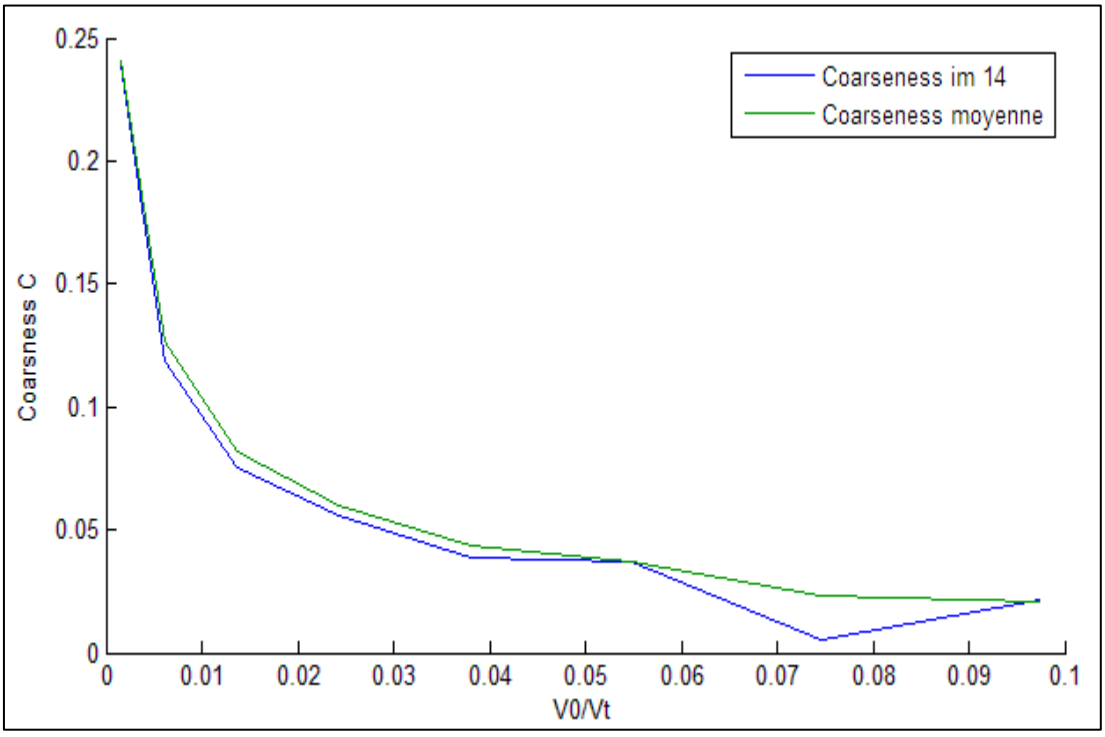

Appendix 1 : Coarseness for non-overlapping samples

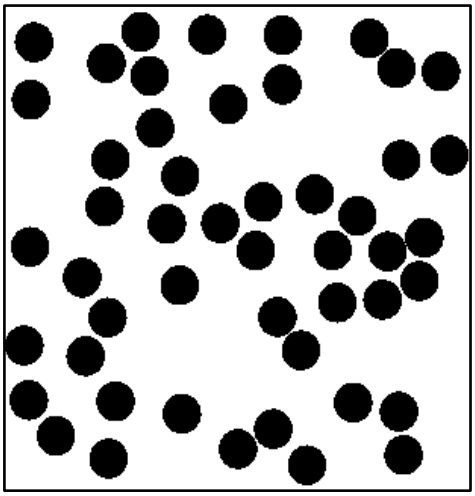

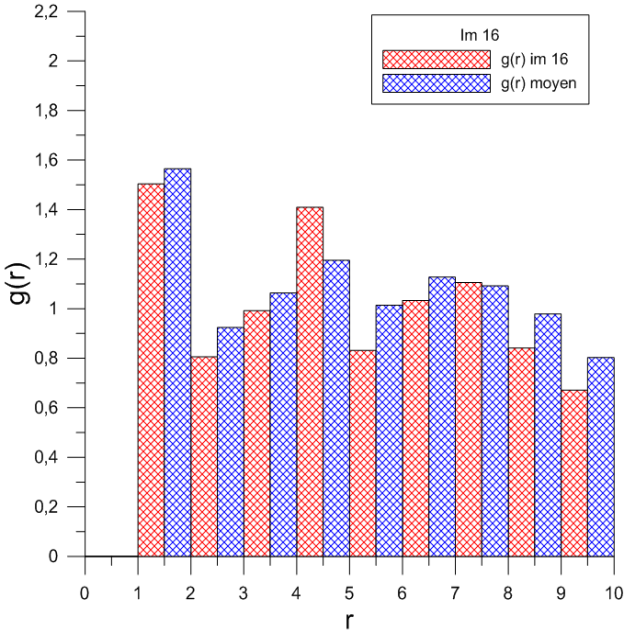

$\boldsymbol{k} = 16.15\ GPa$

$\boldsymbol{k_{average}} = 15.22\ \ GPa$

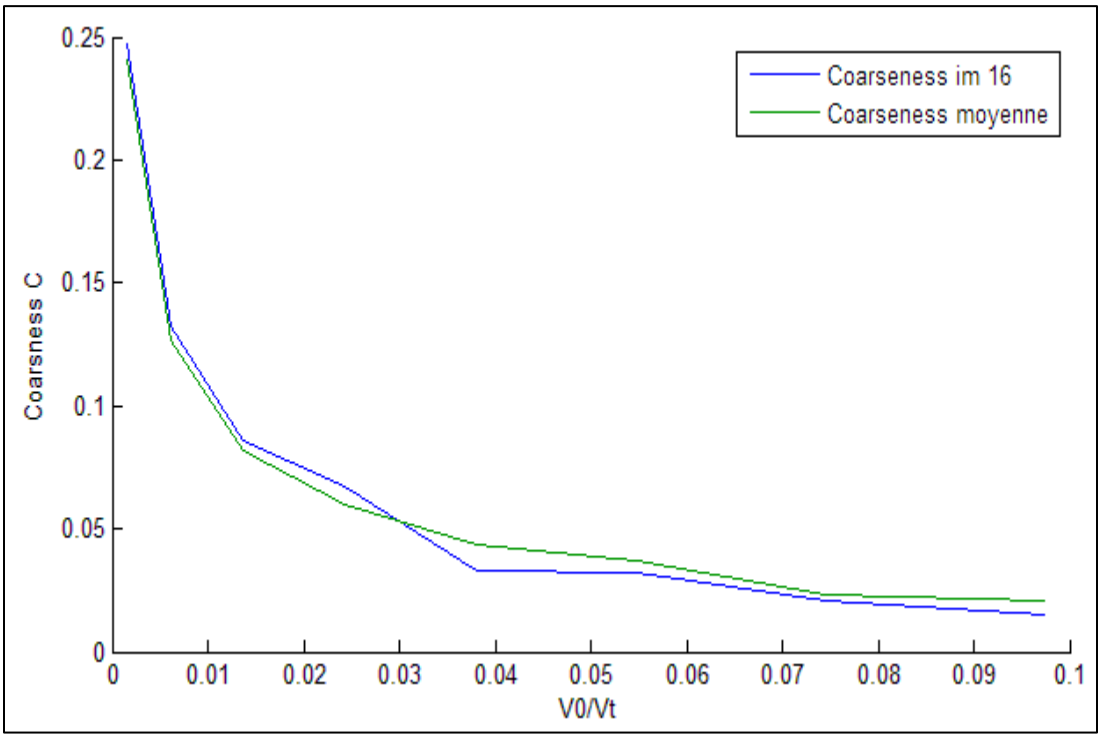

Appendix 1 : Coarseness for non-overlapping samples

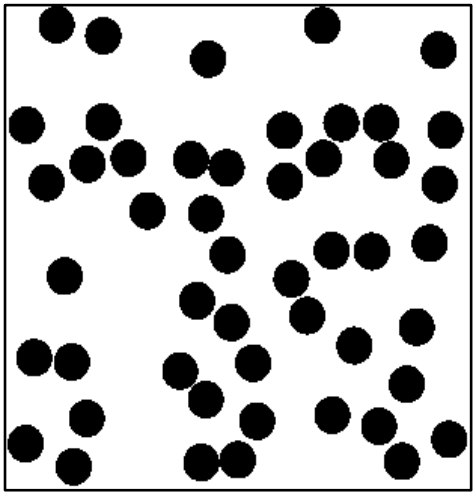

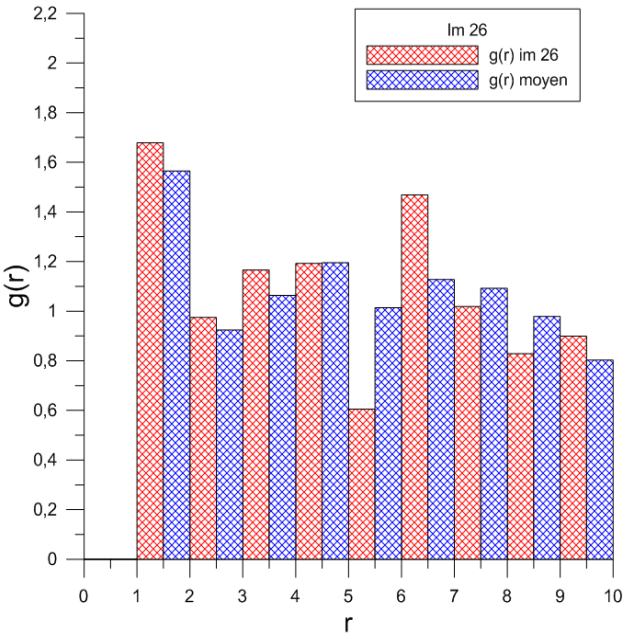

$\boldsymbol{k} = 14.52\ GPa$

$\boldsymbol{k_{average}} = 15.22\ \ GPa$

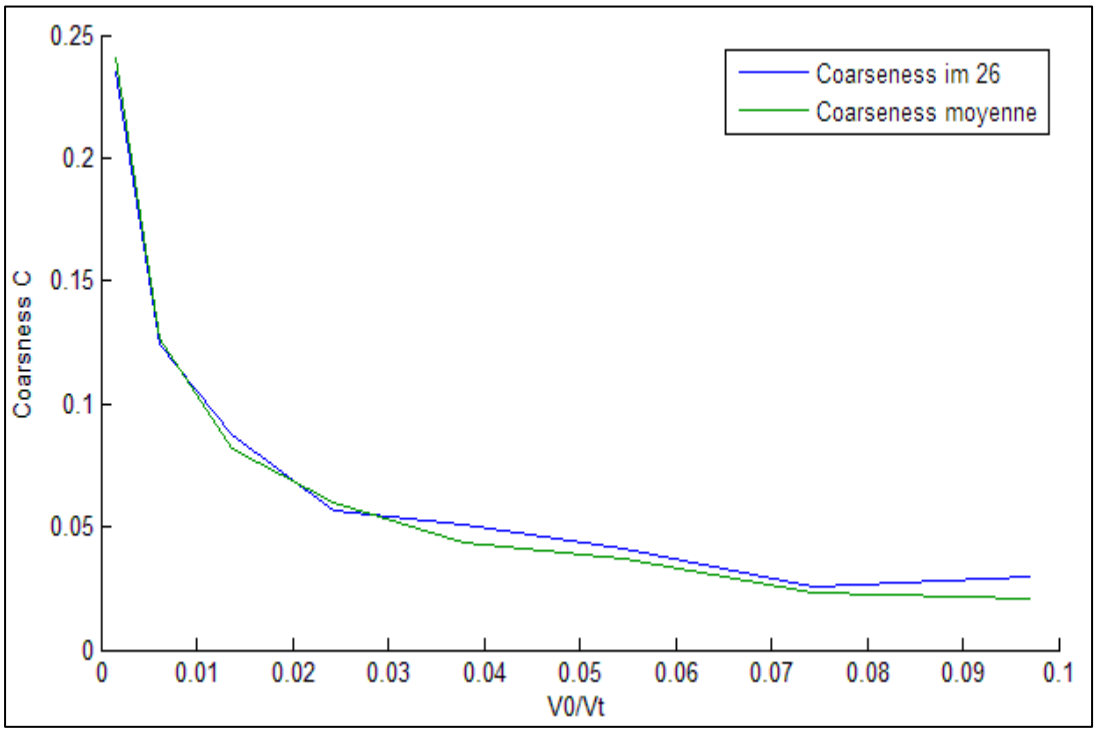

Appendix 1 : Coarseness for non-overlapping samples

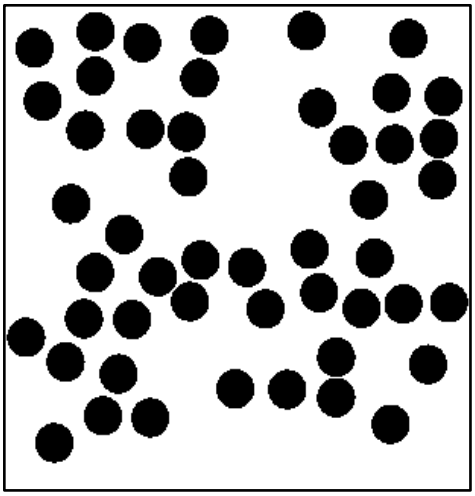

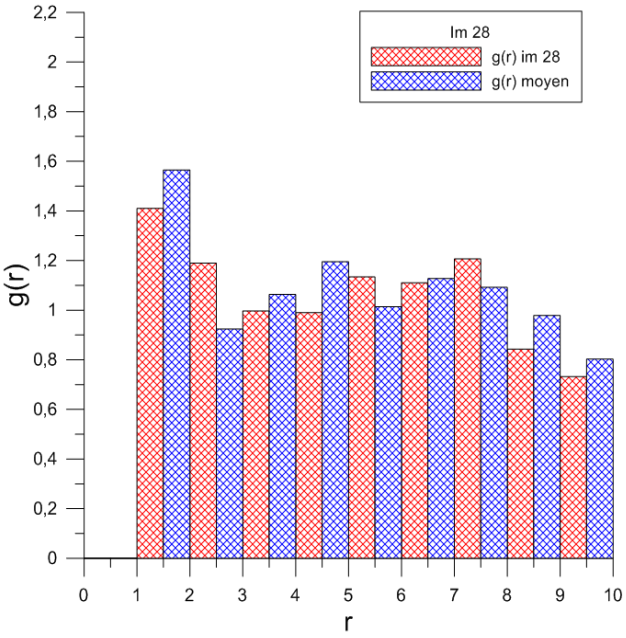

$\boldsymbol{k} = 16.85\ GPa$

$\boldsymbol{k_{average}} = 15.22\ \ GPa$

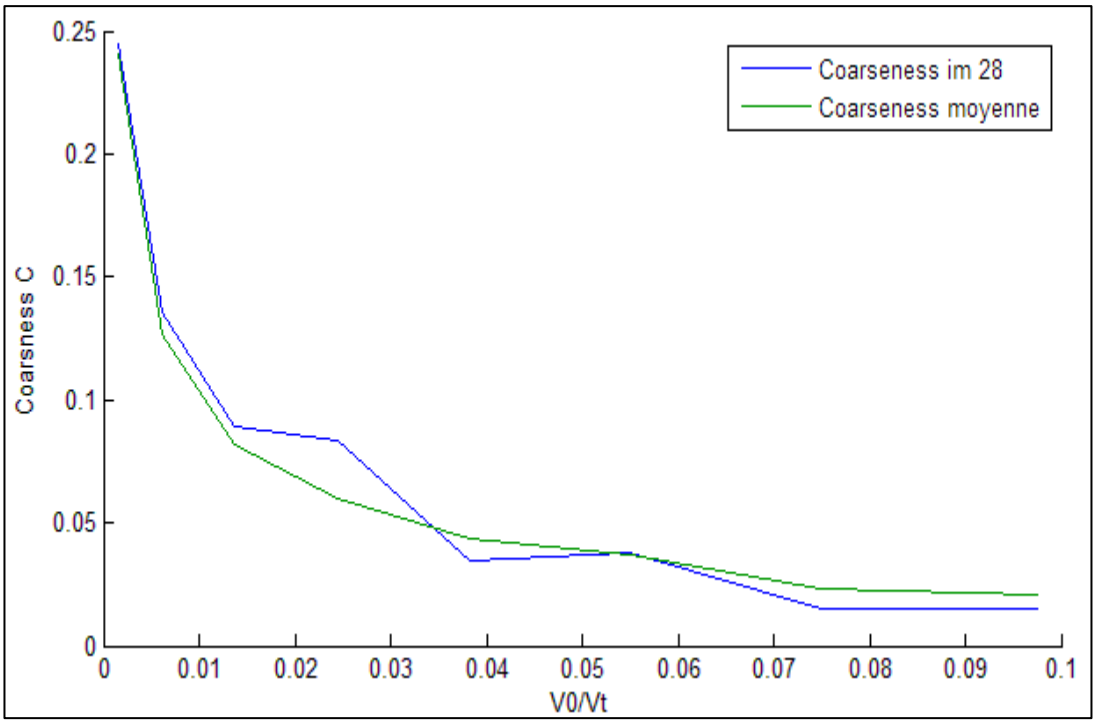

Appendix 1 : Coarseness for non-overlapping samples

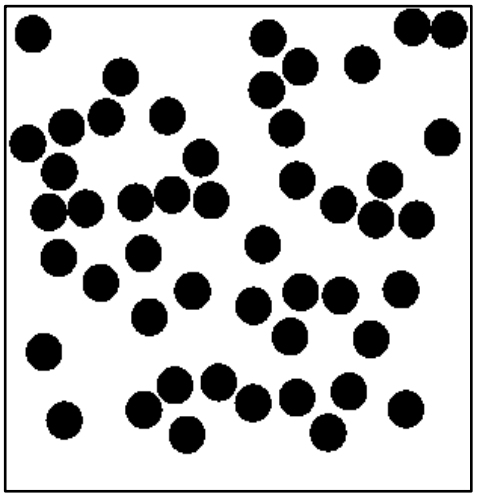

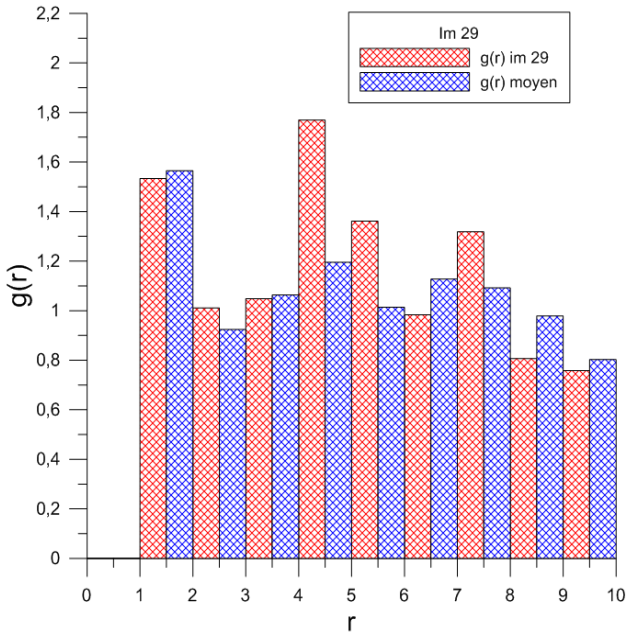

$\boldsymbol{k} = 14.48\ GPa$

$\boldsymbol{k_{average}} = 15.22\ \ GPa$

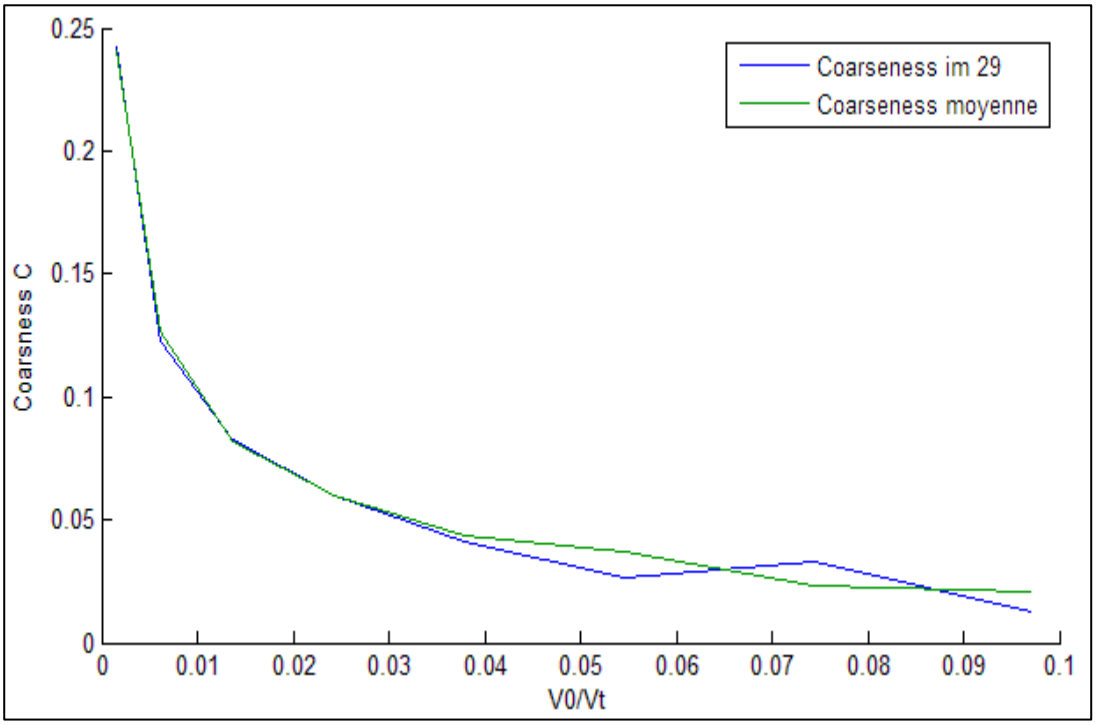

Appendix 2

The following histograms of local bulk and shear moduli were evaluated for the sample below:

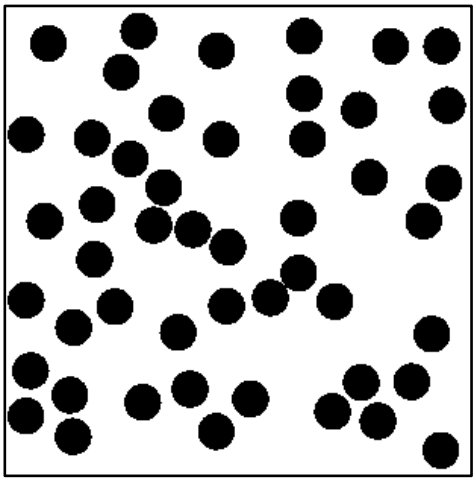

Non-overlapping image sample of $V_f = 24.36\%$

This study was carried out for different contrasts.

Appendix 2: Histograms of local values of bulk modulus for different contrasts

Contraste 1.1

$$C(0) = 0.0165\ GPa^2$$

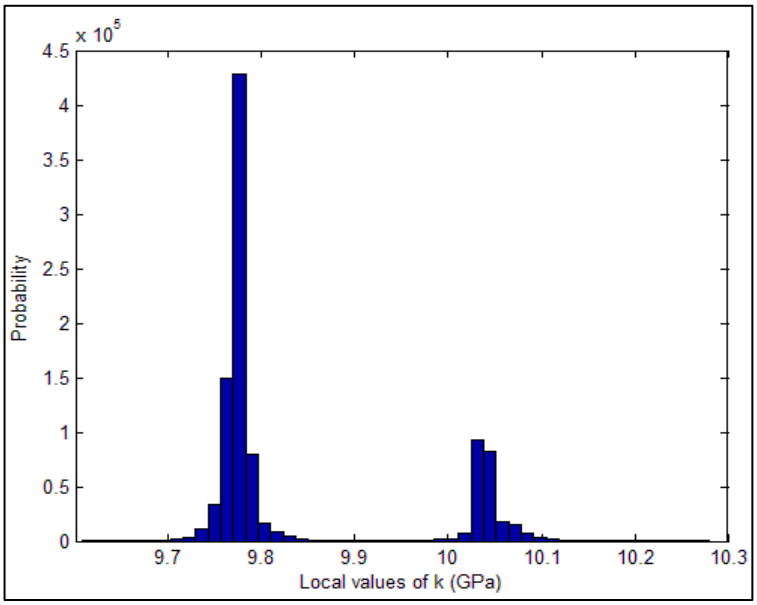

Contraste 1.5

$$C(0) = 0.3112 GPa^2$$

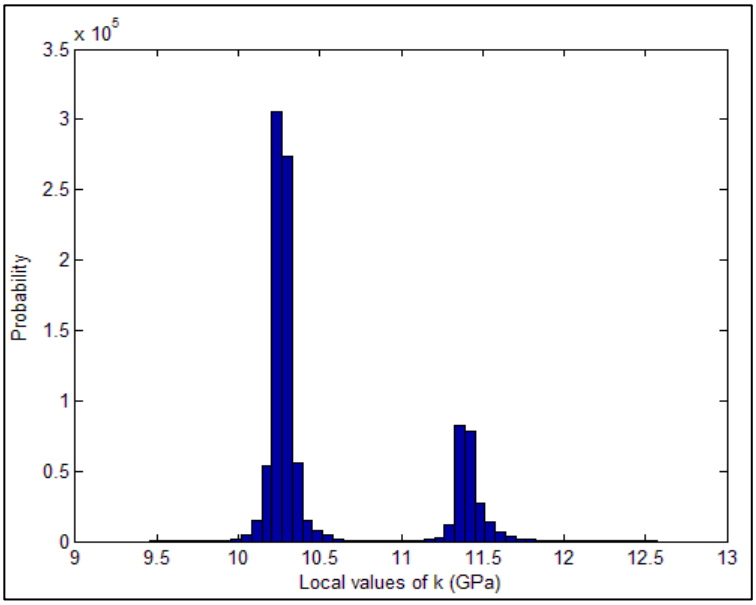

Contraste 2

$$C(0) = 0.9255 GPa^2$$

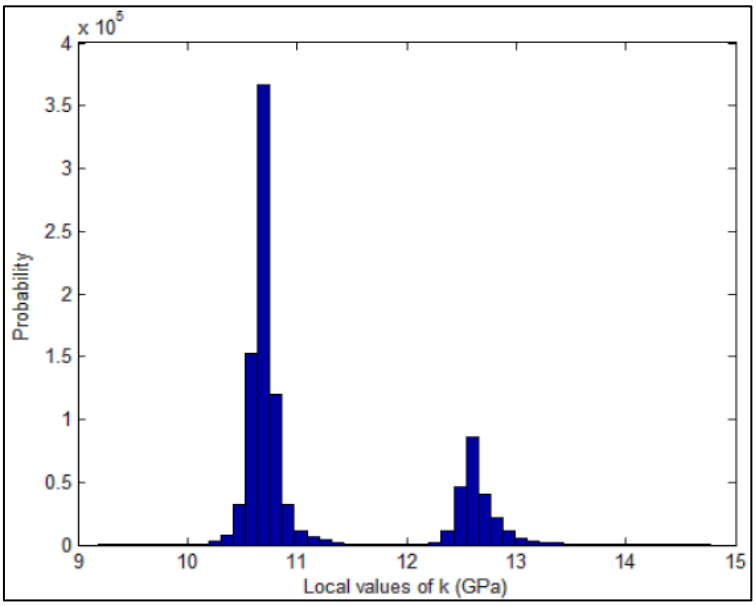

Contraste 5

$$C(0) = 4.6655\ GPa^2$$

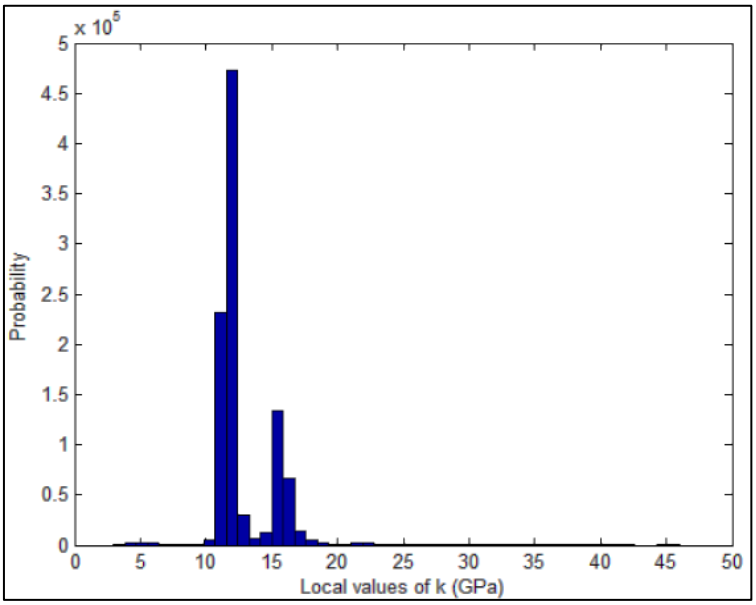

Contraste 10

$$C(0) = 8.6297 Pa^2$$

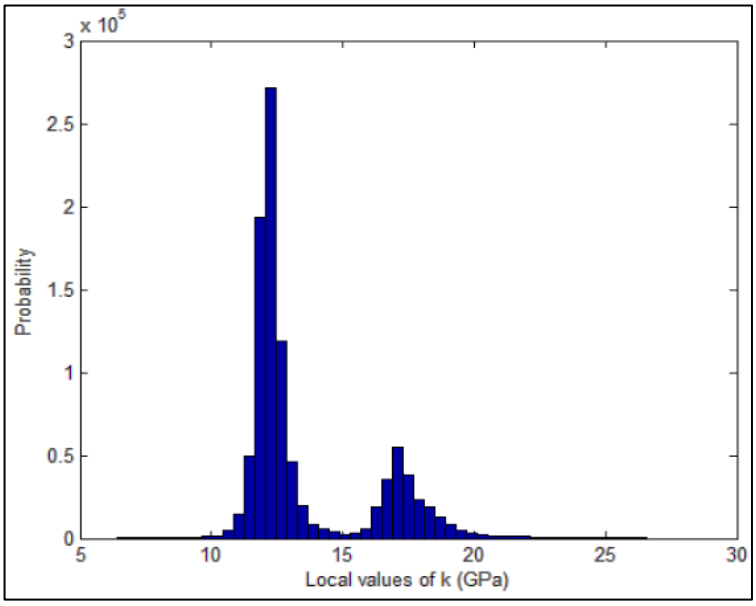

Contraste 30

$$C(0) = 14.6582\ GPa^2$$

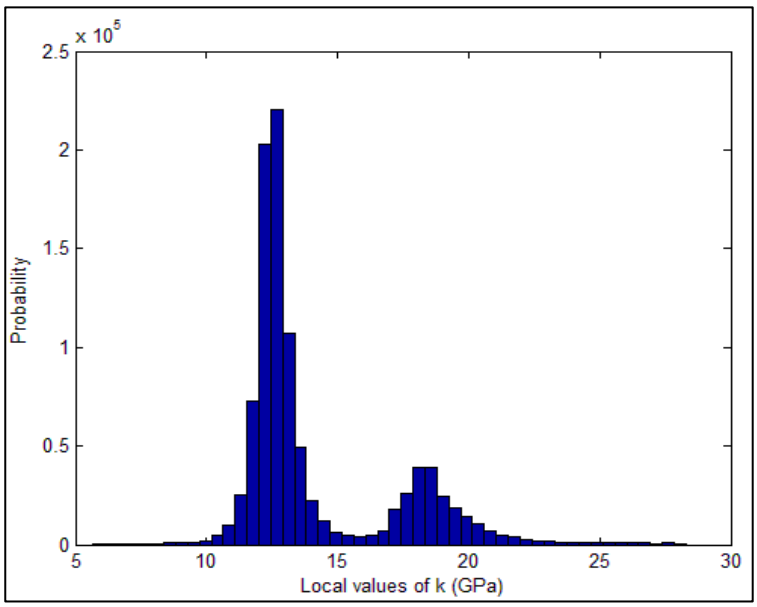

Contraste 60

$$C(0) = 19.0002\ GPa^2$$

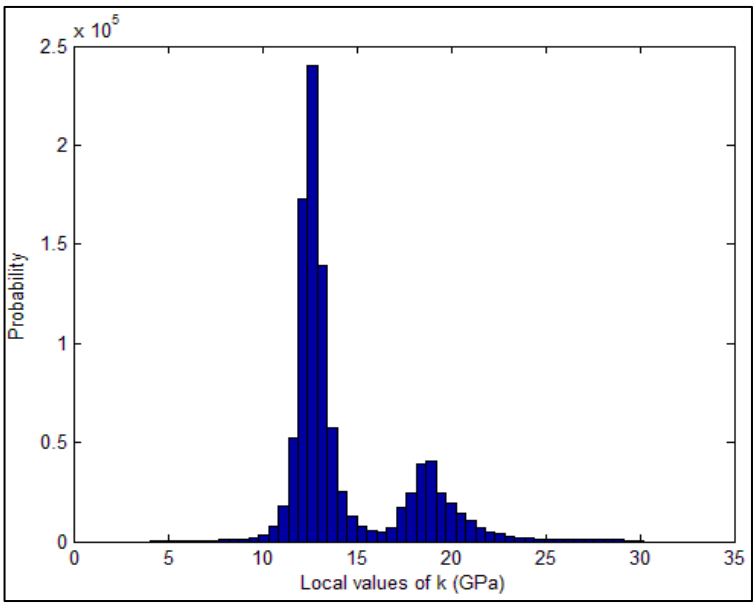

Contraste 85

$$C(0) = 21.6511\ GPa^2$$

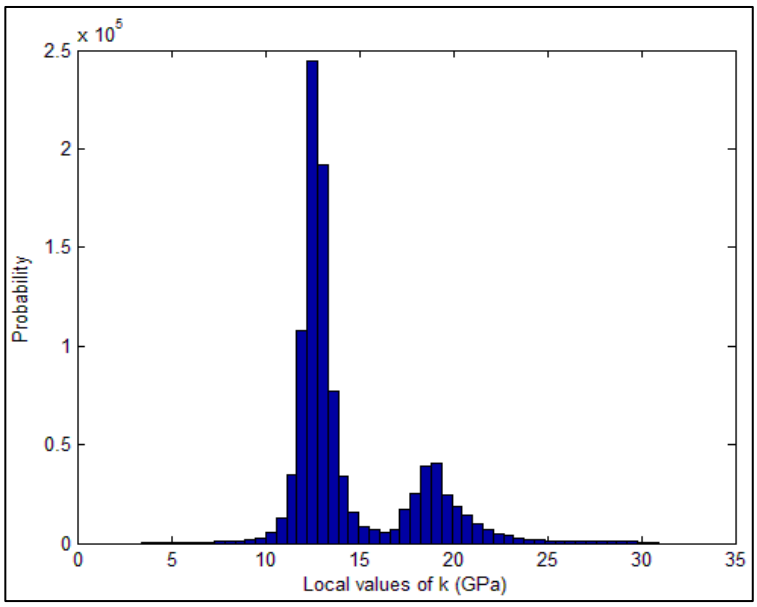

Contraste 100

$$C(0) = 24.0719\ GPa^2$$

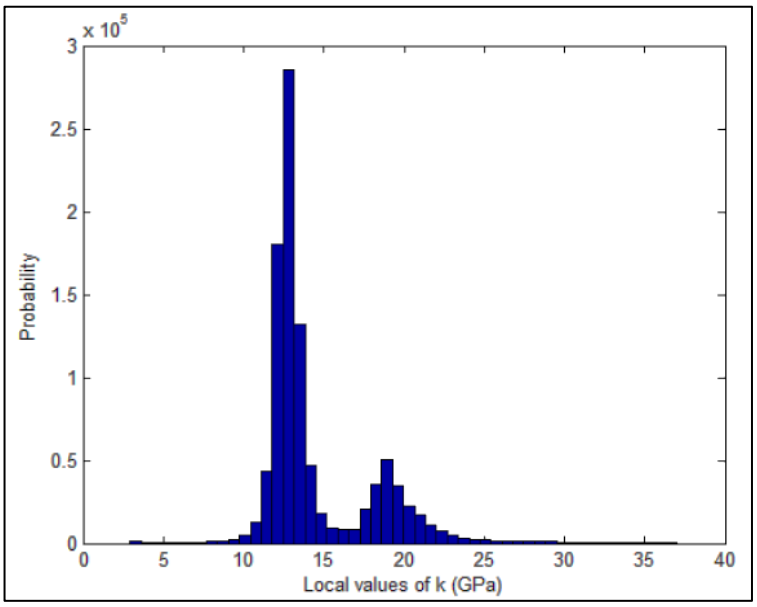

Contraste 1.01

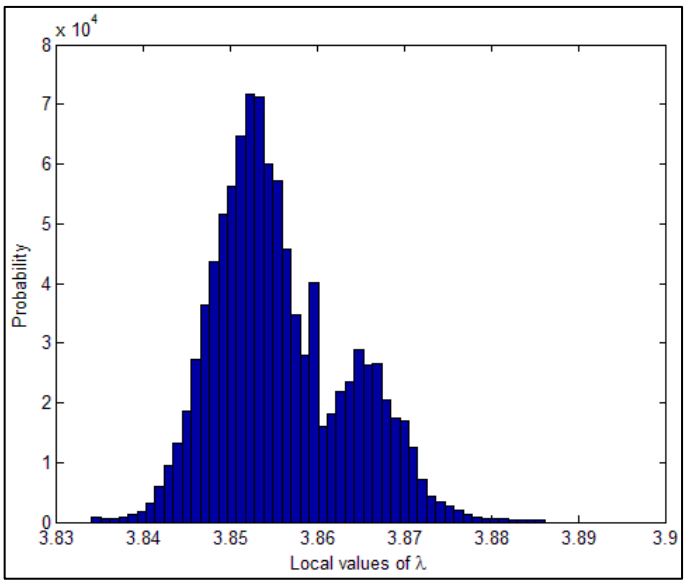

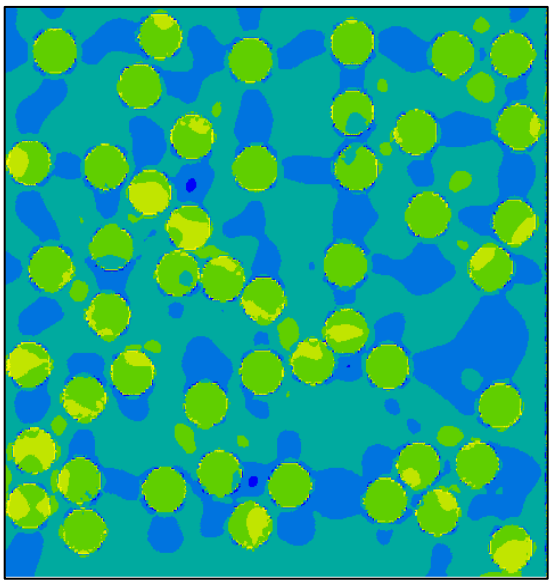

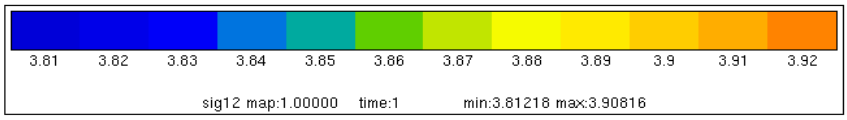

Contraste 1.1

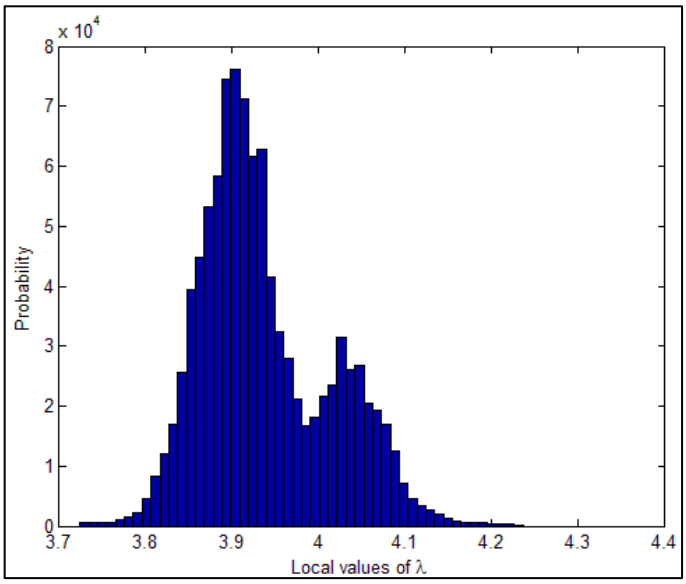

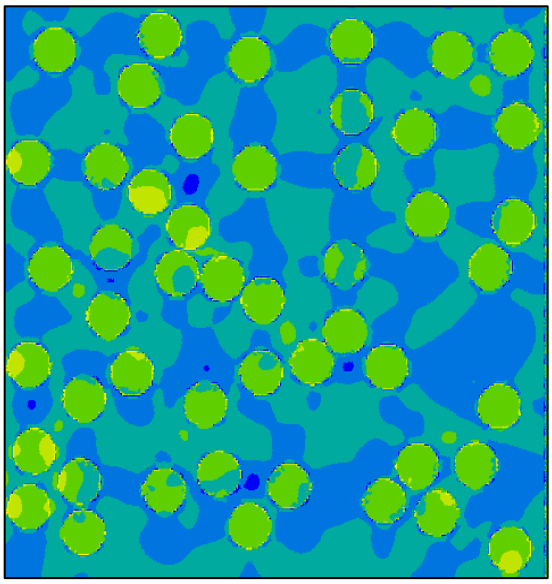

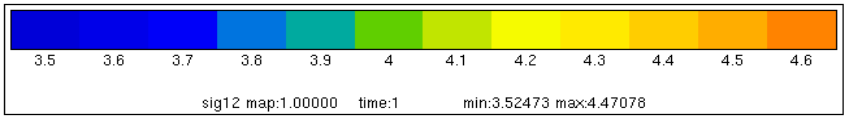

Appendix 2: Histograms of local values of shear modulus for different contrasts

Contraste 1.5

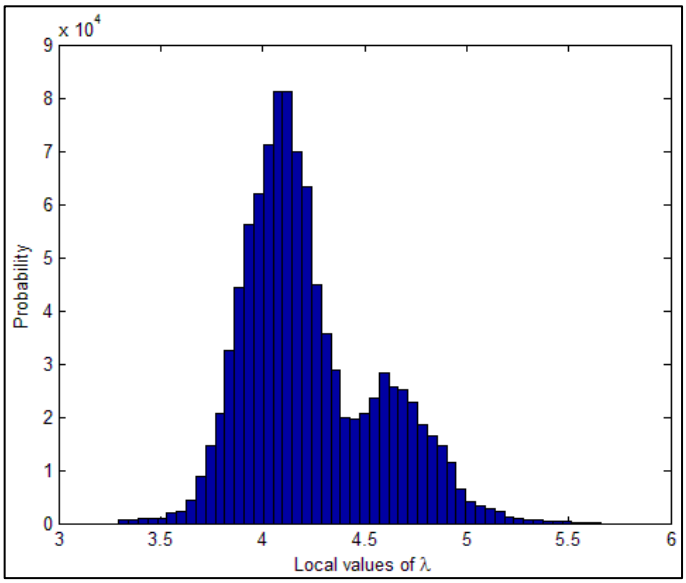

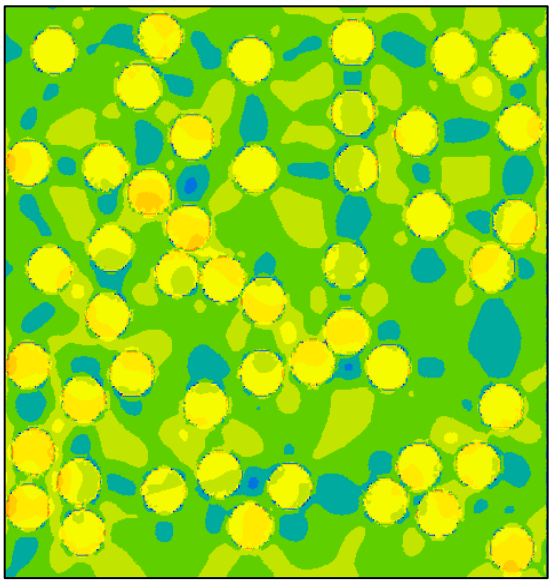

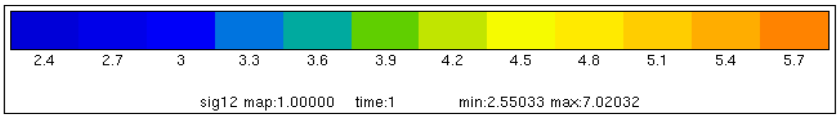

Contraste 2

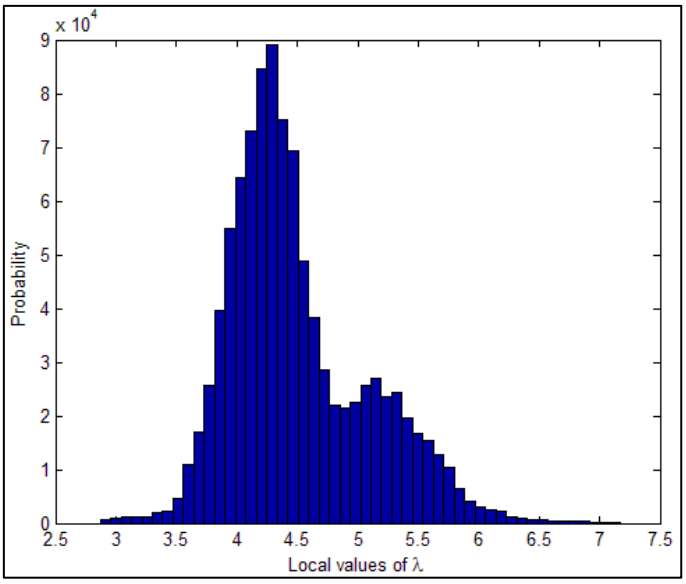

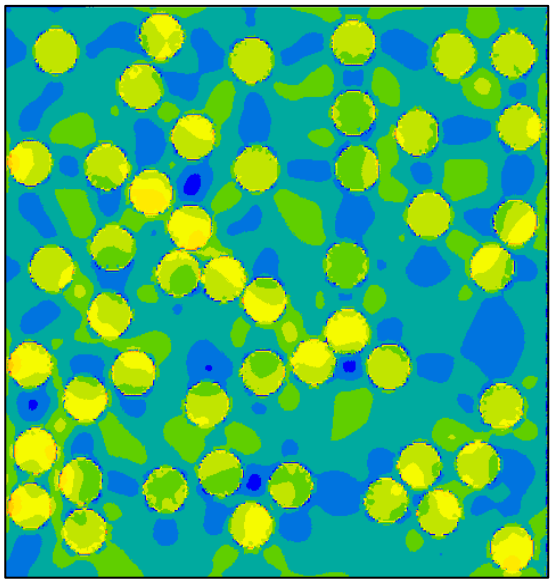

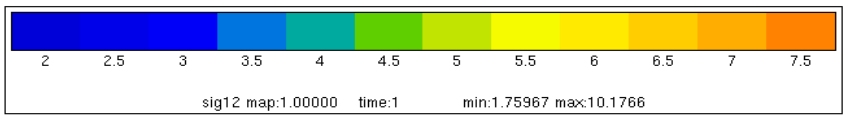

Appendix 2: Histograms of local values of shear modulus for different contrasts

Contraste 10

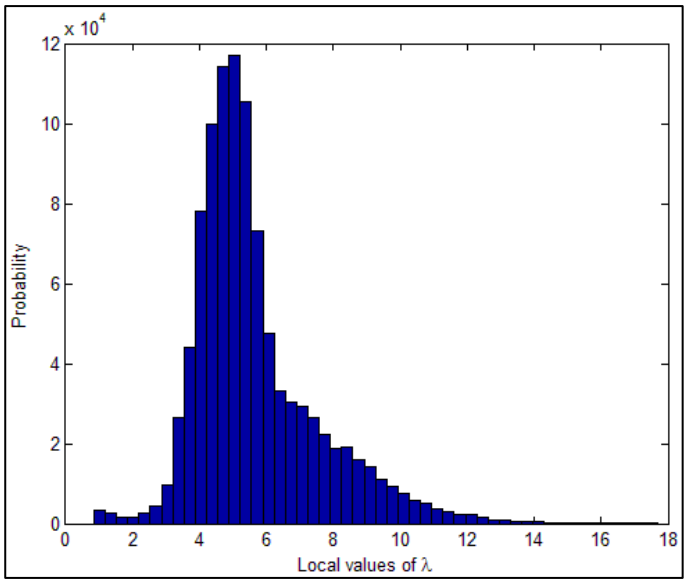

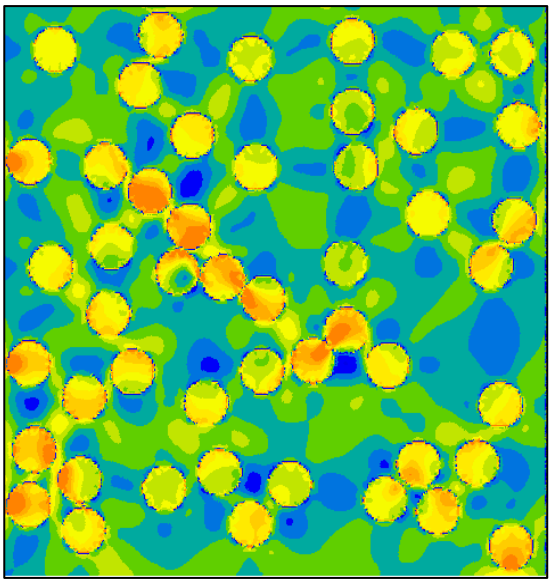

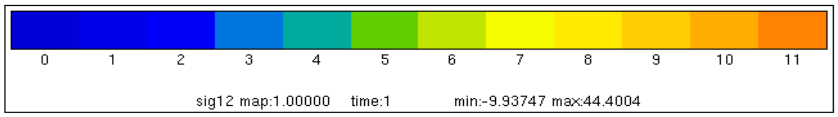

Contraste 30

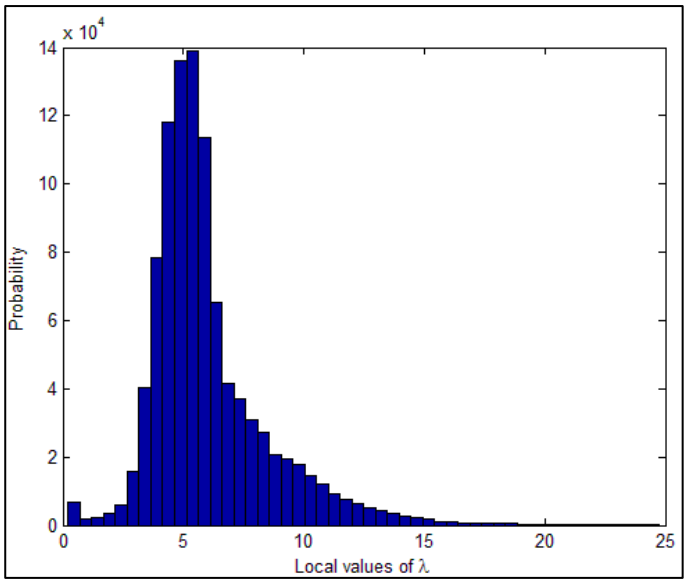

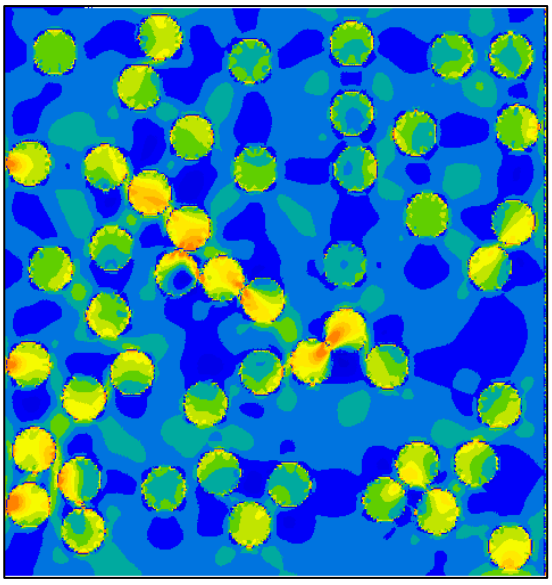

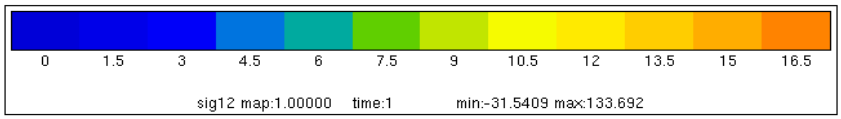

Appendix 2: Histograms of local values of shear modulus for different contrasts

Contraste 60

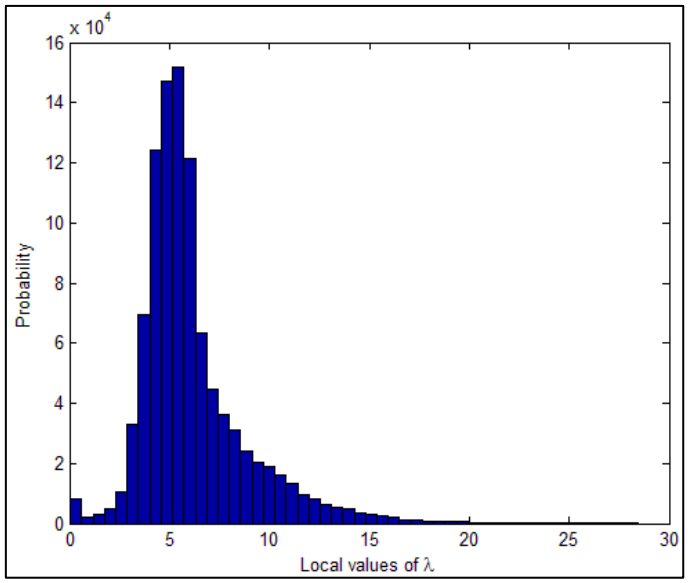

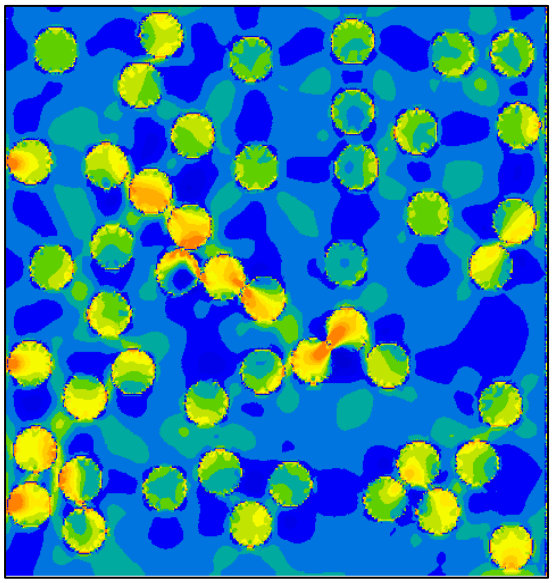

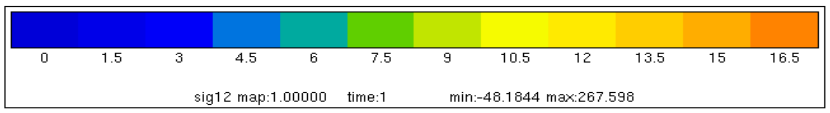

Contraste 85

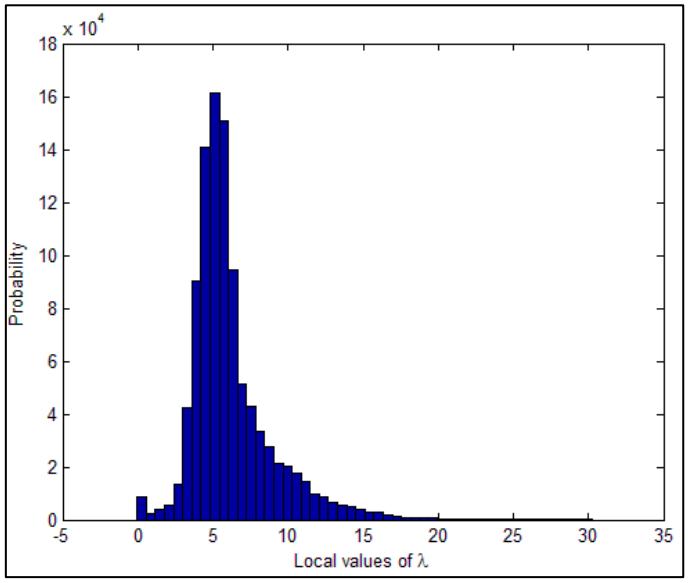

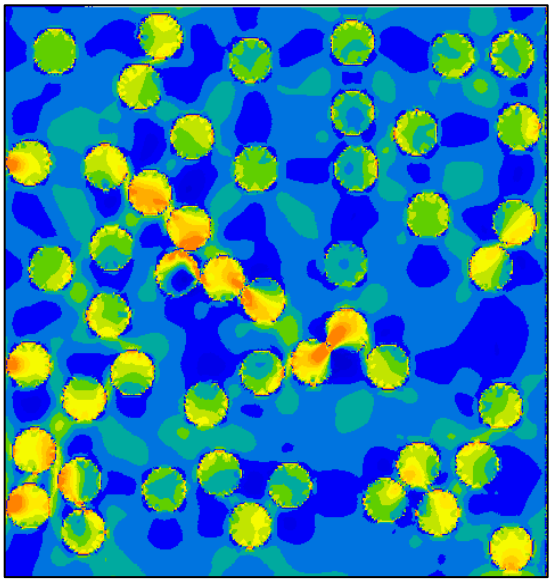

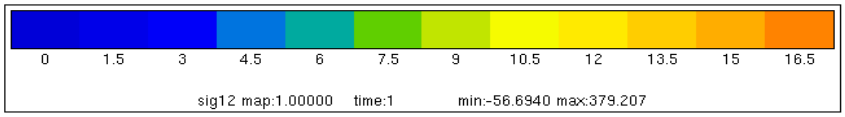

Contraste 100

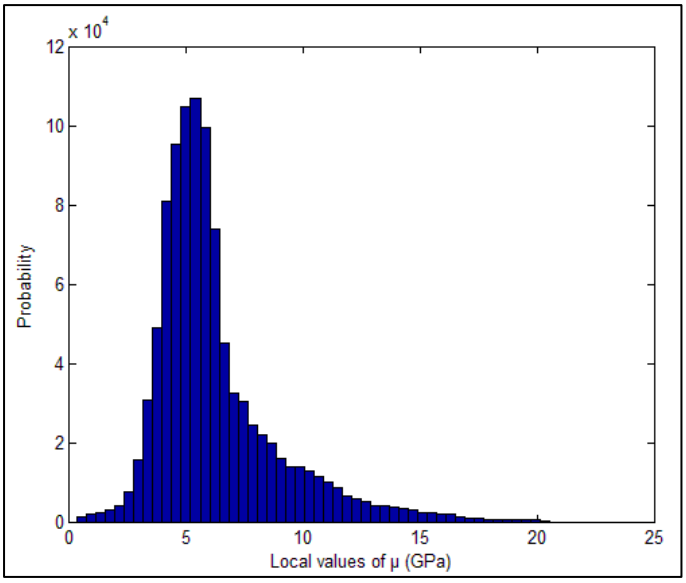

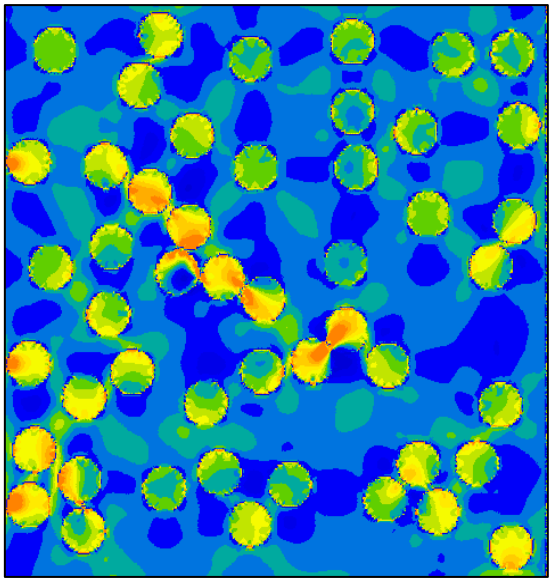

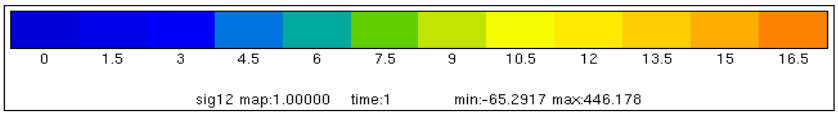

Refrences

Adda-Bedia *et al.* (2008) [M. Adda-Bedia *et al.*, Solution of the Percus-Yevick equation for hard disks, 2008, The Journal of Chemical Physics 128, 184508].

Beicha *et al.* (2016) [D. Beicha *et al.,* Effective transverse elastic properties of unidirectional fiber reinforced composites, 2016, Mechanics of Materials 102, 47–53].

Beran (1965) [M. J. Beran, Use of the Vibrational Approach to Determine Bounds for the Effective Permittivity in Random Media, 1965, Il Nuovo Cimento, Vol.XXXVIII, N. 2].

Beran and Molyneux (1966) [M. J. BERAN and J. MOLYNEUX, Use of classical variational principles to determine bounds for the effective bulk modulus in heterogeneous media, 1966, Quarterly of Applied Mathematics, Vol. 24, No. 2, pp. 107-118].

Beran and Silnutzer (1971) [M. J. Beran and N. R. Silnutzer, Electrical, Thermal and Magnetic Properties of Fiber Reinforced Materials, 1971, J. Composite Materials, Vol. 5, p. 246].

Berryman and Milton (1988) [J. G. Berryman and G. W. Milton, Microgeometry of random composites and porous media, 1988, J. Phys. D: Appl. Phys. 21 87].

Bertsimas and Tsitsilis (1993) [D. Bertsimas and J. Tsitsilis, Simulated annealing, 1993, Statistical science, Vol. 8, No. 1, 10-15].

Botsis *et al.* (1994) [J. Botsis, C. Beldica and D. Zhao, 1994, Int. J. Fract. 68, 375].

Boyer *et al.* (1995) [D. Boyer *et al.,* Percus–Yevick-like integral equation for random sequential addition, 1995, J. Chem. Phys., Vol. 103, No. 4, 22 July].

Bravo and Santos (1993) [S. Y. Bravo and A. Santos, A heuristic radial distribution function for hard disks, 1993, J. Chem. Phys., Vol. 99, No. 3].

Brown (1955) [Solid Mixture Permittivities. The Journal of chemical physics, 1955, Volume 23. N. 8].

Bruggeman (1935) [D. A. G. Bruggeman, Calculation of various physics constants in heterogenous substances I Dielectricity constants and conductivity of mixed bodies from isotropic substances, 1935, Ann. Phys. 24, 636–664].

Budiansky (1965) [B. Budiansky, On the elastic moduli of some heterogeneous materials, 1965, Journal of the Mechanics and Physics of Solids, vol. 13, pp 223–227].

Buryachenko (2006) [V. A. Buryachenko, Micromechanics of Heterogeneous Materials, 2006].

Cavalcante and Pindera (2014) [Marcio A. A. Cavalcante and Marek-Jerzy Pindera, Generalized FVDAM Theory for Periodic Materials Undergoing Finite Deformations, 2014, Journal of Applied Mechanics, Vol. 81 / 021005-1].

Christensen (1980) [R. M. Christensen, A Nonlinear Theory of Viscoelasticity for Application to Elastomers, 1980, J. Appl. Mech. 47, 762].

Corson (1974) [P. B. Corson, Correlation functions for predicting properties of heterogeneous materials. IV. Effective thermal conductivity of two-phase solids, 1974, Journal of Applied Physics 45, 3180].

Drugan and Willis (1996) [W. J. Drugan and J. R., Willis, A micromechanics-based nonlocal constitutive equation and estimates of representative volume element size for elastic composites, 1996, J. Mech. Phys. Solids 44, 497–524].

Einstein (1906) [A.Einstein. Eine neue bestimmung der molek¨uldimensionen. Ann. Physik., 19:289–306].

Elsayed and McCoy (1973) [M. A. Elsayed and J. J. McCoy, Effective Physical Properties of Composite Materials, 1973, J. Composite Materials, Vol. 7, p. 466].

Erchiqui (2017) [F. Erchiqui, Application of genetic and simulated annealing algorithms for optimization of infrared heating stage in thermoforming process, 2017, Applied Thermal Engineering 128, 1263-1272].

Eshelby (1956) [J. D. Eshelby, Progress in solid state physics (Seitz and Turnbull,Eds.), 1956, Academic Press, New York and London, Vol.3, p.79].

Eshelby (1957) [J. D. Eshelby, The force on an elastic singularity, 1957, Phil.Trans.A, 244, 87].

Eshelby (1957) [J. D. Eshelby, The determination of elastic field of an ellipsoidal inclusion, and related problems, 1957, Proceedings of the Royal Society A: Mathematical, Physical and Engineering Sciences, 241(1226), 376–396].

Flory (1969) [Paul J Flory, Statistical Mechanics of Chain Molecules, 1969, Interscience Publishers, NY.].

Gibiansky and Torquato (1993) [L. V. Gibiansky and G. W. Milton, Link between the conductivity and elastic moduli of composites, 1993, Phys. Rev. Lett. 71, 2927-2930].

Gibiansky and Torquato (1994) [L. V. Gibiansky and G. W. Milton, Rigorous link between the conductivity and elastic moduli of fiber-reinforced composite materials, 1994, Trans. Roy. Sot. London A (in press)].

Gibiansky and Torquato (1995) [L. V. Gibiansky and S. Torquato, Geometrical parameter bounds on the effective moduli of composites, 1995, J. Mech. Phys. Solids, Vol. 43, No. 10, pp. 1587-1613, 1995].

Gibiansky and Torquato (1996a) [L. V. Gibiansky and G. W. Milton, Connection between the conductivity and elastic moduli of isotropic composites, 1996a, Proc. R. Sot. Lond. A 452,253-283].

Gitman (2007) [I. M. Gitman *et al*., Representative volume: Existence and size determination, 2007, Eng. Fract. Mech. 74, 2518–2534].

Halpin and Tsai (1967) [J. Halpin J. and S. Tsai, Environmental factors in composite materials design, 1967, US air force technical report. AFML TR 67–423].

Hansen and McDonald (2006) [J.P Hansen and I.R. McDonald, Theory of Simple Liquids, 3rd edition (2006)].

Hashin and Shtrikman (1962) [Z. Hashin and S. Shtrikman, A Variational Approach to the Theory of the Effective Magnetic Permeability of Multiphase Materials, 1962, J. Appl. Phys. 33, 3125–3131].

Hashin and Shtrikman (1963) [Z. Hashin and S. Shtrikman, A variational approach to the theory of the elastic behaviour of multiphase materials, 1963, J. Mech. Phys. Solids 11, 127–140].

Hashin (1970) [Z. Hashin, Mechanics of Composite Materials (Edited by F. W. Wend& H. Liebowitz and N. Perrone) Pergamon, New York (1970)].

Hashin (1983) [Z. Hashin, Analysis of Composite Materials - A Survey, 1983, Journal of Applied Mechanics, vol. 50, pp 481–505].

Hill (1963) [R. Hill, Elastic Properties of Reinforced Solids: Some Theoretical Principles, 1963, Journal of the Mechanics and Physics of Solids, vol. 11, pp 357–372].

Hill (1965) [R. Hill, A Self-Consistent Mechanics of Composite Materials, 1965, Journal of the Mechanics and Physics of Solids, vol. 13, pp 213–222].

Hinrichsen (1986) [E. L. Hinrichsen *et al*., Geometry of random sequential adsorption, 1986, Volume 44, Issue 5–6, pp 793–827].

Islam (2016) [Mohammad R. Islam, Microstructure modeling of random composites with cylindrical inclusions having high volume fraction and broad aspect ratio distribution, 2016, Computational Materials Science 125:309-318].

Jeulin (2016) [D. Jeulin, Power Laws Variance Scaling of Boolean Random Varieties, 2016, Methodol Comput Appl Probab (2016) 18:1065–1079].

Jiang *et al.* (2010) [Q. Jiang, Y. Brunet and T. Kanit, Microstructure of the solid phase in fluidized beds for non-Stokes regimes, 2010, European Journal of Mechanics B/Fluids 29 435_441].

John and Kamal (1999) [K. John R. and S. Kamal, A Hybrid Experimental/Theoretical Scattering Model for Dense Random Media, 1999, IEEE Transactions on geoscience and remote sensing, Vol. 37, No. 1, January].

Joslin and Stell (1986) [C.G. Joslin and G. Stell , Bounds on the properties of fiber-reinforced composites, 1986, J. Appl. Phys. 60(5)].

Kanit *et al.* (2003) [T. Kanit *et al*., Determination of the size of the representative volume element for random composites: statistical and numerical approach, 2003, Int. J. Solids Struct. 40, 3647–3679].

Kirkpatrick *et al.* (1983) [S. Kirkpatrick *et al*., Optimization by Simulated Annealing, 1983, Science, New Series, Vol. 220, No. 4598. (May 13, 1983), pp. 671-680.].

Lakhal *et al.* (2019) [L. Lakhal, Y. Brunet and T. Kanit, Evaluation of second-order correlations adjusted with simulated annealing on physical properties of unidirectional non-overlapping reinforced materials (UD Composites)International, 2019, Journal of Modern Physics C, Vol. 30, Nos. 2 & 3 (2019) 1950017].

Lippmann *et al.* (1997) [N. Lippmann *et al*., 3D-finite-element-modelling of microstructures with the method of multiphase elements, 1997, Computational Materials Science 9, 28-35].

Lu and Torquato (1990) [B. Lu and S. Torquato, Local volume fraction fluctuations in heterogeneous media, 1990, 3452 J.Chem. Phys. 93(5).].

Lu and Torquato (1990a) [Binglin Lu and S. Torquato, n-point probability functions for a lattice model of heterogeneous media, 1990, Phys. Rev. B 42, 4453].

Lu and Torquato (1990b) [B. Lu and S. Torquato, $\mathbf{n}$ −point probability functions for a lattice model of heterogeneous media, 1990, Phys. Rev. B 42, 4453].

Maxwell (1873) [J. C. Maxwell, A Treatise on Electricity and Magnetism, I and II, 1873, Oxford University Press].

McCoy (1970) [J. J. McCoy, Recent Advances in Engineering Sciences, 1970, Gordon and Breach, New York, Vol. 5, p. 235].

Metropolis *et al.* (1953) [N. Metropolis *et al*., Equation of state calculations by fast computing machines, 1953, The Journal of Chemical Physics, Vol. 21, No. 6].

Miller (1969) [M. N. Miller, Bounds for effective bulk modulus of heterogeneous materials, 1969, Journal of Mathematical Physics, Volume 10, Issue 11, 1969, Pages 2005-2013].

Miller and Torquato (1991) [C.A. Miller and S. Torquato, Improved bounds on elastic and transport properties of fiber-reinforced composites: Effect of polydispersivity in fiber radius, 1991, J. Appl. Phys. 69(4)].

Milton (1982) [G. W. Milton, Bounds on the Elastic and Transport properties of two-component composites, 1982, J. Mech. Phys. Solids Vol. 30, No. 3, pp. 177-191].

Milton (1984) [G. W. Milton, Correlation of the electromagnetic and elastic properties of composites and microgeometries corresponding with effective medium approximations, 1984, AIP Conf. Proc. 107, 66].

Mori and Tanaka (1973) [T. Mori T. and K. Tanaka, Average Stress in Matrix and Average Elastic Energy of Materials with Misfitting Inclusions, 1973, Acta Metallurgica, vol. 21 n◦ 5, pp 571–574].

Ostoja-Starzewski (1998) [M. Ostoja-Starzewski, Random field models of heterogeneous materials, 1998, Int. J. Solids Struct. 35, 2429–2455].

Percus-Yevick (1958) [J. K. Percus and G. I. Yevick, Analysis of Classical Statistical Mechanics by Means of Collective Coordinates, 1958, Phys. Rev. 110, 1].

Rényi (1958) [A. Rényi, On a one-dimensional problem concerning random space-filling, 1958, Publications of Mathematical Institute of Hungarian Academy of Sciences, 3, 109-127].

Reuss (1929) [A. Reuss, Berechnung der Fließgrenze von Mischkristallen auf Grund der Plastizitätsbedingung für Einkristalle, 1929, ZAMM - Z. Für Angew. Math. Mech. 9, 49–58].

Ricci (1992) [S. M. Ricci, Random sequential adsorption of anisotropic particles II. Low coverage kinetics, 1992, J. Chem. Phys., Vol. 97, No. 7].

Rintoul and Torquato (1997) [Rintoul M. and Torquato S., Reconstruction of the Structure of Dispersions, 1997, Journal Of Colloid And Interface Science 186, 467–476].

Sab (1992) [K. Sab, On the homogenization and the simulation of random materials, 1992, Eur. J. Mech. Solids 11, 585–607.].

Sanei *et al.* (2017) [S. H. R. Sanei *et al*., Characterization, synthetic generation, and statistical equivalence of composite microstructures, 2015, Journal of Composite Materials 0(0) 1–13].

Seaton and Glandt (1986) [N.A. Seaton and E.D. Glandt, Monte Carlo simulation of adhesive disks, 1986, J. Chem. Phys. 84, 4595].

Seyed Hamid Reza *et al.* (2017) [Seyed Hamid Reza S, Ercole J B, David L and Ray S Fetig III, Characterization, synthetic generation, and statistical equivalence of composite microstructures. Journal of Composite Materials 2017; 51(13):1817-1829.]

Terada *et al.* (2000) [K. Terada *et al*., Simulation of the multi-scale convergence in computational homogenization approaches, 2000, Int. J. Solids Struct. 37, 2285–2311].

Torquato and Stell (1982) [S. Torquato and G. Stell, Microstructure of two-phase random media. I. The n-point probability functions J. Chem. Phys. 77, 2071].

Torquato and Beasley (1986) [S. Torquato and J. D. Beasley, Effective properties of fiber-reinforced materials: II-Bounds of the effective elastic moduli of dispersions of fully penetrable cylinders, 1986, Int. J. Engng Sci. Vol. 24. No. 3, pp. 435-447].

Torquato and Lado (1988) [S. Torquato and F. Lado, Bounds on the Effective Transport and Elastic Properties of a Random Array of Cylindrical Fibers in a Matrix, 1988, Journal of Applied Mechanics, Vol. 55/347-353].

Torquato (1991) [S.Torquato, Random heterogeneous media : microstructure and improved bounds on effective properties, 1991, Appl. Mech. Rev. 44(2), 37-76].

Torquato (1998) [S. Torquato, Morphology and effective properties of disordered Heterogeneous Media, 1998, Int. J. Solid Struct. 35 (19), 2385–2406.].

Torquato (2002) [S. Torquato, Statistical Description of Microstructures, 2002, Annu. Rev. Mater. Res. 2002. 32:77–111].

Voigt (1889) [W. Voigt, Ueber die Beziehung zwischen den beiden Elasticitätsconstanten isotroper Körper, 1889, Ann. Phys. 274, 573–587].

Walpole (1966) [L. J. Walpole, On bounds for the overall elastic moduli of inhomogeneous systems—II, 1966, Journal of the Mechanics and Physics of Solids Volume 14, Issue 5, Pages 289-301].

Widom (1966) [B. J. Widom, Random Sequential Addition of Hard Spheres to a Volume, 1966, J. Chem. Phys. 44: 3888–3894].